Numerical Investigation of Single and Multiphase Supersonic Swirl Flow in Convergent-Divergent Nozzle

Ehsan Eslamian Koupaei

Department of Engineering and Built Environment

Anglia Ruskin University

This dissertation is submitted for the degree of

Doctor of Philosophy

Faculty of Science and Technology Aug 2015

I would like to dedicate this thesis to my loving parents

Safar-Ali Eslamian

and

Ashraf Hosseini

Declaration

I hereby declare that except where specific reference is made to the work of others, the contents of this dissertation are original and have not been submitted in whole or in part for consideration for any other degree or qualification in this, or any other University. This dissertation is the result of my own work and includes nothing which is the outcome of work done in collaboration, except where specifically indicated in the text.

Ehsan Eslamian Koupaei
Aug 2015

Acknowledgements

I would like to express my sincere gratitude to my supervisor, Prof. H. Shirvani, for his support, trust and encouragement throughout my Ph.D project. I am grateful that I had the opportunity of benefiting from his knowledge, brilliant advice and guidance.

Very especial thanks to Dr. A. Ramezanpour for sharing his considerable experience in CFD and understanding of flow physics with me, as well as kind encouragements and comments in this study.

I am grateful to all my friends and colleagues at Anglia Ruskin University not only for their support and comments that improved my work, but also for making enjoyable time at Anglia Ruskin University.

Finally, I would not have come this far without the support of my parents. They have always encouraged me to pursue in whatever I like, and gave me constant support and advice throughout my whole life.

Ehsan Eslamian K.
August 2015

Abstract

For decades, abrasive flow blasting, has been used for surface cleaning. As with all surface cleaning methods, of course the challenge is to achieve effective cleaning without damaging the surface. In abrasive flow process, the supersonic air flow is made to accelerate the suspended solid media particles transferring the momentum of the particles to a surface force creating the cutting/cleaning action. Therefore, the crucial performance parameters are those associated with the jet. However, the exhaustive literature search was unable to find much relevant reported work on improving the efficiency and energy consumption of sand blasting process. It is believed that the inherent problems associated with analysis of multiphase flow may be one reason for this.

Accordingly, this study has focused on single and multiphase jet flow with swirl in supersonic convergent-divergent nozzle using different range of inlet pressures (150kPa-400kPa). The Swirl was achieved by patented helical insert at the inlet of the nozzle, where the swirl effect provides a better mixing feature inside the nozzle and hence reduces the cleaning process time and energy consumption above 35%.

Numerical modelling was used to simulate both single and multiphase supersonic swirling flow inside and outside the nozzle. Eulerian and Lagrangian multiphase simulations were performed and it has been shown that for abrasive particles, the Lagrangian model (DPM) provides more accurate results. FLUENT and OpenFOAM, CFD software were used to solve governing equations of the flow with RANS turbulence modelling.

This research has found that the swirl effect reduces the shock cells strength inside the nozzle and increases the damping ratio on shock waves. The shock structure and separation zone for the non-swirl nozzle simulations was symmetrical; however, the nozzle with helical insert showed a very complex unsteady and asymmetric flow pattern. Additionally, it was observed that the swirl flow inside the nozzle creates larger separation zones at the exit of the nozzle which helps to improve the mixing feature. Furthermore, in this type of flow it was shown that, even if the nozzle was choked, increasing the inlet pressure increases the mass flow rate.

Keywords: CFD, Swirl, Supersonic nozzle, Multiphase, Discrete Phase Model

Contents

List of Figures

List of Tables

Nomenclature

Roman Symbols

$\mathbf{u}_r$	Relative velocity vector	$[L/T]$
ε	Turbulence dissipation	$[L^2/T^3]$
C	Courant number	[–]
c	Wave speed	$[T^2/L^2]$
C_d	Drag coefficient	[–]
C_l	Lift coefficient	[–]
c_p	Specific heat at constant pressure	$[L^2/T^2\theta]$
c_v	Specific heat at constant volume	$[L^2/T^2\theta]$
C_{vm}	Virtual mass coefficient	[–]
E	Energy of turbulent eddies	$[L^2/T^2]$
e	Internal energy per unit mass	$[L^2/T^2]$
e_t	Total energy per unit mass	$[L^2/T^2]$
F	Flux	$[M/T]$
F_d	Drag force	$[ML/T^2]$
F_i	Force in i direction	$[ML/T^2]$
F_l	Lift force	$[ML/T^2]$
F_{vm}	Virtual mass force	$[ML/T^2]$

g	Gravitational acceleration	$[L/T^2]$
I	Moment of inertia	$[ML^2]$
k	Turbulent kinetic energy	$[L^2/T^2]$
M	Mach number	[–]
m	Mass	$[M]$
p_0	Total pressure	$[M/LT^2]$
p_p	pressure at patch	$[M/LT^2]$
p_s	Separation pressure	$[M/T^2L]$
p_s	Static pressure	$[M/LT^2]$
p_t	Supply pressure	$[M/T^2L]$
Q	Rate of heat transfer per unit mass	$[L^2/T^3]$
q	Heat flux density	$[M/T^3]$
R	Specific gas constant	$[L^2/T^2\theta]$
Re	Reynolds number	[–]
S	Rate of transfer of mass per unit total volume	$[M/TL^3]$
S_ϕ	Source term	[–]
T	Temperature	$[\theta]$
t	Time	$[T]$
T_0	Total temperature	$[\theta]$
T_s	Static temperature	$[\theta]$
u	Velocity	$[L/S]$
u_τ	Shear velocity	[L/T]
v	Velocity in y direction	$[L/T]$

W	Rate of work per unit mass	$[L^2/T^3]$
w	Velocity in z direction	$[L/T]$
x	Length	$[L]$
A	Area	$[L^2]$
p	Pressure	$[M/T^2L]$

Greek Symbols

α	Volume fraction	[–]
δ	Kronecker delta	[–]
ε_{ijk}	Levi-Civital	$[--]$
γ	Blending factor	[–]
γ	Specific heats ratio	[–]
κ	von Karman constant	[–]
κ	wave number	$[1/L]$
λ	Under-relaxation factor	[–]
μ	Dynamic viscosity	$[M/LT]$
μ_t	Turbulent vscosity	$[M/LS]$
ν	Kinematic viscosity	$[L^2/T]$
ω	Angular velocity	$[1/T]$
ω	Vorticity	$[1/T]$
ϕ	Scalar quantity	[–]
ψ	Compresibility	$[T^2/L^2]$
ρ	Density	$[M/L^3]$
τ	Shear stress	$[M/LT^2]$

Γ_ϕ	Diffusivity	[–]

Abbreviations

AJM	Abrasive Jet Machining
AUSM	Advection Upstream Splitting Method
BD	Blended differencing
CAD	Computer Aided Design
CD	Central differencing
CD	Converging-Diverging
CFD	Computational Fluid Dynamic
CPU	Central processing unit
CV	Control volume
DNS	Direct Numerical Simulation
DPM	Discrete Phase Model
DVCS	Distributed Version Control System
E-E	Eulerian-Eulerian
E-L	Eulerian-Lagrangian
FSS	Free Shock Separation
GPL	GNU general public licence
HPC	High Performance Computing
LES	Large Eddy Simulation
MUSCL	Monotone Upwind Schemes for Scalar Conservation Laws
OF	OpenFOAM
OpenFOAM	Open Source Field Operation and Manipulation

PISO	Pressure-Implicit with Splitting of Operators
PR	Pressure ratio
psig	Pound per square inch gauge
RANS	Reynolds-Averaged Navier-Stokes
RNG	Renormalisation group theory
RSM	Reynolds Stress Model
RSS	Restricted Shock Separation
SIMPLE	Semi-Implicit Method for Pressure-Linked Equations
SOU	Second order upwind
TVD	Total Variation Diminishing
UD	Upwind differencing
V&V	Verification and Validation
VCS	Version Control System
VLES	Very Large Eddy Simulation
WENO	Weighted Essentially Non-Oscillatory

Subscripts

$(.)_C$	Continuous phase
$(.)_D$	Disperse phase
$(.)_e$	Exit of nozzle
$(.)_i$	Component in i direction
$(.)_j$	Component in j direction
$(.)_k$	Component in k direction
$(.)_N$	phase N

$(.)_t$	Throat of nozzle

Superscript

$\overline{\phi}$	Mean value
$\phi^{'}$	Fluctuating component

Chapter 1

Introduction

1.1 Problem statement

Sand blasting, which is formed by the nozzle with a mixture of air, water and abrasive media, has been used for many industrial applications such as cleaning or removing coating from different types of surfaces, surface strengthening and surface modification (Deng *et al.*, 2006) and can provide a perfect surface treatment for different materials such as plastics, composites, steel, aluminium, brass, ceramic tile, concrete, asphalt, decorative pavers, stone, brick, etc. (Jianxin *et al.*, 2003). In sandblasting treatment, abrasive material is accelerated through a nozzle due to pressure difference. As a result, in any sandblasting method nozzle geometry, jet velocity and impact angle (Bouzid and Bouaouadja, 2000) are the most important parameters to improve the effectiveness of sand blasting systems. Some sand blasting applications are illustrated in Figure 1.1.

There have been different studies and patents such as Chitjian (1987); Pawlik *et al.* (1981); Spitz (1987) who have looked at improving sandblasting making the process faster and more efficient, but none of them are working on fluid dynamic and pressure distribution inside nozzle. Blast cleaning for deposit removal is cost effective, although it can be time consuming. It has been shown that deposit removal and substrate deformation are strong functions of particle stream power, particle kinetic energy and impact angle (Raykowski *et al.*, 2001). In the sandblasting process the coating is removed primarily as a result of abrasive impact with a surface, therefore, increasing the impact area is another key parameter to making the process faster.

The main parameter that defines the speed and distribution of abrasive media is air. In order to provide high speed flow with lower pressure difference, a nozzle is used in abrasive blasting to increase jet velocity. Based on pressure difference and the fact that air is subsonic

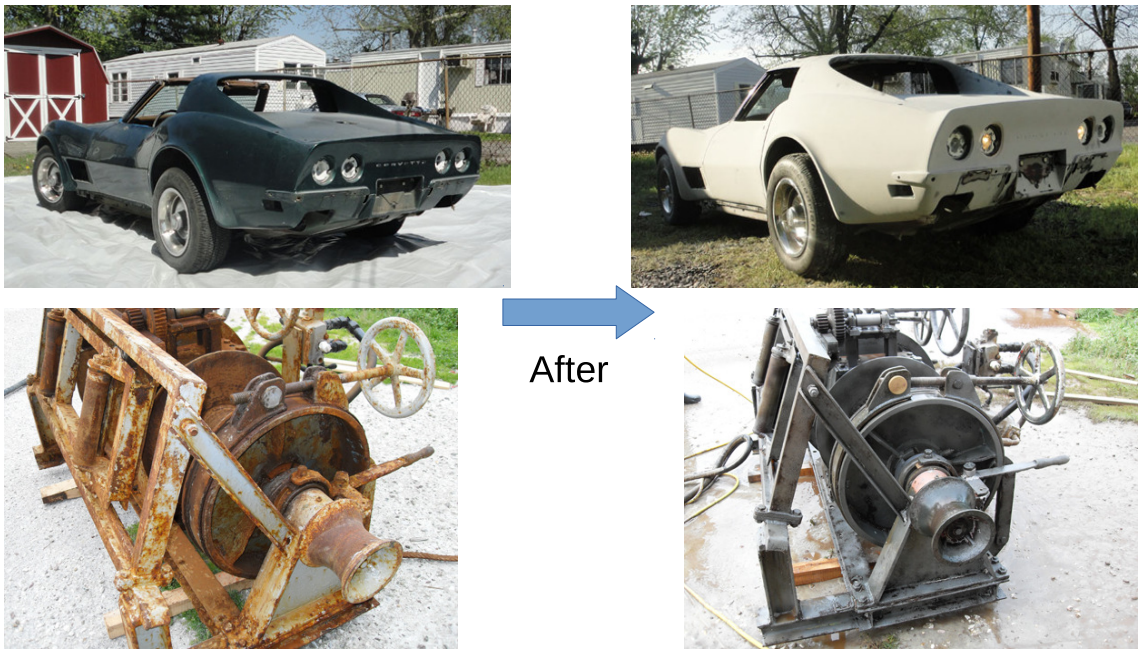

Figure 1.1: Abrasive blasting applications (Courtesy of Farrow System ®).

Figure 1.2: Abrasive blasting application on hospital wall (Courtesy of Farrow System ®).

or supersonic, a converging or Converging-Diverging (CD) nozzle will be used respectively. Almost all the studies on sand blasting nozzles relate to formal CD ones, which provides sufficient impact force with supersonic air. The major problem here is that abrasive media will be concentrated on the centre of the nozzle due to the pressure distribution inside the nozzle; hence the impact area will be reduced and could damage the substrate. Some studies, like Abbasalizadeh (2011) have used high temperature air in order to increase the impact area of the nozzle, which has proved to be successful. But increasing energy consumption in order to provide high temperature air is another key issue, and because an active system has been utilised maintenance costs will also increase.

Investigation into supersonic flow inside CD nozzles has been the subject of several numerical and experimental studies in the past (Anderson, 2000, 2003) because of their great application in propulsion, steam turbines and sand blasting but there is little research on the effect of swirl flow inside CD nozzles. Swirling flows are very common in technical applications, such as turbo machinery, cyclone or separators and they require rather sophisticated modelling. The effect of swirl inside a nozzle can intensify heat and mass transfer and improve mixing features of the flow by increasing turbulence and vorticity inside a nozzle, which can be useful not only in sand blasting methods, but also in combustion injectors for flame stability (Syred and Beér, 1974) or jet engines for noise reduction (Lu *et al.*, 1977; Schwartz, 1975), also swirl flow will change the shock structure and its interaction with the boundary layer. These numerous viscous and compressible phenomena affect the flow behaviour inside and outside of a nozzle.

The need for an accurate understanding of flow features inside the nozzle with swirl is very important in order to predict its effect. Since experimental data for the swirl flow inside a high speed nozzle is scare, the numerical results are vital to understanding the flow and determining further analyses. Computational Fluid Dynamic (CFD) can analyse flow inside and outside of a nozzle for less than it costs to set up the experiment. With the advances in computer hardware technology, powerful processors with high memory are now available. Consequently, CFD is the preferred tool for design optimisation and investigation for many engineering companies.

1.2 Present approach

This thesis is concerned with studying the idea of using swirl flow inside the nozzle in order to increase the performance of the sand blasting nozzle. The effect of swirl will provide a better mixture of sand inside the nozzle, which will increase the impact area without damaging the

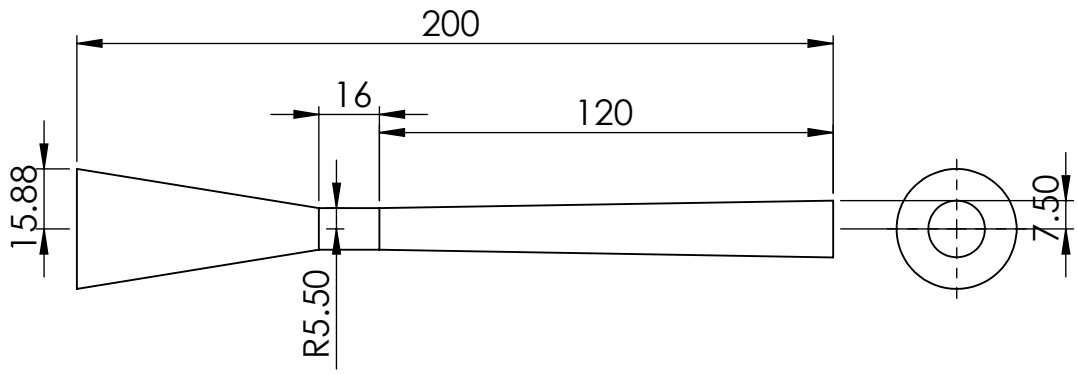

Figure 1.3: Geometry of the nozzle. This is inside geometry with zero thickness for the wall.

substrate. There are different ways to provide swirl flow, but for this study a helical insert was placed at the inlet of the nozzle to generate swirl flow. This is a totally passive system without any extra energy consumption or maintenance costs.

1.2.1 Geometry

The dimension of the nozzle, where the flow inside it has been investigated, is shown in Figure 1.3, the length of the nozzle is 200mm and has three sections. The first 64mm is the convergence section, then it is 16mm in constant 11mm diameter and the divergence section length is 120mm with an outlet diameter of 15mm. It should be pointed out that the thickness of the nozzle is zero. This is a standard geometry, which is used widely by sand blast companies.

In order to create swirl flow inside the nozzle, a helical insert has been added to the inlet of the nozzle. The geometry is not expensive to manufacture and is easy to install on any sandblasting nozzle. The geometry of the helical section is shown in Figure 1.4, it has a 31.75mm diameter with a length of 76.45mm, the spiral part has two revolutions with a start angle of 45 degrees.

The whole geometry is presented in Figure 1.5, where the helical insert and the nozzle will screw to each other. The total length of the domain is 276.45mm. All analyses are with the same geometry but different pressure ratios (PR).

1.3 Methodology

Any numerical methodology consists of mathematical representation and the solution procedure. The mathematical representation includes equations and matrices of physical or chemical

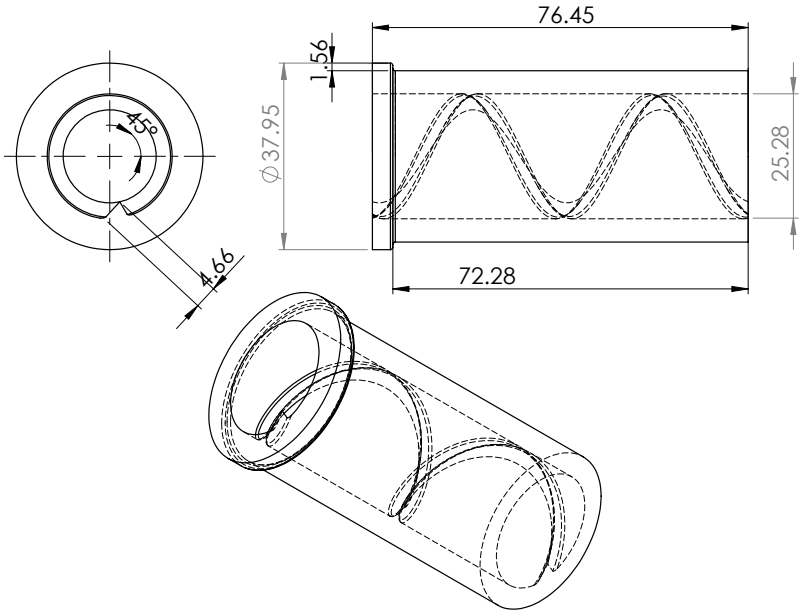

Figure 1.4: Geometry of the helical insert

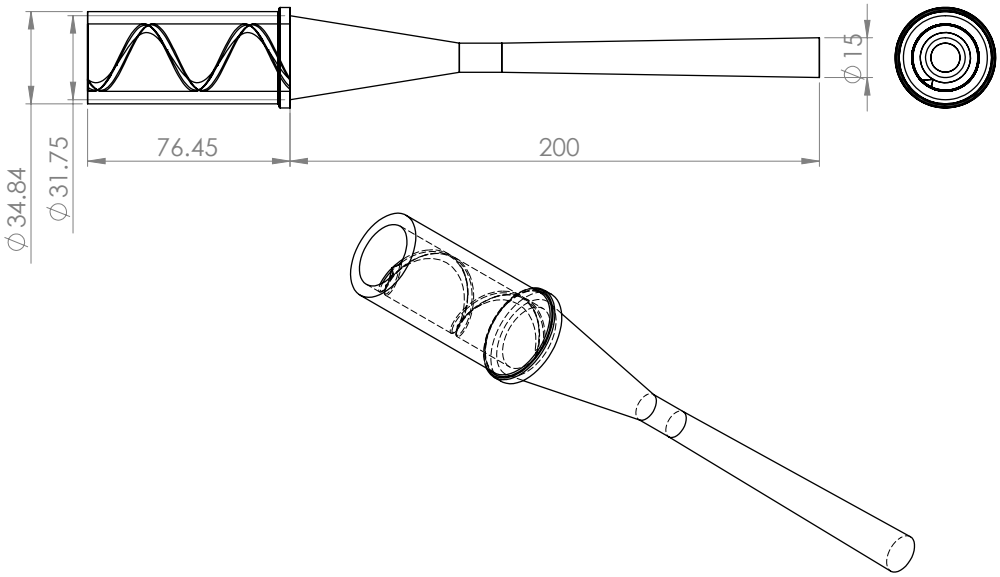

Figure 1.5: Geometry of the nozzle with helical insert

process to be simulated. The solution procedure is the way to solve or approximate mathematical equations numerically.

Two types of simulations have been conducted to understand the swirl flow the nozzle: single phase simulation of air and multiphase simulation of air and sand.

1.3.1 Single phase

As previously explained, air is the main factor inside a nozzle that defines the performance of the nozzle. Although in sand blasting the process is not single phase, understanding the air inside nozzle is a key factor to improving it. Phenomena such as shock waves and expansion fans, turbulence and viscosity have strong impact on sand distribution inside a nozzle

The starting point of the work is using commercial software, FLUENT, for single phase simulation of air inside the nozzle with a helical insert to create swirl flow. Different Reynolds-Averaged Navier-Stokes (RANS) turbulence models such as$k-\varepsilon$,$k-\omega$, and Reynolds Stress Model (RSM) has been used to accurately simulate swirl flow inside the nozzle. Advances in computer speeds have made it possible to use Large Eddy Simulation (LES) and Direct Numerical Simulation (DNS) for many applications. For supersonic flow and complex configurations such as high speed swirl flow, DNS or even LES is still impractical because of grid spacing requirements and the time required for running simulations (Lillard, 2011).

Because of CPU limitation with commercial software licensing, it was not possible to use FLUENT for higher mesh resolutions as running each model would take a very long time. To take advantage of parallel processing, OpenFOAM[1]2.2.x code was used to solve flow parameters inside and outside the nozzle. OpenFOAM is a C++ toolbox based on object oriented programming (Weller *et al.*, 1998) under the GNU general public license (GPL) (OpenFOAM, 2013). OpenFOAM offers the flexibility to solve all different types of engineering problems and in contrast to closed source programmes, allows the freedom to study, modify and compile the source code to match your requirements. In this research, OpenFOAM provided the opportunity to study and modify boundary conditions and create non reflective, pressure variable outlet for more realistic simulation of flow inside and outside the nozzle.

OpenFOAM also provides the ability to efficiently use, Version Control System (VCS) to backup and have collaborative work. VCS records changes to a set of files and makes it possible to revert to any specific version later. There are different types of VCS but for this research "Git" which is Distributed Version Control System (DVCS) has been used. In DVCS repository is mirrored between server and clients. All OpenFOAM cases already exist on the

[1]Open Source Field Operation and Manipulation

"bitbucket[2]" website for future use and improvement by other researchers and engineers.

1.3.2 Multiphase flow

The term multiphase flow refers to any fluid flow consisting of more than one phase or component. Phases considered here are at scales well above molecular level. The ability to simulate multiphase flow is an important addition to the arsenal of CFD techniques, and provides more realistic simulation for engineering challenges.

Sand blasting could be a two phase flow, air and sand (dry blast), or three phase flow, which are air, sand and water (wet blast). In either of these cases, the flow regime will be dispersed flow. Dispersed flow consists of finite particles, drops or bubbles (disperse phase) in connected volume of continuous phase[3].

Dispersed flows can be modelled in two ways, one is Discrete Phase Model (DPM)[4] where the motion of the dispersed phase is obtained by solving its own equation of motion, this is also called the Lagrangian approach. An alternative approach, the dispersed phase is treated as a continuous phase where each phase will satisfy governing equations individually, this is also called the Eulerian approach (Ishii, 1975). Both models have been used to simulate the sandblasting process with swirl flow inside the nozzle.

1.3.2.1 Lagrangian approach

The DPM considers that the topology of multiphase flow is dispersed. Therefore, there is one continuous phase and one or more dispersed phases. In the Lagrangian approach, each individual dispersed phase elements are tracked through the flow domain by solving the equation of motion. The equation of motion is the conservation equation of momentum obtained in Lagrangian formulation, in which dependent variables and particle properties are followed by particle motion. However, the conservation equations for continuous phase are expressed in Eulerian frame, where fluid properties and dependent variables are solved in an absolute (global) frame of reference. Because of the mixed treatment of DPM it is also referred to as the Eulerian-Lagrangian model (E-L). In Figure 1.6 "Fluid1" represents the continuous phase where dispersed phase "particles" are moving through it.

An important advantage of DPM lies in the possibility to store data of each dispersed phase such as rotational speed, size, shape, etc. separately, and because there is one equation

[2] www.bitbucket.org/EhsanESL

[3] The other type of multiphase flow regime is separated flow, which consists of two or more continuous phases separated by an interface.

[4] In some literature is called Discrete Phase Element (DPE).

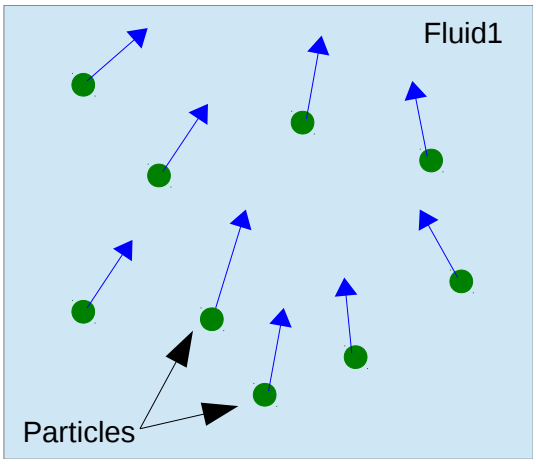

Figure 1.6: Multiphase Lagrangian approach

of motion for each particle, it is easy to find the distribution of particle sizes. However, its limitation is when the volume fraction of a dispersed phase is above 10-12% (Ansys, 2010), because on high volume fractions, increased coupling between continuous phase and discrete phase elements could create numerical stability problems (Kralj, 1996).

1.3.2.2 Eulerian approach

In the Eulerian model, all phases are considered continuous and each phase is described by solving Eulerian conservation equations in fixed coordinate; Hence it is also called the Eulerian-Eulerian model (E-E). The mathematical conservation equations are similar to single phase equations with extra terms related to the transfer of mass and momentum between phases. Figure 1.7 shows a sketch of E-E model, where Fluid1 and Fluid2 are both continuous phase and they are solved within the control volume to find the velocity and volume fraction of each phase.

The Eulerian model is the preferred method for problems with high volume fraction. However, because it solves all conservation equations for each phase individually, its performance and number of phases are limited by the amount of memory available.

1.4 Aim and objectives

The aim of this research is to provide full numerical analysis of swirl flow inside and outside of a CD nozzle. This includes both single phase and multiphase flow modelling. Results will be used primarily for sand blasting to make the process faster and more efficient. The goal is to make deposits removal faster while minimising substrate deformation. This will be achieved

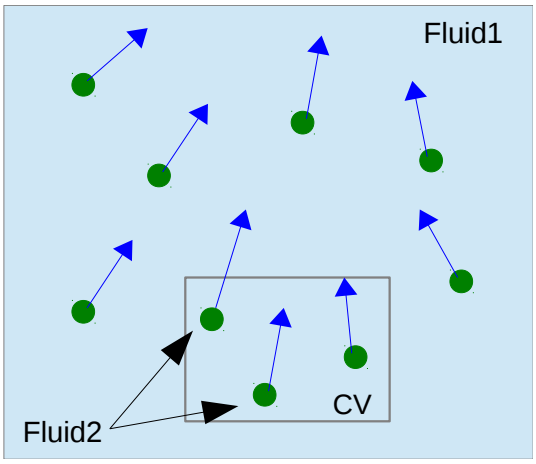

Figure 1.7: Multiphase Eulerian approach

by a better mixture of air and abrasive media, and increasing the impact area of the nozzle. Below are a list of objectives which have been derived to guide this study toward completion:

- Understand supersonic swirl flow inside the nozzle.
- Understand supersonic swirl flow outside of the nozzle.
- Study characteristics of supersonic swirl flow.
- Study multiphase swirl flow inside the nozzle.
- Identify limitations of commercial CFD software (FLUENT).
- Develop OpenFOAM setup for inside and outside the supersonic nozzle.
- Develop boundary condition setup for nozzle simulation of OpenFOAM.
- Perform parallel processing for mesh generation (snappyHexMesh).
- Study the effect of swirl on flow features and shock wave structure at different pressure ratios.
- Investigate differences of shock waves in the nozzle with and without swirl flow.
- Study mass flow rate and choking phenomena in a nozzle with and without swirl flow.

1.5 Thesis structure

This thesis is divided into seven chapters. Chapter two covers a literature review of different topics. It begins with an overview of previous research in abrasive blasting and by describing different types of it. It continues by reviewing numerical and experimental works on multiphase flow with particle simulations and supersonic nozzles. This chapter ends by reviewing previous swirl flow applications and the effect of swirl on noise reduction.

Chapter 3 provides a detailed description of numerical methods used in this research. This includes governing equations for single phase and multiphase flows, discretisation methods and schemes for governing equations, numerical solution procedures for pressure based and density based solvers, boundary condition types for FLUENT and OpenFOAM, and finally turbulence modelling methods used for simulations.

Chapter 4 includes all FLUENT results. First single phase simulations are performed for inside and outside the nozzle for inlet pressures 2atm to 4atm. Results for non swirling and swirling flows are compared to each other. Multiphase simulations are then performed with both Eulerian and Lagrangian methods. The effect of particle distribution inside the nozzle with swirl effect has been investigated.

Chapter 5 presents the findings from OpenFOAM simulations. Inside the nozzle and full domain simulations are performed for various inlet pressures from 150kPa to 400kPa. The effect of inlet pressure on mass flow rate is investigated. In addition, the influence of swirl flow on flow separation, shock cells structure and jet boundary instabilities is analysed.

Chapter 6 outlines the verification and validation process for numerical simulations. The verification includes code verification, grid independence test, residual monitoring and y^+ distribution. In the validation section, a benchmark experiment has been used to validate numerical models for supersonic simulations inside the nozzle.

Chapter 7 includes conclusions from the results obtained in this research. Additionally, recommended direction and topics for future studies are discussed.

Chapter 2

Literature review

2.1 Abrasive blasting

Abrasive blasting or sandblasting is a process of propelling a stream of high velocity abrasive media against a surface to smooth rough surface or remove surface containments such as rust, dirt, colour and any other surface coating. It became famous as sandblasting because sand was sprayed as only abrasive material in old times. Nowadays Aluminium oxide, glass grit, plastic, walnut shell and some other materials (explained in Appendix B) are used as abrasive material. It has become more economical to use recyclable, non-metallic media and also it is important for sandblasting companies to use safe and environmental friendly abrasive media. If the abrasive waste is hazardous or toxic, disposal options become limited and the cost of disposal can exceed the original cost of the abrasive.

Porter *et al.* (2002) has compared Pulmonary toxicity of six different abrasive materials on an animal and found out that specular haematite did not significantly elevate actate dehydrogenase (LDH) or polymorphonuclear leukocytes (PMN) levels. In contrast, coal slag caused greater pulmonary damage and inflammation than blasting sand, while Garnet, staurolite, and treated sand exhibited toxicity and inflammation that were close to blasting sand.

A chemist, Benjamin Chew Tilghman in 1870, invented the first sandblasting process[1]. In his system the abrasive media had been shot to a surface by steam instead of high pressure air. He designed both direct air pressure type and suction type. In direct air pressure type, the abrasive media directly jets from pressurized tank to a nozzle, however on suction type, abrasive media are sucked to a nozzle due to negative pressure by high speed air inside a nozzle. The first modern sandblasting machine was invented by Leonard Muste in 1923 (Muste, 1923).

[1] US patent 104,408

Table 2.1: Fuel consumption at various compressor discharge pressures. (Seavey, 1985)

Compressor discharge pressure(psig*)	Fuel consumption (gph)
80	9.13
100	10.06
120	10.85
140	11.71

*Pound per square inch gauge

There are two major types of sand blasting: wet blast and dry blast. In wet blast abrasive particles are mixed with the water before jetting from a nozzle but in dry blast abrasive particles are shot to a surface by just the air. The water droplets in wet blasting are used for suppressions of dust produced by crashing of sand particles. The machinery that is used today has been refined over almost 150 years, to have better performance, consume less energy and being environmentally friendly. Modern sandblasting machines are designed and engineered to operate at wide pressure range with minimal pressure drop. Further to that, they have to provide an optimum mixture of air and abrasive for a full range of abrasive materials with different size and composition.

Sandblasting machines operate at a pressure range from 30-130psi. However, for most of the applications they are operating at pressures less than 60psi to avoid damaging a working surface and save energy. Although the experimental study by Seavey (1985) for abrasive blasting in excess of 100psi at the nozzle, shows that by increasing the pressure from 60psi to 140psi, productivity and efficiency continues to increase. This has been shown for different abrasive materials in Figure 2.1. However, as the discharge pressure increases, the fuel consumption increases as well to provide horsepower requirements for compressor system (Table 2.1). Keener *et al.* (1993) explains that if a sandblasting machine uses steel abrasive media, its productivity will increase 125-150 percent by operating in the range of 120-150psi; But using mineral abrasive at these high pressures does not improve productivity because of the excess energy will breakdown particles and increases abrasive consumption.

Up to 1950s sandblasting nozzles had a converging section along constant area pipe shape. Introduction of converging-diverging nozzles made the abrasive blasting process more efficient than before (Kline *et al.*, 1988). The computational and experimental research by Settles and Garg (1996) demonstrates that there is a lot to gain in abrasive blasting by technology transfer from aerospace engineering such as rocket propulsion. It has been shown that for maximum productivity, nozzles should always operate higher than their design pressure. The

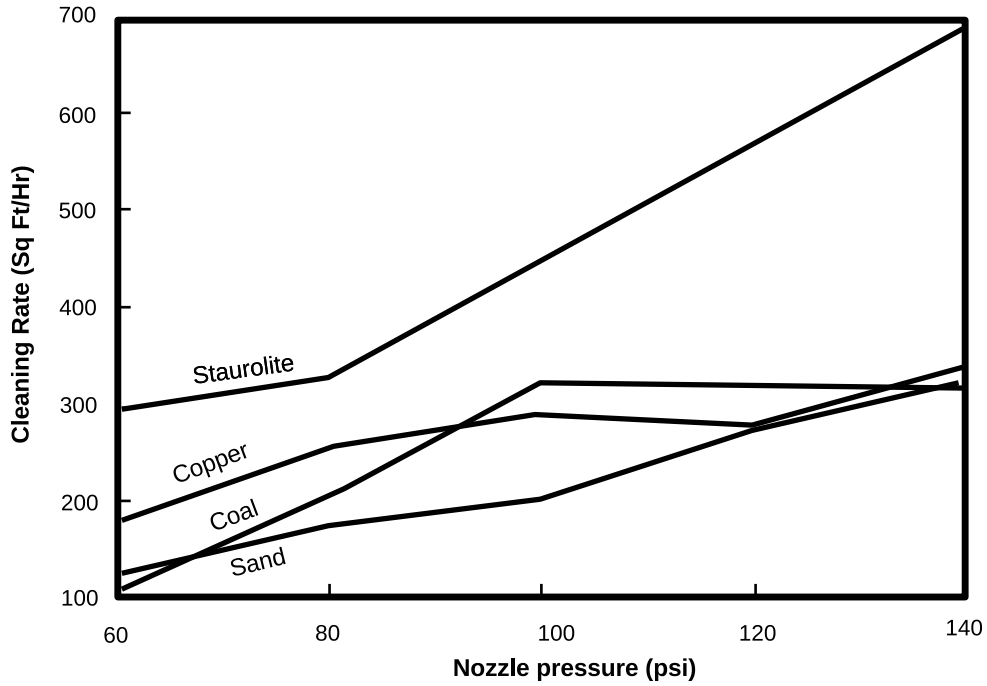

Figure 2.1: Effect of nozzle pressure on cleaning rate. (Seavey, 1985)

efficiency of a typical blasting machine can be raised from 10 to 18 percent just by improved nozzle design.

2.1.1 Dry-ice blasting

Using chemicals in jet cleaning processes could involve high reconditioning and disposal costs. Also, for delicate and sensitive materials, abrasive blasting with sand, steel or glass might cause damage to a part. Cold Jet© completed the first patented and commercial dry-ice blasting machine in 1988.

This process is pneumatic jet-based and operates with dry-ice pellets as the single-way blast medium. Dry-ice pellets consist of solid carbon dioxide CO_2 at a temperature of -78.5ºC (Spur *et al.*, 1999).

The study of dry-ice blasting process, optimization and application was presented by Spur *et al.* (1999). The active mechanism of dry-ice blasting process and impact force were investigated. In addition, the diameter and velocity of the CO_2 pellets in the jet measured. According to this method, the silicone seals in exchange engine production removed without significant changes in structure or surface damage.

2.1.2 Micro abrasive blasting

Micro abrasive blasting[2] is becoming an important cost effective method for the fabrication of micro devices and reliable technique for advancing the life of tools under the process of turning, milling, drilling, punching and cutting. For micro abrasive the air pressure range is between 0.2 and 0.9MPa and particles with diameter between 4 to 100μm are used. In micro abrasive the productivity is high and heat affected layer caused by material removal are very thin, thus it is suitable micro machining method for hard and brittle materials (Park *et al.*, 2004). Dry micro abrasive is an important technology for the production of micro-parts of semiconductors and LCD.

Karpuschewski *et al.* (2004) has shown that a line shape Laval nozzle offers the best performance as provide homogeneously dispersed particles with velocities in the supersonic regime. A simple converging round nozzle results in uncontrollable material erosion due to high concentration of particles at a centre of nozzle, which is consequence of boundary layer effect. In this research, in order to calculate particle exit velocity they have developed a one dimensional compressible model which particle-particle and particle-wall interactions were excluded.

For micro abrasive blasting the area of blast spot A_s, is calculated by Achtsnick *et al.* (2005)

$$A_s = 2\tan(\delta)NTD(x_0 + y_0) \tag{2.1}$$

where $(x_{0,}y_0)$ is the nozzle dimension, δ is dispersion angle and NTD is the nozzle tip distance. The airflow properties were calculated using the standard equations for one-dimensional compressible isentropic flow through a duct and particle-particle and particle-wall interactions were excluded. Achtsnick *et al.* (2005) demonstrated that de-Laval nozzle which provides homogeneous dispersed particles with velocities in the supersonic regime, delivers the best results for micro abrasive blasting process.

Kennedy *et al.* (2005) has discovered that micro shot blasting of cutting tips and tools has a positive effect on component surfaces by increasing toughness, operating life, improving hardness and surface finish. It is found out that micro blasting will change resistance to fatigue fracture, resistance to stress corrosion, change in residual stresses and modification of surface finish in a material's surface.

[2] Also called Abrasive Jet Machining (AJM).

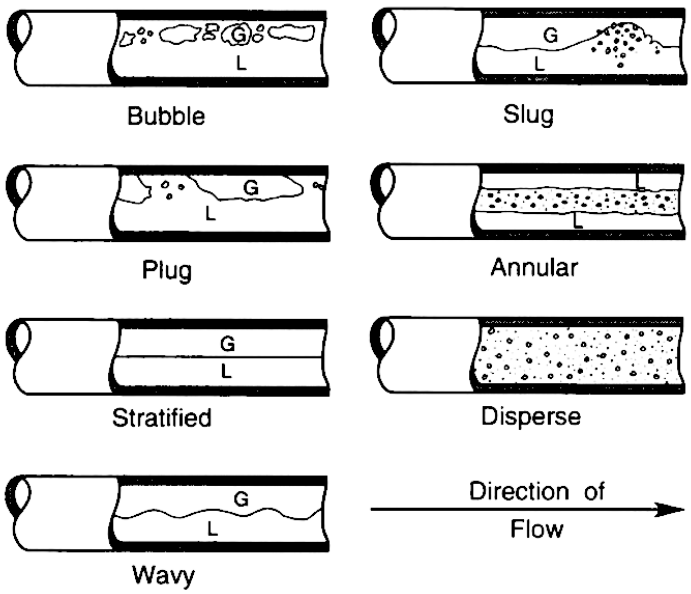

Figure 2.2: Flow regime for multiphase air-water mixture in horizontal 5.1cm diameter pipe (Brennen, 2005).

2.2 Multiphase flow

In multiphase flow there is simultaneous flow of either materials with different states or phases (gas, solid or liquid), or materials with the same state or phases but different chemical properties. In multiphase flow terminology a phase is called "continuous" if it occupies continuously connected region of space and is called "disperse" when it occupies disconnected region of space. Disperse phase is in shape of particles and they are denoted as bubbles if are in the gas phase, while particles in fluid phase are denoted as drops.

Multiphase flows can appear in different types of phase distribution that are usually called flow regime or flow pattern. For example, Figure 2.2, shows flow regimes for air-water mixture in a horizontal pipe. In horizontal pipe flow pattern depends on component volume fluxes, volume fraction and properties such as viscosity, density and surface tension (Rouhani and Sohal, 1983). Gas-solid multiphase flows are classified in the two dense or dilute regimes. If the volume fraction of particles is less than 10^{-3} then the gas-solid is in dilute regime and when the volume fraction of particles is greater than 10^{-3}, the flow regime is dense (Elghobashi, 1994). For dilute regimes with volume fraction less than 10^{-6} one way coupling ($Fluid \rightarrow Particle$) and for dilute regimes with greater volume fraction two way coupling is required ($Fluid \longleftrightarrow Particle$), while for dense regimes four way coupling ($Fluid \leftrightarrow Particle \leftrightarrow Particle$) is essential.

In multiphase flow there are three types of forces acting on phases. Volume forces such as gravity, inertia and buoyancy force, surface forces such as pressure or viscous force, and line forces like surface tension force. For a particle immersed in a continuous fluid, there are pressure forces and viscous forces that are acting on a surface of a particle. Therefore, the resulting force (drag force) implemented by a surrounding fluid on a particle is closed integral of the pressure and viscous stresses acting on a particle surface (Wörner, 2003).

The two fluid model (Eulerian-Eulerian) can in principle be used to solve any multiphase flow regime, considering adequate closure relations for the momentum equation are provided. However, Eulerian-Lagrangian model is suitable only for disperse flows. In the E-E approach the flow variables are function of space and time and hence are represented as fields. In the E-L method particles are considered individually and the position and velocity of each particle are only functions of time. Therefore, in E-L approach Navier-Stokes equations are solved for the continuous phase (similar to E-E method). However, for disperse phase positions and velocity of each particle is obtained from Newton's second law.

The research by Oesterle and Petitjean (1993) has presented a Lagrangian simulation technique for dense gas-solid suspension flows. In contrast to dilute gas-solid flows, when there is high concentration of particles as a second phase the effect of particle to particle collision becomes important. Campbell and Brennen (1985) has simulated two dimensional granular shear flow with cylindrical particles. The simulations were based on the simultaneous calculation of several particles trajectories, in order to predict the flow of a particle cluster; But this method will be limited by memory size for computation of small particles over long distance. Oesterle and Petitjean (1993) method has introduced artificial inter particle collisions during trajectory calculations to compute reasonable number of successive particle trajectories.

Granular materials that are created from crushing or mining operations are generally highly angular or plastics abrasive media usually are in cylindrical shape. However, most of computational analyses of multiphase granular flows are performed for perfect sphere. Some studies such as Vu-Quoc *et al.* (2000) and Džiugys and Peters (2001) have worked on elliptical shape particles that are created from combination of spheres or study by Hopkins and Shen (1992) that has worked on sphere and disk shape particles. The major problem for non-spherical particles is to detect the contact with the neighbour particle and to calculate the overlap area. For spherical particles, it is easy to detect collision and contact area as the orientation of particles are not important. It is suggested by Campbell (1990) that spherical particles are good approximations for sand particles. Although sand particles are angular, but still are roughly in spherical shape and even they will become more spherical after collisions break off any bumps.

Hu *et al.* (2001) has developed Direct Numerical Simulations (DNS) of fluid–solid system using the Arbitrary Lagrangian Eulerian technique. In this method moving finite element unstructured mesh is used to find position of particles. The particle positions are updated explicitly, while particle velocities and fluid flow are solved implicitly. Also, different models of particle collisions in channel flow are investigated.

Kuan *et al.* (2007) have performed CFD simulations of dilute gas-solid flow through a curved 90º duct bend with the E-L model. The flow parameters were calculated based on differential Reynolds Stress Model[3] at $Re = 10^5$. The study shows that prediction of gas flow parameters has a strong influence in the prediction of particle velocities. Investigation on the effect of particle wall interaction has also shown that it can considerably affect particle velocities and distribution of particles near the wall.

Hou *et al.* (2007) has studied numerically inside and outside of the abrasive water jet nozzle. The Eulerian two phase model has been adopted to simulate flow fields. It has been shown that due to the nozzle geometry swirl flow is created inside the nozzle. Because of the swirl effect abrasive particles are distributed along the nozzle wall and there is not concentration of particles in the centre of the nozzle. Although the results are acceptable, but Hou *et al.* (2007) has also demonstrated that the Eulerian two phase model is not able to predict the velocity of solid phase correctly.

In the research by Van Wachem *et al.* (2001) different formulations for two phase gas-solid flow in Eulerian-Eulerian framework have been compared. It has been shown that governing equations for gas-solid flow is different to gas-liquid flow. In fluidized bed test case, the main dominant forces were drag and gravity, and the model was not sensitive to different solid stress models.

Particle behaviour near a flat wall in a dilute turbulent gas-solid boundary layer is investigated numerically by Dehghan and Tabrizi (2012). The E-E model with two way coupled is used to investigate flow density, material density, particle diameter and free stream velocity. It has been shown that particle viscosity and the accuracy of viscosity simulation have a significant effect on velocity of solid particles especially near the wall. However, particle trajectory away from the wall is independent of solid-phase viscosity.

2.2.1 Fluidized bed

Modern sandblasting machines either dry or wet blast have pressurised blasting tank or fluidized bed to mix particles with the air. Fluidized bed is a tank with solid particles that mix and

[3] in algebraic RSM, algebraic equations are solved for Reynolds stress components; However, in differential RSM, differential transport equations are solved individually for Reynolds stresses.

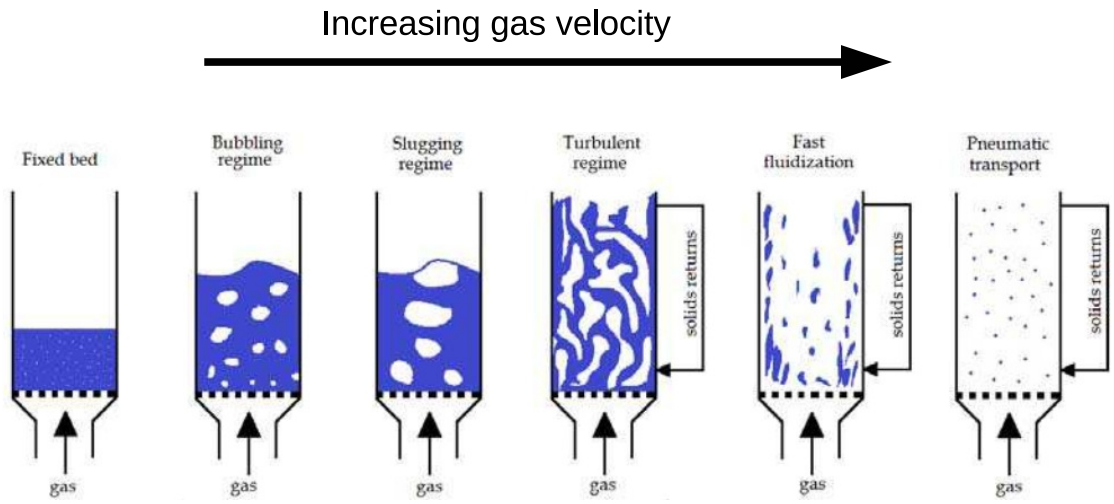

Figure 2.3: Flow regimes of gas–solid Fluidization (Silva *et al.*, 2012).

interact with pressurized fluid to behave like fluid for different purposes. The first fluidized bed was developed in Germany by Fritz Winkler in the 1922 for a coal gasification process (Crowe, 2014) in which dried coal is mixed with oxygen and steam in fluidized bed. Then in 1930 the US oil industry began developing fluidized bed technology for oil feedstock catalytic cracking (Tavoulareas, 1991). Fluidization happens when the drag force from velocity of a gas on particles is equal to downward gravitational forces (buoyed weight), causing particles to suspend within the fluid.

In dry abrasive blasting there is two phase gas-solid flow regimes. Different flow regimes will be observed in gas-solid fluidized bed based on the velocity of a gas. As the velocity increases the flow regime will change from fixed bed to bubbling regime, slugging regime, turbulent regime, fast fluidization and pneumatic transport (Figure 2.3). The bubbling, slugging and turbulent regime is called 'aggregative fluidization' as well. Bubbles coalesce as they rise through the bed, and form large bubbles that are called slugs. The bubbles appear to be very similar to gas bubbles formed in a liquid and they behave in a same manner. Flow regimes for gas-solid fluidization are explained in detail by Bi and Grace (1995).

The effect of inter-facial drag coefficient for CFD simulation of gas-solid flow in circulating fluidized bed has been investigated with the energy-minimization multi-scale (EMMS) approach by Yang *et al.* (2003). It is suggested that the mechanisms of gas–solid interactions should be analysed for different scales: the interaction between a single particle and the nearby fluid inside both the dense and dilute phases (micro-scale), and the interaction between clusters and the surrounding dilute broth (meso-scale). The simulation results of Yang *et al.* (2003) show that the drag coefficient calculated from the EMMS model is much lower than

that from the Ergun and Orning (1949) correlations. It is observed from the average value of outlet flux that Ergun drag model (Ergun and Orning, 1949) is over predicting the drag coefficient.

The research by Xu and Yu (1997) has numerically modelled gas-solid flow in fluidized bed by combining discrete phase model (DPM) and CFD. In DPM-CFD model, the gas flow properties are solved by Navier-Stokes equation and motion of individual particles is derived by Newton's second law of motion. The results from Xu and Yu (1997) simulations indicate that DPM-CFD model can provide accurate and realistic solutions for two phase gas-solid model such as fluidized bed at different levels.

Van der Hoef *et al.* (2008) has reviewed numerically gas-solid fluidized bed on the basis of whether a Lagrangian or an Eulerian model is used for the gas or particulate flow. It is suggested the Lagrangian-Lagrangian (L-L) model that both gas phase and solid phase are represented by particles, is useful only for gas-solid flow at extremely small scales, in which the thermal fluctuations of the gas phase have an influence on the motion of the large particles (Brownian motion). On the other end of the scale is Eulerian-Eulerian (E-E) approach, in which both gas phase and solid phase are solved based on continuum description. The interaction between two phases is resolved by drag force correlations which depends to the relative velocity of phases and volume fraction of solid phase. The problem of this model is that it does not accurately model gas-particle and particle-particle interactions. To overcome this drawback the Eulerian-Lagrangian model (or DPM) has been proposed. Van der Hoef *et al.* (2008) has concluded that for gas-solid fluidized bed the DPM model provides the best results and E-E model can simulate fluidized beds only at engineering scales (height 1-2m) where particles size are at least one millimetre.

Pei *et al.* (2012) has used Eulerian-Eulerian model to simulate gas-solid two phase flow for jetting fluidized beds. Zero particle viscosity is used and it has shown that the selection of inter phase drag force model has significant influence on the simulation of jetting fluidized bed. It is as well shown that E-E model (two fluid model) could not predict all flow parameters accurately.

In wet blasting, pressurized tank has three phases: gas, solid and liquid. Three-phase flow regimes inside the fluidized bed were investigated by Chen *et al.* (1995). In this study, the pressure fluctuation characteristics were applied for recognizing different regimes such as total homogeneous bubble regime, total transient regime, and total turbulent bubble regime. On the other hand, depending on the operating conditions they could observe two or all three regimes simultaneously at different heights of fluidized bed.

Chen *et al.* (1995) found that flow regimes are independent on radial positions across the

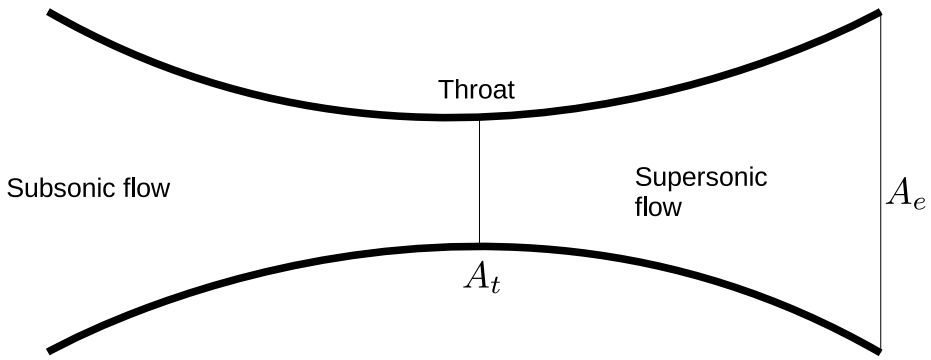

Figure 2.4: Schematic of Converging-Diverging nozzle.

fluidized bed. In addition, three-phase flow regimes inside the fluidized bed depend on operating conditions could vary in axial direction. Finally, the axial distribution of solid particles hold-up in three-phase fluidized bed is modelled by the exponential function.

The recognizing of the boundary between particles and circulating three-phase fluidization regimes are applicable by analysing of the fluctuations of the voltage signals (Vatanakul *et al.*, 2005). In this method, the particle size, liquid viscosity, gas flow rate, superficial liquid velocity, and solid circulating rate are significantly effective on the characteristic of the voltage signals.

2.3 Supersonic nozzle

In order to accelerate a flow to speeds higher than Mach 1, it is essential to use converging-diverging (C-D) nozzle (Figure 2.4). The C-D nozzle is called de Laval as well as it was invented by Swedish engineer Gustaf de Laval in 1888 to improve steam turbine performance.

For isentropic one-dimensional flow through a C-D nozzle, the Mach number at any cross section of surface area can be calculated from Stodola's area-Mach number relation (Stodola, 1903):

$$\left(\frac{A}{A_t}\right)^2 = \frac{1}{M^2}\left\{\frac{2}{\gamma+1}\left[1+\frac{1}{2}(\gamma-1)M^2\right]\right\}^{\frac{\gamma+1}{\gamma-1}} \tag{2.2}$$

where A_t is throat area and γ is ratio of specific heat. This is still widely used correlation, and some researches such as Haselbacher *et al.* (2010); Thakre and Yang (2008); Zhang *et al.* (2009) have used it to verify code or provide initial condition for their compressible solver. However, in order to find the solution for equation 2.2, it is required to perform iteration or

utilize numerical root finding. The study by Majdalani and Maicke (2013) has introduced analytical solutions that are derived from Burmann's theorem and Method of successive Approximation. The analytical solution makes easier to accommodate temperature variation specific heat ratio. Olles *et al.* (2004) and Majdalani and Maicke (2011) as well have provided closed analytical formulation, which produces the Mach numbers explicitly as a function of the area ratio and the ratio of specific heats.

Simulation of solid-propellant rockets with Aluminium droplets has been performed by Najjar *et al.* (2006) in which burning of aluminium droplets generate aluminium-oxide smoke. The effects of injected droplet size distribution were investigated. Eulerian formulation for simulation of fine smoke particles has been used in conjunction with a Lagrangian formulation for the larger aluminium droplets.

A supersonic coaxial jet has been investigated experimentally and numerically by Cutler and White (2001). The centre jet in this research is a light gas and the co-flow jet is air. For CFD simulations Wilcox $k-\omega$ model and Reynolds Stress Model with $k-\omega$ model were tested. It has been found out that both turbulence models under predicted mixing at the outer edge of the centre jet and at the interface between co-flow jets with ambient mixing layer.

The study by Li and Li (2005) has numerically analysed the behaviour of spray particles in cold spray gun nozzle. Two phase flow DPM relation along $k-\varepsilon$ turbulence model were used for simulations. CFD results show that the nozzle exit diameter has significant influence on particles velocity. It is mentioned that particles velocity will reduce significantly along the shock waves outside of the nozzle. It has been found out that the particle velocity will increase with increasing gas inlet temperature. This is shown by Dykhuizen and Smith (1998) as well, where in cold spray the velocity of the gas is derived from:

$$V_g = M\sqrt{\gamma R T_g} \tag{2.3}$$

where V_g and T_g are velocity and temperature of the gas.

Mixing performance of the rectangular nozzle with trailing edge modification was investigated experimentally by Kim and Samimy (1999). In the underexpanded modified nozzle the spanwise pressure gradient was significant enough to create streamwise vortices and therefore substantial mixing enhancement was achieved. However, in the overexpanded nozzle the streamwise vortices were not strong enough and thus mixing enhancement was not substantial.

Mouronval *et al.* (2003) has studied numerically two-dimensional asymmetric nozzle flows. Finite difference with the fifth order WENO scheme and Lax-Friedriches splitting at cell interfaces were used to capture shock waves and other discontinuities without oscillations. The

CFL number used in simulations was set to 0.8. It has been found out that the strength of the primary shock wave decreases at the beginning of the start up process while the strength of the secondary shock wave increases. In Mouronval *et al.* (2003) calculations, the shock velocities on the centreline matched their one dimensional counter parts.

2.3.1 Separated nozzle flow

The realistic behaviour of the flow inside of supersonic nozzles is not compatible with the theoretical inviscid description. Because in reality, there could be oblique shock wave inside a nozzle therefore the flow may separate from the walls (Figure 2.5). Separation happens at the upstream of where a normal shock would occur and the pressure on the wall will rise much more rapidly to ambient pressure (Morrisette and Goldberg, 1978).

Two types of separation pattern can be observed in a supersonic nozzle, the free shock separation (FSS) and the restricted shock separation (RSS). In FSS flow separates from the nozzle wall due to oblique shock, and the separation zone continuous to exit of a nozzle as a free jet. In RSS, the separation is restricted to a limited size, and will reattach to a nozzle wall before exit of a nozzle. Both FSS and RSS can be observed in a nozzle at different operating conditions, which highly depends to shock boundary layer interactions.

It was observed by Summerfield *et al.* (1954), the flow separation in overexpanded conical nozzles will happen as soon as the wall pressure at the nozzle exit was lower than about 40 percent of the ambient pressure. Hence, the corresponding formula has been called "Summerfield criterion"

$$p_{sep} \approx 0.4 p_a \tag{2.4}$$

It was shown that once the flow was separated, no reattachment occurred. With extensive investigation of the flow separation by Frey and Hagemann (1998) it was observed from series of parallel experiments that Mach number was different at separation point. Therefore, it was suggested some parameters such as contours, temperature influence, wall roughness and even hysteresis effects severely affect the separation behaviour.

Lijo *et al.* (2010) has studied numerically flows in the axisymmetric overexpanded nozzle. Side loads and flow separation at nozzle walls were investigated during start-up and shut down processes. The separation zones and transition from FSS to RSS were well captured by the RSM turbulence model and shows good agreement with experimental data.

The flow separation of the supersonic jet emerging from converging-diverging nozzle at

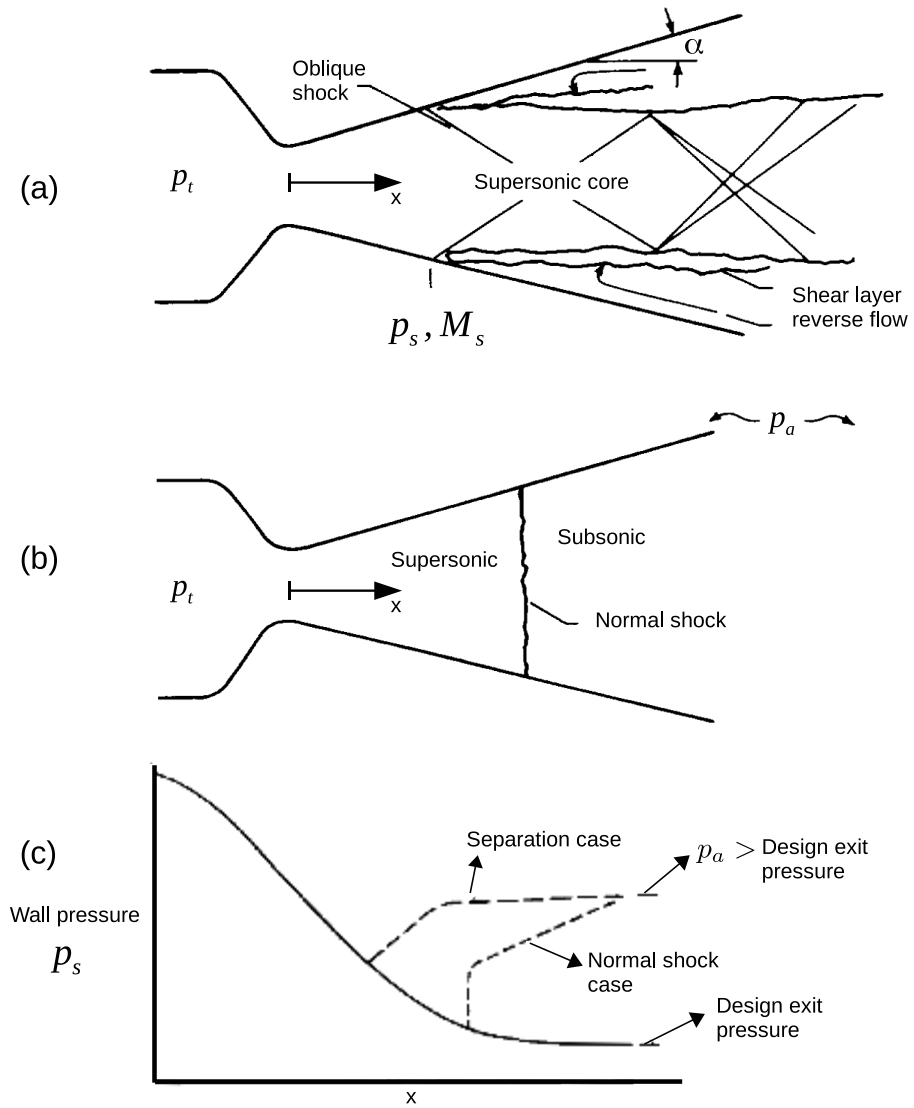

Figure 2.5: Flow at overexpanded nozzle in (a) separation case, viscid flow (b) normal shock, inviscid case (c) wall pressure distribution. (Morrisette and Goldberg, 1978)

different area ratios ($A_e/A_t = 1.0 - 1.8$) and pressure ratios (1.2-1.8) have been investigated by Xiao *et al.* (2009). It has been shown that the SST $k - \omega$ model of Menter *et al.* (2003) provides the best results to predict shock location and pressure distribution. For all A_e/A_t and PRs greater that 1.4 has been resulted to asymmetric separation pattern with large FSS zone on one wall and small FSS zone on the other wall.

Romine (1998) has presented a new theory for calculation of separation location, in over-expanded nozzle during the ignition process of rocket motors. It is shown that the separation inside the nozzle is because the flow is adjusting to a constant back pressure.

Chen *et al.* (1994) has studied numerically separation in the axisymmetric overexpanded nozzle. It has used finite volume solver[4] with a high resolution total variation diminishing (TVD) scheme and modified version of Baldwin-Lomax turbulence model (Chima, 1996). In this study three types of separation and flow structure has been observed; First is the fully separated flow without any vortex behind the Mach disk, second one is the small separation zone with a vortex behind the Mach disk, and the third one is the separated flow that reattaches to the nozzle wall with a vortex behind the Mach disk. In order to validate the results the computed nozzle wall pressures were compared with experimental measurements.

Hunter (1998) has performed extensive research on theoretical, numerical and experimental study of separated nozzle flows. The theoretical results were calculated from the NPAC code (Barnhart, 1997), that is based on one dimensional compressible flow theory and boundary layer characteristic of 2D C-D nozzles. For computational analyses the RANS CFD code (PAB3D) in conjunction with two equation $k - \varepsilon$ turbulence model has been used. Roe's upwind scheme was used to solve explicit section of governing equations and van-Leer scheme was adopted for implicit section. It has been shown that for NPR$\leq$1.8 the separation is 3 dimensional and unsteady with RSS pattern, while at NPR$\geq$ 2 separation is steady and fully detached and as pressure ratio increases the separation pattern becomes even more two dimensional. It is observed that computational results became undesirable at low pressure ratios. Also, the numerical method was unable to predict accurately the shock boundary layer interaction.

Flow separation in nozzles could be beneficial for creating better mixing features or improving thrust and performance in rocket motors. However, the flow separation also causes dangerous lateral forces (side loads) due to asymmetry in the flow separation that could damage a nozzle and is undesirable. In order to prevent determinant consequences of flow separation in nozzles, some control methods can be applied to increase mechanical energy level of boundary layer low speed region. Some researches such as Delery (1985) and Green Jr and

[4]USA Navier-Stokes code

Nall (1957) have worked on these control methods. Some suggested techniques are :

- Wall cooling.
- Local change of the wall contour.
- Suction and/or injection of mass at the wall (also termed bleed effect).
- Tangential injection by a high-speed jet (also called boundary layer blowing).
- Use of vortex generators.
- Boundary layer removal by strong suction through a large slot.

2.4 Swirl flow

Swirling flows are found in many engineering applications, including turbofan or turbojet engines, injection system for combustion engines, spin-stabilized rockets and cyclones. This type of flow could have favourable effects on various aspects of flow fields, such as mixing enhancement, jet growth and noise reduction. Swirling flows show strong, three dimensional behaviour due to anisotropic turbulence and therefore makes it extremely complex to perform accurate numerical simulations. Recent advances in computer powers have provided a way to study complicated turbulent flow fields by using CFD to solve Navier-Stokes equations with sophisticated turbulence models. This study investigates the effect of swirl flow in the overexpanded nozzle.

Thompson and Hoffmann (1990) has investigated numerically and experimentally the effect of swirl flow on dump combustor nozzle propulsion system. The results show that swirl has a strong effect on the stagnation pressure distribution, which maximum losses occur near the swirl axis. It is suggested that the swirl effect reduces the system discharge coefficient[5]. The effect of swirl on the nozzle stream thrust efficiency was minimal, which has been reduced by about 0.5% for the highest swirl tested. The numerical model solves three dimensional, unsteady, inviscid flow fields in super-elliptical nozzles.

Swirling flow in supersonic C-D propulsion nozzles has been studied numerically by Dutton (1987). The time dependent finite difference numerical method under the assumption of inviscid axisymmetric flow was employed. The specified inlet properties were selected as the stagnation pressure and stagnation temperature. Results indicate that significant reduction in

[5]The discharge coefficient is the ratio of the measured to the ideal mass flow rate

the discharge coefficient may occur. It has been observed that the swirl effect increased the velocity near the nozzle axis significantly.

Swirling flow in choked de Laval nozzle was investigated numerically by Pandolfi (1976). The swirling flow is achieved through surface located at inlet of the nozzle. The time dependent technique for two dimensional axisymmetric configurations has been deployed. The centrifugal forces due to the tangential velocity act in increasing the pressure at outer boundaries and in decreasing it at the inner boundaries.

Liu *et al.* (2008) has investigated supersonic flow inside adiabatic C-D which was introduced by two identical tangential inlets. The numerical simulations in this study were steady state and all the flow parameters are independent of the time. For boundary conditions total pressure and temperature with critical mass flow rate was employed. For turbulence modelling RSM was used. It has been concluded that both the axial velocity and the tangential velocity increases and the swirling flow with a large centrifugal acceleration that is produced at the inlet can get through the shock wave at the throat up to outlet of the nozzle.

Numerical simulations of air-jet spinning in the 3D subsonic nozzle ($Ma = 0.6 - 0.9$) by injecting tangentially high velocity compressed air has been performed by Guo *et al.* (2009). The nature of the swirl flow creates a considerable degree of anisotropy in stress and dissipation tensors and hence leading to anisotropic eddy viscosity. This has been experimentally proven by Yajnik and Subbaiah (1973), in which swirl number S in a pipe is defined in terms of axial and angular fluxes associated with the mean flow as:

$$S = \frac{\int_0^R UVr^2 dr}{R\int_0^R U^2 r dr} \tag{2.5}$$

where U and V are axial and tangential components of the mean velocity at a point in a pipe with radius R and distance r from the axis. Therefore, standard $k-\varepsilon$ model did not provide accurate results, and realizable $k-\varepsilon$ model was adopted for simulations. Although the RSM model showed more reliable results, but consuming large amount of memory and processing time made it difficult to get all the solutions. It is suggested that the second order upwind scheme for conservation equations along QUICK scheme for turbulence model provides high accuracy data for swirling flows. Simulations show with swirl effect, reverse flow appears near the wall and a spiral type vortex breakdown is observed at downstream of the injectors. The flow reversal region increases as the swirl intensity decreases. It has been shown that the maximum tangential velocity near the wall decreases as swirl decays. On the other hand, maximum axial velocity increases with increase in axial distance.

Kobayashi and Yoda (1987) has compared standard $k-\varepsilon$ model with modified $k-\varepsilon$ model for simulating turbulent swirling flow in a straight pipe. Results demonstrated that standard $k-\varepsilon$ model is not capable of predicting axial and tangential velocity profile and the model cannot describe the force-free combined vortex type profiles; even $k-\varepsilon$ model with higher order terms has minor effect on predicting velocity profiles. However, modified $k-\varepsilon$ model with anisotropic formulation successfully predicts both axial and tangential velocity profiles. Saqr *et al.* (2010) has proposed modified version of standard $k-\varepsilon$ for highly strained flows by adding an extra source term in dissipation equation. This model predicted the tangential velocity more accurately compare to standard or RNG $k-\varepsilon$ models.

The properties of turbulent swirling decaying flow induced by eight tangential inlets in a divergent pipe using realizable $k-\varepsilon$ turbulent model at $Ma \approx 1$ were investigated by Guo and Chen (2009). Because there were not experimental data for swirling flow in a divergent pipe the computations were first validated with available experimental data for cylindrical tube. Results show that the swirling flow pattern is completely unsteady. The recirculation zone in upstream of injectors first increases and then reduces, while in downstream of injectors conical breakdown can form from the bubble breakdown. The maximum axial velocity happened near the wall, although the axial velocity decays gradually with the wall distance.

CFD simulations of swirl flow induced by tangential inlets at low speed (10-15m/s) showed complex, steady, non-axisymmetric flow patterns at various swirl intensities (Jiajun *et al.*, 1999). It has been shown in this study that high order schemes such as van Leer scheme, is needed to capture the main flow features. There was complex three dimensional flow behaviour behind inlets, but the swirl intensity continued to decay at the downstream of inlets.

Turbulent flow field in the pipe with tangential injections has been experimentally studied by Chang and Dhir (1994). The experiments were based on using hot wire anemometer. The ratio of momentum flux through the injectors (M_t) to the total momentum flux through the test section (M_T) is defined as

$$\frac{M_t}{M_T} = \frac{\dot{m}_t}{\dot{m}_T}\frac{A}{A_j} \tag{2.6}$$

where $\dot{m}_t$ is the total mass flow rate through the injectors and $\dot{m}_T$ is the total mass flow rate through the test section. A is the cross sectional area of test section and A_j is the total area of injectors. A large anisotropy among the three Reynolds stress components was shown in this experiment. There are two significant terms in the turbulence energy production, which were obtained from Reynolds stress components and velocity gradients:

$$-\overline{uv}\frac{\partial U}{\partial r} \qquad and \qquad -\overline{vw}r\frac{\partial}{\partial r}\left(\frac{W}{r}\right)$$

where U and W are mean axial and tangential velocities, respectively. The first term exists in both axial flow and swirl flow, while the second term is the extra term due to the swirl motion. The turbulence production due to the radial gradient of the axial velocity was found to have high value near the wall. This indicates the existence of high shear near the wall. The turbulence production from the radial gradient of tangential velocity (second term) was significantly increased in the annular region where the tangential velocity decreased with radius. From the tangential velocity profile in this research, the swirl flow has been divided into core region and annular region. Core region was characterised by force vortex motion and annular region was characterised by free vortex motion. In this experiment, flow reversal region was observed in the core of the tangentially injected swirl flow. It was shown that the size of the flow reversal region shrinks as the swirl intensity decreases.

Swirling flows in stationary cylindrical pipes were investigated experimentally by Murakami *et al.* (1976). At the beginning of the pipe, the swirling component of velocity shows combined forced-free vortex type, where in the central part is a forced vortex and at the outer part is a free vortex one. By moving further along the axial distance, forced vortex region extends and a free vortex outer zone shrinks. This continues until force vortex type swirl, dominates all the pipe. It has been illustrated that a swirl flow in a straight circular, duct decays exponentially, and the decay exponent depend on the roughness of the pipe wall.

A free vortex type swirling flow in a long circular pipe was investigated experimentally by Kitoh (1991). It has been shown that, based on the tangential velocity distribution, the flow has three regions: wall, annular and core. In the wall region the only effect that appears is the centrifugal destabilizing; Therefore the classical mixing length model can predict the flow in wall region. The annular region is characterised by a flow skewness. Tangential velocity in core region was expressed as a sum of forced and free vortex motions. It is difficult to use an analytical approach to predict flow features in this region. It was suggested that using the Reynolds Stress Model which can handle anisotropic turbulence will be more promising tool to predict the flow compared to an eddy viscosity model such as $k-\varepsilon$. The core region is characterized by a forced vortex motion and the flow is dependent upon the upstream conditions; In this region turbulence motion has very low frequency and the flow is non-dissipative. Hence, there is a long history effect in the core region.

Buntic-Ogor *et al.* (2006a) has suggested using Very Large Eddy Simulation (VLES) turbulent model for swirling flows as LES is time consuming and immoderate for most engin-

eering flow applications. VLES is a favourable compromise between LES and RANS for industrial applications. In VLES large turbulent structures are resolved in an unsteady simulation and small structures are modelled with the sophisticated turbulence model. In contrast, standard $k-\varepsilon$ model showed poor results for unsteady swirling flows which the main reason for it was the modelled turbulent eddy viscosity tends to damp all unsteadiness of the time resolved flow field.

In simulation of compressible jets, modelling the nozzle geometry will bring the dynamics of the flow field as well as the emission of sound pressure waves to the far field closer to the conditions found in experiments (Bühler *et al.*, 2010). In this research, non-reflecting boundary conditions were applied to outflow and validation was performed by the convergence of the spatial discretisation schemes.

Singh and Ramamurthi (2009) has investigated numerically and experimentally, using PIV, the conditions that form a Coanda jet by swirled gas jet (tangential inlets) issuing from a sharp edge nozzle. It has been explained that recirculation in swirl flows, happens when adverse pressure gradients, developed in the flow, cannot be overcome by kinetic energy of the flow. The recirculation location and size depends on the geometry of the flow and relative magnitude of the tangential and axial momentum. For turbulence modelling, realizable $k-\varepsilon$ was adopted, as was shown that provides a good prediction for separated flows, shear flows and recirculation flows. It has been concluded that a jet changing into a wall attached Coanda jet is associated with hysteresis, where a Coanda jet is capable of sustaining itself even at lower values of Re and swirl number. The Coanda jet was formed with the inception of the two recirculation bubble near the nozzle exit.

Abdelhafez (2009) has investigated numerically and experimentally the effect of swirl flow on supersonic nozzles. It has been found out that the swirl flow will reduce the axial Mach number component. The mass flow rate through the nozzle was found to be function of throat static pressure and axial Mach number. Thus, the swirl effect reduces the axial Mach number and consequently the mass flow rate will reduce. On the other hand, greater reservoir pressures (inlet pressure), results in higher throat static pressure and therefore higher mass flow rate. It has been shown that subsonic Mach number profiles for swirling flows are similar to non-swirling applications. In terms of shock strength, at matched inlet pressures, the swirl flow weakens the shock structure. However, with the matching mass flow rate, the swirl flow resulted in a stronger shock structure. It has been found out that swirl flow enhances supersonic mixing significantly, due to swirl induced vortices that mix different regions of flow field.

Temperature distribution in swirling jets has been studied by Shtern *et al.* (1998). In this study energy equations were solved analytically to show strong effects of swirl flow in heat

exchange and heat isolation of a wall. For heat diffusion from a hot jet to a cold ambient, the maximum temperature decayed considerably faster in a swirling jet than in a swirl free jet. The enhancement in heat exchange is due to the development of the swirl induced recirculation that increases the contact surface area between the jet and ambient fluid. However, swirl can cause flow separation from a wall that leads to a significant decrease in heat transfer.

2.4.1 Vortex breakdown

Vortex break down is an appreciable axial component of motion in addition to swirl or azimuthal component. Vortex break down happens in many engineering applications such swirling flows through nozzles, diffusers and combustion chambers. It has an important role in production of turbulence in the boundary layer. There are three main conditions for vortex break down to happen, firstly happen in highly swirling flows. A second necessary condition is the positive or adverse pressure gradient in axial direction. A third condition is a divergence of the stream tubes in the vortex core immediately upstream of breakdown (Hall, 1972).

Luginsland and Kleiser (2011) has developed numerical method to simulate swirling jet flow undergoing vortex breakdown. The code uses high order numerical scheme to solve compressible Navier-Stokes equations in cylindrical coordinates. At the outflow and in the far field, non-reflecting boundary conditions are implemented. The study shows, including a nozzle into the computational domain provide more realistic results. Luginsland *et al.* (2010) used a parallel LES code for numerical modelling of swirling jets undergoing vortex break down. In order to calculate the derivative in azimuthal direction it was required to decompose the domain in three directions.

Vortex breakdown in swirling jets for laminar and incompressible flows was investigated numerically by Ruith *et al.* (2003). It has been explained that for the accurate numerical simulation of axisymmetric, swirling flows exhibiting vortex break down, is required to solve the full Navier-Stokes equations (using DNS) in cylindrical coordinates for three dimensional, unsteady flows. Solving N-S equations in cylindrical coordinates needs special attention duo to singular behaviour of some terms near the axis. The CFD simulations showed, the lowers *Re* considered leads to a viscous core without any vortex break down even for high swirl flows. Increasing the *Re* leads to one antisymmetric bubble, and increasing *Re* even further creates temporally periodic flow.

2.4.2 Noise reduction

The main sources of noise produced by a supersonic jet are turbulent mixing noise and shock associated noise[6]. The turbulent mixing noise is present in both subsonic and supersonic jets. It is generated from the interaction between the large turbulent structures propagating downstream, and surrounding atmosphere (Tanna, 1977a). It is the main source of the noise at subsonic nozzles or nozzles that operate at supersonic design conditions.

When a converging-diverging nozzle operates at design pressure ratio, the acoustic spectrum is broad and smooth, and consists of pure turbulent mixing noise. However, when a C-D nozzle operates at off design pressure ratio (overexpanded or underexpanded) the resulting acoustic spectrum shows an extra noise element (addition to turbulent mixing noise), due to the presence of shock waves in the jet flow. The shock associated noise can be either screech or broadband noise. The screech component is discrete in nature and usually with several harmonics; On the other hand the broadband noise has a well defined peak frequency. The overall intensity of shock associated noise is a function of the jet pressure ratio only and is essentially independent of the jet temperature or observer angle (Tanna, 1977b).

The three basic components of an imperfectly expanded supersonic jet measured by Seiner and Yu (1984), is shown in Figure 2.6. For the Strouhal number ($St = fD/U_j$), f, D and U_j are the frequency, nozzle exit diameter and fully expanded jet velocity, respectively. The low frequency broadband peak is the turbulent mixing noise and the high frequency to the right of the screech tone, is the broadband shock associated noise. The intensity of these three components is a strong function of the direction of observation. In the downstream direction of the jet, turbulent mixing noise is the dominant component; while in the upstream direction, the broadband shock associate noise is the major component. For circular jets, the screech tones radiate primarily in the upstream direction (Tam, 1995).

Figure 2.7 represents noise intensity of a supersonic jet from a converging-diverging nozzle of a design Mach number M_d, as a function of jet Mach number M_j. As the jet becomes supersonic, strong shock cells and normal shock are formed in supersonic part of the jet. At this stage the nozzle is highly overexpanded and has shock associated noise as well as basic turbulent mixing noise. By increasing the jet Mach number, the noise intensity increases until Mach number reaches to point C. From this point Mach disks start to disappear from shock cells system and therefore the noise intensity decreases with an increase in the jet Mach number. The noise reduction at this stage is mainly due to reduction in shock associated noise. This continuous up to point A, design Mach number, where at this Mach number the noise is

[6]In some literatures “Mach wave radiation” is also considered as a noise source.

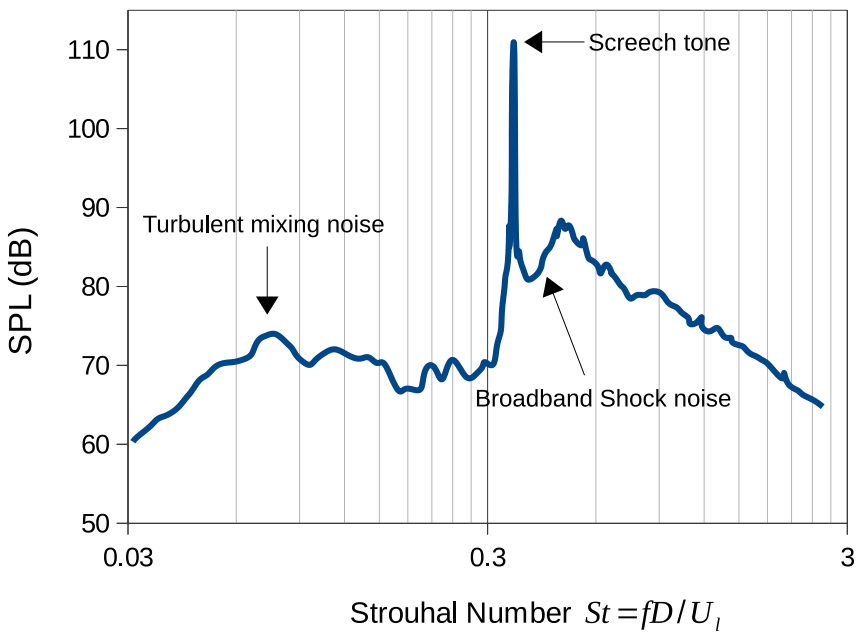

Figure 2.6: Noise spectrum of an imperfectly expanded supersonic jet (Reproduced from Tam (1995)).

entirely due to turbulent mixing noise. For a Mach numbers greater than M_d, the nozzle is in an underexpanded condition and periodic shock cells reappear in this range of Mach number. From point A the jet noise again consists of shock associated noise and turbulent mixing noise, which both of them will increase with Mach number.

Yu and Chen (1997) has studied the effect of supersonic swirling jets in screech tone noise. It has been found out that, the characteristics such as the directionality, were similar to non-swirling jets. The swirl effect has not eliminated the quasi-periodic shock structure which is key in creating screech noise in non-swirling jets. Therefore, the sound pressure level of the swirling jets was similar to that of non-swirling jets. It has been concluded that, whether or not the jet is swirling, screech tone exist because of the shock cell structures and instabilities on the jet boundary at downstream of the nozzle.

On the other hand, effect of fluid rotation on noise reduction in supersonic jets, produced by a converging nozzle, was investigated experimentally by Neemeh *et al.* (1999). It was obtained from Schlieren photography that the swirl effect did change the jet structure. Increase in swirl resulted a decrease in shock cell length and a decrease in the number of cells due to the increase in mixing with the surrounding fluid. Acoustically, it has been proven that swirl in supersonic jets reduces screech noise. Although the low swirl reduced the maximum sound pressure level (SPL) as well as high swirl by as much as 15dB for jet Mach number between

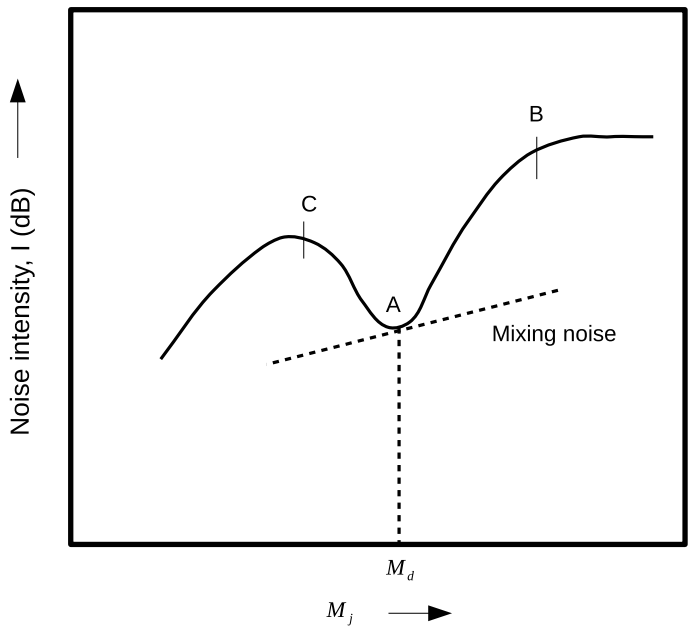

Figure 2.7: Noise intensity of a supersonic jet from a convergent-divergent nozzle of design Mach number M_d, as a function of jet Mach number M_j. (Tam and Tanna, 1982)

1.18 to 1.4. It has been suggested that for subsonic jets, it is better to use the low swirl in order to minimise the turbulent mixing noise resulting from the swirl.

Most recently, Ahmad (2011) has investigated the noise reduction in circular jet at Mach 1.3 with introduction of tangential components to the flow. Internal tangential injection at an injection mass flow ratio of 40% induced adverse pressure gradients within the nozzle resulting in a deceleration of the axial velocity. Although this resulted in a thrust penalty of 5% but the screech noise level reduced by 6.4dB. External tangential injection at the exit of nozzle was found to increase the centre line velocity that caused 0.8% increase in thrust level. In external injection, shock associated broadband and harmonic screech peaks were reduced by 3.7dB and 7.5dB respectively. Thus, external injection was shown to be more effective than inside nozzle injection.

Chapter 3

Numerical methods

3.1 Governing equations

The numerical procedure for all CFD codes is based on three fundamental equations:

1. Conservation of mass (Continuity equation)
2. Conservation of momentum (Newton Second law)
3. Conservation of energy (First law of thermodynamic)

To represent these equations in continuum mechanics, an infinitesimally element is considered fixed in the space, which time and length scales are much greater than inter atomic distances, therefore, the conservation form (divergence) are:

- Conservation of mass

$$\frac{\partial \rho}{\partial t} + \frac{\partial}{\partial x_i}(\rho u_i) = 0 \tag{3.1}$$

- Conservation of momentum

$$\frac{\partial}{\partial t}(\rho u_i) + \frac{\partial}{\partial x_j}\left(\rho u_i u_j + p\delta_{ij} - \tau_{ji}\right) = 0 \tag{3.2}$$

- Conservation of energy

$$\frac{\partial}{\partial t}(\rho e_t) + \frac{\partial}{\partial x_j}\left(\rho u_j e_t + u_j p + q_j - u_i \tau_{ij}\right) = 0 \tag{3.3}$$

where u is velocity, ρ is density, q is the heat flux, p is pressure, e is the total energy per unit mass and τ_{ij} is shear stress which for Newtonian fluid is defined as:

$$\tau_{ij} = \mu\left[\left(\frac{\partial u_i}{\partial x_j} + \frac{\partial u_j}{\partial x_i}\right) - \frac{2}{3}\left(\frac{\partial u_k}{\partial x_k}\delta_{ij}\right)\right] \tag{3.4}$$

here , μ is molecular or dynamic viscosity and δ is Kronecker delta. The total energy e_t for moving fluid element, consists of two parts: the internal energy e, due to random molecular motion and kinetic energy due to translational movement of fluid element. The kinetic energy per unit mass is $u_i u_i/2$.

3.1.1 Constitutive relations

Looking at equations 3.1, 3.2 and 3.3 shows that, there are five equations and six unknown variables p, u_i, ρ and e. In order to close the system it is necessary to specify extra relation. In aerodynamics, it is acceptable to assume the gas is a perfect gas (Anderson Jr, 1985). So equation of state for a perfect gas is

$$p = \rho R T \tag{3.5}$$

where R is specific gas constant. Now there is one new, unknown variable, temperature (T), so a seventh equation to close the system is thermodynamic relation between equation3.5 parameters.

$$e = e(p, T) \tag{3.6}$$

The above equation for calorically perfect gas would be:

$$e = c_v T \tag{3.7}$$

where c_v is specific heat at constant volume.

3.1.2 Multiphase flow

For multiphase flow the conservation equations are satisfied for each phase separately based on volume fraction of phase N (α_N), where:

$$\sum_{N=1}^{n} \alpha_N = 1 \tag{3.8}$$

therefore, the volume of phase N will be .

$$V_N = \iiint_V \alpha_N dV \tag{3.9}$$

Conservation of mass The continuity equation for phase N is:

$$\frac{\partial}{\partial t}(\rho_N \alpha_N) + \frac{\partial(\rho_N \alpha_N u_{Ni})}{\partial x_i} = S_N \tag{3.10}$$

where S_N is the rate of transfer of mass to the phase N from the other phases per unit total volume. For disperse phase, S_N is zero because no particle is created or destroyed.

Conservation of momentum The momentum balance for phase N is

$$\frac{\partial}{\partial t}(\rho_N \alpha_N u_{Nj}) + \frac{\partial}{\partial x_i}(\rho_N \alpha_N u_{Nj} u_{Ni}) = \alpha_N \rho_N g_j - \delta_N \left(\frac{\partial p}{\partial x_j} - \frac{\partial \tau_{ji}}{\partial x_j}\right) + F_{Nj} \tag{3.11}$$

where δ_N is zero for disperse phase and unity for continuous phase. F_N is the total force (per unit total volume) imposed on component N within the control volume, which is composed of drag force, virtual mass force and lift force (Hill, 1998)

$$\mathbf{F}_N = \mathbf{F}_d + \mathbf{F}_{vm} + \mathbf{F}_l + \mathbf{F}_b \tag{3.12}$$

where $\mathbf{F}_d$ represents the drag force, $\mathbf{F}_{vm}$ the virtual mass force, $\mathbf{F}_l$ the lift force and $\mathbf{F}_b$ is the Basset force. The drag force is the relative motion between particles or droplets and surrounding fluid will create drag force and it has two main components: skin friction and form drag. Skin friction is related to the shear stress on the surface of a submerged particle

while the latter is related to non uniform pressure distribution at the surface. The drag force on a single particle in terms of relative velocity is (Hill, 1998):

$$\mathbf{F}_d = \frac{1}{2}\rho_c C_d A|\mathbf{u}_r|\mathbf{u}_r \tag{3.13}$$

where $\mathbf{u}_r$ is the relative velocity ($\mathbf{u}_r = \mathbf{u}_c - \mathbf{u}_N$), C_d is dimensionless drag coefficient, ρ_c is the density of continuous phase[1] and A is the projected area of particle.

The virtual mass force is the additional force required to accelerate the particle or phase N due to the mass of primary phase c in its vicinity, which also need to be accelerated. The virtual mass effect can be calculated as (Drew *et al.*, 1979):

$$\mathbf{F}_{vm} = C_{vm}\alpha_N\rho_c\left(\frac{D_c}{D_t}\mathbf{u}_c - \frac{D_N}{D_t}\mathbf{u}_N\right)\Bigg(\tag{3.14}$$

where C_{vm} is the dimensionless coefficient and in FLUENT because all particles are considered as sphere is set to 0.5 (Ansys, 2010). D_k/Dt stands for the substantial derivative which is defined as:

$$\frac{D_k}{Dt} = \frac{\partial}{\partial t} + \nabla.\mathbf{u}_k \tag{3.15}$$

The lift force is the lateral force experience by particle due to pressure gradient and rotation of particle itself. The expression for lift force have been derived by Drew and Lahey Jr (1987) and is:

$$\mathbf{F}_l = C_l\alpha_N\rho_c\left(\mathbf{u}_c - \mathbf{u}_N\right)\times\left(\nabla\times\mathbf{u}_c\right) \tag{3.16}$$

where C_l is dimensionless coefficient and for spherical particles is calculated to be 0.5 (Drew and Wallis, 1994). The lift force for gas-liquid flows is important as can have a large effect on phase distribution, but for solid-liquid flows is negligible compared to other forces (Drew and Lahey Jr, 1987).

The Basset force, similar to virtual mass force is related to the acceleration of continuous phase (primary fluid). However, the Basset force represents the delay of boundary layer development on particles, which is neglected in most practical calculations (Rusche, 2003).

[1] Primary phase

Conservation of energy The first law of thermodynamic for phase N is

$$\frac{\partial}{\partial t}\left(\rho_N \alpha_N e_{tN}\right) + \frac{\partial}{\partial x_i}\left(\rho_N \alpha_N e_{tN} u_{Ni}\right) = Q_N + W_N + \delta_N \frac{\partial}{\partial x_j}\left(-u_i p + u_i \tau_{ij} - q_N\right) \tag{3.17}$$

where δ_N is zero for disperse phase and unity for continuous phase. Q_N is the rate of heat addition to phase N and W_N is rate of work done to phase N

3.1.3 Discrete phase model

In DPM each discrete phase element is tracked through flow domain. The trajectory of particles is obtained by solving second law of Newton for each particle

$$m_D \frac{d\mathbf{u}_D}{dt} = \sum \mathbf{F_D} \tag{3.18}$$

$$I_D \frac{d\omega_D}{dt} = T_D \tag{3.19}$$

where m_D is the mass of disperse phase, $\sum \mathbf{F}$ is all forces acting on particle, I_D is the moment of inertia of particle, ω_D is the angular velocity of particle and T is the torque arising from tangential component of contact forces on particle (Kafui *et al.*, 2002). There are different type of forces acting on individual particles, depending to the nature of flow, but for complicated flow regimes are still not fully understood. In this research and for high Reynolds number flows, equation 3.18 can be shown as:

$$m_D \frac{d\mathbf{u}_D}{dt} = m_D \mathbf{F}_d \left(\mathbf{u}_C - \mathbf{u}_D\right) + m_D \frac{\rho_C}{\rho_D}\left(\frac{D\mathbf{u}_C}{Dt}\right) + \mathbf{g} m_D \left(1 - \frac{\rho_C}{\rho_D}\right) \tag{3.20}$$

where g is the gravitational acceleration and u_c is the speed of continuous phase. The right hand side of equation 3.20 represents the drag force due to relative motion, the force due to pressure gradient and viscous stresses and the buoyancy force respectively. The drag force F_d

on sphere particles is (Andrews and O'rourke, 1996)

$$
\begin{aligned}
F_d &= \frac{3}{8} C_d \frac{\rho_C \left|\mathbf{u}_C - \mathbf{u}_D\right|}{\rho_D r_D} \\
C_d &= \frac{24}{Re} \quad 1 + \frac{Re^{2/3}}{6} \Bigg) \Bigg(\\
Re &\equiv \frac{2\rho_C \left|\mathbf{u}_C - \mathbf{u}_D\right|}{\mu}
\end{aligned}
\tag{3.21}
$$

where μ is the molecular viscosity, r_D is the radius of particle and Re is the Reynolds number.

The difficulty in Lagrangian approach lies in the fact that continuous and dispersed phases are closely coupled; So the continuous phase flow will affect the motion and distribution of particles, and also particles will influence the flow characteristics of continuous phase. The motion of continuous phase is describes in Eulerian framework (fixed in space), while the motion of particles is described in the Lagrangian framework (fixed to particle).

3.2 Discretisation

This section explains how to solve numerically the equations of single phase and multiphase flows, derived in section 3.1. Discretisation for different methods such as finite volume or finite difference, have three main steps

Domain discretisation The space is divided into a finite number of regions, called control volume or mesh.

Temporal discretisation In transient problems, splitting time domain into finite number of time steps or time intervals.

Equations discretisation Creating algebraic expression form partial differential equations of governing equations, in terms of discrete quantities defined in each cell in the domain.

The both codes (FLUENT and OpenFOAM) that have been used for simulations of this study are based on finite volume method, therefore the attention will be on this method. Finite volume method is based on an integral form of governing differential equations over each control volume. In both of these software's partial differential equations are solved with segregated approach (Van Doormaal *et al.*, 1987), in which they are solved sequentially for each dependent variable, with inter equation coupling treated in an explicit manner.

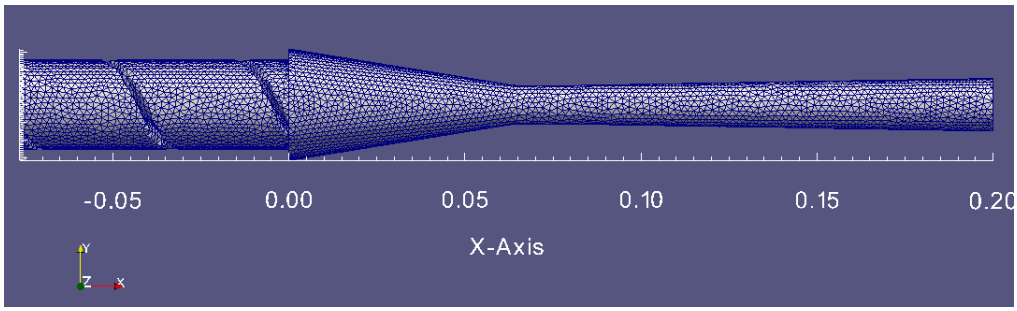

Figure 3.1: Tetrahedral mesh inside nozzle

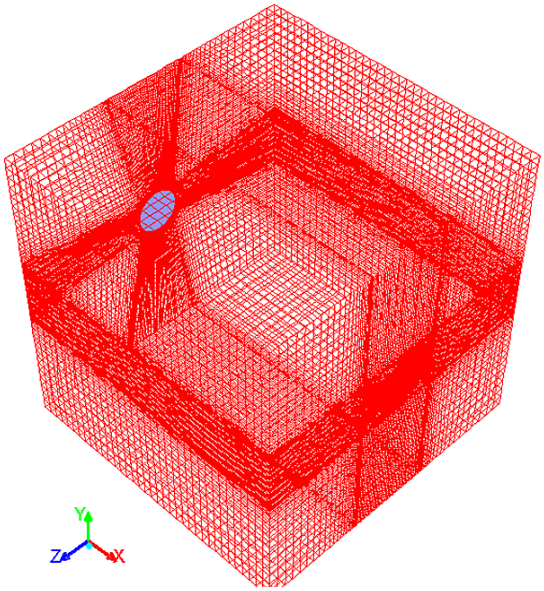

Figure 3.2: Hexahedral mesh outside nozzle

3.2.1 Discretisation of the solution domain

The flow domain is subdivided into tetrahedral or hexahedral meshes where governing equations are solved subsequently. Figure 3.1 and 3.2 shows the computational domain for inside and outside of the nozzle. For transient problems, discretisation of time is also required, where time is broken in to time steps Δt. The time step could be changed during simulations based on Courant number[2]. The time step must be less than a certain time in explicit simulations, otherwise the simulation will either produce wrong results or creates instability in solutions (Anderson, 1995). For one dimensional case, Courant number has the following form

$$C = \frac{u\Delta t}{\Delta x} \leq C_{max} \tag{3.22}$$

[2]CFL condition

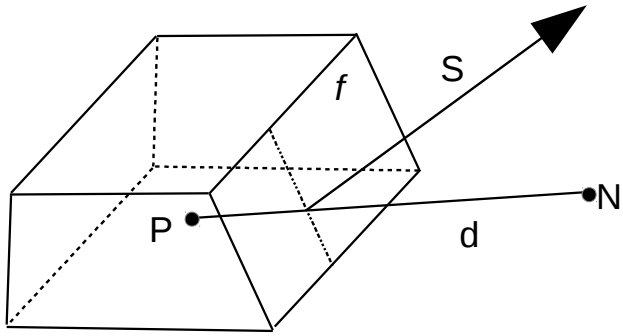

Figure 3.3: Control volume

Discretisation of space in finite volume method requires subdividing the domain to control volumes (CV) or cells. Control volumes do not overlap and completely fill the domain. The cell faces can be divide in the two groups, internal faces, which are faces between control volumes, and boundary faces, which are faces at the boundary of domain. Figure 3.3 shows schematic of control volume, where **S** is the normal vector on face f and points outward, P is the centre point of CV, vector **d** connects centre point P to neighbour N. For orthogonal mesh the angle between **d** and **S** must be zero. The computational point P is defined as

$$\iiint_V (x - x_P)\, dV = 0 \tag{3.23}$$

Depending on the geometry and solution algorithm, discretisation of a domain can be done in two main categories, structured or unstructured mesh.

Structured mesh In which position of cells is defined solely from adopted cell numbering scheme. They are usually three dimensional cube blocks (hex) with known number of mesh along each side. This type of mesh is good for simple geometries and creates a high quality mesh, although for complex geometries is difficult and needs complicating topology and blocking to provide good quality mesh.

Unstructured mesh The cells can be arranged in any convenient manner. Number and size of the cells are defined by global values. Unstructured meshes provide greater freedom for refinement in specific region and are much easier to generate for complicated geometries.

3.2.1.1 Mesh generation

There are different softwares for mesh generation and domain discretisation, where some of them are open source and some of them are proprietary. For this study the combination of different packages has been used with structured and unstructured meshes.

Ansys ICEM

ICEM[3] is proprietary software package, which can produce structured, unstructured and hybrid meshes from various CAD files. It has different features to clean-up CAD models. We have used ICEM to mesh inside and outside of nozzle for both FLUENT and OpenFOAM simulations.

enGrid

enGrid[4] is an open source mesh generation software with CFD capabilities in mind. enGrid uses the Netgen library (Schöberl, 1997) to generate tetrahedral meshes and has in-house development for prismatic boundary layer grids. enGrid has been used mainly to create mesh inside nozzle with helical insert for OpenFOAM.

blockMesh

Is the most basic mesh generator in OpenFOAM and relies on single dictionary file `blockMeshDict`. blockMesh creates structured hexahedral blocks with the option of straight line, arcs or Spline for edges. It is not possible to import CAD model to blockMesh, therefore it is very difficult for complex geometries to be meshed with it. blockMesh has been used to generate mesh for inside and outside of nozzle without helical insert to be solved by OpenFOAM.

snappyHexMesh

The snappyHexMesh utility is supplied by OpenFOAM and generates three dimensional meshes containing hexahedral and split-hexahedral automatically from triangulated surface geometries in Stereolithography (STL) format. It is capable to generate meshes for any complex geometry from STL file. It is one the few mesh generator software which is capable of running in parallel as well. It first creates castellated mesh, then snaps and morphs the resulting

[3] Ansys ICEM v12 has been used.
[4] enGrid v1.4 has been used.

mesh to the surface. snappyHexMesh was used to generate mesh inside and outside of the nozzle with helical insert.

3.2.2 Discretisation of governing equations

In order to solve governing equations in discretised domain, it is necessary to transform governing equations into a corresponding system of algebraic equations. The standard form of transport equation in single phase[5] for scalar quantity ϕ is

$$\underbrace{\frac{\partial(\rho\phi)}{\partial t}}_{Time\,derivative} + \underbrace{\nabla.(\rho\mathbf{u}\phi)}_{convection\,term} - \underbrace{\nabla.\left(\rho\Gamma_\phi\nabla\phi\right)}_{diffusion\,term} = \underbrace{S_\phi(\phi)}_{source\,term} \tag{3.24}$$

where ρ is density, $\mathbf{u}$ is velocity vector, Γ is diffusivity and $S_\phi(\phi)$ is the source term for quantity ϕ. The first term in left hand side is the rate of increase of ϕ of fluid element, the second term is the net rate of flow of ϕ out of fluid element and the third term is the rate of transport of ϕ due to diffusion. Right hand side of equation represents the rate of production or destruction of ϕ. This is second order equation, because the diffusion term has second derivative of ϕ in space.

The finite volume method requires equation 3.24 to be formulated in integral form over control volume V_P and time

$$\begin{aligned}\int_t^{t+\Delta t}\left[\frac{\partial}{\partial t}\int_{V_P}\rho\phi dV + \int_{V_P}\nabla.(\rho\mathbf{u}\phi)\,dV - \int_{V_P}\nabla.\left(\rho\Gamma_\phi\nabla\phi\right)dV\right]dt \\ = \int_t^{t+\Delta t}\left(\int_{V_P}S_\phi(\phi)\,dV\right)dt\end{aligned} \tag{3.25}$$

the divergence theorem[6] is applied to convert integrals over volume V to integrals over bounding surface of volume S. The mathematical representation for divergence theorem is

$$\int_V(\nabla.\mathbf{F})\,dV = \int_S(\mathbf{F}.\mathbf{n})\,dS \tag{3.26}$$

[5]For multiphase flows, α will be added to each term in left hand side of equation 3.24
[6]Gauss's theorem

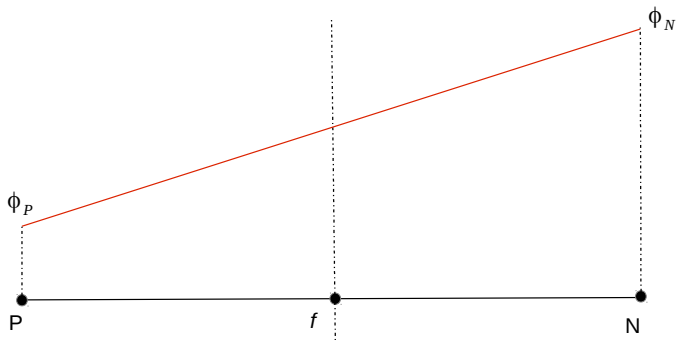

Figure 3.4: Face interpolation

so the equation 3.25 can be written as

$$\int_t^{t+\Delta t} \left[\frac{\partial}{\partial t} \int_{V_P} \rho \phi dV + \int_S \mathbf{n}.\left(\rho \mathbf{u} \phi\right) dS - \int_S \mathbf{n}.\left(\rho \Gamma_\phi \nabla \phi\right) dS \right] dt = \int_t^{t+\Delta t} \left(\int_{V_P} S_\phi\left(\phi\right) dV \right) dt \tag{3.27}$$

In finite volume method the values of scalar ϕ for each control volume is stored in cell centres, therefore interpolation of cell centres to face centres is important part of finite volume method. The face value for ϕ can be evaluated from the values of neighbouring cells by using different schemes (figure 3.4). To get accurate results, it is necessary for the order of discretisation not to be less than the order of equation; As equation 3.25 is in second order, the discretisation schemes need to be at least in second order. There are several studies on equation discretisation (Ferziger and Perić, 2002; Jasak, 1996; Patankar, 1980; Rusche, 2003). The set of face interpolating schemes used for simulations of this research will be explained next:

3.2.2.1 Interpolation schemes

Central differencing(CD) It is linear interpolation between the two nearest nodes. In this method the value of ϕ on face f (ϕ_f), is calculated as

$$\phi_f = f_x \phi_P + \left(1 - f_x\right) \phi_N \tag{3.28}$$

where f_x is the ratio between fN and PN.

$$f_x = \frac{x_f - x_N}{x_f - x_N \ + \ x_f - x_P} \tag{3.29}$$

equation 3.28 is second order accurate, which can be calculated by using Taylor series of ϕ_P around point N to eliminate first order derivatives. This is the simplest and most widely used second order scheme and may produce oscillatory solutions (Ferziger and Perić, 2002).

Upwind differencing(UD) Calculates ϕ_f based on the direction of the flow (Gentry *et al.*, 1966)

$$\phi_f = \begin{cases} \phi_P & if\ (\mathbf{v}.\mathbf{n})_f > 0 \\ \phi_N & if\ (\mathbf{v}.\mathbf{n})_f < 0 \end{cases} \tag{3.30}$$

This is only first order accurate, but guaranties boundedness of the solution which means it will never yield to oscillatory solutions. Although, it will be numerically diffusive. As it is in first order of accuracy it is necessary to have very fine grid to get accurate results (Ferziger and Perić, 2002).

Blended differencing(BD) Provides both boundedness and accuracy for solution by linear combination of UD (equation 3.30) and CD (equation 3.28) (Peric, 1985)

$$\phi_f = (1-\gamma)\left(\phi_f\right)_{UD} + \gamma\left(\phi_f\right)_{CD} \tag{3.31}$$

where γ is blending factor, $0 < \gamma < 1$, and determines how much numerical diffusion will be introduced. At $\gamma = 0$ the scheme reduces to UD.

Second order upwind differencing(SOU) In which higher order of accuracy at face centre is achieved through the expansion of Taylor series. Therefore, the value ϕ_f will be

$$\phi_f = \phi_N + \nabla\phi_N.\left(x_N - x_f\right) \tag{3.32}$$

So in this scheme it is necessary to calculate $\nabla\phi$ at each cell. The gradient term, $\nabla\phi$ can

be calculated in a variety of ways which are explained in section 3.2.2.2.

MUSCL scheme This is the third order bounded scheme for convection term and It is considered as Total Variation Diminishing (TVD). MUSCL scheme is a combination of central differencing and second order upwind schemes (Van Leer, 1979).

$$\phi_f = \gamma\left(\phi_f\right)_{CD} + (1-\gamma)\left(\phi_f\right)_{SOU} \tag{3.33}$$

MUSCL scheme is applicable to any sort of mesh[7] and will increase accuracy by reducing numerical diffusion. In case of supersonic flows with discontinuity like shock waves, to avoid unphysical oscillations in solutions, flux limiter function ($\phi\left(r\right)$) is applied (Sweby, 1984; Van Leer, 1979). In this study vanLeer limiter is applied spatially for OpenFOAM simulations to bound the results.

$$\phi\left(r\right) = \frac{r+|r|}{1+|r|} \tag{3.34}$$

where

$$r_i = \frac{u_i - u_{i-1}}{u_{i+1} - u_i} \tag{3.35}$$

Limited linear differencing Is second order TVD scheme, bounded using Sweby limiter (Sweby, 1984).

3.2.2.2 Gradient schemes

In this study following methods have been utilised to find $\nabla\phi$

Gauss integration The discretisation is performed by applying Gauss theorem to the volume integral

$$\int_V \nabla\phi dV = \iint_S d\mathbf{S}\phi \approx \sum_f \mathbf{S}_f \phi_f \tag{3.36}$$

This operation finds the cell centred value for gradient of ϕ. At this stage the value of ϕ_f on face f can be evaluated using any of interpolation schemes described in section 3.2.2.1.

[7] In contrast to QUICK scheme which is only for structured hexahedral meshes.

Least squares method In this method value at point P can be extrapolated to neighbouring point N using the gradient at P. At first step for discretisation the tensor G is calculated at every point P by summing over neighbours N

$$G = \sum_N w_N^2 \mathbf{dd} \tag{3.37}$$

where $\mathbf{d}$ is the vector from point P to N and the weighting function (w_N) is $w_N = 1/|\mathbf{d}|$, then the gradient at point P is evaluated as

$$(\nabla\phi)_P = \sum_N w_N^2 G^{-1}.\mathbf{d}\,(\phi_N - \phi_P) \tag{3.38}$$

Surface normal gradient The gradient normal to a surface $\mathbf{n}_f.(\nabla\phi)_f$ can be approximated using following scheme

$$(\nabla\phi)_f = \frac{\phi_N - \phi_P}{|\mathbf{d}|} \tag{3.39}$$

where vector $\mathbf{d}$ is between the centre of the cell of interest P and the centre of neighbouring cell N. This scheme is second order accurate when the vector $\mathbf{d}$ is parallel to surface vector $\mathbf{S}$ (orthogonal to face plane). In case of non-orthogonal meshes the correction term is applied .

3.2.2.3 Temporal discretisation

This research focuses on transient simulation, therefore the equation 3.27 is discretised both in space and time. The first time derivative integrated over control volume is

$$\frac{\partial}{\partial t}\int_{V_P} \rho\phi dV \tag{3.40}$$

The first order accurate discretisation will be

$$\frac{\partial}{\partial t}\iiint_{V_P} \rho\phi dV = \frac{(\rho_P\phi_P V)^{t+\Delta t} - (\rho_P\phi_P V)^t}{\Delta t} \tag{3.41}$$

The second order accurate discretisation is

$$\frac{\partial}{\partial t}\iiint_{V_P} \rho\phi dV = \frac{3\left(\rho_P\phi_P V\right)^{t+\Delta t} - 4\left(\rho_P\phi_P V\right)^{t} + \left(\rho_P\phi_P V\right)^{t-\Delta t}}{2\Delta t} \tag{3.42}$$

The second time derivative integrated over control volume in equation 3.27 is

$$\frac{\partial}{\partial t}\iiint_{V_P} \rho\frac{\partial\phi}{\partial t} dV = \frac{\left(\rho_P\phi_P V\right)^{t+\Delta t} - 2\left(\rho_P\phi_P V\right)^{t} + \left(\rho_P\phi_P V\right)^{t-\Delta t}}{\Delta t^2} \tag{3.43}$$

which is first order accurate in time. In OpenFOAM all discretisation schemes for time derivatives are implicit *i.e.* the rest of equation 3.27 is discretised at future time step $t+\Delta t$, however FLUENT has explicit discretisation for the time derivatives in density based solver as well where the rest of equation 3.27 is discretised at current time step t.

OpenFOAM also offers Crank-Nicolson scheme (Crank and Nicolson, 1947) for first time derivative which is obtained by taking the average of explicit and implicit schemes. This scheme is second order accurate in time and in space. This method is unconditionally stable but does not guarantee boundedness of the solution (Hirsch, 2007).

3.2.2.4 Convection term

Discretisation of convection in equation 3.27 is performed by using Gauss theorem as follows:

$$\iint_S \mathbf{n}.\left(\rho\mathbf{u}\phi\right) dS \approx \sum_f \mathbf{S}.\left(\rho\mathbf{u}\phi\right)_f = \sum_f \mathbf{S}.\left(\rho\mathbf{u}\right)_f \phi_f = \sum_f F\phi_f \tag{3.44}$$

where F represents the mass flux through the face f

$$F = \mathbf{S}.\left(\rho\mathbf{u}\right)_f \tag{3.45}$$

At this stage the value of ϕ_f can be evaluated using one of methods described in section 3.2.2.1.

3.2.2.5 Diffusion term

Discretisation of diffusion term in equation 3.27 is done by converting it to surface integral

$$\iint_S d\mathbf{S}.\left(\Gamma\nabla\phi\right) \approx \sum_f \Gamma_f \left(\mathbf{S}.\nabla_f\phi\right) \tag{3.46}$$

For orthogonal meshes the face normal gradient $\mathbf{S}.\nabla_f\phi$, was approximated with second order accuracy in section 3.2.2.2. However, for non-orthogonal meshes, in order to keep the second order accuracy, an extra correction term is introduced

$$\mathbf{S}.\nabla_f\phi = \underbrace{\Delta.\left(\nabla\phi\right)_f}_{orthogonal\,contribution} + \underbrace{\mathbf{k}.\left(\nabla\phi\right)_f}_{non-orthogonal\,correction} \tag{3.47}$$

where the two vectors Δ and $\mathbf{k}$, have to satisfy following condition (Jasak, 1996)

$$\mathbf{S} = \Delta + \mathbf{k} \tag{3.48}$$

vector Δ is chosen to be parallel with $\mathbf{d}$.

3.2.2.6 Source term

All terms of an equation that cannot be considered as convection, diffusion or temporal terms are treated as sources. The source term $S_\phi\left(\phi\right)$, can be general function of ϕ. There are different methods for source terms treatment explained by Patankar (1980). The simplest procedure is to linearised these terms before discretisation

$$S_\phi\left(\phi\right) = \phi S_L + S_K \tag{3.49}$$

where S_L and S_K can also depend on ϕ. Source terms volume integral over control volume will be

$$\iint_{V_P} S_\phi\left(\phi\right) = S_L\phi_P V_P + S_K V_P \tag{3.50}$$

To choose the correct discretisation method for source term, its interaction with other terms in the equation and its effect on the boundedness and accuracy should be examined. It is advised

by Jasak (1996) to treat these terms as implicitly as possible.

3.2.2.7 Final form of discretised equation

The discretisation of transport equation based on procedure explained, yields to an equation for ϕ written in terms of the neighbouring cell values of ϕ. Grouping the coefficient of the considered cell and its neighbours, and dividing it by volume of cell, then the transport equation can be written as

$$a_P \phi_P^{t+\Delta t} = \sum_{f=1}^{nb} a_{nb} \phi_{nb}^{t+\Delta t} + S_K \tag{3.51}$$

where a_P is cell centre coefficient and a_{nb} represents the neighbouring cell coefficient. The cell centre coefficient can be calculated by (Brennan, 2001)

$$a_P = \sum_{f=1}^{nb} a_{nb} - S_L \tag{3.52}$$

3.3 Numerical Solution procedure

The finite volume numerical solution of compressible supersonic flow equations can be addressed using different approaches, such as pressure based or density based solvers with different inter equations coupling treatments. The numerical solution procedure for OpenFOAM and FLUENT is explained in this section.

3.3.1 Pressure equation

The pressure equation is derived from semi-discretised form of momentum equation. In equation 3.51, substituting $\phi = \mathbf{u}$, then extracting the pressure will result to semi-discretised form of momentum equation

$$a_P \mathbf{u}_P^{t+\Delta t} = \sum a_{nb} \mathbf{u}_{nb}^{t+\Delta t} + S_K - (\nabla p)_P \tag{3.53}$$

Where a_p and a_n are a function of $\mathbf{u}$. The pressure gradient term is not discretised at this stage (Rhie and Chow, 1983). Rearranging equation 3.53 by combining the transport term and the

source term, and dropping superscript $t+\Delta t$ for simplicity, will be

$$\begin{aligned} a_P \mathbf{u}_P &= \mathbf{H}(\mathbf{u}) - \nabla p \\ \mathbf{H}(\mathbf{u}) &= \sum a_{nb} \mathbf{u}_{nb}^{t+\Delta t} + S_K \end{aligned} \tag{3.54}$$

The velocity vector $\mathbf{u}$ can be expressed as

$$\mathbf{u}_P = \frac{\mathbf{H}(\mathbf{u})}{a_P} - \frac{1}{a_P} \nabla p \tag{3.55}$$

The velocity on cell faces are calculated by face interpolation of equation 3.55

$$(\mathbf{u})_f = \left(\frac{\mathbf{H}(\mathbf{u})}{a_P} \right)_f - \left(\frac{1}{a_P} \nabla p \right)_f \tag{3.56}$$

As the pressure changes are always finite, this method is valid for all spectrums of Mach numbers. OpenFOAM solvers are primary based on pressure equation as they have better performance on all different flow regimes. FLUENT offers pressure based solver as well. In this study OpenFOAM simulations are based on *sonicFoam* solver, which is pressure based transient transonic/supersonic solver for laminar or turbulent flow of a compressible gas.

3.3.1.1 Pressure-velocity coupling

Combining equations 3.55 and 3.56 with continuity equation, will result in the form of an equation with dependency between velocity and pressure. Special treatment is required to solve this inter equation coupling. There are two main algorithms to treat this inter-equation: segregated and coupled algorithm.

Coupled algorithm It works by solving all systems of equations simultaneously over the whole domain. The resulting matrix is several times larger than the number of computational points; Therefore the execution time and the amount of used memory will be very large. This procedure is preferred when there is low density mesh and the number of simultaneous equations are not too large.

Segregated algorithm The equations are solved in sequence, and special treatment is required for inter-equation coupling. PISO (Issa, 1986), SIMPLE (Patankar, 1980) and their derivatives are the most used methods to deal with inter-equation coupling in pressure equation system.

PISO

This algorithm introduced by Issa (1986), is mainly used for unsteady simulations[8]. It is based on using pressure and velocity as a dependent variable therefore it is applicable to both incompressible and compressible flows. The PISO algorithm can be summarised as follows:

1. The momentum equation is solved first, where the pressure gradient term is predicted from previous time step. This will approximate new velocity field.
2. The new predicted velocity is used to calculate $\mathbf{H}(\mathbf{u})$, then the pressure equation is solved to estimate the new pressure field.
3. From new pressure filed the flux ($F = \mathbf{S}.\mathbf{u}_f$) is calculated.
4. As a result of new pressure distribution, the velocity is corrected in an explicit manner, using equation 3.55.

To limit the error, it is necessary to correct $\mathbf{H}(\mathbf{u})$ term, find new pressure field and correct the velocity field. The procedure is repeated until predefined tolerance is achieved.

SIMPLE

SIMPLE algorithm is usually more superior for steady state situations. This algorithm was introduced by Patankar (1980), and the procedure can be described as:

1. The pressure gradient term is approximated from previous time step or initial guess.
2. The momentum equation is solved to approximate velocity field.
3. The momentum equation is under-relaxed in an implicit manner with velocity under-relaxation factor.
4. The pressure distribution is derived from the new pressure equation.
5. A new set of fluxes is calculated, and then the pressure equation is under-relaxed.

The whole procedure is repeated until a converged solution is obtained. In SIMPLE algorithm, it is assumed that velocity corrections adjacent to the pole cell is negligible (Barton, 1998).

[8] In OpenFOAM, PISO is just for transient simulations. However, in FLUENT is possible to use PISO for steady simulations as well

PIMPLE

PIMPLE is a hybrid algorithm of PISO and SIMPLE (OpenFOAM, 2013). It is basically looping over PISO algorithm within one time step, which will allows for under-relaxation to take place between loops. This will make the algorithm more robust, efficient and can be used for larger time steps and Courant numbers.

3.3.1.2 Under-relaxation

Under relaxation is required to improve the stability of results for discretised transport equation due to non linear coupling between equations. The value at next iteration is calculated according to

$$\phi_P = \lambda\,\phi_P^{t+\Delta t} + (1-\lambda)\,\phi_P \tag{3.57}$$

3.3.2 Density based

The density based scheme, employs the density as a primary variable and extract pressure from the equation of state. It is not possible to use density based method for incompressible or low Mach number flows, because the density changes become very small and therefore the density-pressure coupling becomes very weak (Karki and Patankar, 1989). However, in FLUENT, this issue is solved by applying preconditioning technique to reduce the numerical stiffness of equations (Ansys, 2010).

Within the OpenFOAM, *rhoCentralFoam* is the density based solver, which applies Kurganov central upwind scheme (Kurganov and Tadmor, 2000) for flux calculations in order to capture high speed flow features like shock waves with non oscillatory solutions.

In FLUENT, the density based solver, solves governing equations (continuity, momentum and energy) simultaneously as a set or vector of equations (equation 3.58). For additional scalars, the governing equations will be solved sequentially (segregated) similar to pressure equation. For coupled equations FLUENT offers two algorithms: coupled-implicit and coupled-explicit.

The Navier-Stokes equations for compressible flow in vector mode can be written in conservation form as (MacCormack, 1982)

$$\frac{\partial}{\partial t}\int_V \mathbf{W}dV + \oint\left([\mathbf{F}-\mathbf{G}]\,.d\mathbf{A}\right. = \int_V \mathbf{H}dV \tag{3.58}$$

where vector **H** is the source term and vectors **W**, **F** and **G** are defined as

$$\mathbf{W} = \begin{Bmatrix} \rho \\ \rho u \\ \rho v \\ \rho w \\ \rho e_t \end{Bmatrix}, \mathbf{F} = \begin{Bmatrix} \rho u_i \\ \rho u_i u + p\hat{\mathbf{i}} \\ \rho u_i v + p\hat{j} \\ \rho u_i w + p\hat{\mathbf{k}} \\ \rho u_i e_t + p u_i \end{Bmatrix}, \mathbf{G} = \begin{Bmatrix} 0 \\ \tau_{xi} \\ \tau_{yi} \\ \tau_{zi} \\ \tau_{ij} u_i + q_j \end{Bmatrix} \tag{3.59}$$

Here as explained before, e_t is total energy per unit mass and q is the heat flux. The inviscid flux vector **F** is evaluated by upwind, flux differencing splitting (Roe, 1986), where discrete flux at each face is obtained by

$$F_f = \frac{1}{2}(F_L + F_R) - \frac{1}{2}\sum \alpha_k |\lambda_k| \mathbf{e}_k \tag{3.60}$$

where $\mathbf{e}_k$ are the right eigenvectors of Jacobian matrix of $\partial\mathbf{F}/\partial\mathbf{W}$, α_k is the strength of kth wave and λ_k is the eigenvalue of $\partial\mathbf{F}/\partial\mathbf{W}$, which represents the velocity of kth wave. The fluxes are computed on left (F_L) and right (F_R) hand side of the face.

3.4 Boundary conditions

The boundary conditions and even the initial conditions dedicate the particular solutions to be obtained from governing equations. Also, they have a strong impact on error and numerical instability.

In partial differential equations, using incorrect boundary or initial conditions leads to divergence in solution or even wrong results. In this case the problem will be "ill-posed" problem. However, if for a partial differential equation the solution exist, and the solution is unique, and small changes to coefficients, parameters and initial or boundary condition alternates the solution behaviour continuously, then the problem is "well-posed" (Sizikov, 2005). Therefore, is very important for CFD to ensure the problem is well-posed, especially in high speed flow analysis inside nozzle were both subsonic and supersonic flow exist.

Two classes of boundary conditions can be defined: a physical boundary condition, were

Table 3.1: Number of physical boundary conditions required for well-posedness of 3D flow (Poinsot and Lelef, 1992)

Boundary type	Euler	Navier-Stokes
Supersonic inflow	5	5
Subsonic inflow	4	5
Supersonic outflow	0	4
Subsonic outflow	1	4

specifies for one or more of the dependent variables, the known physical behaviour at the boundaries. These conditions will not change with numerical methods used to solve governing equations. The number of physical boundaries needed for different flow regimes suggested by theoretical analysis is shown in Table 3.1 (Poinsot and Lelef, 1992).

To solve a problem numerically, knowing just physical boundary conditions is not enough. If the number of physical boundary conditions is less than the number of main variables, we will impose a "soft or numerical" conditions. When there is not any explicit boundary condition value for one of the dependent variables, but the numerical solution requires defining something about it, a soft boundary will be used. This usually happens in outflow conditions or whenever the physics of the problem have not assigned any specific value to the boundary. Soft conditions are divided into two groups:

- Using extrapolation for a variable which is not defined by a physical boundary conditions. Imposing zero gradient value to dependent variable is one of examples.
- A more precise procedure is to solve the same conservation equations in the domain at the boundary.

There are different forms of boundary conditions but most of them can be divided in to two forms:

Dirichlet assignees specific value for dependent variable at the boundary

von Neumann prescribes the gradient of dependent variable normal to the boundary

As explained before two software have been used for simulations: FLUENT and OpenFOAM. The boundary conditions setup for each one are as follows.

3.4.1 FLUENT

Set of boundary conditions implemented for FLUENT cases are as follows:

Pressure inlet The flow inside nozzle is solved for different pressure ratios; So at the inlet of nozzle total pressure is known, but velocity and mass flow rate are not known. The total pressure for compressible flow is defined as

$$p_0 = p_s \left(1 + \frac{\gamma - 1}{2} M^2\right)^{\gamma/(\gamma-1)} \qquad M = \frac{u}{\sqrt{\gamma R T_s}} \tag{3.61}$$

where p_0 is the total pressure, p_s is the static pressure, M is Mach number, T_s is static temperature and γ is ratio of specific heats (c_p/c_v). For a case of incompressible flow the above equation is not valid any more and FLUENT uses a different formula. For compressible flows, isentropic relations for ideal gas is used to calculate velocity, static pressure and total pressure at inlet boundary. The static temperature at inlet boundary is calculated from total temperature T_0

$$\frac{T_0}{T_s} = 1 + \frac{\gamma - 1}{2} M^2 \tag{3.62}$$

Pressure outlet The pressure outlet boundary condition is selected for all outlet boundary conditions, which includes outlet of nozzle for inside the nozzle simulations and free stream area for outside of the nozzle simulations. The specified static pressure is used only when the flow is subsonic. However, for supersonic conditions pressure, like other dependent variables is extrapolated from the flow in interior. In order to reduce convergence difficulties reverse flow condition can be specified.
In density based solver the pressure at the patch of the pressure outlet boundary condition is solved using pressure splitting procedure based on AUSM+ scheme (Liou, 1996). In compressible flows, if the flow leaving exit boundary is subsonic then the pressure is computed using a weighted average of the left and the right state of the face boundary, but if the flow becomes locally supersonic then the pressure is extrapolated from interior cell pressure.

Wall boundary condition This boundary condition is used for solid regions, with no slip conditions. This is imposed on all wall boundaries to consider the effect of viscosity of

the flow. The wall shear stress for laminar flows are calculated based on the velocity gradient at the wall as

$$\tau_w = \mu \frac{\partial u}{\partial n} \tag{3.63}$$

It is important to have sufficiently fine grid near the wall, specially in high velocity gradient situations like this research, to accurately resolve boundary layer.

3.4.2 OpenFOAM

There are three types of boundary conditions in OpenFOAM: basic, primitive and derived.

3.4.2.1 Basic type

These types of boundaries, which also called physical boundaries, are purely described in terms of geometry. There are several basic boundaries in OpenFOAM such as patch, wall, symmetry, empty etc. The set of basic boundaries used for this research are as follows

Impermeable non-slip wall The velocity of fluid at the wall is the same as the velocity of the wall and the flux through it is zero.

Empty OpenFOAM always solves in three dimensions, so to set OpenFOAM for two or one dimensional simulations, empty boundary condition is implemented on each plane normal to second or third dimension.

3.4.2.2 Primitive type

The primitive boundaries are base numerical patch conditions. Following primitive boundaries have been used for simulations:

Fixed value It is used to specify fixed value (ϕ_B) at boundary face (ϕ_f). If the face gradient $(\nabla\phi)_f$ for diffusion term is required, it will calculate it using the boundary face value and cell centre value

$$\mathbf{S}_f.(\nabla\phi)_f = S_f \ \frac{\phi_B - \phi_P}{|\mathbf{d}|} \tag{3.64}$$

this is second order accurate.

Fixed gradient For the fixed gradient boundary condition (g_B), the dot product of the gradient and unit normal to the boundary is applied on boundary

$$g_B = \left(\frac{\mathbf{S}}{|\mathbf{S}|} . \nabla \phi \right)_f \tag{3.65}$$

The face value ϕ_f (for convection term) is estimated by interpolating the cell centre value to the boundary

$$\phi_f = \phi_P + \mathbf{d}.(\nabla \phi)_f = \phi_P + g_B \tag{3.66}$$

and for the diffusion term where face gradient is required, is written as

$$(\rho \Gamma_\phi)_f \left(\mathbf{S}_f \;\; g_B \right. \tag{3.67}$$

The zero gradient boundary condition is fixed gradient boundary condition with $g_B = 0$.

3.4.2.3 Derived type

These are complex patch conditions derived from primitive type. OpenFOAM has a lot of different derived boundaries. Following derived boundaries have been used for supersonic nozzle analysis[9].

Total pressure Which provides total pressure condition. For compressible subsonic condition is defined as

$$p_P = p_0 - 0.5\rho |u|^2 \tag{3.68}$$

where p_p is the pressure at patch. For compressible transonic flow ($Ma \leq 1$)

$$p_P = \frac{p_0}{1 + 0.5\psi |u|^2} \tag{3.69}$$

where ψ is compressibility and is expressed as

$$\psi = \frac{1}{RT} \tag{3.70}$$

[9]The foul list of derived boundaries can be found at $FOAM_SRC/finiteVolume/fields/fvPatchFields/derived

Finally for compressible supersonic flow ($Ma > 1$)

$$p_P = \frac{p_0}{(1+0.5\psi\frac{\gamma-1}{\gamma}|u|^2)^{\frac{\gamma}{1-\gamma}}} \tag{3.71}$$

which is similar to equation 3.61, the total pressure equation for compressible flow in FLUENT.

Total temperature Applies the total temperature boundary condition and is defined as

$$T_P = \frac{T_0}{\left(1+0.5\psi\frac{\gamma-1}{\gamma}|u|^2\right)} \tag{3.72}$$

which is exact equation for total temperature in FLUENT (equation 3.62).

InletOutlet provides a generic outflow condition, with specified inflow for the case of return flow.

Wave transmissive This boundary condition provides a wave transmissive outflow condition based on solving

$$\frac{D}{Dt}(\psi u) = 0 \tag{3.73}$$

the wave speed is calculated using:

$$c_P = \frac{\phi_P}{|S_f|} + \sqrt{\frac{\gamma}{\psi_P}} \tag{3.74}$$

where c_p is wave speed on patch face, ϕ_p is flux on patch face, ψ_P is compressibility on patch face and S_f is area of patch face.

3.5 Turbulence modelling

Almost all fluids flow encountered in engineering practise are turbulent. Therefore, it is important in CFD simulations to capture physical feature of a flow with minimum complexity. Turbulence modelling is one of three key elements in CFD, after grid generation and algorithm development. There is no clear definition for turbulence flow, but it is characterised by (Tennekes and Lumley, 1972)

Irregularity Turbulent flows are random, chaotic and consist of a spectrum of different eddy sizes; Therefore it is impossible to find and solve their exact equations instead all analysis are based on statistical methods.

Increased diffusivity Which will increase rates of momentum, heat and mass transfer and causes rapid mixing.

Large Reynolds number Turbulent flows always occur at high Reynolds numbers.

Energy dissipation Where kinetic energy is transferred from large eddies to small eddies and from small eddies is transferred to internal energy. The process of transferring energy from large eddies to small eddies is called *cascade process*.

Three dimensional Turbulence is rotational and three dimensional. In two dimensional turbulence modelling, vortex stretching, which is an important mechanism in vorticity maintenance is absent.

Continuum Turbulence is continuum phenomena, and it is determined by governing equations of fluid mechanics.

In cascade process kinetic energy is transferred from the largest scales to small scales, then at small scales the frictional forces and viscous stresses becomes too large and kinetic energy is dissipated to internal energy. The dissipation (ε) is energy per unit time and unit mass. The dissipation is proportional to kinematic viscosity and fluctuating velocity gradient (Davidson, 2011). The smallest scales where dissipation of kinetic energy to internal energy occurs are called Kolmogorov scales.

The interaction between velocity gradient and vorticity is an essential factor to create and maintain turbulence. The vorticity is the curl of velocity vector

$$\omega = \nabla \times \mathbf{u} = \varepsilon_{ijk} \frac{\partial u_k}{\partial x_j} \tag{3.75}$$

where ε_{ijk} is the Levi-Civital tensor. The vorticity vector can be split up into symmetric (diagonal) and skew-symmetric (off-diagonal) terms. The symmetric term is called vortex stretching and the skew-symmetric term represents vortex tilting/rotation. vortex stretching and vortex tilting shows that the interaction between vorticity and velocity gradient will create vorticity in all three directions; Therefore the turbulence always must be three dimensional.

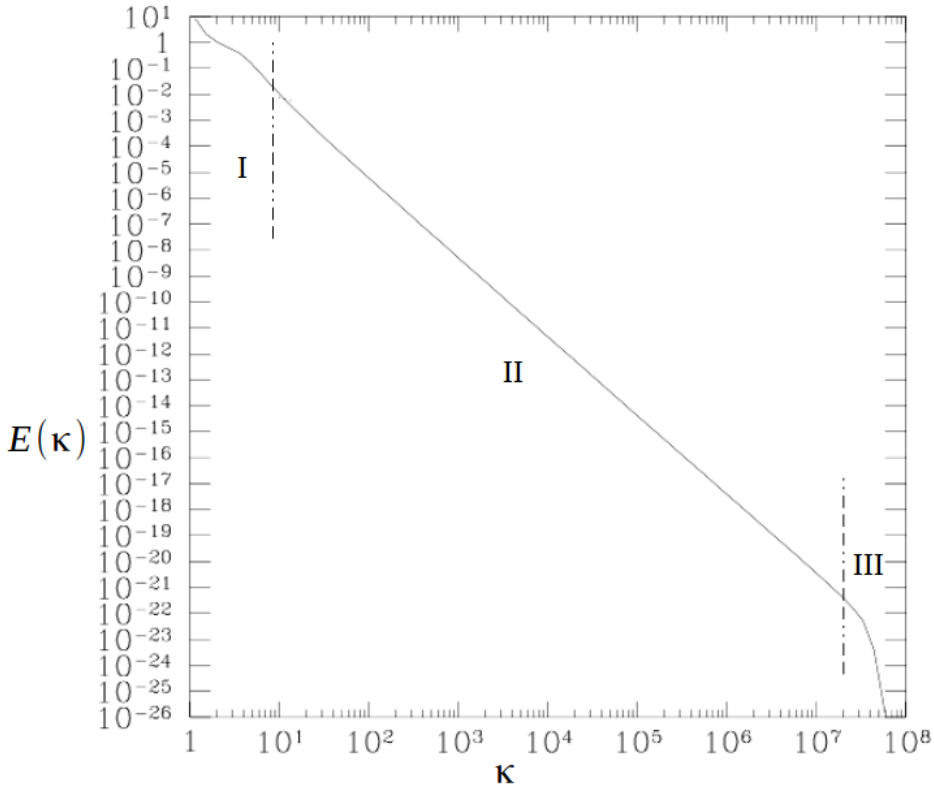

Figure 3.5: Energy spectrum for two dimensional steady state turbulent with high Reynolds number (Bowman, 1996)

In turbulent flows, the average turbulent kinetic energy per unit mass is obtained by

$$k = \int_0^\infty E(\kappa)\, d\kappa \tag{3.76}$$

where κ is the wave number and is proportional to eddy's radius ($\kappa \propto 1/r$). The spectrum of $E(\kappa)$ for two dimensional steady state turbulent flow is shown in Figure 3.5. However, for any turbulent flow, the energy spectrum has three regions:

I. In this region, large eddies are carrying most of the energy. They get energy from mean flow and their energy is transferred to smaller eddies.

II. This region is called inertial range. The existence of this region requires high Reynolds number and acts as a transport region in cascade process.

III. Dissipation range. It is the area which dissipation of eddies kinetic energy to the internal

energy happens. The eddies are small and isotropic and they are called Kolmogrov scales.

Kraichnan (1971) has suggested that for both two and three dimensional flows, inertial range can exhibit energy transfer of the form of

$$E(\kappa) = C\varepsilon^{2/3}\kappa^{-5/3} \tag{3.77}$$

where C is constant and will be different for two or three dimensional flows. Equation 3.77 is also called Kolmogorov law and states that for fully turbulent flow, the energy spectra in inertial range should decay by slope of -5/3.

There are several approaches for turbulent flow simulations, depend on accuracy and computer power. The most accurate approach is Direct Numerical Simulation (DNS), where Navier-Stokes equations are solved without any approximation other than numerical discretisation (Eswaran and Pope, 1988; Moin and Mahesh, 1998). DNS requires very high demand of computer resources due to requirements for mesh resolution and time step size, which makes it impractical for engineering applications.

The second approach is Large Eddy Simulation (LES). As explained before large scale eddies are carrying more energy than small scales ones, and they have more effect on fluid properties. Therefore, in LES spatial filtering is applied to separate different length scales in turbulent flows. The large scale eddies that can be solved numerically by the given mesh are called "supergrid" scales. The effect of unresolved small scale eddies (subgrid scale) on resolved scales is modelled (Ghosal and Moin, 1995). The reason for filtering is that the small scale eddies are more homogeneous and isotropic and therefore easier to model. The size of the mesh has important effect on filtering size of eddies.

The two models described above are still not cost effective for complex engineering applications, as they require huge computer power. So the third approach is statistical simulation of turbulent flows. It is called Reynolds Average Navier-Stokes (RANS) equations introduced by Reynolds (1895), where flow variables are decomposed into mean value and fluctuation around mean value.

$$\phi(x_i,t) = \overline{\phi}(x_i,t) + \phi^{'}(x_i,t) \tag{3.78}$$

The three main methods to find the mean value in turbulence modelling are time averaging, spatial averaging and ensemble averaging (Ferziger and Perić, 2002; Wilcox, 1998). For

steady state flow and stationary turbulence, $\bar{\phi}$ is calculated with *time averaging* method

$$\overline{\phi}\left(x_i\right) = \lim_{T\to\infty} \frac{1}{T} \int_{t_0}^{t_0+T} \phi\left(x_i,t\right) dt \tag{3.79}$$

here T is the averaging interval and should be large enough compared to time scale of fluctuations. *Spatial averaging* is appropriate for homogeneous turbulence[10]

$$\overline{\phi}\left(t\right) = \lim_{V\to\infty} \frac{1}{V} \iiint \phi\left(x_i,t\right) \tag{3.80}$$

For unsteady flows, *ensemble averaging* is the most general form which $\bar{\phi}$ is calculated from N identical experiments

$$\overline{\phi}\left(x_i,t\right) = \lim_{N\to\infty} \frac{1}{N} \sum_{n=1}^{\infty} \phi_n\left(x_i,t\right) \tag{3.81}$$

For compressible flows, in order to reduce the complexity of the equations, density-weighted averaging procedure (*Favre averaging*) is applied (Wilcox, 1998). Therefore $\overline{\phi}$ for compressible steady state situation can be defined as

$$\overline{\phi}\left(x_i\right) = \frac{1}{\overline{\rho}} \lim_{T\to\infty} \int_{t}^{t+T} \rho\left(x_i,t\right) \phi\left(x_i,t\right) dt \tag{3.82}$$

where $\overline{\rho}$ is conventional time averaging of density.

For incompressible flow, applying above averaging method into instantaneous continuity equation 3.1 and N-S equations 3.2 without body forces yields to

$$\frac{\partial \rho}{\partial t} + \frac{\partial\left(\rho \overline{u}_i\right)}{\partial x_i} = 0 \tag{3.83}$$

$$\frac{\partial\left(\rho \overline{u_i}\right)}{\partial t} + \frac{\partial}{\partial x_j}\left(\rho \overline{u}_j \overline{u}_i + \rho \overline{u_j' u_i'}\right) = -\frac{\partial \overline{p}}{\partial x_i} + \frac{\partial \overline{\tau}_{ji}}{\partial x_j} \tag{3.84}$$

The term $\rho \overline{u_j' u_i'}$, is called the Reynolds stress tensor. This will add six unknown components along another four unknown properties (three velocity and pressure), so the system will not be closed. To close the system extra turbulence modelling is required.

[10]Uniform in all directions.

3.5.1 Algebraic models

The Algebraic models[11] are the simplest of all turbulence modelling known. In these models the Reynolds stress tensor is computed from Boussinesq assumption. In Boussinesq assumption the Reynolds stress is related to mean rates of deformation (Ferziger and Perić, 2002)

$$-\rho\overline{u_i'u_j'} = \mu_t\left(\frac{\partial\overline{u_i}}{\partial x_j} + \frac{\partial\overline{u_j}}{\partial x_i}\right) - \frac{2}{3}\rho\delta_{ij}k \tag{3.85}$$

where k is turbulent kinetic energy

$$k = \frac{1}{2}\left(\overline{u_i'u_i'}\right) \tag{3.86}$$

and μ_t is the turbulent or eddy viscosity, therefore the kinematic turbulence or eddy viscosity is obtained by $\nu_t = \mu_t/\rho$.

The turbulent viscosity in Boussinesq formula can be calculated from Parndtl mixing length theory (Prandtl, 1927)

$$\mu_t = \rho L_{mix}^2 \frac{\partial\overline{u}}{\partial y} \tag{3.87}$$

where y is direction normal to the wall, and L_{mix} is the mixing length. Considering $\partial\overline{u}/\partial y$ as the only significant velocity gradient, the Reynolds stress tensor will be described by

$$-\rho\overline{u_i'u_j'} = \rho L_{mix}\frac{\partial\overline{u}}{\partial y}^{2} \tag{3.88}$$

This is called *mixing length* model and is not an accurate model. one of the problem is that the value of L_{mix} is unknown. There are more advance algebraic models proposed by Cebeci (2012) and Baldwin and Lomax (1978) which are used frequently for aerodynamics of airfoils.

3.5.2 Energy equation models

There are two types of turbulence energy equation models, one equation models and two equation models. Both of these two models are based on Boussinesq assumption (equation 3.85). Two equation models provide an equation for turbulent length scale, thus they predict flow properties more accurately. In this research different types of two equation models were

[11] Also known as eddy viscosity models.

adopted.

The eddy viscosity in terms of density, turbulent length scale and turbulent kinetic energy (equation 3.86) from dimensional analysis will be

$$\mu_t = constant.\rho k^{1/2} L \tag{3.89}$$

where k is determined by taking trace[12] of Reynolds stress tensor

$$-\rho \overline{u_i' u_i'} = -2\rho k \tag{3.90}$$

3.5.2.1 One equation models

In this model one extra equation of dissipation is introduced to close the turbulent kinetic energy equation. So the dissipation is related to L and k by

$$\varepsilon = C\frac{k^{3/2}}{L} \tag{3.91}$$

where C is called closure coefficient. However, the turbulent length scale is still unknown and some algebraic expression is required to find it (Wolfshtein, 1969).

The Spalart-Allmaras model (Spalart and Allmaras, 1992) is the most used one equation model. It has shown good results for boundary layers with adverse pressure gradient and turbomachinery applications. The Spalart-Allmaras model and even other one equation models are generally for low Reynolds number flows to solve viscous affected region of boundary layer.

3.5.2.2 Two equation models

Many of simulations done in this research are based on two equation turbulence modelling. These models provide equation for both turbulent kinetic energy and length scale, therefore they are “complete” models and can predict the properties of given turbulent flow with no prior knowledge of the turbulent structure.

[12] Sum of the elements on main diagonal arrays of tensor.

Table 3.2: Coefficient values in standard $k-\varepsilon$ model (Launder and Spalding, 1974)

C_μ	C_1	C_2	σ_k	σ_ε
0.09	1.44	1.92	1.0	1.31

The $k-\varepsilon$ model

The $k-\varepsilon$ model is the most popular two equation model. The main model is called "standard $k-\varepsilon$ model" developed by Launder and Spalding (1974). The turbulent length scale and turbulent viscosity are computed from

$$L = \frac{k^{3/2}}{\varepsilon} \tag{3.92}$$

$$\nu_t = \frac{\mu_t}{\rho} = C_\mu k^{1/2} L = C_\mu \frac{k^2}{\varepsilon} \tag{3.93}$$

where C_μ is dimensionless constant and for standard $k-\varepsilon$ model is universal and equal to 0.09. At high Reynolds numbers, the transport equations for k and ε may be expressed as

$$\frac{D\varepsilon}{Dt} = \frac{1}{\rho}\frac{\partial}{\partial x_j}\left[\frac{\mu_t}{\sigma_\varepsilon}\frac{\partial \varepsilon}{\partial x_j}\right] + \frac{C_1 \mu_t}{\rho}\frac{\varepsilon}{k}\left(\frac{\partial \overline{u_i}}{\partial x_j} + \frac{\partial \overline{u_j}}{\partial x_i}\right)\frac{\partial \overline{u_i}}{\partial x_j} - C_2\frac{\varepsilon^2}{k} \tag{3.94}$$

$$\frac{Dk}{Dt} = \frac{1}{\rho}\frac{\partial}{\partial x_j}\left[\frac{\mu_t}{\sigma_k}\frac{\partial k}{\partial x_j}\right] + \frac{\mu_t}{\rho}\left(\frac{\partial \overline{u_i}}{\partial x_j} + \frac{\partial \overline{u_j}}{\partial x_i}\right)\frac{\partial \overline{u_i}}{\partial x_j} - \varepsilon \tag{3.95}$$

The constants in equations 3.94 and 3.95 are derived from extensive examination of free turbulent flows and are shown in table 3.2.

One of limitation of standard $k-\varepsilon$ model is accuracy of ε equation in flows with large rates of deformation. Yakhot and Orszag (1986) has applied renormalisation group method (RNG) to modify ε equation with extra strain dependent correction term for C_1in equation 3.94, which has yield to the turbulence model called "RNG $k-\varepsilon$ model". The RNG model also has improvements for swirl flows and low Reynolds numbers flows.

The recent development by Shih *et al.* (1995a) has lead to "realizable $k-\varepsilon$ model". This model consists of new dissipation rate equation, based on the dynamic equation of the mean-square vorticity fluctuation at large turbulent Reynolds number; And new eddy viscosity formulation based on realizability constraints. It has significant improvement compare to stand-

ard $k-\varepsilon$ model on rotating homogeneous flows, boundary free sheer flows such as planar and round jets, and backward facing step separated flows.

The new dissipation rate equation in realizable $k-\varepsilon$ model for large Reynolds number flows is obtained from

$$\varepsilon = \nu_t \overline{\omega_i \omega_i} \tag{3.96}$$

The term $\overline{\omega_i \omega_i}$, is the dynamic equation of the mean square vorticity fluctuation. Therefore the new modelled dissipation rate equation will be

$$\frac{D\varepsilon}{Dt} = \frac{1}{\rho}\frac{\partial}{\partial x_j}\left[\frac{\mu_t}{\sigma_\varepsilon}\frac{\partial \varepsilon}{\partial x_j}\right] + C_1 S\varepsilon - C_2\frac{\varepsilon^2}{k+\sqrt{\nu\varepsilon}} \tag{3.97}$$

where C_1 coefficient is obtained from

$$\begin{gathered} max\left\{0.43, \frac{\eta}{5+\eta}\right\} \\ \eta = Sk/\varepsilon \qquad S = \sqrt{2S_{ij}S_{ij}} \end{gathered} \tag{3.98}$$

In realizable $k-\varepsilon$ model, C_μ is not constant. Shih *et al.* (1995b) proposed new formulation for C_μ

$$C_\mu = \frac{1}{A_0 + A_s \bar{u}^{(*)k/\varepsilon}} \tag{3.99}$$

where

$$\begin{aligned} \bar{u}^{(*)} &= \sqrt{S_{ij}S_{ij} + \tilde{\Omega}_{ij}\tilde{\Omega}_{ij}} \\ \tilde{\Omega}_{ij} &= \Omega_{ij} - 2\varepsilon_{ijk}\omega_k \\ \Omega_{ij} &= \overline{\Omega}_{ij} - \varepsilon_{ijk}\omega_k \\ S_{ij} &= \frac{1}{2}\left(\frac{\partial \overline{u}_i}{\partial x_j} + \frac{\partial \overline{u}_j}{\partial x_i}\right) \end{aligned} \tag{3.100}$$

ω_i and Ω_i are the fluctuating and mean vorticities which are obtained from

$$\Omega_i = \varepsilon_{ijk}\frac{\partial \overline{u}_k}{\partial x_j} \qquad \omega_i = \varepsilon_{ijk}\frac{\partial u_k'}{\partial x_j} \tag{3.101}$$

In equation 3.100, $\overline{\Omega}_{ij}$ is the mean rotation rate viewed in a rotating reference frame with the angular velocity ω_k. A_0 is constant and in OpenFOAM is set to 4.0 and in FLUENT is 4.04.

Table 3.3: Default model coefficients correspond to the realizable $k-\varepsilon$ model

σ_k	σ_ε	C_1	C_2	C_μ	A_0
1.0	1.2	equation 3.98	1.9	equation 3.99	OpenFOAM 4.0
					FLUENT 4.04

A_s is derived from

$$A_s = \sqrt{6}\cos\phi \qquad \phi = \frac{1}{3}\arccos\left(\sqrt{6}W\right)$$
$$W = \frac{S_{ij}S_{jk}S_{ki}}{\tilde{S}^3} \qquad \tilde{S} = \sqrt{S_{ij}S_{ij}} \tag{3.102}$$

The default coefficients for realizable $k-\varepsilon$ are summarised in table 3.3.

The $k-\omega$ model

The model was proposed by (Wilcox, 1988, 1998), and it is the prominent alternative to $k-\varepsilon$ model. It solves the same standard k equation, but to determine the length scale, the ω equation will be solved instead. The ω which is called *specific dissipation*[13] is defined by $\omega \propto \varepsilon/k$. The form of equations for k and ω are

$$\frac{D(\rho k)}{Dt} = P_{ij}\frac{\partial u_i}{\partial x_j} - \beta^*\rho\omega k + \frac{\partial}{\partial x_j}\left[(\mu+\sigma^*\mu_t)\frac{\partial k}{\partial x_j}\right] \tag{3.103}$$

$$\frac{D(\rho\omega)}{Dt} = \left(\frac{\gamma\omega}{k}\right)P_{ij}\frac{\partial u_i}{\partial x_j} - \beta\rho\omega^2 + \frac{\partial}{\partial x_j}\left[(\mu+\sigma\mu_t)\frac{\partial\omega}{\partial x_j}\right] \tag{3.104}$$

where

$$\mu_t = \gamma^*\frac{\rho k}{\omega}$$
$$P_{ij} = 2\mu_t\left[S_{ij} - \frac{1}{3}\frac{\partial u_k}{\partial x_k}\delta_{ij}\right] - \frac{2}{3}\rho k\delta_{ij} \tag{3.105}$$
$$\varepsilon = \beta^*\omega k \qquad L = \sqrt{k}/\omega$$

The values for closure coefficients are summarised in table. In equation 3.105, for compressible flows the term S_{ij} is replaced by $S_{ij} - (1/3)S_{kk}\delta_{ij}$.

[13] It is also called turbulent frequency with $1/s$ dimension.

Table 3.4: Closure coefficients for $k-\omega$ model

β	β^*	γ	γ^*	σ	σ^*
3/40	9/100	5/9	1	1/2	1/2

One of advantages of $k-\omega$ model to $k-\varepsilon$ model is in regions of low turbulence when k and ε go to zero. The term ε^2/k in ε equation becomes infinite as $k \to 0$. However in ω equation both k and ε will go to zero at correct rate to avoid numerical destruction.

Menter (1994) proposed the shear stress transport (SST) $k-\omega$ model, which has the robust and accurate formulation of $k-\omega$ model in near wall region and advantage of the free stream independence of $k-\varepsilon$ model. In compare to original $k-\omega$ model, it has an additional cross diffusion term in ω equation and the modelling for constants are different.

3.5.3 Reynolds Stress Model (RSM)

The two equation turbulence models are incapable of capturing anisotropy of normal stresses and computing the effect on turbulence of extra strain and body forces. The RSM models[14] considers all these effects by solving transport equations for the Reynolds stresses, together with an equation for the dissipation rate (Launder *et al.*, 1975). This will add extra seven transport equations for three dimensional flows[15]. On the downside RSM will increase the amount of storage and CPU usage run time significantly.

The exact transport equation of Reynolds stress($\rho\overline{u_i'u_j'}$) can be written as following

$$\frac{\partial}{\partial t}\left(\rho\overline{u_i'u_j'}\right) + \underbrace{\frac{\partial}{\partial x_k}\left(\rho\overline{u}_k\rho\overline{u_i'u_j'}\right)}_{Convection\ term} = P_{ij} + D_{ij} - \varepsilon_{ij} + \Pi_{ij} + \Omega_{ij} \tag{3.106}$$

where P_{ij} is the rate of production of Reynolds stress, D_{ij} is transport of Reynolds stress by diffusion, ε_{ij} is the rate of dissipation, Π_{ij} is the transport of Reynolds stress due to pressure-strain interaction and finally Ω_{ij} is the transport of Reynolds stress by rotation. The production term is

$$P_{ij} = -\left(\rho\overline{u_i'u_k'}\frac{\partial\overline{u}_j}{\partial x_k} + \rho\overline{u_j'u_k'}\frac{\partial\overline{u}_i}{\partial x_k}\right) \tag{3.107}$$

[14] Also called second order closure model.

[15] For two dimensional flows this will be five extra equations

The rotation term is formulated as

$$\Omega_{ij} = -2\omega_k \left(\overline{u'_j u'_m} \varepsilon_{ikm} + \overline{u'_i u'_m} \varepsilon_{jkm} \right) \tag{3.108}$$

where the ω_k is the rotation vector. The diffusion term is modelled as

$$D_{ij} = \frac{\partial}{\partial x_m} \left(\frac{\nu_t}{\sigma_k} \frac{\partial}{\partial x_m} \left(\rho \overline{u'_i u'_j} \right) \right) \tag{3.109}$$

with $\sigma_k = 1.0$. The kinematic viscosity is defined as

$$\nu_t = C_\mu \frac{k^2}{\varepsilon} \qquad C_\mu = 0.09 \tag{3.110}$$

The dissipation rate of turbulent is calculated by

$$\begin{aligned} \varepsilon_{ij} &= (2/3)\, \rho \varepsilon \delta_{ij} \\ \varepsilon &= \nu \overline{\frac{\partial u'_i}{\partial x_k} \frac{\partial u'_j}{\partial x_k}} \end{aligned} \tag{3.111}$$

The scalar dissipation rate is modelled with the same equation of standard $k - \varepsilon$ model (equation 3.94).

The pressure-strain interaction term in equation 3.106, is the most difficult one to model and consists of two parts. First the slow pressure-strain term or return to isotropy term, secondly rapid pressure-strain term.

$$\Pi_{ij} = \underbrace{-C_1 \frac{\varepsilon}{k} \left(\rho \overline{u'_i u'_j} - \frac{2}{3} k \delta_{ij} \right)}_{Slow\ pressure-strain} \underbrace{-C_2 \left(P_{ij} - \frac{2}{3} P \delta_{ij} \right)}_{Rapid\ pressure-strain} \tag{3.112}$$

the default coefficient values are: $C_1 = 1.8$ and $C_2 = 0.6$.

3.5.4 Wall functions

At high Reynolds numbers, the viscous sublayer of a boundary layer becomes so thin that very fine grid is needed to resolve large gradient of variables in the boundary layer. Using fine grids

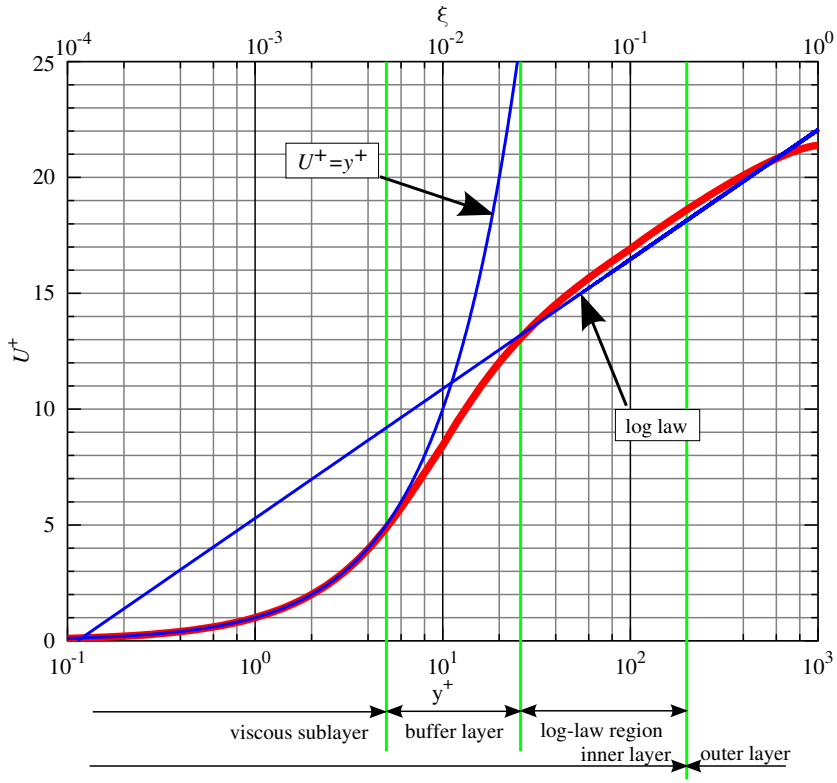

Figure 3.6: Turbulent boundary layer

near the wall will increase significantly the computer resources and run time for simulations. This issue can be solved by using *wall function* which assumes that the flow near the wall is fully turbulent. The velocity profile of turbulent boundary layer is shown in Figure 3.6.

The Boundary layer is almost laminar in viscous sublayer and fully turbulent in log-law region. As mentioned before turbulence models are valid for fully turbulent flows, therefore semi empirical formulas "wall functions", are used to model flow properties between the wall and log-law region. In log-law region the profile is

$$u^+ = \frac{1}{\kappa}\ln y^+ + B = \frac{\overline{u}}{u_\tau} \tag{3.113}$$

where κ is von Karman constant ($\kappa = 0.41$), u_τ is the shear velocity given by $u_\tau = \sqrt{|\tau_w|/\rho}$ and τ_w is the shear stress at the wall, $\overline{u}$ is the mean velocity parallel to the wall, B is an empirical constant related to the thickness of viscous sublayer and y^+ is dimensionless parameter which shows distance from the wall and is defined as

$$y^+ = \frac{\rho u_\tau y}{\mu} \tag{3.114}$$

In viscous sublayer $u^+ = y^+$ but in buffer layer where $5 < y^+ < 30$, neither law holds. In buffer layer the effect of viscosity and turbulent are equally important.

Reynolds numbers in this study are reasonably high, so using wall functions will provide proper accuracy without limiting computing resources. However, for low Reynolds numbers "near wall modelling" is required to capture even viscous sublayer. Both OpenFOAM and FLUENT provide range of wall functions for high and low Reynolds numbers.

Chapter 4

CFD (FLUENT) Analysis of Single and Multiphase Flow Using Variable Inlet Pressure

In this chapter the simulation results with Ansys FLUENT will be represented. The results include both single phase and multiphase simulations. The simulations include inside and outside of the nozzle but separately.

Ansys FLUENT is commercial software and the license file defines the number of processors can be used. Because of limitations on license which was limited to just 4 core processors it was impossible to provide results in limited time for full domain. To overcome this problem, the domain was decomposed in the two sections, inside nozzle and external domain. First the inside nozzle simulations were performed and then external domain simulations were done by using boundary conditions from inside nozzle simulations.

4.1 Single phase simulations

The nature of sandblasting is multiphase flow. However, due to pressure difference inside the nozzle, the air becomes supersonic, therefore the air has a major role in distribution of sands inside nozzle and overall performance of sandblasting system. The single phase simulations also will be used for validation of numerical solutions.

The major emphasis in this section is to understand and investigate the effect of swirl of flow parameters and shock waves structure.

Table 4.1: Boundary conditions for FLUENT inside nozzle simulations.

Zone	Type	Value
Inlet	Pressure-inlet	2, 3, 4 atm
Outlet	Pressure-outlet	0 gauge pressure
Wall	Wall	No slip
		Standard wall functions for turbulence

4.1.1 Inside nozzle

Sandblasting machines normally work at high pressure ratios (P_{in}/P_{out}), around 80psi[1]. One of the key elements in this research was to optimise the nozzle using swirl flow to provide a system that works at lower pressures to save energy and reduce the cost. Experimental and numerical analyses by Abbasalizadeh (2011) showed that it is possible to use low pressure sandblasting system by adding heat to the system. In this study the effect of swirl flow on low pressure system will be investigated. The geometry of nozzle was explained in section 1.2.1.

The grid was generated using ICEM tetrahedral algorithm to generate the main mesh and then adding 10 prism layers at wall boundaries with the total number of 318,917 cells (Figure 4.1). The partial differential equations are solved in transient mode with implicit density based solver. The discretisation method for the gradient is least square, and for flow is second order upwind and third order MUSCL methods.

The RSM model has been adopted for turbulence modelling of swirl flow and standard $k-\omega$ has been used for without swirl effect simulations, with first order upwind method for both discretisation. The RSM has been selected due to high order of anisotropy in swirl flows. Other turbulence models also have been tested for swirl flow, $k-\varepsilon$ standard and RNG models did not provide stable results as they are mainly for isotropic turbulence modelling, however the realizable $k-\varepsilon$ model proved to be stable for some swirl simulations. More research is required in turbulence modelling of swirl flows.

The results for three inlet pressures (2, 3 and 4 atm) have been presented here. The boundary conditions are explained in Table 4.1. The inlet boundary is pressure-inlet, and the outlet boundary is set to atmospheric pressure, all in Cartesian coordinate system.

Experimental and numerical simulations represent two separation patterns for an over-expanded nozzle, the Free Shock Separation (FSS) and Restricted Shock Separation (RSS) (Hadjadj and Onofri, 2009). In FSS the separation region extends from the separation point

[1] 5.51bar

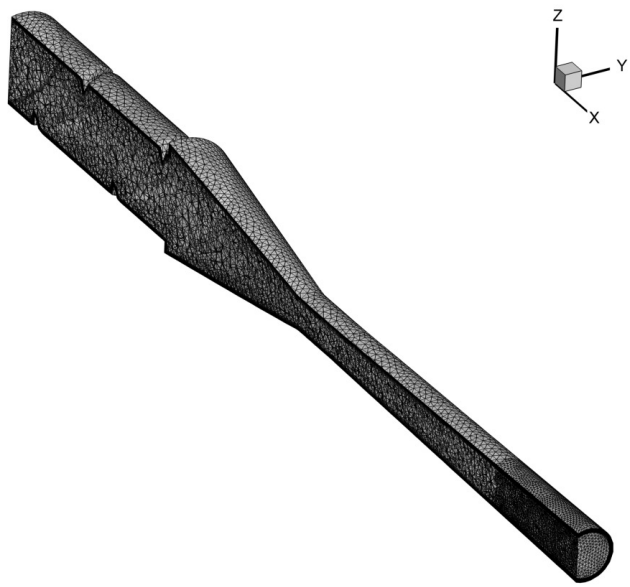

Figure 4.1: Inside nozzle domain mesh

to the end of the nozzle, but in RSS the separation zone reattaches to the surface and creates recirculation bubbles.

4.1.1.1 Inlet Pressure 2atm

Mach number contours of the nozzle without helical insert for inlet pressure 2atm is presented in Figure 4.2. The shock waves structure and separation zones are symmetric. There are two small FSS regions close to the wall. By adding swirl effect with helical insert the flow pattern will not remain symmetric any more. There is a large FSS region at the top and a very small RSS at the lower wall (Figure 4.3). The larger separation zone will provide better a mixing feature for nozzle, although will reduce the effective cross section at the exit of nozzle.

The static pressure diagram is shown in Figure 4.4, the zero point on the X axis is the inlet of nozzle and negative X represents helical insert before the inlet of the nozzle. The helical insert has reduced the axial velocity, therefore the main Mach disk has moved to upstream; But shock waves and expansion fans are weaker. For both swirl and non-swirl conditions the pressure ratio is 2.

4.1.1.2 Inlet Pressure 3atm

The Mach number contours at inlet pressure 3atm without helical insert is shown in Figure 4.5. The nozzle is overexpanded with one strong shock wave at the exit of nozzle. The shock

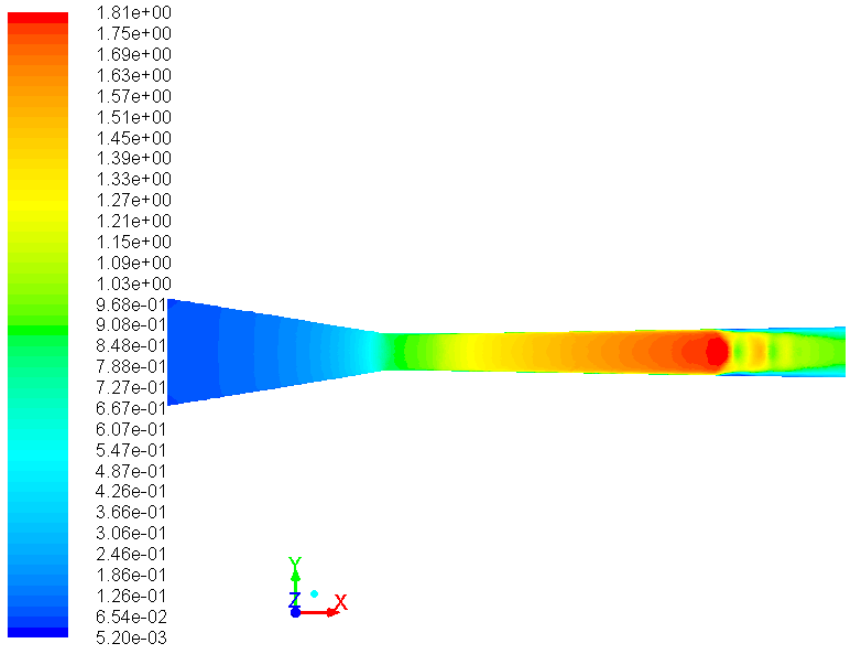

Figure 4.2: Mach number contours for inside nozzle simulations without helical insert at inlet pressure 2atm.

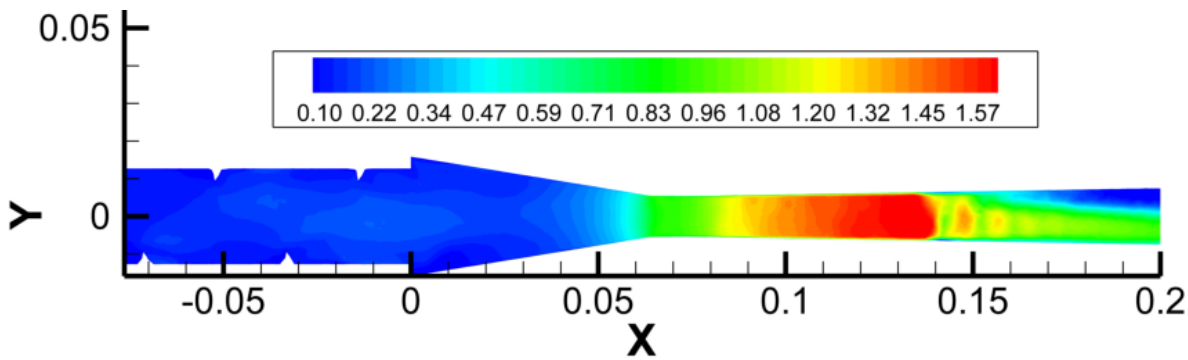

Figure 4.3: Mach number contours for inside nozzle simulations with helical insert at inlet pressure 2atm.

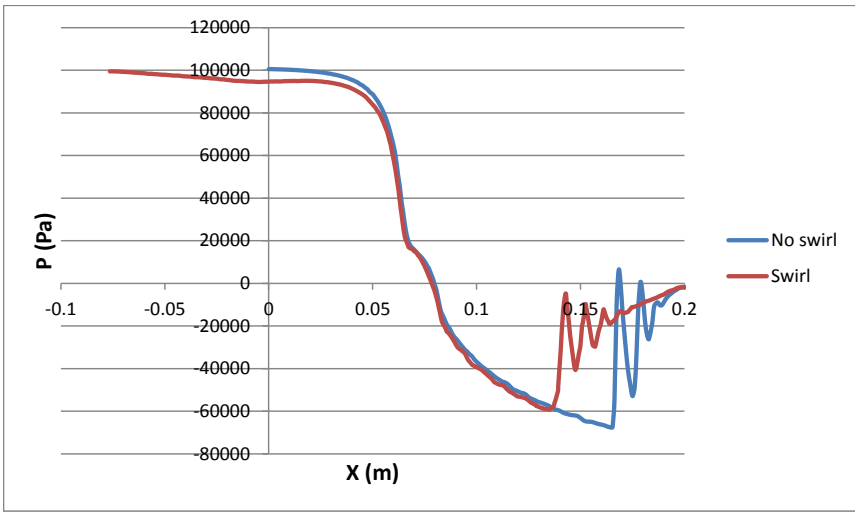

Figure 4.4: Static pressure graph at the centre of nozzle for inlet pressure 2atm.

wave is symmetric with the small separation zone. Without swirl condition the flow inside nozzle is steady state and the results from transient simulations were similar to steady state solutions.

Adding the swirl effect by helical insert will change the flow pattern and shock wave structure. The Mach number contours for swirl flow is shown in Figure 4.6. The flow is not steady state any more and due to high pressure gradient there is larger separation zone.

The schematic structure of lambda shocks and the separation zone for inlet pressure 3atm is illustrated in Figure 4.7. As a result of Coanda effect the shock wave structure is asymmetric and the flow tends to attach to the surface where creates RSS pattern on downside of nozzle and FSS on upper side. The separation zone starts at the interaction point between oblique shock wave and the nozzle wall which creates a high adverse pressure gradient. Reflection of oblique shock wave on the shear layer generates expansion fans. Since the separation zone is very large the flow remains attached to the downside of nozzle (Coanda effect), therefore the only change between time steps is just in position of shear layer.

The static pressure diagram in the centre of the nozzle is shown in Figure 4.8. It can be seen that by adding the swirl effect, there are series of weaker shock waves and expansion fans instead of one strong shock wave. These results are in good agreement with Abbasalizadeh (2011) experimental tests and simulations on the same nozzle. The pressure ratio for swirl condition is 3 as air reaches to atmospheric pressure, however, for non-swirl condition the air pressure goes below atmospheric pressure therefore the pressure ratio will increase to 4.8.

The tangential velocity at the exit of the nozzle, along the outlet, is illustrated in Figure 4.9. The swirl effect has increased tangential velocity. By distancing from the centre, the

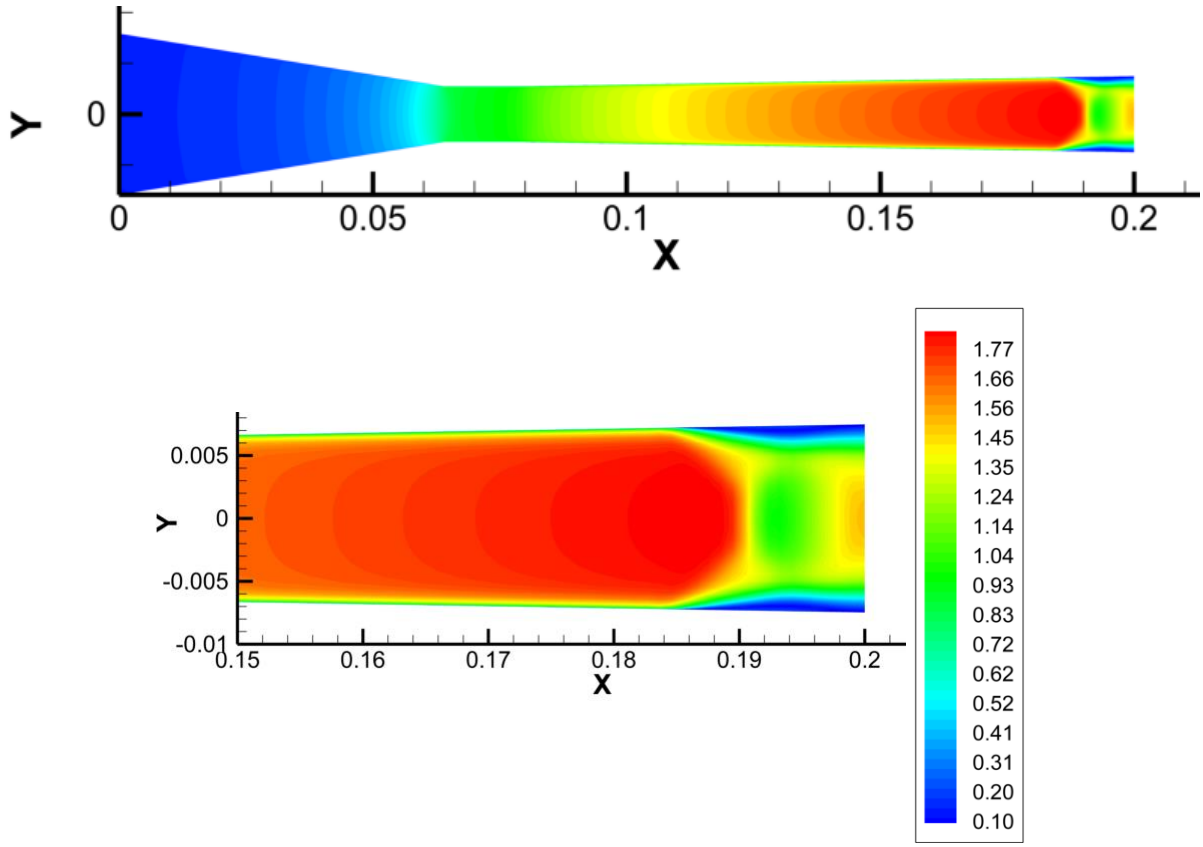

Figure 4.5: Mach number contours of inside nozzle simulations without swirl attachment at inlet pressure 3atm.

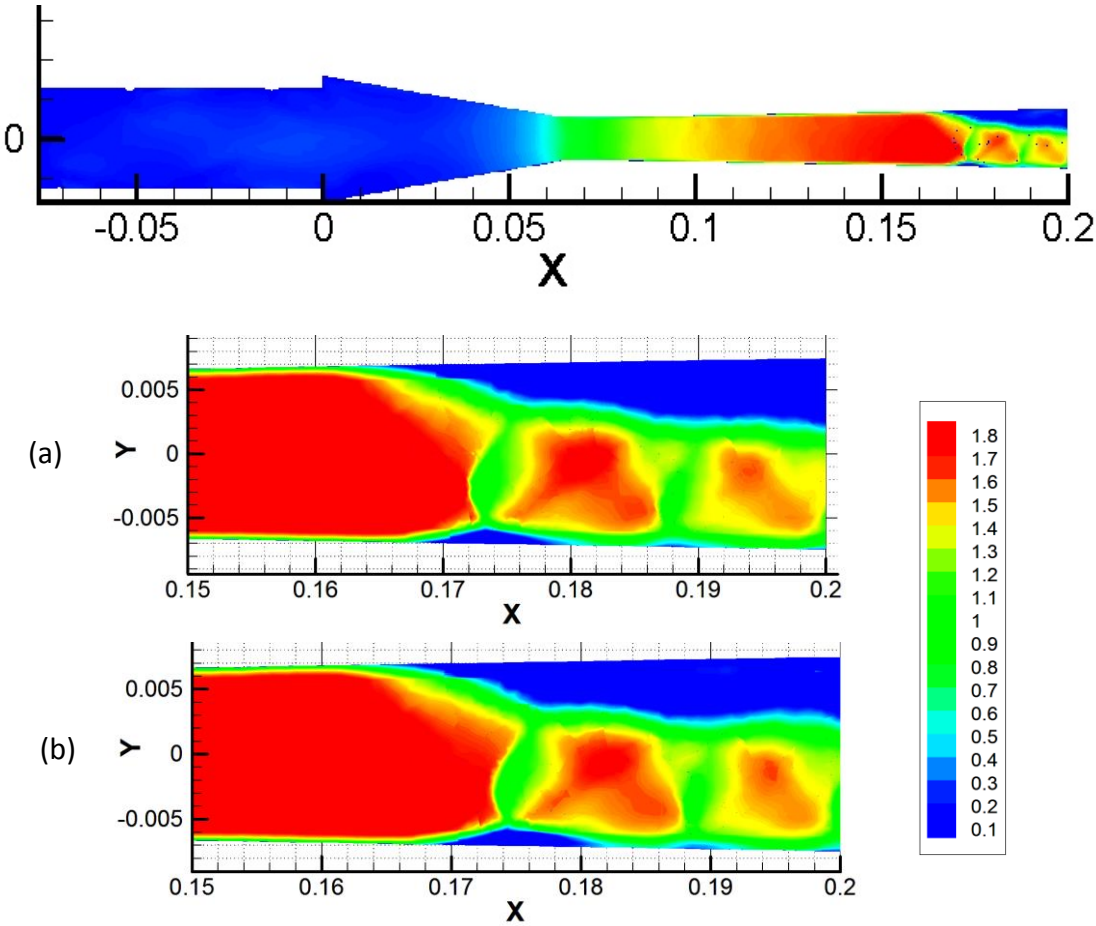

Figure 4.6: Mach number contours for inside nozzle simulations with helical insert for inlet pressure 3atm at (a) t=0.8e-2s and (b) t=1.8e-2s.

tangential velocity is increasing, where r is increasing in equation 4.1. This means if ω is constant the flow will be forced vortex motion.

$$v_\theta = r\omega \tag{4.1}$$

4.1.1.3 Inlet Pressure 4atm

Mach number contours for inlet pressure 4atm without swirl effect is shown in Figure 4.10. As the pressure increases inside the nozzle shock waves will move out of the nozzle. But with the swirl effect, there are still some weak shock waves. As oblique shock waves become weaker,

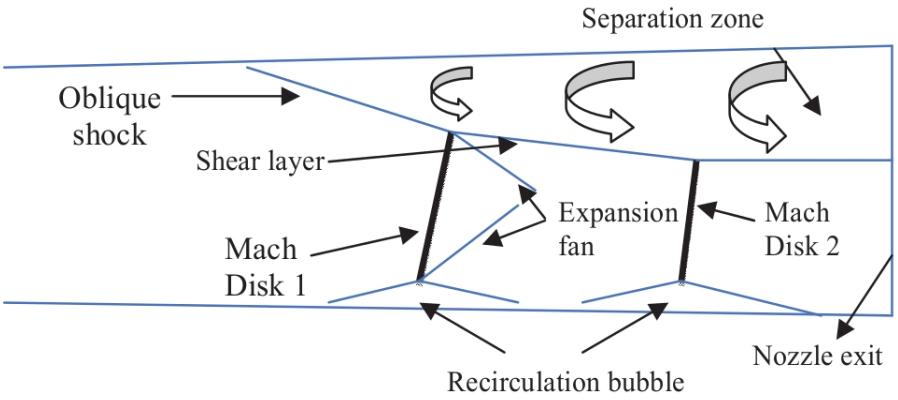

Figure 4.7: Schematic of shock waves structure inside nozzle at inlet pressure 3atm.

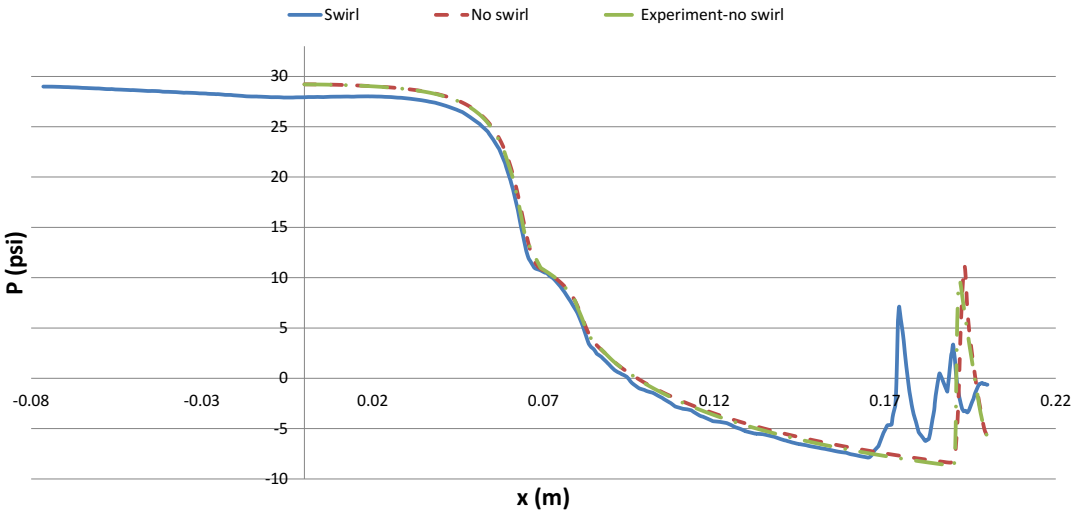

Figure 4.8: Static pressure at the centre of nozzle for inlet pressure 3atm.

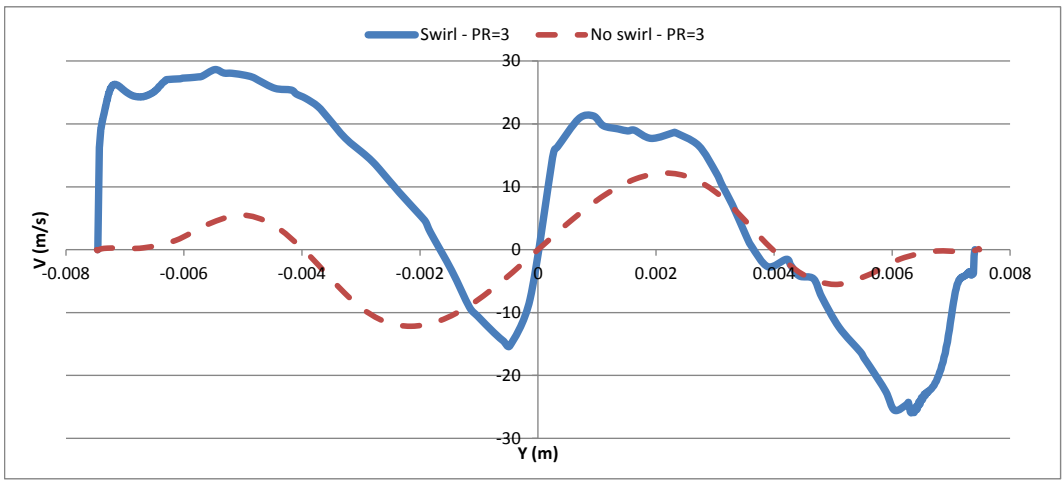

Figure 4.9: Tangential velocity at the exit of nozzle for inlet pressure 3atm.

the separation zone moves downstream of the nozzle and is significantly smaller (Figure 4.11). At firs time step t=0.8e-2 (Figure 4.11a) There are two Mach disks, but at the second time step, t=2.8e-2 (Figure 4.11b) the second Mach disk moves out of nozzle. Calculations for extra 1000 time steps does not show any changes to shock waves structure apart from shear layer movement and the flow pattern remains asymmetric.

Static pressure at the centre of the nozzle is illustrated in Figure 4.12. It can be seen that, adding swirl effect will create shock waves at the exit of the nozzle which improves sandblasting nozzle performance by providing better mixing features. The results for without swirl effect are matched with simulations from Abbasalizadeh (2011). For swirl condition, air pressure goes close to atmospheric pressure where the pressure ratio is 3.52, but for nozzle without helical insert the pressure goes to 6.75 as the air pressure drops to 8.7psi.

4.1.1.4 Mass flow rate

The mass flow rate for different pressure ratios has been presented in Table 5.2. The difference between mass flow rates of swirl and none swirl flow are very small. The inlet for the non-swirl condition is 31.75mm and for swirl condition with helical insert is 25.43mm, therefore there is cross sectional difference on swirl nozzle that reduces the total mass flow rate.

As the pressure ratio increases (Increasing inlet pressure) the mass flow rate also increases, and as shown in Figure 4.13, the slope of diagram for non-swirl situation is different to swirl condition. In all pressure ratios, there is sonic point at throat ($Ma = 1$ at throat), therefore the nozzle is choked. As suggested by White (2003), for a given stagnation condition, the maximum possible mass flow passes through a nozzle when its throat is at the critical or

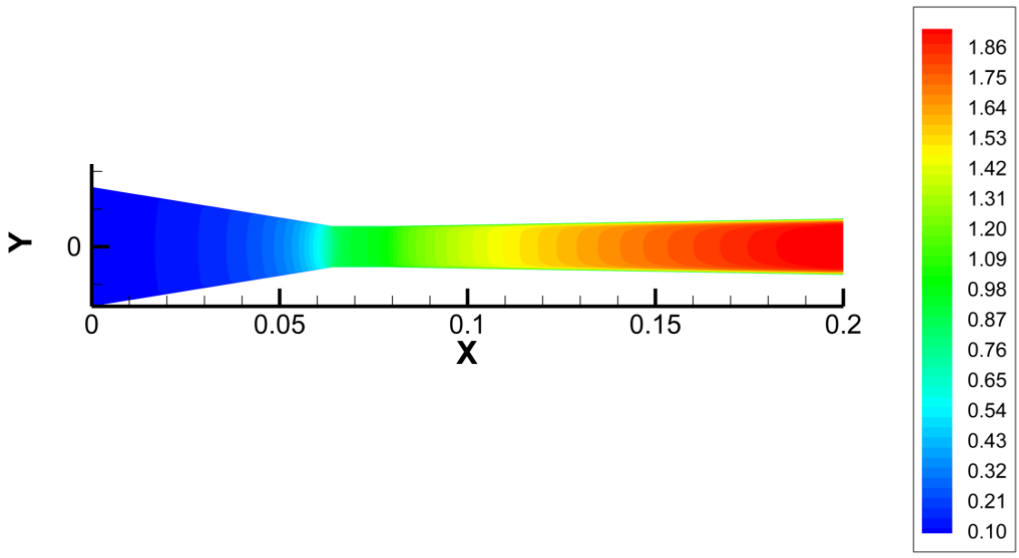

Figure 4.10: Mach number contours of inside nozzle simulations without helical insert at inlet pressure 4atm.

Table 4.2: Mass flow rate and PR for inside nozzle simulations.

Inlet pressure	2atm		3atm		4atm	
With swirl	0.0420 kg/s	PR 2	0.0632 kg/s	PR 3	0.0847 kg/s	PR 3.52
Without swirl	0.0428 kg/s	PR 2	0.0641 kg/s	PR 4.8	0.0855 kg/s	PR 6.75

sonic condition. However, choked flow happens only when the upstream pressure is fixed and downstream pressure is changing and in these simulations, the upstream pressure is increasing, thus the mass flow rate will increase as well. Further simulations on the effect of upstream pressure on mass flow rate will be done in the next chapter.

4.1.2 External domain

The results at the outlet of the nozzle will be presented in this section. The mesh structure is illustrated in Figure 4.14, and it was created using ICEM hexahedral mesh algorithm with the total number of 1,063,556 cells. The length of the domain is 10 times the exit diameter of the nozzle. The numerical equations are solved in transient mode with density based solver from FLUENT. The Reynolds Stress Model (RSM) turbulence modelling is adopted which was explained in section 3.5.3. The formulation is implicit and the discretisation method for the gradient is least square, for the flow is second order upwind and for the turbulence is first order upwind. The MUSCL scheme also has been tested for flow discretisation, though the

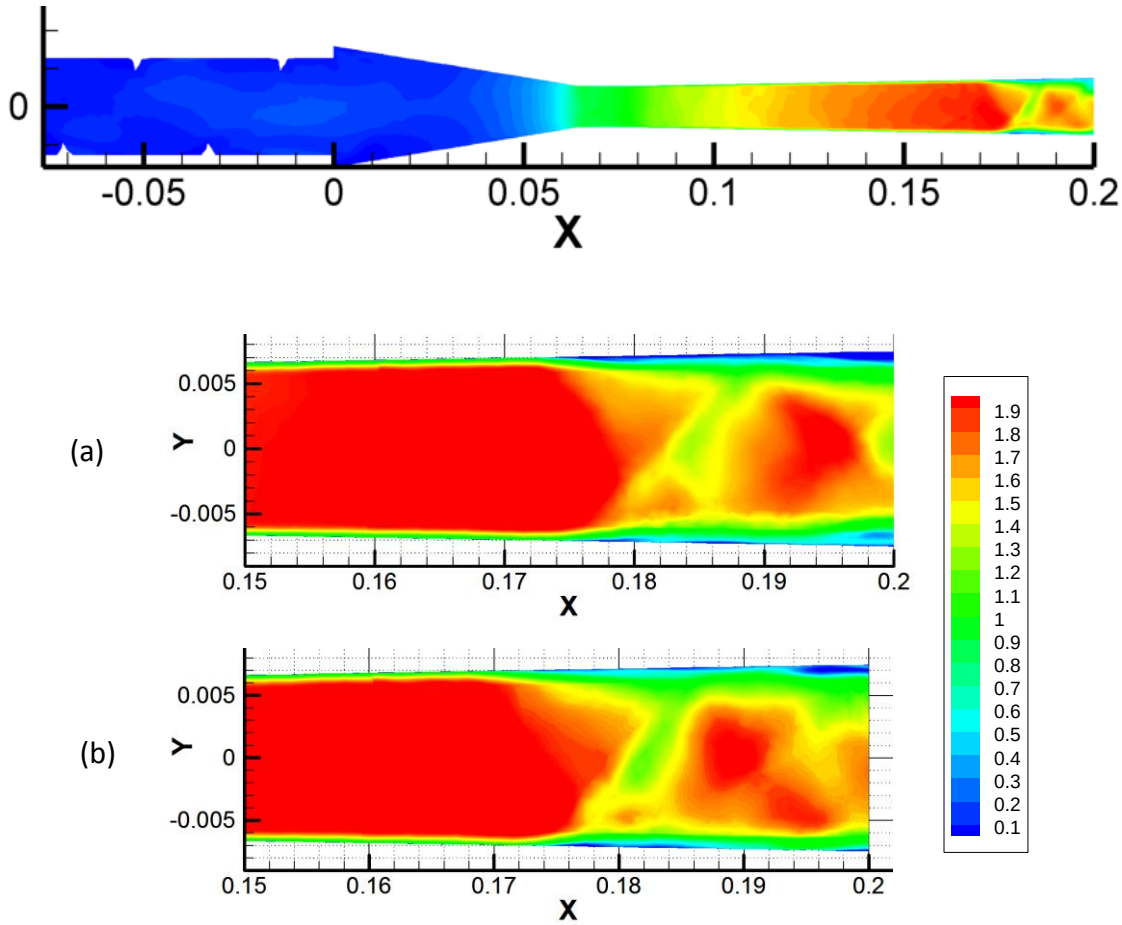

Figure 4.11: Mach number contours for inside nozzle simulations with helical insert for inlet pressure 4atm at (a) 0.8e-2 (b)2.8e-2

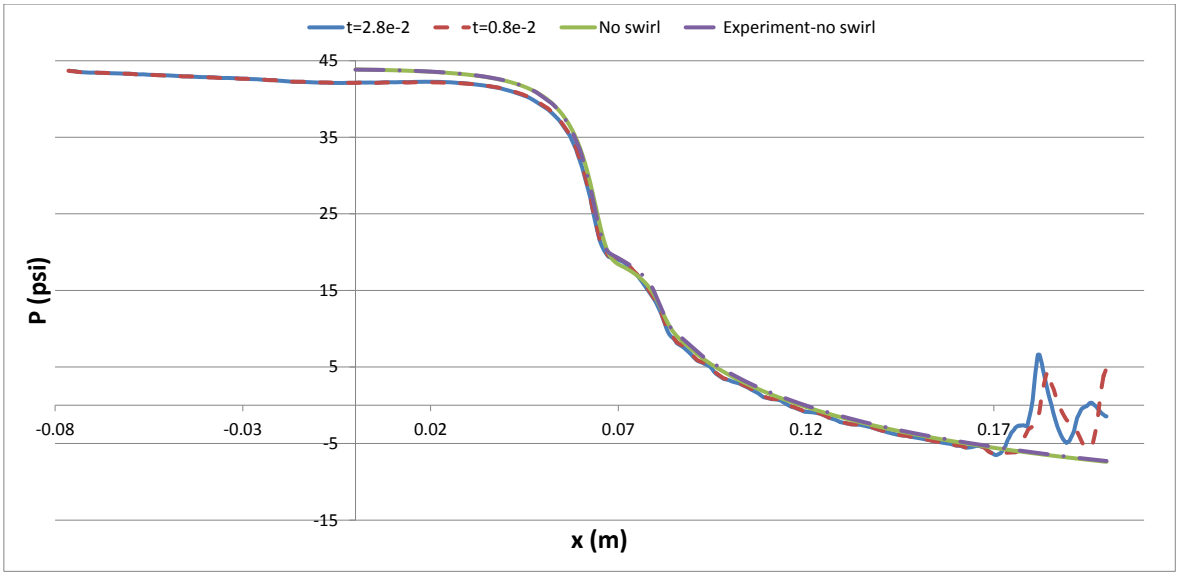

Figure 4.12: Static pressure diagram at the centre of nozzle for inlet pressure 4atm.

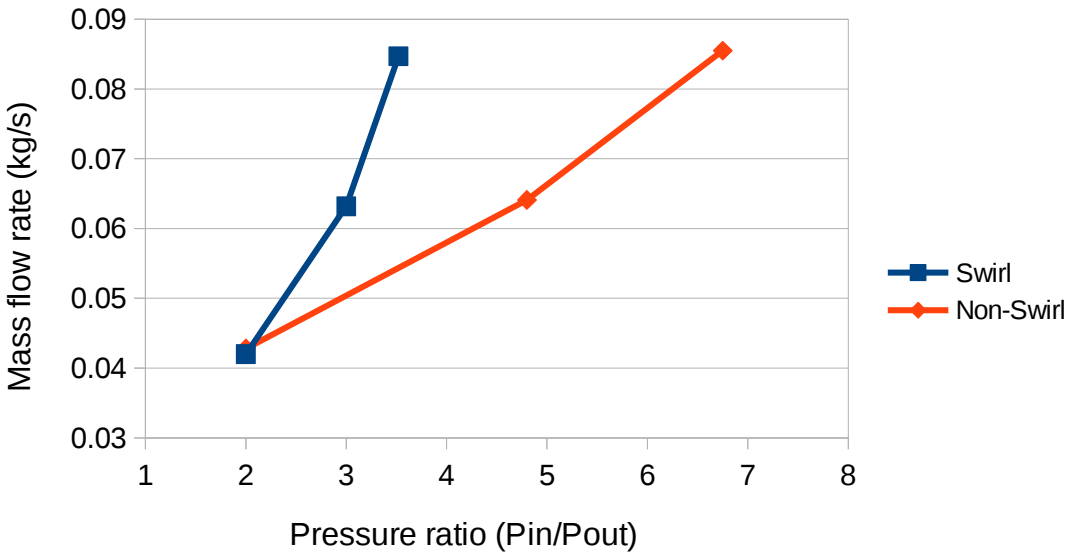

Figure 4.13: Mass flow rate diagram for inside nozzle simulations.

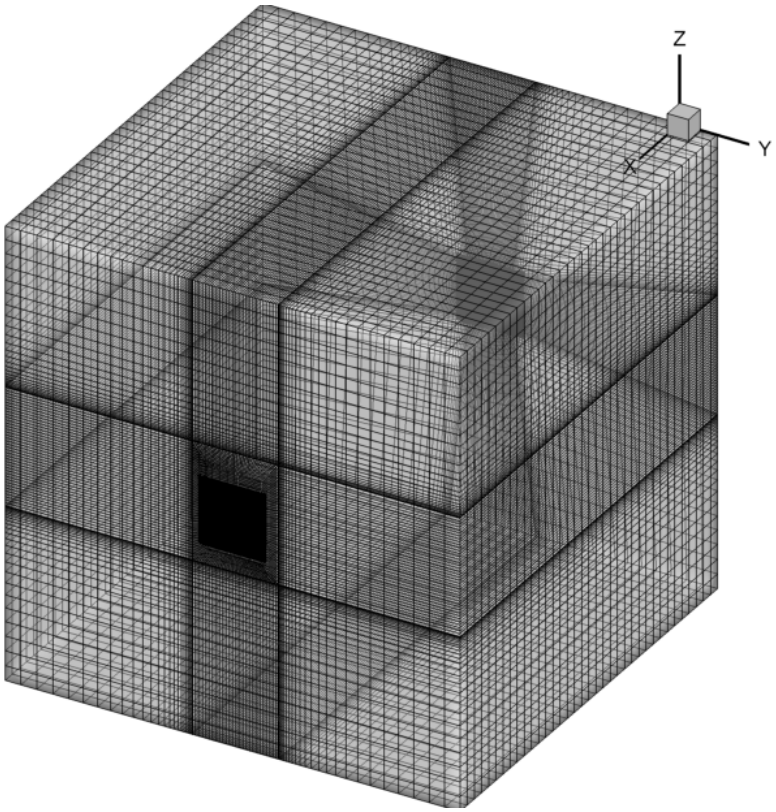

Figure 4.14: External domain mesh

results were identical to second order upwind method.

The boundary conditions are explained in Table 4.3. The inlet value has been extracted from the outlet of inside nozzle simulations and then inserted as a “velocity inlet”. All other boundary conditions are pressure outlet with 0 gauge pressure. The results here are for pressure ratio 3, which means the inlet is extracted from the outlet of inside nozzle simulation with pressure ratio 3. All boundary conditions are in Cartesian coordinate system.

The pressure contours for nozzle without helical insert is presented in Figure 4.15 and pressure contours with swirl attachment is shown in Figure 4.16. It can be seen from these Figures that the swirl effect has reduced the strength of shock cells at the exit of nozzle. The pressure variation along the centre line at the exit of the nozzle (inlet of domain) is shown in Figure 4.17. It is obvious from this figure that the swirl effect has increased the damping ratio of pressure, and the pressure variation is reduced significantly.

The weaker shock cells with swirl effect helps to reduce the pressure difference and therefore the noise and aeroacoustic waves. This is important for sandblast machines in order to operate at lower sound levels. Although the simulations were conducted for sandblasting nozzle, but this effect can be useful for noise reduction in many other applications such as jet

Table 4.3: Boundary condition for external domain simulations

Zone	Type	Value
Inlet	Velocity inlet	Extracted from inside nozzle simulations
Outlet (all other boundaries)	Pressure outlet	0 Gauge pressure

engines and internal combustion engines.

The X-velocity[2] contours are presented in Figures 4.18 and 4.19. The swirl effect has reduced the velocity in X direction, but has changed the flow pattern by increasing the velocity in Y and Z directions (Figures 4.20 and 4.21).

In the sand blasting process it is important to increase the effective area; without helical insert the covered area is smaller and there is high velocity air at the centre (Figure 4.22). The higher velocity at the centre creates lower pressure zone which causes for sands to concentrate more at it; This could damage the working surface while reducing the impact area that nozzle can cover. On the other hand the swirl effect increases the tangential velocity components which improves the effective area covered by nozzle (Figure 4.23), and also there is not high velocity area at the centre that helps for better distribution of sands.

In sandblasting one of main problems is that the operator has to move the nozzle in circular pattern to avoid damaging a working surface and make the cleaning process faster. By adding the swirl effect the area that is covered will increase and there won't be any high speed area at the centre. So the cleaning process can get faster without damaging the surface with machines that are working at lower sound levels.

4.2 Multiphase simulations

In any abrasive blasting system, a stream of abrasive particles is shot against a surface to remove coating, dirt or colour and to achieve desired finish on a chosen surface. Despite the high speed air is the key fluid on the performance of the sandblasting system, but still the interaction between sand particles and air is an important parameter in efficiency of sandblasting system.

As explained before in section 1.3.2 there are two types of sand blasting: dry blast and wet blast[3]. In wet blasting there is a third liquid element - usually water - to eliminate dust and achieve smoother and consistent finish by washing the particles after impact. The research by

[2]Main flow direction.
[3]Also called Vapourmatting.

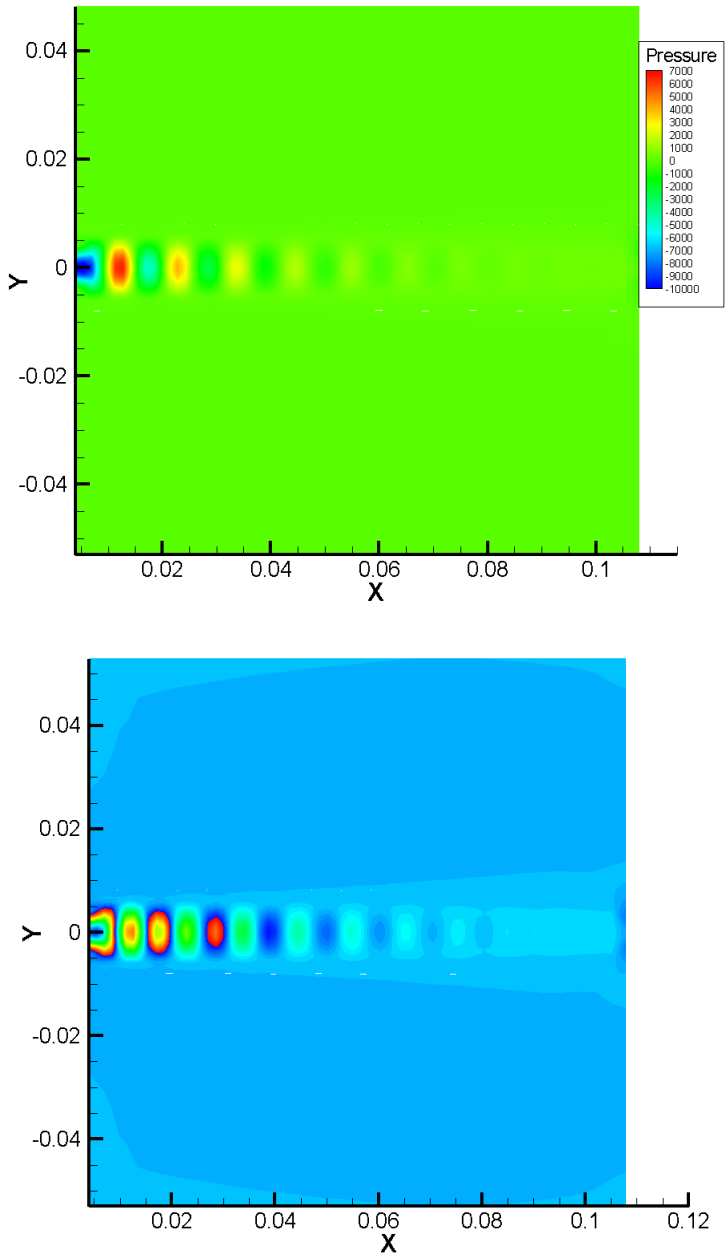

Figure 4.15: Pressure contours at exit domain without swirl attachment (inlet pressure 3atm). The lower image shows the position of shock cells more clearly.

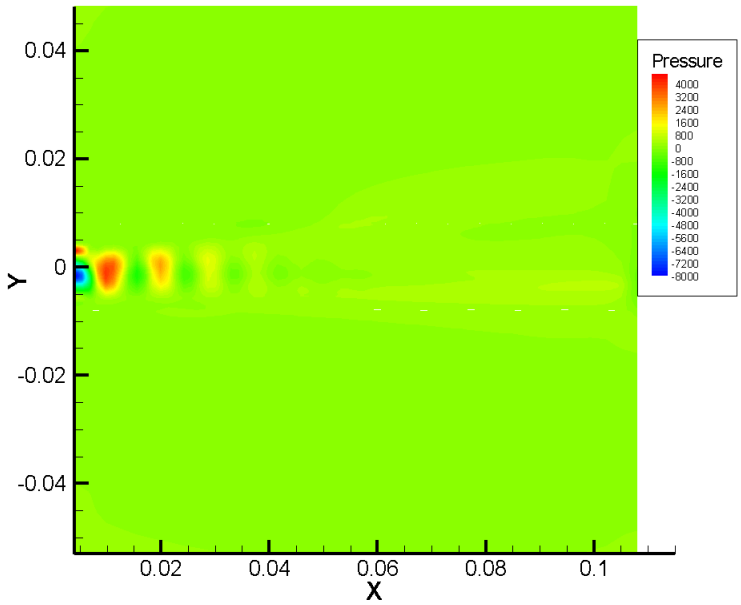

Figure 4.16: Pressure contours at exit of nozzle with swirl attachment (inlet pressure 3atm)

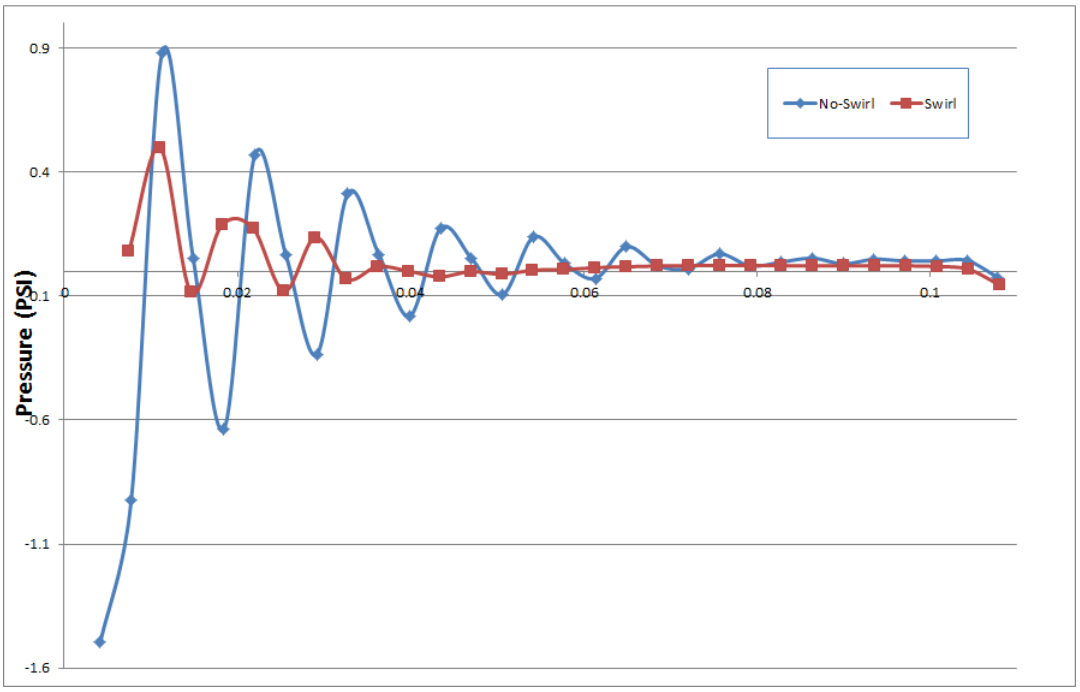

Figure 4.17: Pressure plot along the center at the exit of nozzle (inlet pressure 3atm)

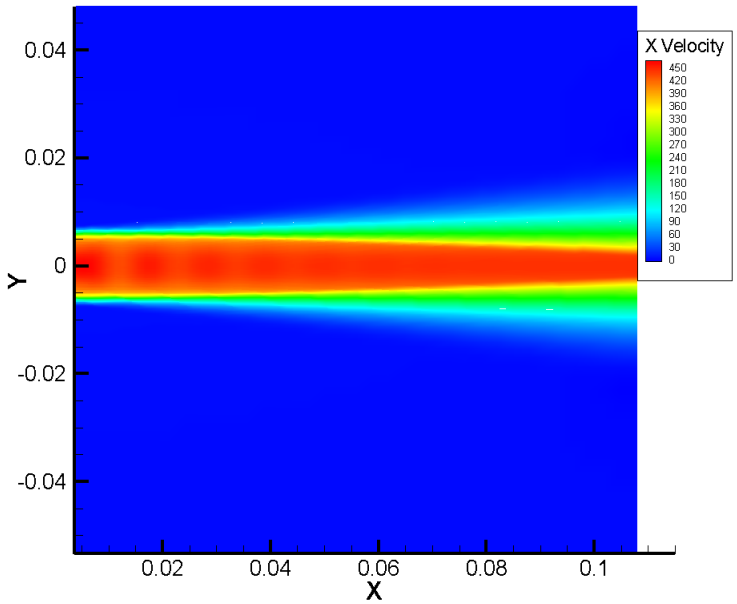

Figure 4.18: X-velocity contours at the exit of nozzle without swirl attachment (inlet pressure 3atm)

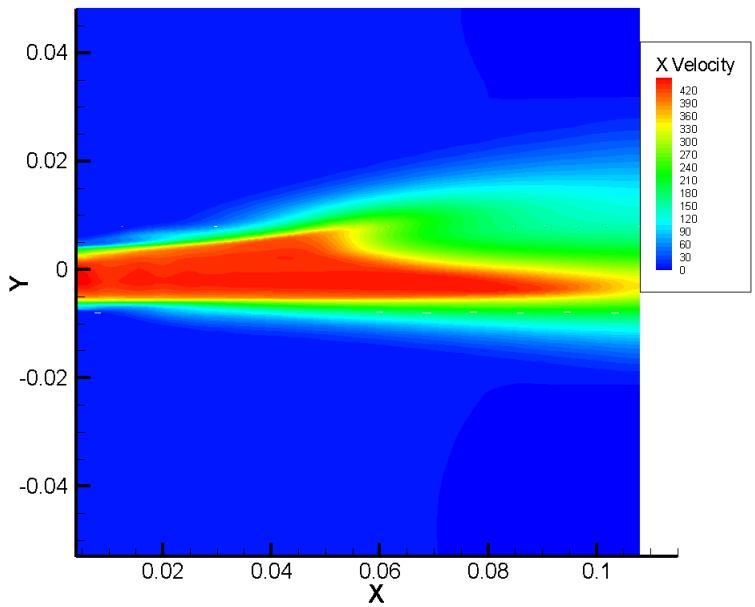

Figure 4.19: X-velocity contours at the exit of nozzle with swirl attachment (inlet pressure 3atm)

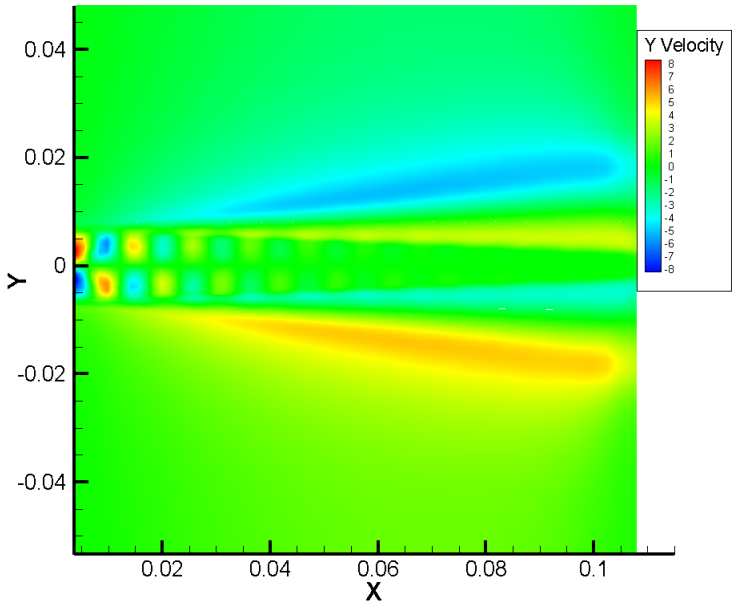

Figure 4.20: Y velocity contours at the exit of nozzle with no swirl attachment (inlet pressure 3atm)

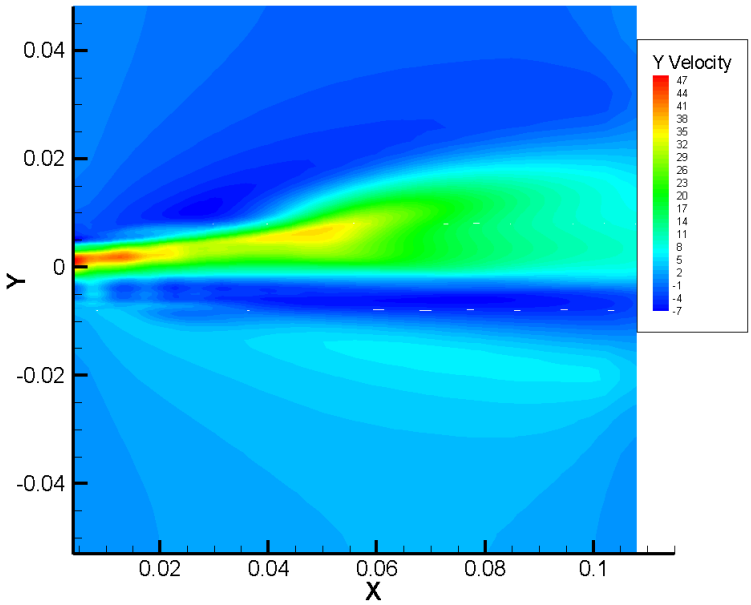

Figure 4.21: Y-velocity contours at the exit of nozzle with swirl attachment (inlet pressure 3atm)

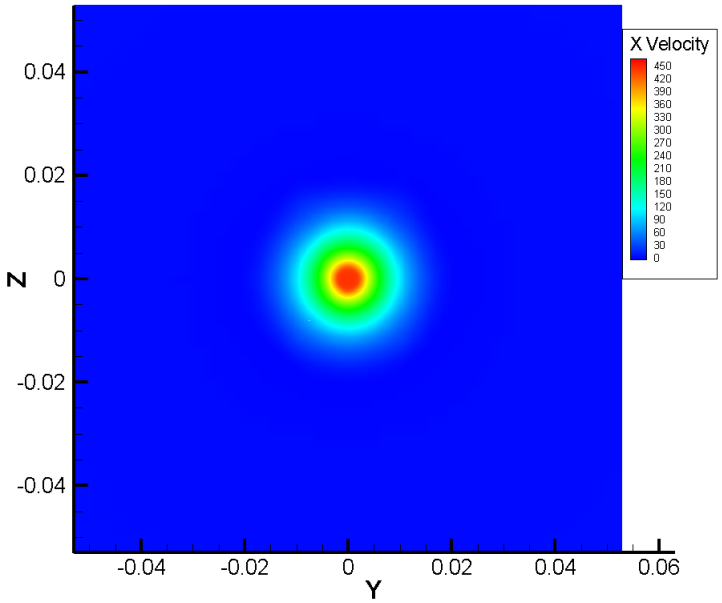

Figure 4.22: X-velocity contours on YZ (at X=0.15m from exit of the nozzle) plane at the exit of nozzle without swirl attachment (inlet pressure 3atm).

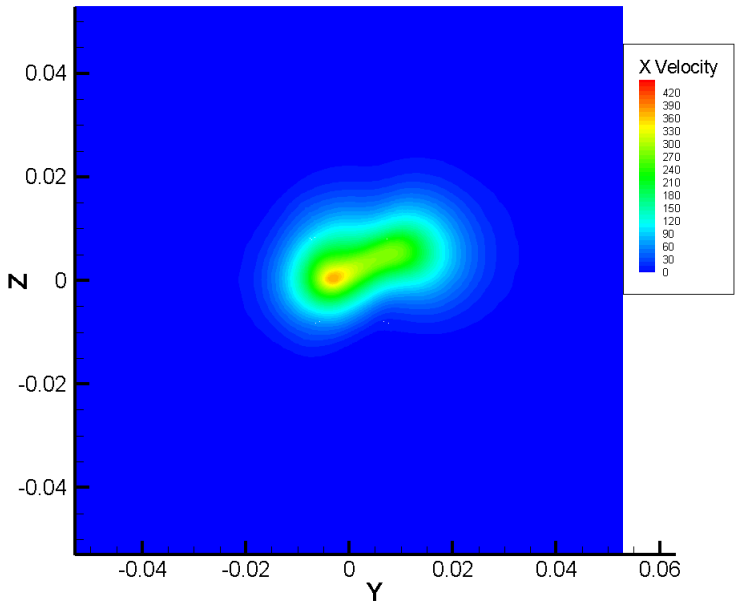

Figure 4.23: X-velocity contours on YZ plane (at X=0.15m from exit of the nozzle) at the exit of nozzle with swirl attachment (inlet pressure 3atm).

Abbasalizadeh (2011) has shown that the water (third phase) has not had a massive impact on flow behaviour and sand distribution inside the nozzle. The Abbasalizadeh (2011) study has proved that the water element is mainly for controlling the flow temperature inside the nozzle and also reducing dust and washing particles from a surface.

In this study the attention is not on the flow temperature; Hence, it focuses on the effect of swirling flow at parameters such as shock waves and particle distribution inside the nozzle. Therefore, to simply the model and reduce computational time for number crunching, the effort has been put on investigation of two phase flow (air and sand particles) for multiphase simulations.

There are different abrasive materials for abrasive blasting machines. Most of these materials are explained in Appendix B. In the last couple of years sand blasting companies have put a lot of effort on providing environmentally friendly media to clean surfaces. Some researches such as Porter *et al.* (2002) have studied the effect of different abrasive media on animal[4] health to find safer substitutes for blasting sand. These days there are two main media used by industry: crushed glass and olivine. Simulations for both of these materials showed similar results as they have almost similar density. Results presented in this section are based on olivine (Olivine and other abrasive media specifications are explained in Appendix B).

Abrasive particles that used in the sandblasting industry have standard size (FEPA, 2010). The major size used for most of the applications is particles with 0.01mm-0.15mm diameter. Although the particles in reality are not in sphere shape, but because of the size of particles that has been studied and also the fact that the attention is not on studying the collision of particles on a surface, the geometry of the particle will not have a huge impact on simulation results. Thus, the simulations are based on spherical particles with 10 microns (0.1mm) diameter.

This section is going to investigate effect of second phase (crushed glass/olivine) on flow structure and performance of the sandblasting system at different inlet pressures.

4.2.1 Eulerian model

The Eulerian model is the most complex multiphase model in FLUENT. The minimum volume fraction that can be used in FLUENT is 10% (Ansys, 2010). Particles in this research are considered as granular particles, which the particle size has been set to 0.1mm with particle density of 3200 kg/m^3. In this section the flow simulations inside of the nozzle without helical insert will be presented.

The Eulerian model does not provide density based solver, and it is only based on pressure

[4]Male Sprague-Dawley, rats weighing 200–300 g.

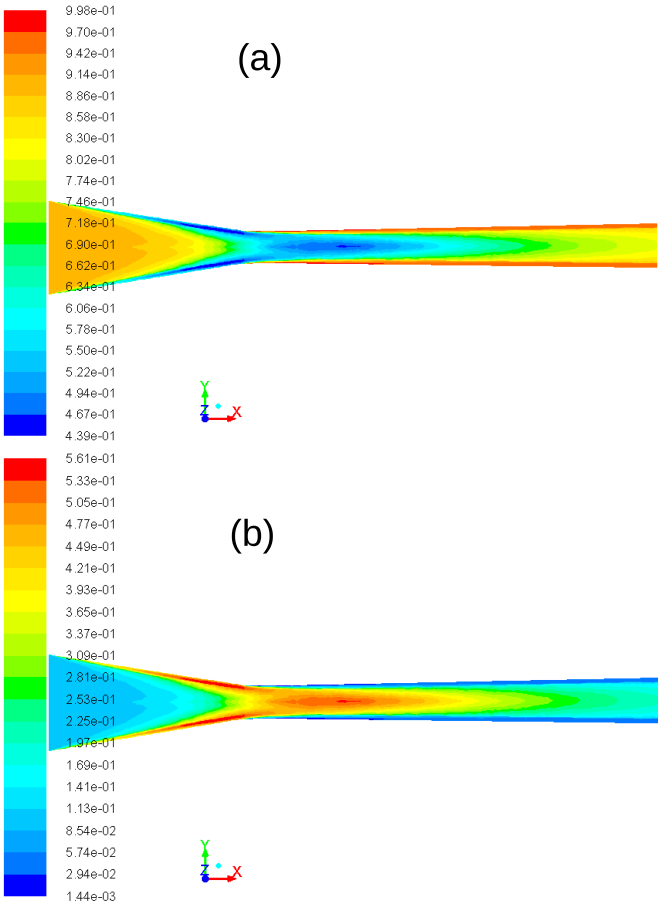

Figure 4.24: Volume fraction of a)phase air b)olivine phase in E-E method for inside nozzle simulation without helical insert.

based solver. The model is set to the implicit steady state solver with phase coupled SIMPLE scheme and second order discretisation. The boundary conditions are same as what explained in Table 4.1, with inlet gauge pressure 2 atm (PR=3). The turbulence modelling is set to standard $k-\varepsilon$ model. Phase one is set to air and phase two is set to olivine. Although olivine is a solid particle, but in Eulerian model is not possible to define solid material, therefore olivine is set as fluid particles.

The volume fraction for both phases (air and olivine) is illustrated in Figure 4.24. The air phase distribution is illustrated in Figure 4.24a, which shows it has higher volume fraction in the areas close to the wall; However Figure 4.24b shows olivine particles have a greater volume fraction toward the centre in the divergent section of the nozzle. This was predictable based on pressure distribution of single phase simulations inside the nozzle.

Velocity contours for both phases is shown in Figure 4.25. For air the velocity is increasing up to critical point (throat) but because it has not reached to $Ma = 1$ the velocity of air will

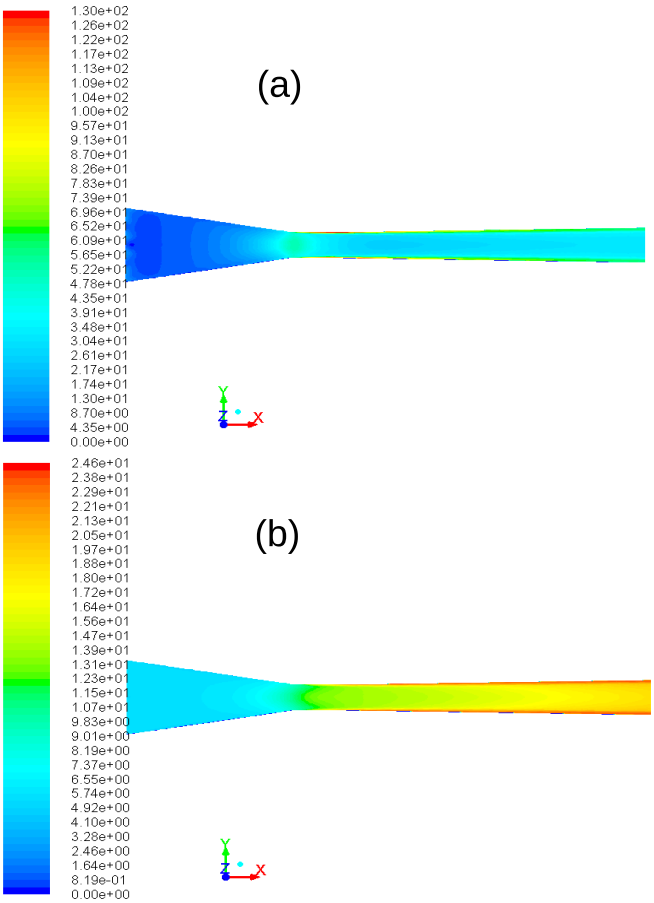

Figure 4.25: Velocity contour of a) phase air b)phase olivine in E-E method for inside nozzle simulation without helical insert.

reduce after the throat. Also, Figure 4.25a shows that air close to the wall has higher velocity compare to centre of the nozzle. On the other hand the velocity of olivine particles will increase even after the throat up to 24.6 m/s (Figure 4.25b), where particles at areas close to the wall have higher velocities.

Figure 4.26 plots the velocity of air at centre of the nozzle. The air will accelerate from start of the nozzle to reach at its maximum velocity of $52m/s$ at the throat. Then the speed of air will reduce in the diverging section as the velocity is subsonic $Ma < 1$ until reaches to atmospheric pressure at the outlet. Therefore, there will not be any shock waves inside nozzle. The velocity of particles at centre of the nozzle is plotted in Figure 4.27. In contrast to the air phase, the velocity of olivine particles will continue to increase even in diverging section. This is because olivine particles have absorbed some of air flow kinetic energy, and momentum is transferred from the air to particles.

Analyses of the above diagrams and contours shows some difficulties with Eulerian mod-

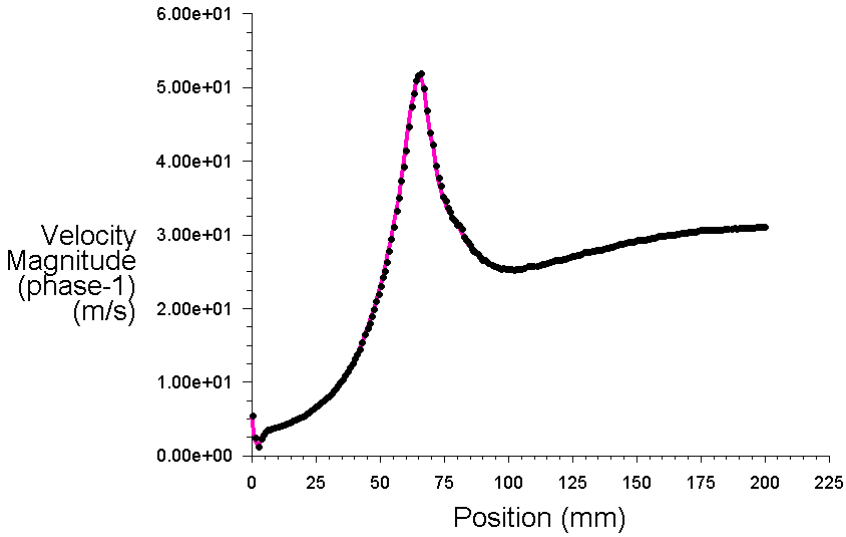

Figure 4.26: Velocity digram along the centre of the nozzle without helical insert with E-E method for phase air.

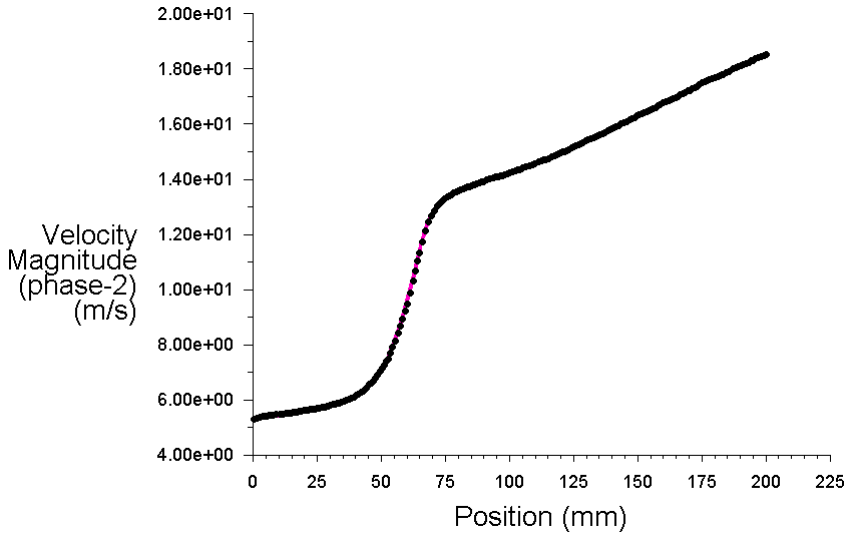

Figure 4.27: velocity diagram along the centre of the nozzle without helical insert for phase olivine.

elling. Although the volume fractions for non swirl flow inside the nozzle is predicted as expected based on pressure contours for single phase simulations, but the velocity data does not look accurate compare to operational and experimental data. The whole concept of using converging-diverging nozzle is to increase the speed of the flow at Mach numbers greater than one; However here the flow is not even getting close to $Ma = 1$. Closer look at other researches in multiphase modelling (explained in chapter 2) also demonstrate, solid dynamics calculations will cause numerical smearing in Eulerian calculations (Fedkiw, 2002). The study by Gerber and Kermani (2004) has showed the Eulerian approach is good for bubble phases in nucleating steam behaviour where the second phase is gas or liquid. Also Fedkiw *et al.* (1999) has used Eulerian method to calculate deformation of gas flows.

The other problem is with limitation on volume fraction. As was explained before the minimum volume fraction in Eulerian model is 10-12%, were in reality particles are smaller and they have lower volume fractions. Due to all these difficulties with Eulerian method for modelling solid particles, extra Eulerian simulations have not been continued for swirling multiphase flow. All other simulations will be done by Lagrangian approach at the next section.

4.2.2 Lagrangian model (DPM)

As explained in the previous section, Eulerian model is not yet capable to solve accurately the interaction between fluid (air) and solid (particles) in such a high speed flow and low volume fractions ($< 10\%$). On the other hand Lagrangian method[5], are accurate and well tested for solid dynamic calculations (Fedkiw, 2002).

Sandblasting machines operate at different pressure and mass flow rate. The mass flow rate for abrasive particles could vary from 0.005 to 0.05 kg/s. In this study based on pressure operation (2-4 atm) and the nozzle dimension, the mass flow rate for olivine injection is considered 0.0211 kg/s. This is the average mass flow rate used in sandblasting companies[6]. The particles (sphere particles with 10 microns diameter) are injected from inlet surface with ambient temperature and zero velocity. All the DPM simulations are based on single phase simulation where unsteady tracking is performed on particles with spherical drag law.

In this section the effect of olivine particles is investigated for inside nozzle simulations.

[5]Called Discrete Phase Model (DPM) as well.

[6]Our calculations are mainly based on data provided by Farrow System®.

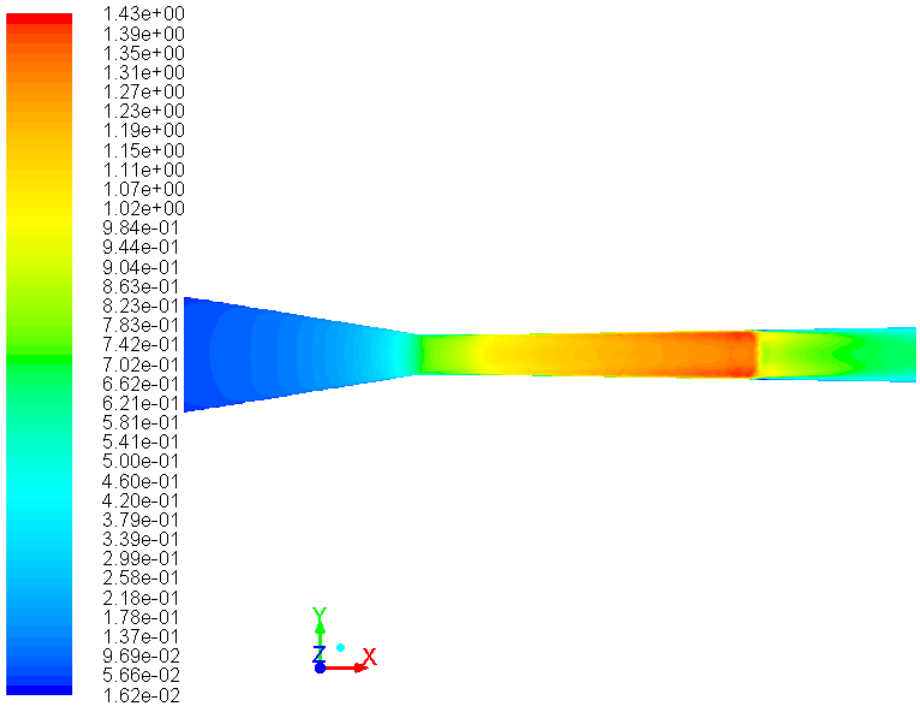

Figure 4.28: Mach number contours of DPM model for the nozzle without helical insert at inlet pressure 2 atm.

4.2.2.1 Inlet pressure 2atm

Mach number contours at inlet pressure 2atm for the nozzle without helical insert is shown in Figure 4.28. Compare to single phase simulation (Figure 4.2), there is just one strong shock wave without any multiple shock and expansion wave after the main Mach disk. There is lower velocity area at the centre due to high concentration of sand (olivine) particles. The maximum velocity has reduced from Mach 1.8 to Mach 1.4, which means a 22 percent reduction. On the other hand the maximum velocity of the DPM model with helical insert (Figure 4.29) has not changed compare to single phase simulation (Figure 4.3) from Mach 1.6 . The Mach number contours for swirl condition with particle injection shows that the structure of shock waves have not changed, and still there is series of shock waves and expansion fans after the main shock wave; However the separation zone has changed and there is a small FSS region at the top and an RSS region on the lower wall.

Particle distribution for the nozzle without helical insert is illustrated in Figure 4.30. Without swirl condition the particles are more toward centre; However, by adding swirl effect to the flow particles are better distributed and they are not concentrated at the centre of the nozzle (Figure 4.31). This will be very helpful to avoid damaging a surface.

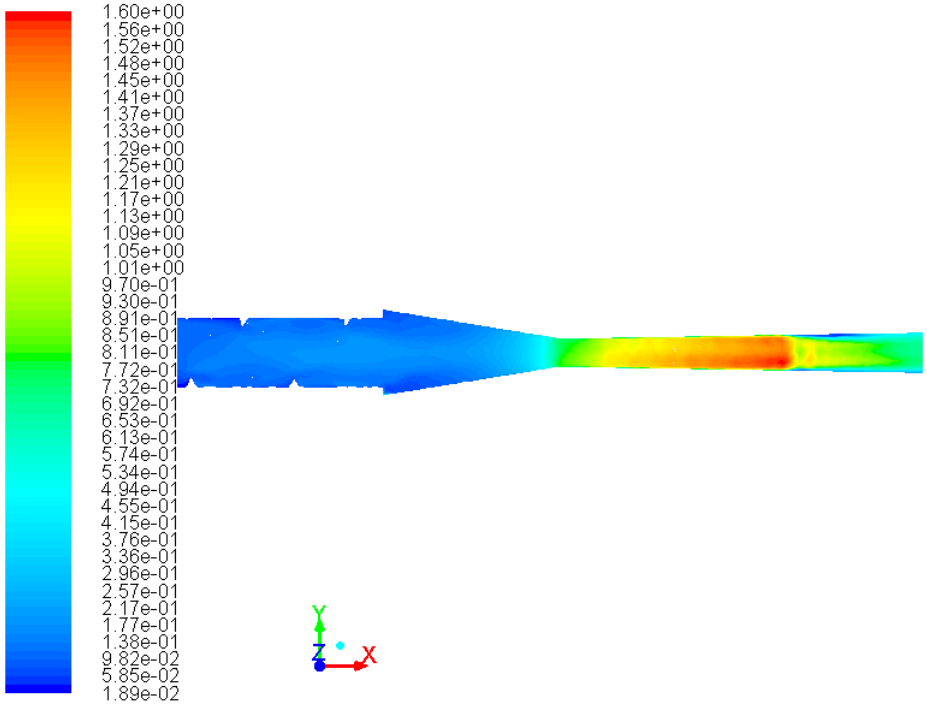

Figure 4.29: Mach number contours of DPM model for the nozzle with helical insert at inlet pressure 2 atm.

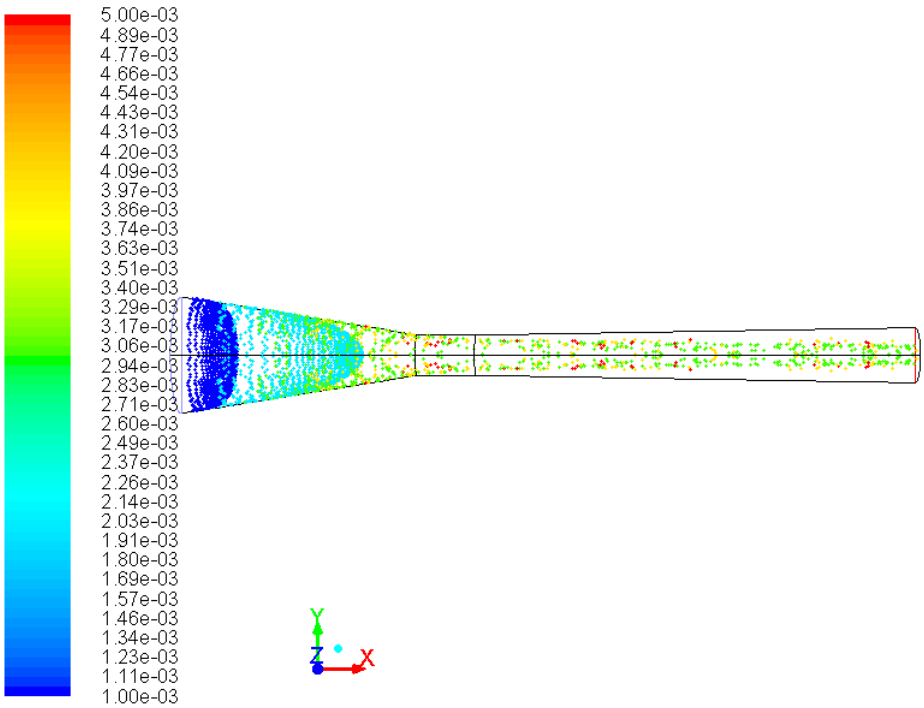

Figure 4.30: Particle trace coloured by particle residence time for the nozzle without helical insert at inlet pressure 2atm.

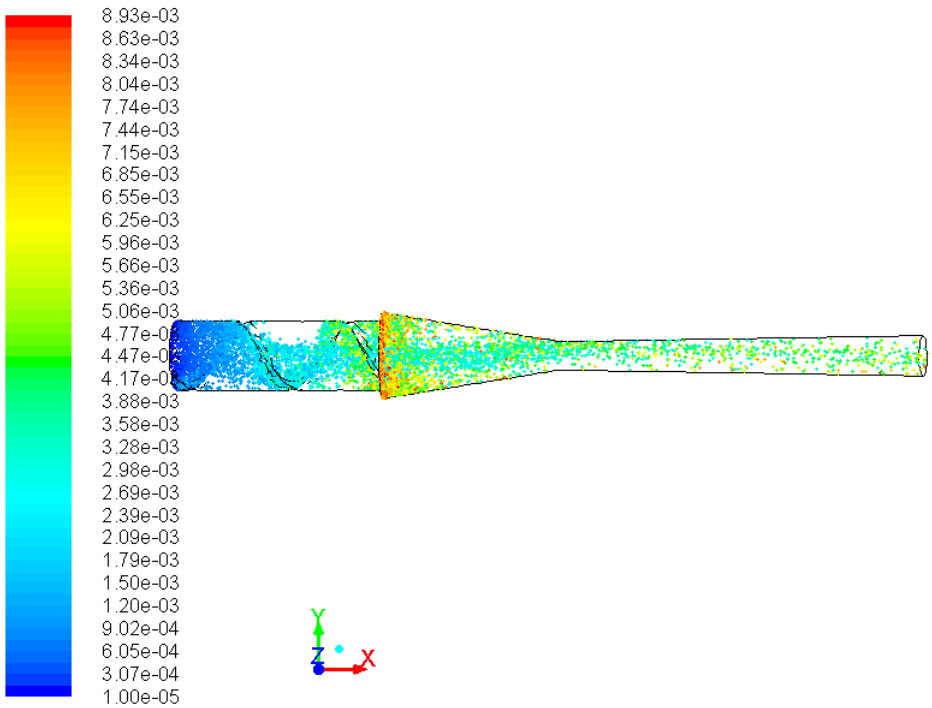

Figure 4.31: Particle trace coloured by particle residence time for the nozzle with helical insert at inlet pressure 2atm.

Pressure along the centre of the nozzle without helical insert is sketched in Figure 4.32. By injecting particles, the structure of shock waves has been changed. Instead of having multiple shock waves and expansion fans there is just one strong shock wave; After the pressure it will gradually increase until reaches to atmospheric pressure at the outlet. In Figure 4.33 the pressure along centre of the nozzle with helical insert is plotted. There is a very small change in pressure behaviour compare to single phase simulation, apart from some oscillations with a very small amplitude before shock waves. There is a small movement on shock location as well, where first shock wave has moved forward.

4.2.2.2 Inlet pressure 3atm

Mach number contours with the enabled DPM model for the nozzle without helical insert is represented in Figure 4.34. In compare to single phase simulations the maximum velocity has reduced by 13 percent from Mach 1.55 to Mach 1.77. However, in the nozzle with helical insert, the maximum velocity is almost unchanged at Mach 1.9 for both DPM model (Figure 4.35) and single phase simulation (Figure 4.6). This proves there is much higher momentum in the swirling flow inside the nozzle even with the particles.

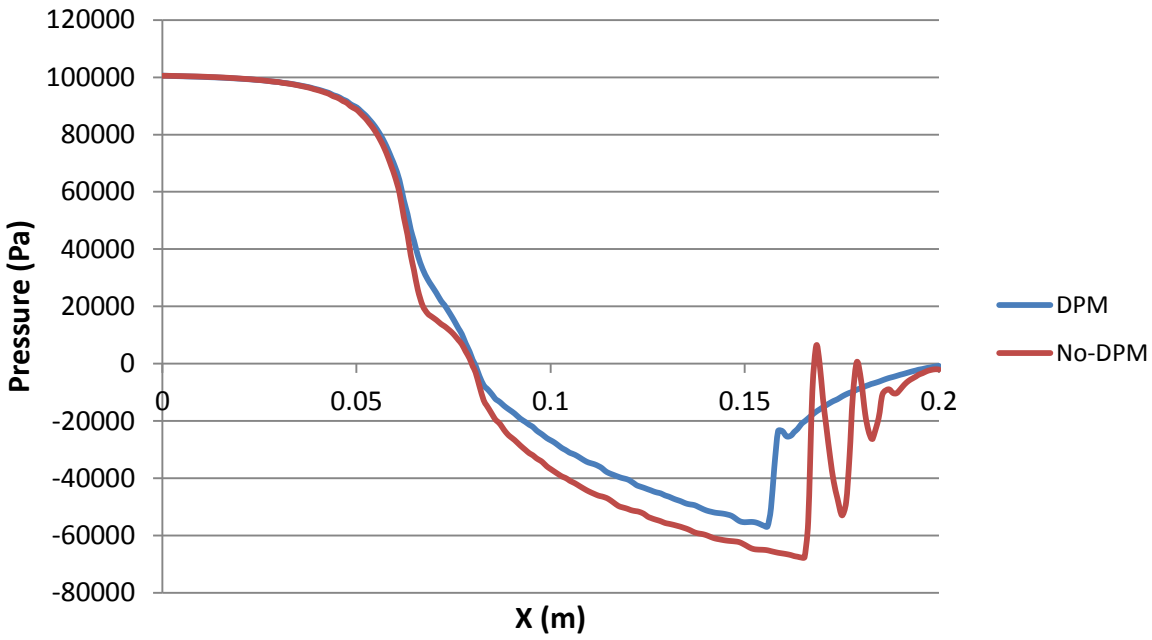

Figure 4.32: Pressure along centre of the nozzle without helical insert for DPM model at inlet pressure 2 atm.

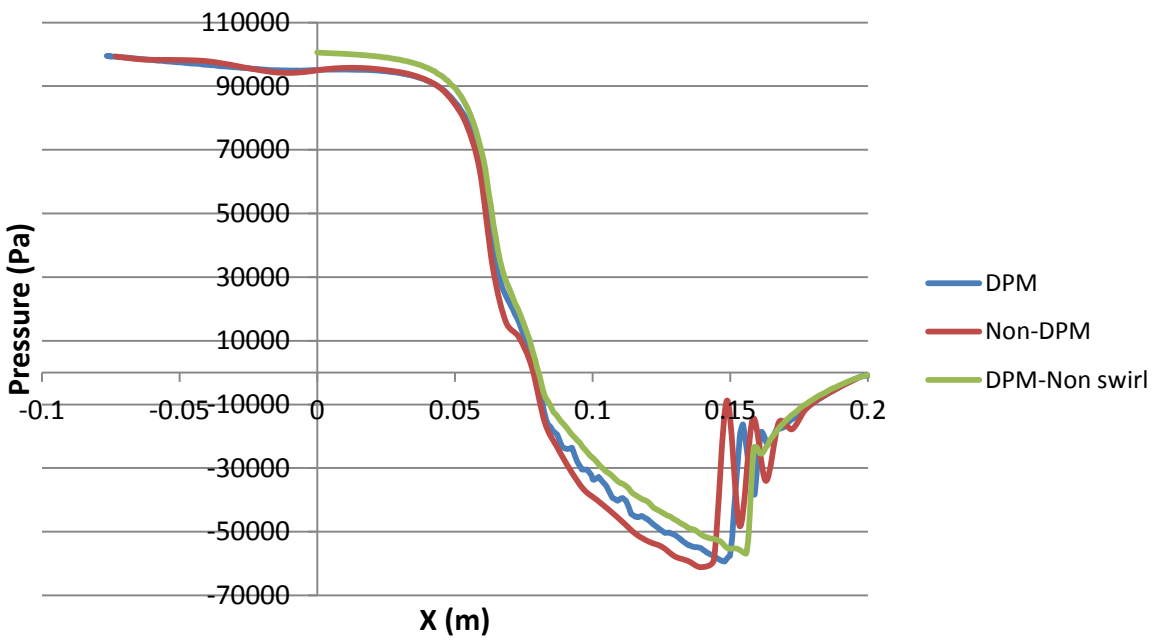

Figure 4.33: Pressure along centre of the nozzle with helical insert for DPM model at inlet pressure 2 atm.

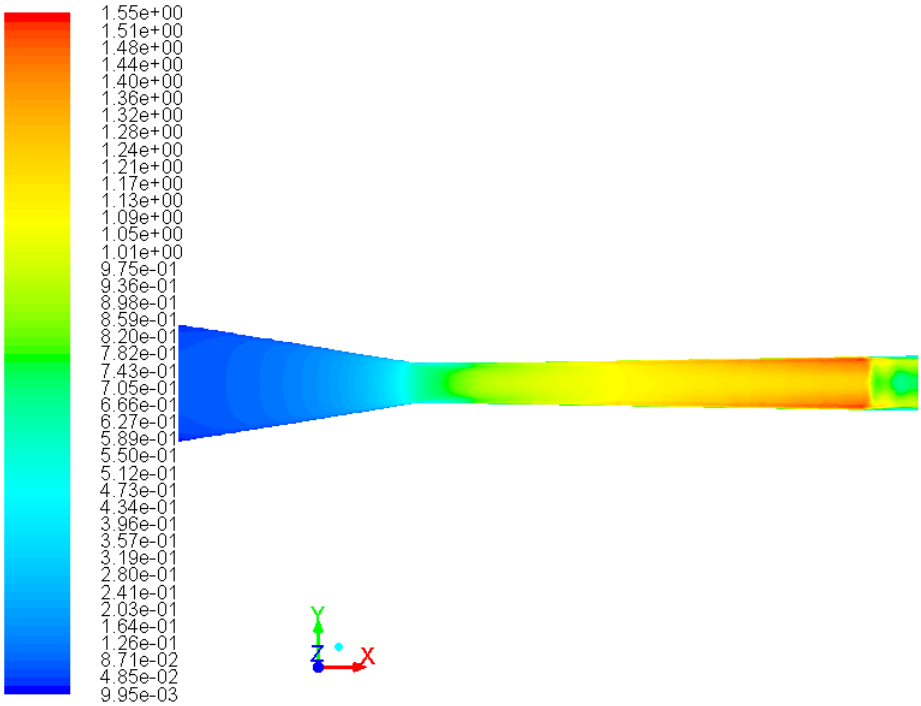

Figure 4.34: Mach number contours of DPM model for the nozzle without helical insert at inlet pressure 3 atm.

Figure 4.34 shows that there is some lower velocity zone at the centre of the nozzle due to high concentration of abrasive particles, but this is not visible on Figure 4.35 which verifies particles are not concentrated at the centre. Both non-swirl and swirl Mach contours with the Lagrangian approach do not show any unsteady pattern inside the domain.

From Figure 4.35 is clear that both FSS separation zone at the top and RSS recirculation zone at the lower wall exist similar to the single phase simulation (Figure 4.6) although these separation areas are much smaller. In the nozzle without helical insert the separation zone has been removed by particles injection.

Particle distribution for the nozzle without helical insert at inlet pressure 3atm is very similar to inlet pressure 2atm, where most of olivine particles are concentrated at the centre of the nozzle in diverging section (Figure 4.36). Particles in the nozzle with helical insert are distributed more evenly, although there is some concentration zone after the helical insert, showed by red particles, due to the diameter difference between the nozzle inlet and helical insert outlet (Figure 4.37).

Pressure along centre of the nozzle without helical insert is plotted in Figure 4.38. In DPM model the shock wave is much weaker and pressure is gradually increasing to get to the atmospheric pressure at the outlet. This is not favourable effect as shock waves at the exit of

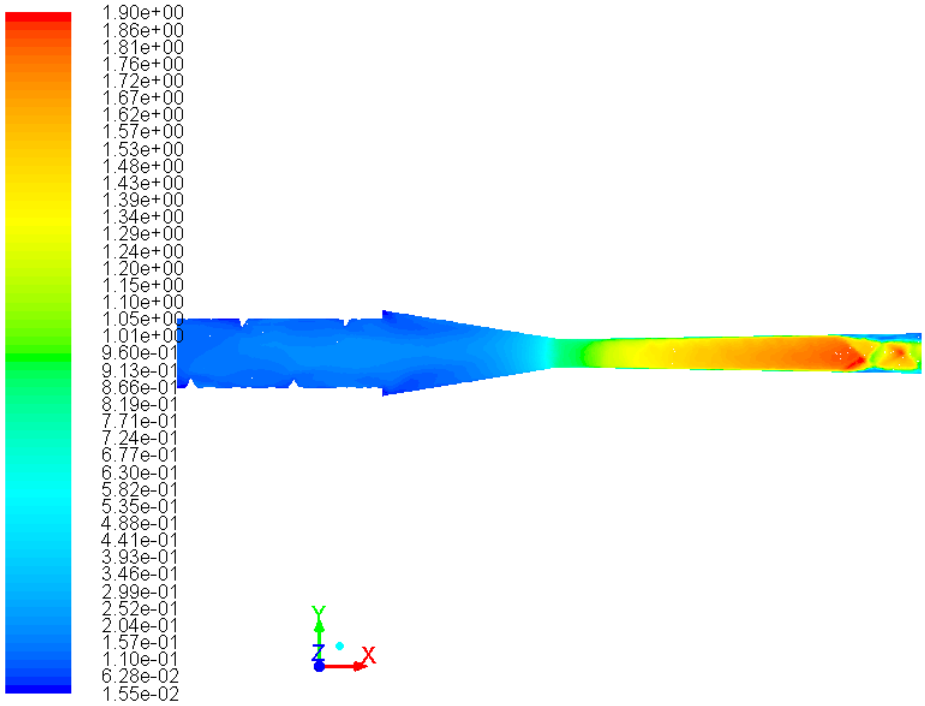

Figure 4.35: Mach number contours of DPM model for the nozzle with helical insert at inlet pressure 3 atm.

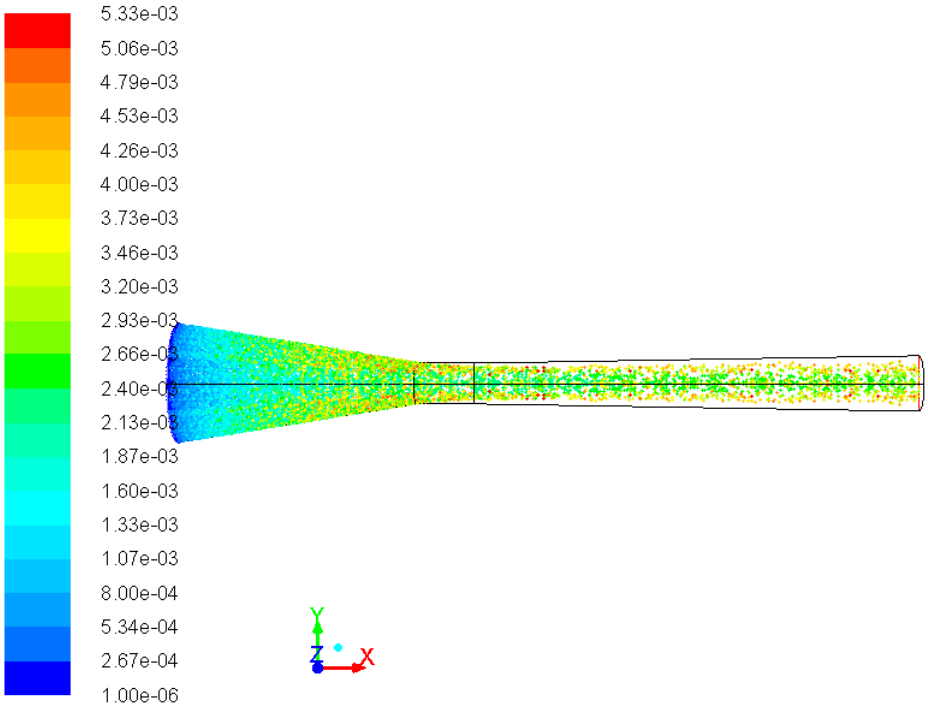

Figure 4.36: Particle trace coloured by particle residence time for the nozzle without helical insert at inlet pressure 3atm.

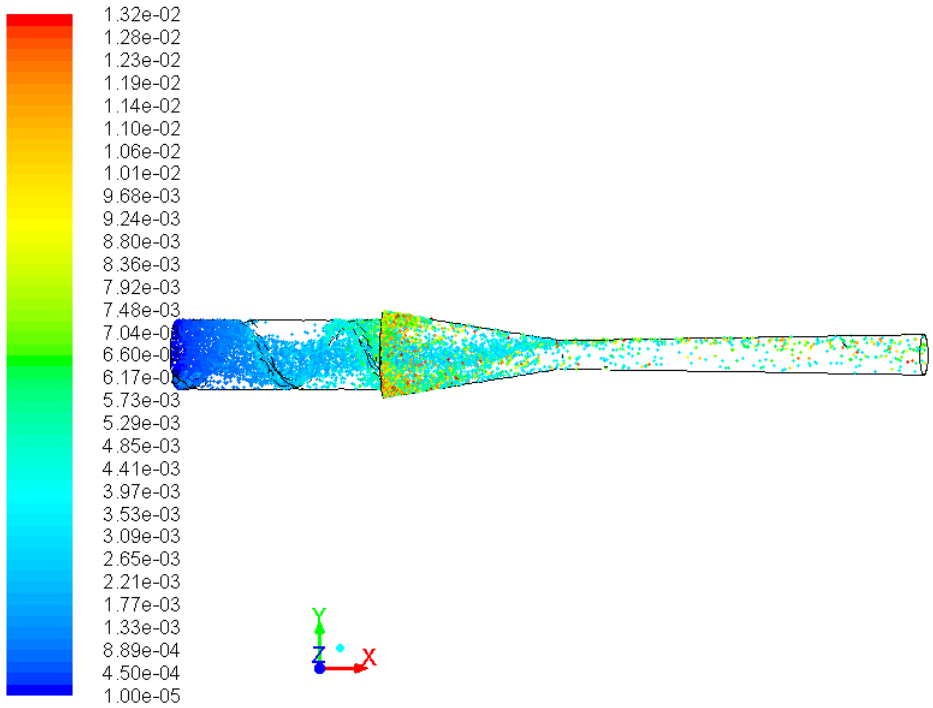

Figure 4.37: Particle trace coloured by particle residence time for the nozzle with helical insert at inlet pressure 3atm.

the nozzle will provide mixing effect. On the other hand, for the nozzle with helical insert, the shock waves are almost unchanged (Figure 4.39). Similar to inlet pressure 2atm, the first shock wave has moved forward and there are small oscillations behind the first shock.

4.2.2.3 Inlet pressure 4atm

Mach number contours for inlet pressure 4atm are shown in Figure 4.40 and 4.41. In single phase simulation without helical insert all the shock waves were outside of the nozzle (Figure 4.10), with the DPM model as well, all the shocks are outside of the nozzle, but there is a 8% reduction on maximum velocity. Similar to lower pressure DPM models for the nozzle without the helical insert, the air closer to the nozzle wall has a higher velocity than the air toward centre of the nozzle; However, at inlet pressure 4atm (Figure 4.40) the velocity change from centre toward the nozzle wall is smaller.

Mach contours of the DPM model for the nozzle with helical insert (Figure 4.41) show similar behaviour to single phase simulations (Figure 4.11). Same as lower pressures there is not any lost on maximum velocity by injecting particles, which proves a great advantage of using swirl flow for abrasive blasting. Although the solver is transient and in single phase

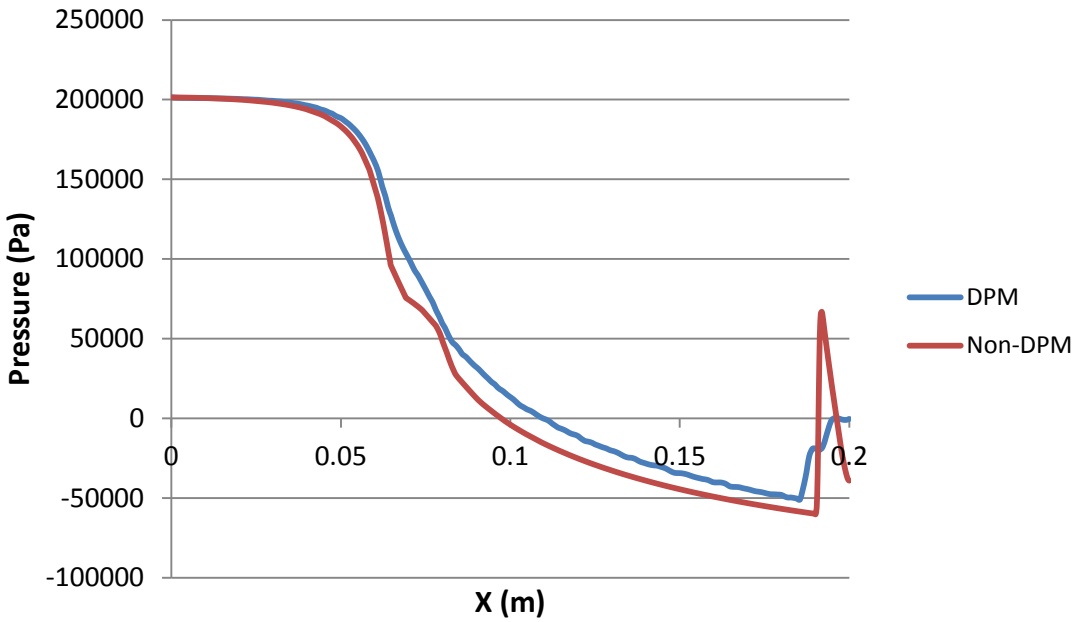

Figure 4.38: Pressure along centre of the nozzle without helical insert for DPM model at inlet pressure 3atm.

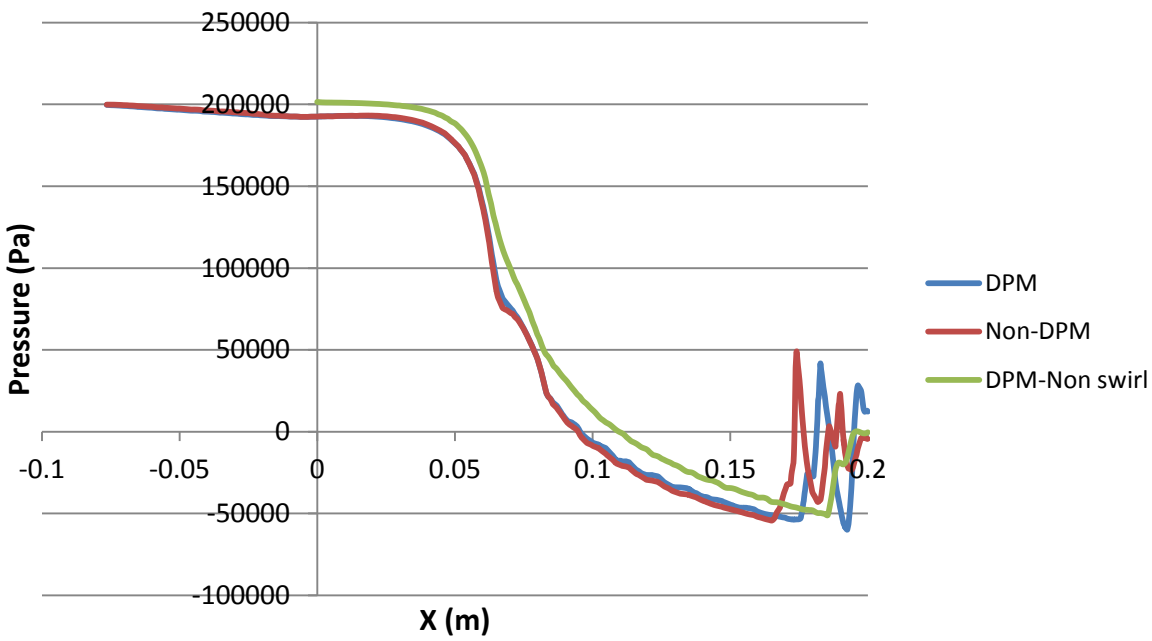

Figure 4.39: Pressure along centre of the nozzle with helical insert for DPM model at inlet pressure 3atm.

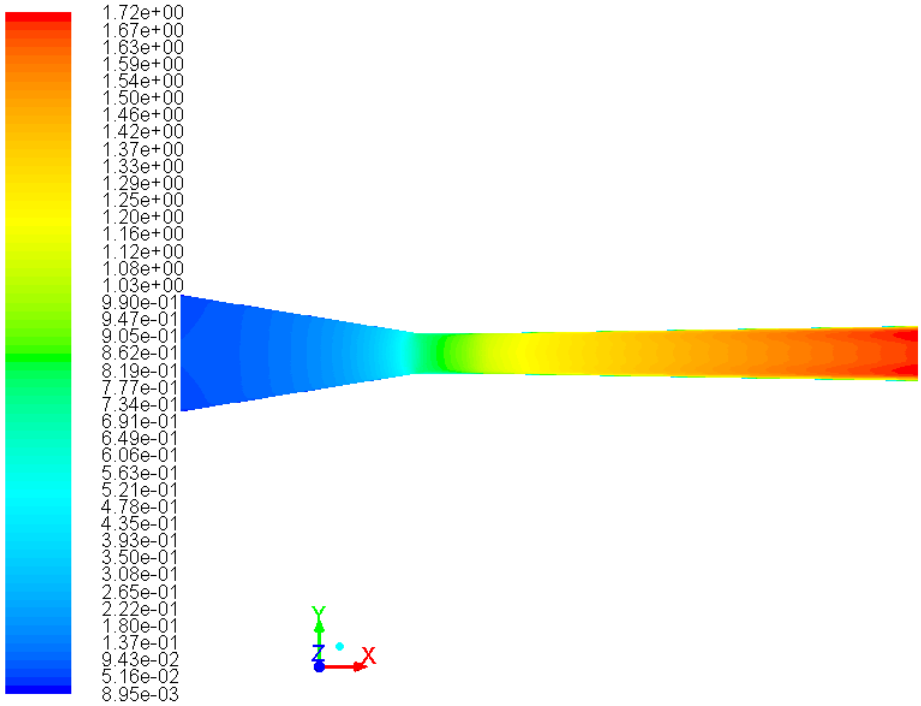

Figure 4.40: Mach number contours of DPM model for the nozzle without helical insert at inlet pressure 4atm.

simulations showed unsteadiness in the flow, but the DPM model for the swirl flow does not demonstrate unsteadiness inside the nozzle. This could be because of reduction on separation zone.

Particle distribution at inlet pressure 4atm it is different to lower pressures. For the nozzle without helical insert (Figure 4.42), unlike lower pressures explained before, particles are distributed more evenly although they are more toward centre of the nozzle. For the nozzle with helical insert (Figure 4.43) particles are more toward the upper wall up to the first shock wave, then they are distributed along the outlet as a mixing effect of shock wave.

Pressure along the centre line of the nozzle without helical insert (Figure 4.44) is almost identical to single phase simulation. This show the particles have less effect on pressure distribution inside nozzle but they have a major effect on shock wave structure as explained for lower inlet pressures. For the nozzle with helical insert (Figure 4.45) there is not any major change even in shock structure. Similar to lower pressures there are small oscillations before the first shock wave in diverging section. Therefore, with the swirl effect, flow parameters will not see major change between single phase simulations and Lagrangian simulations with particle injection.

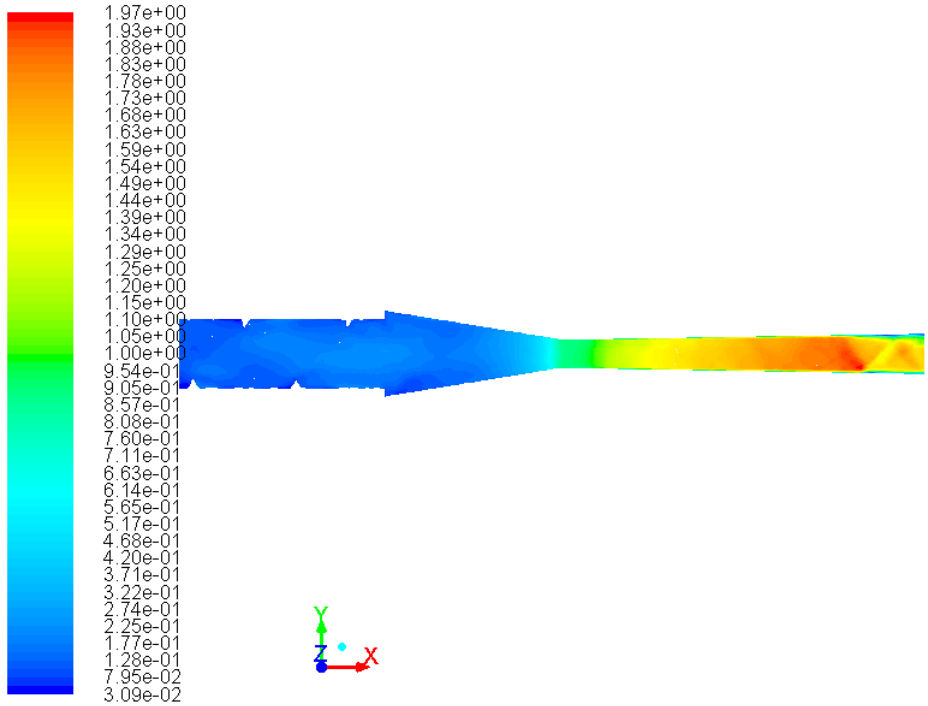

Figure 4.41: Mach number contours of DPM model for the nozzle with helical insert at inlet pressure 4atm.

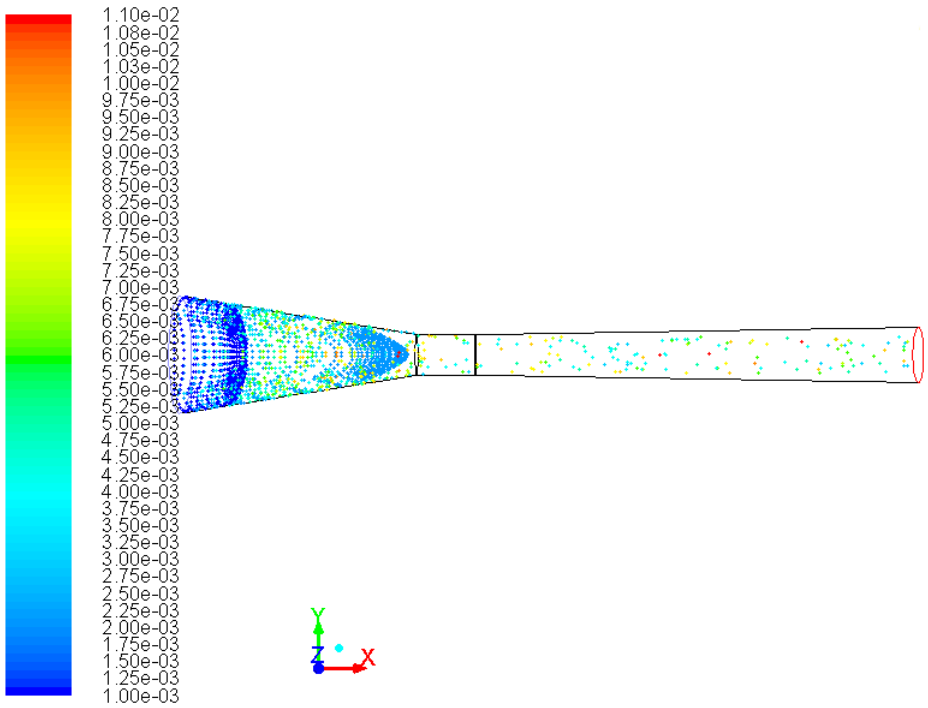

Figure 4.42: Particle trace coloured by particle residence time for the nozzle without helical insert at inlet pressure 4atm.

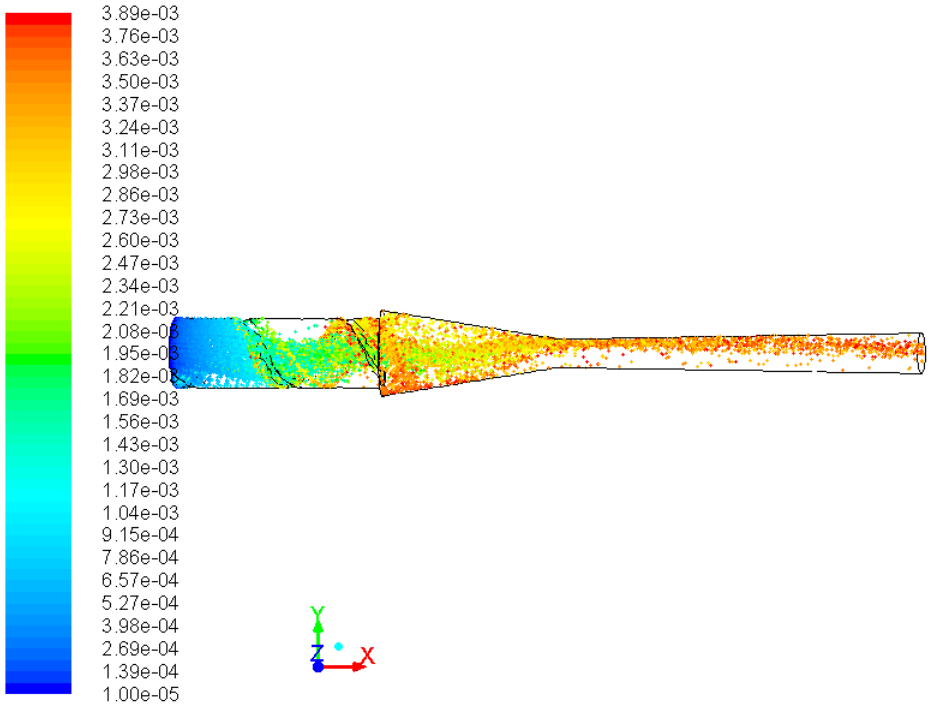

Figure 4.43: Particle trace coloured by particle residence time for the nozzle with helical insert at inlet pressure 4atm.

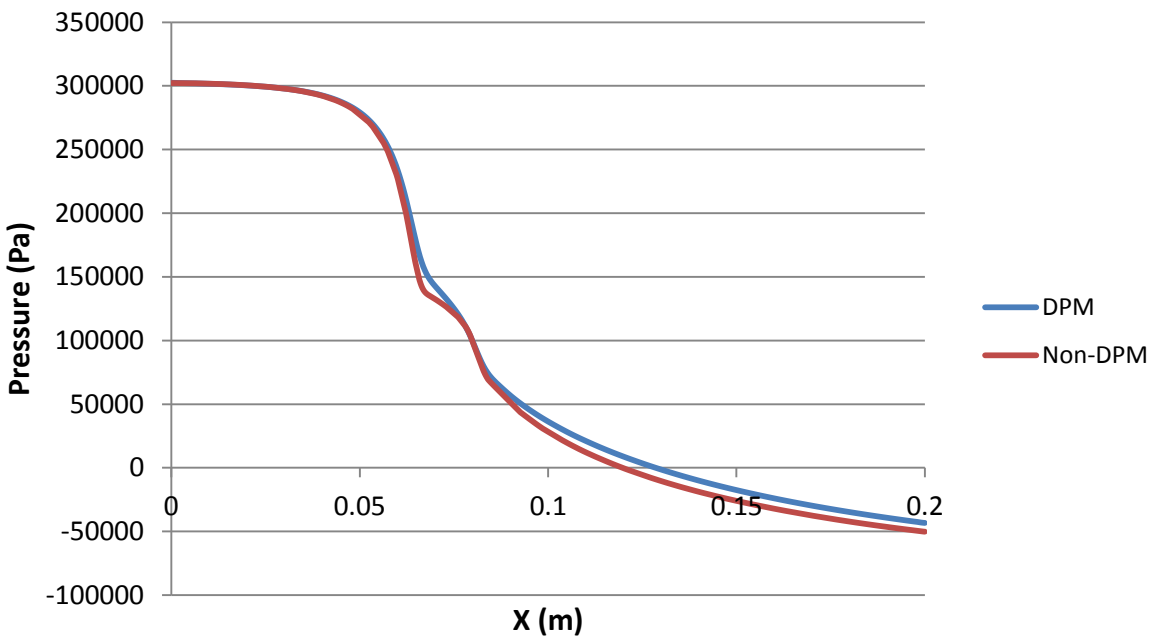

Figure 4.44: Pressure along centre of the nozzle without helical insert for DPM model at inlet pressure 4atm.

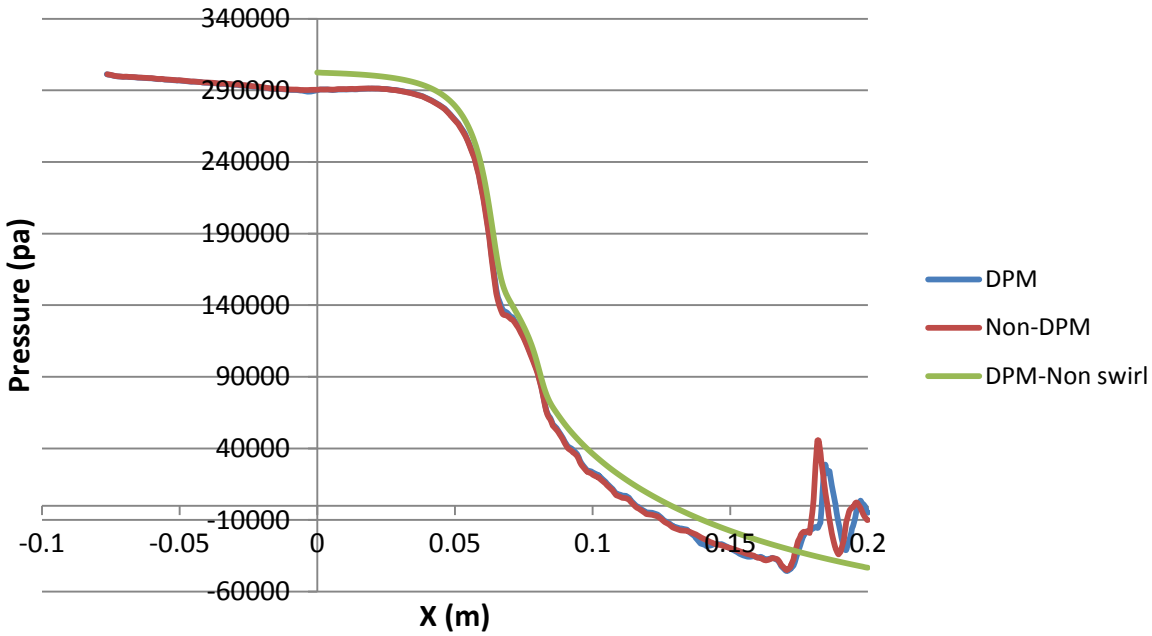

Figure 4.45: Pressure along centre of the nozzle with helical insert for DPM model at inlet pressure 4atm.

Chapter 5

CFD (OpenFOAM) Analysis of Single Phase Flow Using Variable Inlet Pressure

In this chapter numerical solutions for OpenFOAM[1] will be represented. All results in this chapter are for single phase simulations. The results include first inside nozzle simulations and then the whole domain (inside the nozzle and external domain) simulations.

OpenFOAM 2.2.x has been used for this study. OpenFOAM is open source C++ CFD toolbox, licensed under GNU general public license (GPL). This license gives freedom to users to modify and redistribute the software for any specific application. Another advantage of OpenFOAM is the ability to use it for parallel processing on any number of cores. For this research, there were access to 64 core processor server with 64Gb of RAM and Ubuntu operating system.

There is not any graphical user interface for OpenFOAM and it will run only on Linux operating system. This makes possible to use "Git[2]" properly for the backup process. Git will help future researchers to access files with detail comments and changes, and also to collaborate on a project with other researchers (Chacon and Hamano, 2009).

5.1 Inside nozzle

In this section numerical solutions of inside the nozzle simulations will be presented. The results are for the nozzle with helical insert at various inlet pressures with atmospheric condition at the outlet.

[1] Open source Field Operation And Manipulation

[2] Git is a free and open source distributed version control system and source code management.

Table 5.1: Boundary conditions for OF inside nozzle simulations.

Zone	Type-Pressure	Type-Velocity	Type-Temperature
Inlet	totalPressure	presssureInletOutlet	inletOutletTotalTemperature
Outlet	waveTransmissive	inletOutlet	zeroGradient
Wall	fixedFluxPressure/zeroGradient	fixedValue	fixedValue

The mesh is exactly similar to the one used for FLUENT analyses, which has been created by ICEM tetrahedral algorithm with 10 prism layer at walls and total number of 318,917 cells. As it is not possible to export ICEM mesh directly to OpenFOAM format, therefore FLUENT mesh has been converted to FOAM mesh within OF.

The boundary condition set up for inside the nozzle simulations is explained in Table 5.1. In OF for each boundary, all variables need to be defined separately. In supersonic flows there is a large amount of reverse flow, therefore it is crucial for stability of numerical solutions to consider it both in the inlet and the outlet boundaries. The term "inletOutlet" in OF refers to reverse flow.

One of the main problems in the FLUENT was the constant pressure at the outlet, which means for inside the nozzle simulations the outlet pressure was fixed to atmospheric pressure, and the pressure ratio was constant. However, in OF using wave transmissive boundary condition (explained in section 3.4.2.3) provides non-reflective variable pressure at the outlet. The distance to atmospheric pressure and far field condition which is defined as "linf" is crucial in providing accurate results. The long distance will not predict the position of shock waves correctly. In order to find correct value for "linf" number of simulations has been performed and the value of 0.025m has been selected.

The turbulence model selected is realizable $k-\varepsilon$ model. The numerical study by Hamed and Vogiatzis (1997) suggests that for a 2D overexpanded CD nozzle, $k-\varepsilon$ and $k-\omega$ give best results although $k-\varepsilon$ becomes more accurate at higher pressure ratios. The variables to define for turbulence modelling are: k, ε, μ_t and α_t, where μ_t is eddy viscosity (explained in section 3.5.2) and α_t is turbulent thermal diffusivity (Only for compressible flows) and is defined as

$$\alpha_t = \mu_t / Pr_t \tag{5.1}$$

For all turbulence parameters, compressible wall functions were selected at wall boundaries. The discretisation scheme for turbulence parameters ($\nabla.(\phi,k)$ and $\nabla.(\phi,\varepsilon)$) were Gauss up-

wind, where ϕ is the mass flow through the cell faces

$$\phi = \dot{m} = \rho \mathbf{u}.\mathbf{A} \tag{5.2}$$

Thermophysical properties in the OF are constructed as a temperature-pressure $(p-T)$ system which other properties are computed from. For this research where air at high velocity has been used, thermophysical model calculation is based on compressibility ψ. The air has been considered as a pure mixture where properties are calculated for a passive gas mixture. The transport properties are marked as constant and for thermodynamic properties, the specific heat c_p model is constant with evaluation of enthalpy (h) and entropy (s). The equation of state is set to perfect gas and sensible internal energy function is used as the standard internal energy function (Lemmon *et al.*, 2000).

Numerical scheme selected for divergence of momentum $(\nabla.(\phi, \mathbf{U}))$ is *vanLeer*. Although at lower pressures *limited linear* method also provided stable results but at inlet pressures above 200kPa it was not stable. Interestingly MUSCL scheme did not provide stable results. For discretisation of gradient terms the *cell limited* method has been adopted.

The pressure based *sonicFoam* solver has been used to solve numerical equations with PIMPLE algorithm (explained in section 3.3.1.1). All simulations in this chapter are based on sonicFoam, however OpenFOAM also offers density based solver *rhoCentralFoam,* which for this study had numerical instability issues and difficulties for convergence of residuals.

The results for inside the nozzle simulations at different inlet pressures are as follow:

5.1.1 Inlet pressure 150kPa

The Mach number contours for inlet pressure 150kPa is shown in Figure 5.1. There is one strong shock wave with some weak reflections of shock waves and expansion fans on shear layer. The pressure diagram along the centre of the nozzle is shown in Figure 5.2, where the pressure ratio (P_{in}/P_{out}) is 1.48. The point zero represents start of the helical insert and inlet of the nozzle is at the point 0.07645mm. The small bumpy area on the diagram is the end of converging section and flat area before the diverging section.

The shock waves structure inside the nozzle is almost symmetrical, however the exit flow is asymmetric. The Mach contours at the outlet is illustrated in Figure 5.3. This shows that there are FSS separation zones on both sides of the wall where separation zone on one side of the wall is larger than the other side.

Stream lines of the swirling flow inside the nozzle indicates yarn effect inside the flow (Figure 5.4). This could have a major effect on increasing mixing features of the flow. Chas-

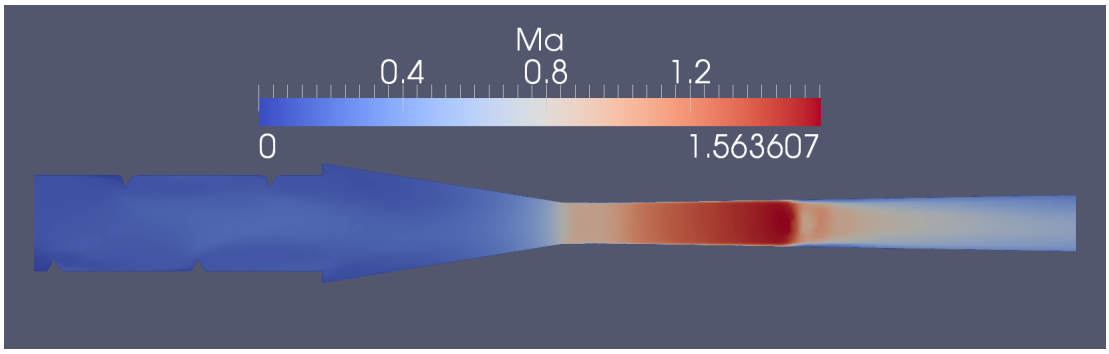

Figure 5.1: Mach number contours for Inside nozzle simulations with helical insert at inlet pressure 150kPa.

mawala *et al.* (1990) has investigated the effect of spinning parameters on the structure and properties of air-jet spinning yarns.

5.1.2 Inlet pressure 170kPa

The Mach number contours for inlet pressure 170kPa is illustrated in Figure 5.5. The shock structure is symmetrical and there are two RSS (Restricted Shock Structure) patterns just after the main shock. After the first strong shock wave, there are number of weak shock waves and expansion fans (Figure 5.6). Compare to inlet pressure 150kPa, reflected shock waves are stronger. The Pressure ratio is 1.75 and the pressure at the exit is below, but close to atmospheric pressure. As the Mach number at the throat is critical ($Ma = 1$) therefore the nozzle is choked.

Although the shock structure inside nozzle is symmetric but the out flow is asymmetric (Figure 5.7) with FSS scheme on both sides of the wall. In comparison to inlet pressure 150kPa, the high speed flow zone at the outlet is more toward centre.

Figure 5.8 presents streamlines effect. The yarn effect is visible and the rotation speed has increased compared to inlet pressure 150kPa. However the structure of the yarn is similar to lower inlet pressure.

5.1.3 Inlet pressure 200kPa

Increasing the inlet pressure to 200kPa will move the main Mach disk more toward the outlet (Figure 5.9). The shock structure remains symmetric with RSS scheme close to the wall. After the main Mach disk there is second weak Mach disk and reflection of it as an expansion fan. The pressure continues to increase after second Mach disk until reaches to exit pressure

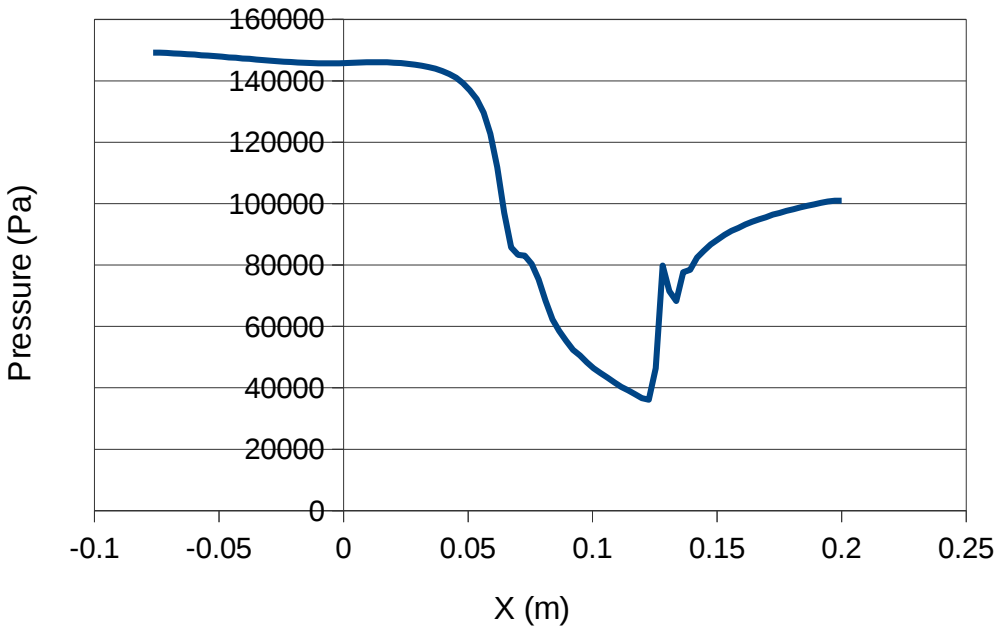

Figure 5.2: Pressure diagram along centre of the nozzle at inlet pressure 150kPa.

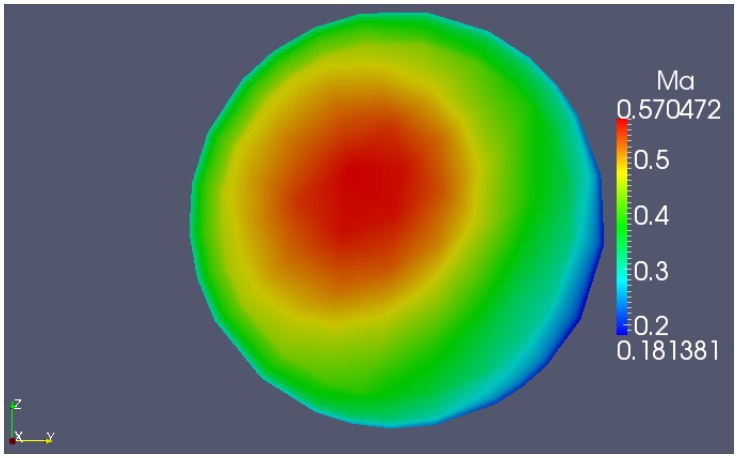

Figure 5.3: Mach number contours at the outlet of nozzle with helical insert for inlet pressure 150kPa.

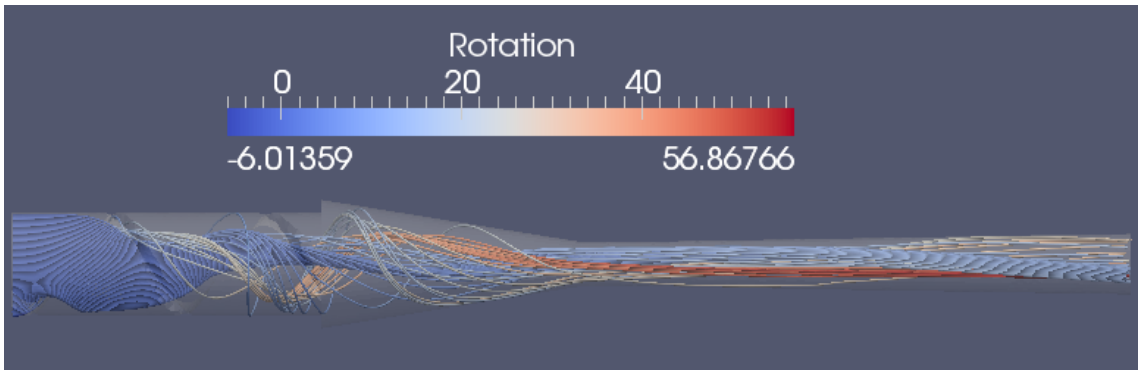

Figure 5.4: Stream lines coloured by rotation for Inside the nozzle simulations with helical insert at inlet pressure 150kPa.

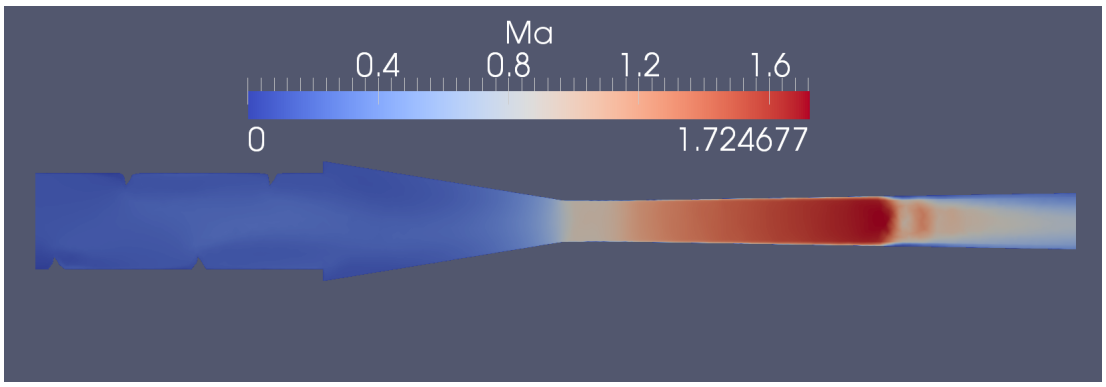

Figure 5.5: Mach number contours for inside nozzle simulations with helical insert at inlet pressure 170kPa.

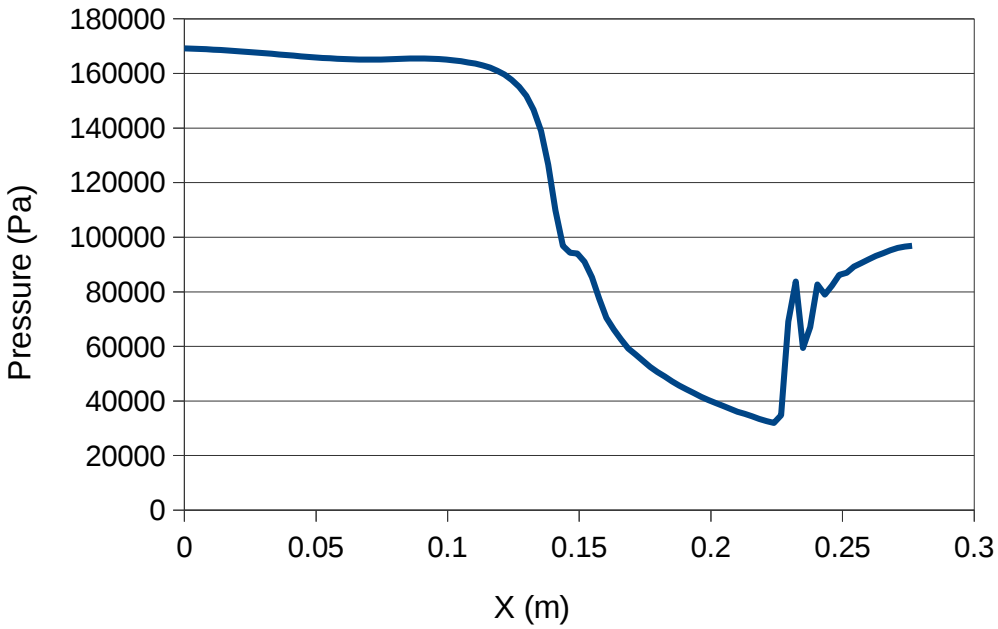

Figure 5.6: Pressure diagram along centre of the nozzle at inlet pressure 170kPa.

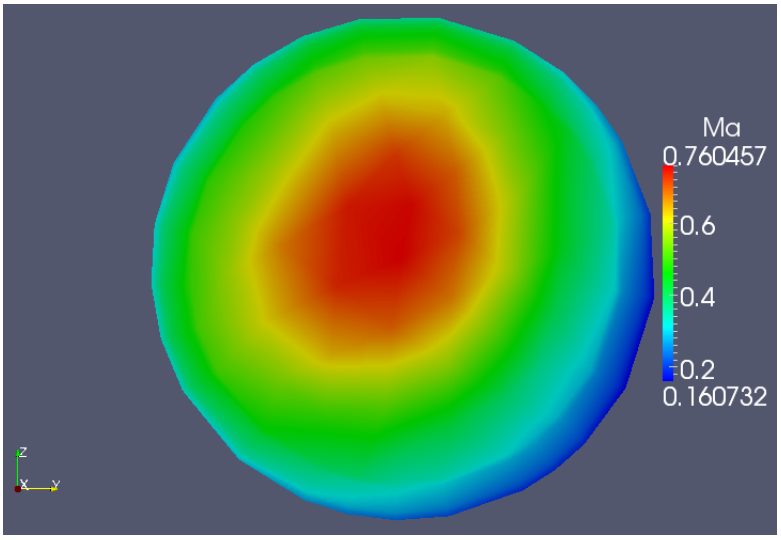

Figure 5.7: Mach number contours at the outlet of nozzle with helical insert for inlet pressure 170kPa.

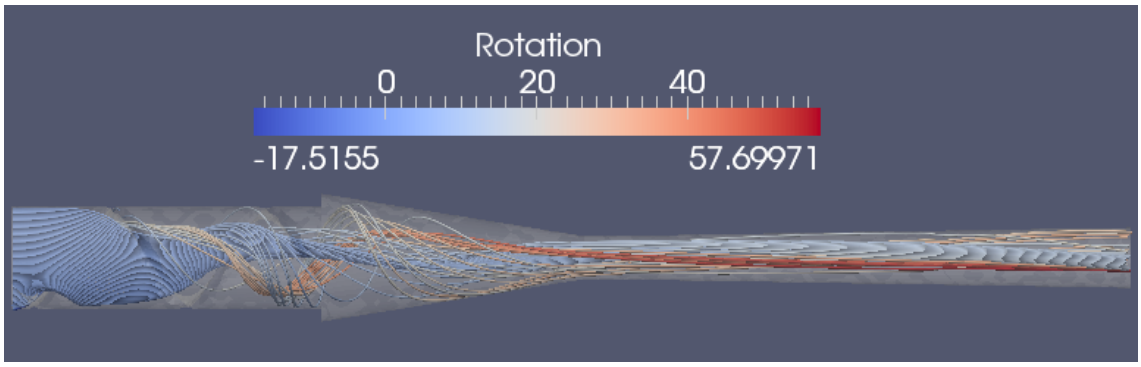

Figure 5.8: Stream lines coloured by rotation for Inside the nozzle simulations with helical insert at inlet pressure 170kPa.

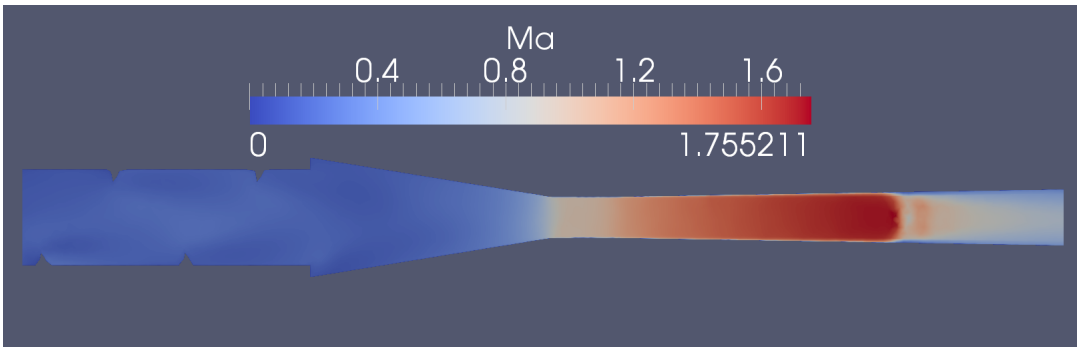

Figure 5.9: Mach number contours for the nozzle with helical insert at inlet pressure 200kPa.

(Figure 5.10).

The flow at the outlet also remains asymmetric, Figure 5.11, however is more symmetrical in comparison to 150kPa and 170kPa (Figures 5.3 and 5.7). It has a much smaller FSS region close to the wall, therefore the reverse flow area is also smaller in contrast to lower pressures.

5.1.4 Inlet pressure 300kPa

When the inlet pressure reaches to 300kPa, the shock waves are still inside the nozzle, the Mach number contours on XY plane is shown in Figure 5.12. However the first Mach disk is weaker compared to lower pressures, Figure 5.13, and it is closer to outlet of the nozzle. There are two Mach disks where the second one is much weaker. As the shock waves are close to the outlet there are not any RSS region, and there is just FSS region close to the wall.

Mach number contours at the outlet is illustrated in Figure 5.14. It is obvious that FSS region has been created around the wall and the out flow is symmetrical.

Stream lines for inlet pressure 300kPa are shown in Figure 5.15. Compare to lower inlet pressures, rotational speed has been reduced and the difference between minimum and max-

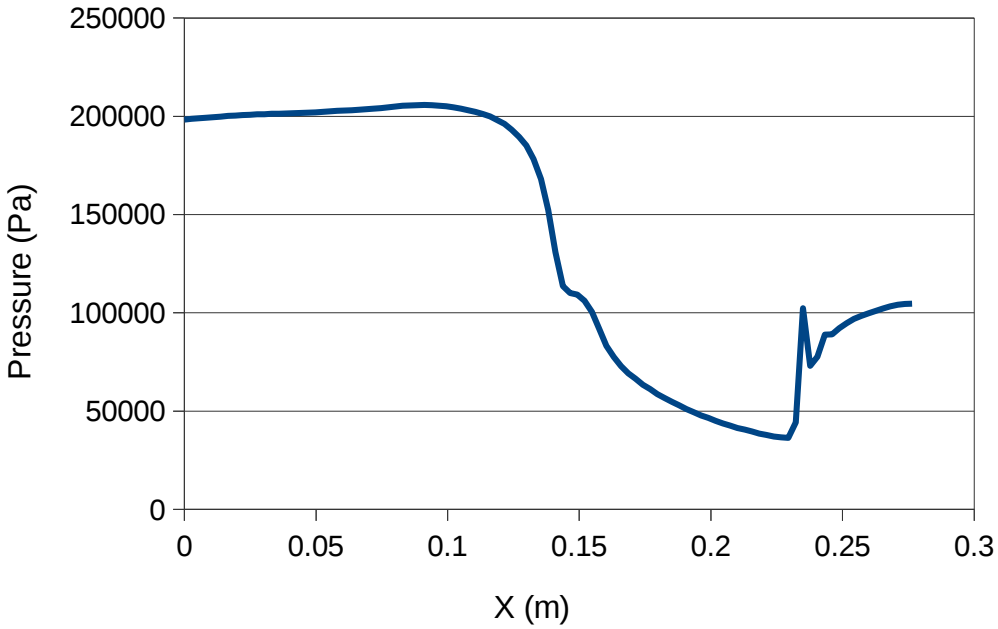

Figure 5.10: Pressure diagram along centre of the nozzle at inlet pressure 200kPa.

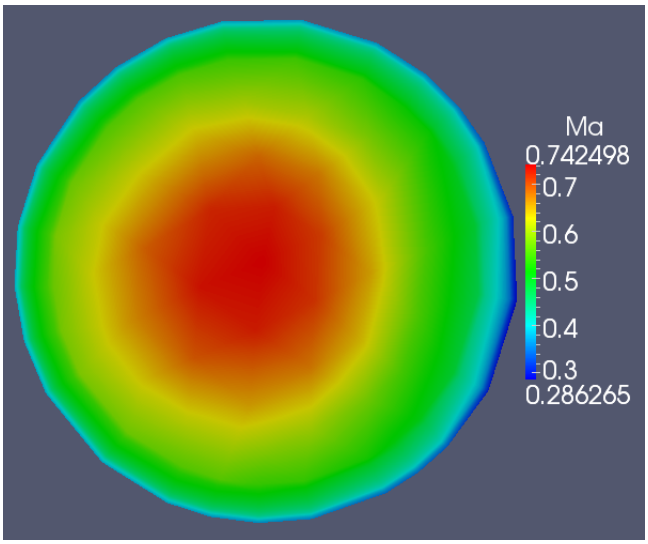

Figure 5.11: Mach number contours at the outlet of nozzle with helical insert for inlet pressure 200kPa.

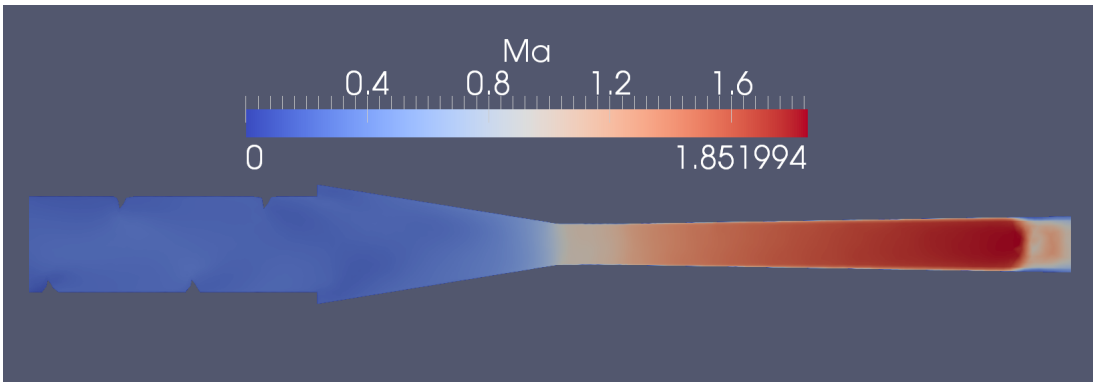

Figure 5.12: Mach number contours of the nozzle with helical insert at inlet pressure 300kPa.

imum values are decreased. Therefore, there is less yarn effect inside the nozzle, although there is enough twist between stream lines to create yarn effect.

5.1.5 Inlet pressure 400kPa

As the inlet pressure extends to 400kPa all shock waves will move out of the nozzle (Figure 5.16) and the speed of the air reaches to Mach 1.92. The pressure along the nozzle continuously drops and goes under atmospheric pressure at 50823Pa, Figure 5.17, therefore the pressure ratio will increase massively to 7.87.

The outflow is completely symmetrical where there is a very small FSS area close to the wall around the outlet (Figure 5.18). Because all shock waves are out of the nozzle, therefore the velocity will reach to its maximum at the outlet.

Figure 5.19 shows stream lines for inlet pressure 400kPa. In contrast to lower pressures, the yarn effect has been reduced and the rotational speed is reduced as well. The swirling effect is more toward the nozzle wall and flow at the centre of the nozzle is less rotational compared to lower pressures. This might reduce the mixing effect of the nozzle.

5.1.6 Mass flow rate

The mass flow rate for each inlet pressure and their pressure ratios can be found from Table 5.2. In all of inlet pressures discussed above the nozzle were choked, where the air at throat has reached to sonic point, $Ma = 1$, thus it has the maximum mass flow rate for giving inlet pressure. As discussed in previous chapter (Section 4.1.1.4), the nozzle is choked when the inlet pressure is fixed and downstream pressure is changing. By increasing the inlet pressure the mass flow rate also will increase despite the nozzle is choked for giving inlet pressure.

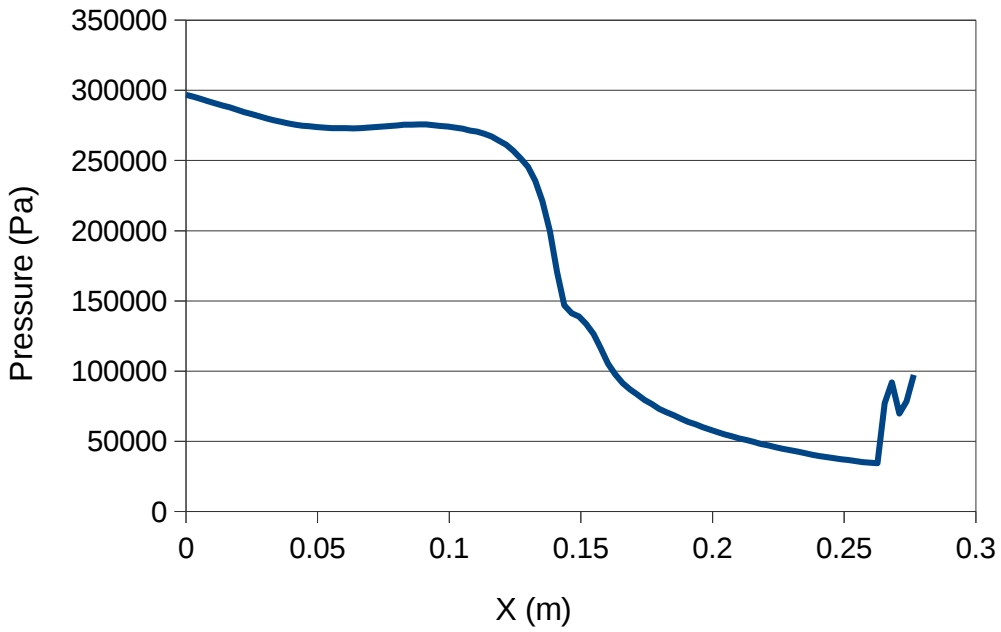

Figure 5.13: Pressure diagram along centre of the nozzle at inlet pressure 300kPa.

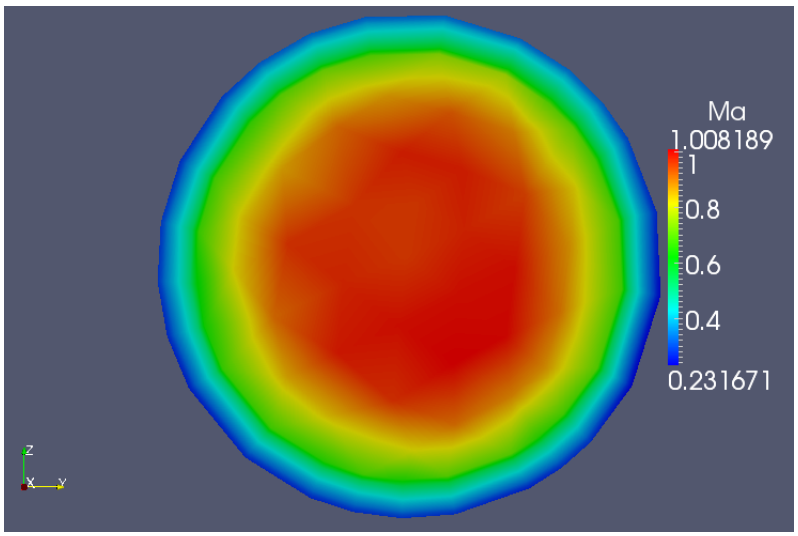

Figure 5.14: Mach number contours at the outlet of nozzle with helical insert for inlet pressure 300kPa.

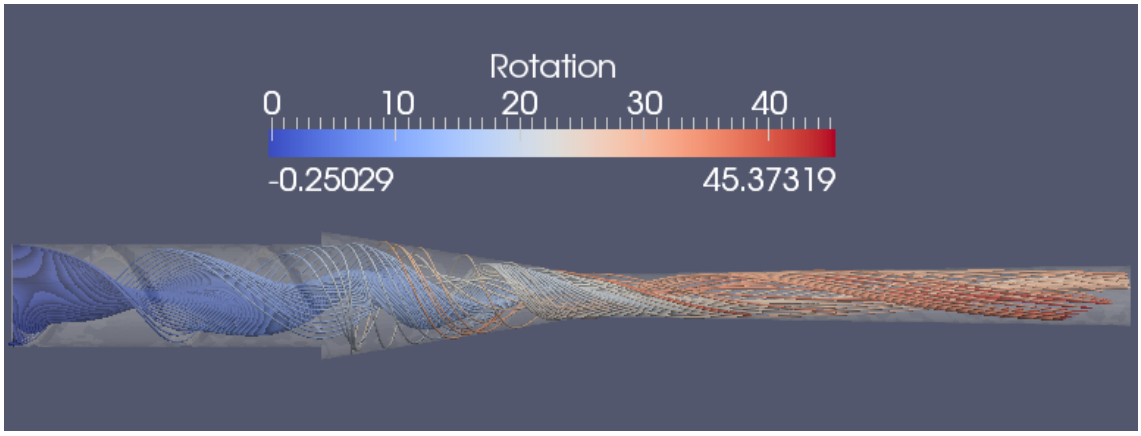

Figure 5.15: Stream lines coloured by rotation for Inside the nozzle simulations with helical insert at inlet pressure 300kPa.

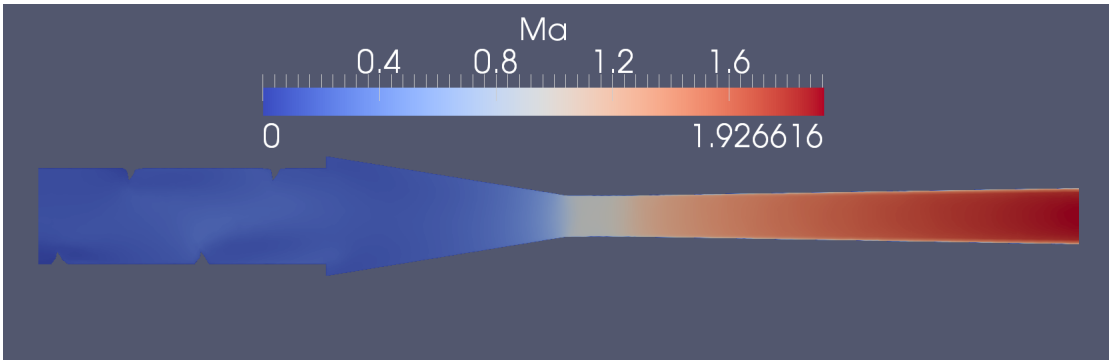

Figure 5.16: Mach number contours of the nozzle with helical insert at inlet pressure 400kPa.

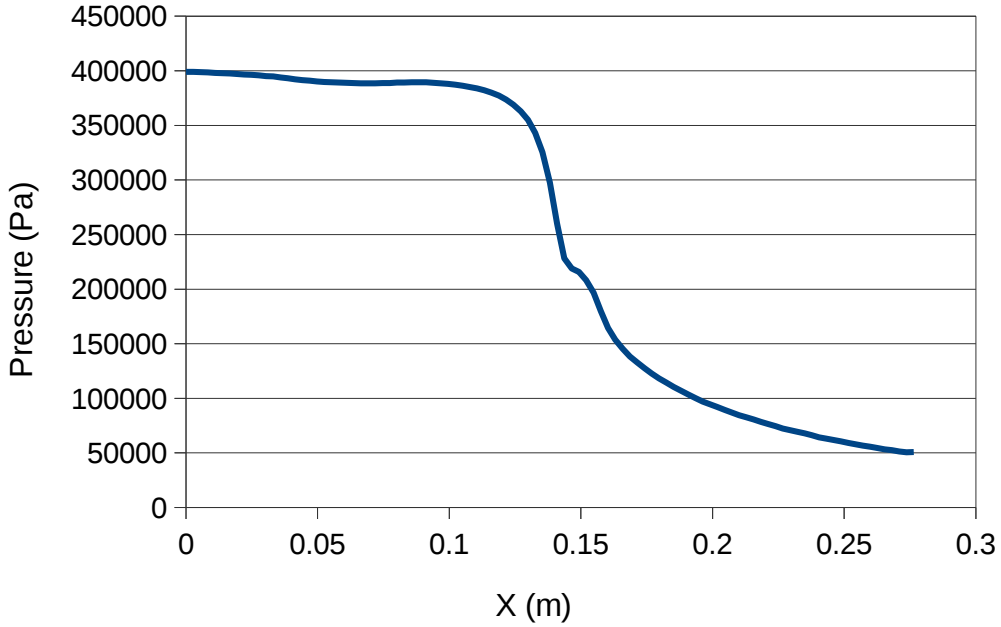

Figure 5.17: Pressure diagram along centre of the nozzle with helical insert at inlet pressure 400kPa.

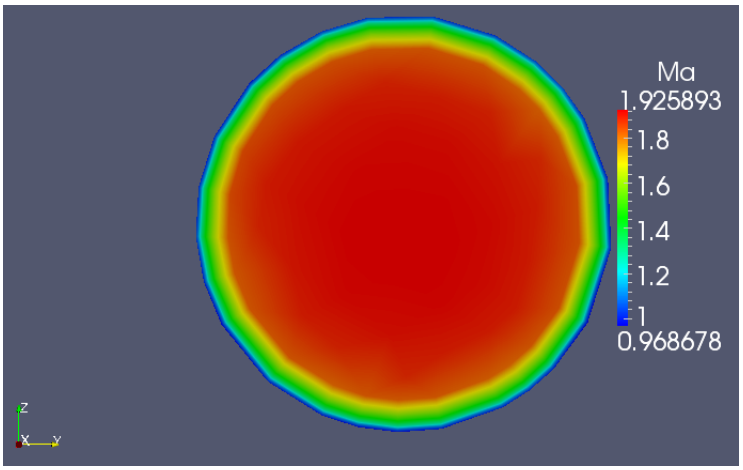

Figure 5.18: Mach number contours at the outlet of nozzle for inlet pressure 400kPa.

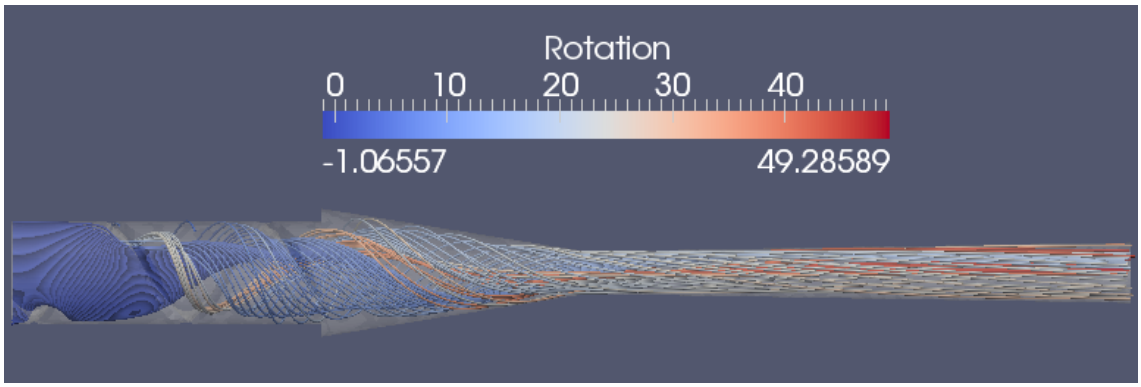

Figure 5.19: Stream lines coloured by rotation for Inside the nozzle simulations with helical insert at inlet pressure 400kPa.

Table 5.2: Mass flow rate and PR for nozzle with helical insert.

Inlet Pressure	150kPa	170kPa	200kPa	300kPa	400kPa
Mass flow rate (kg/s)	0.0307	0.0354	0.0385	0.061	0.08164
Pressure ratio (P_{in}/P_{out})	1.48	1.75	1.91	3.08	7.85

The mass flow rate diagram versus different PRs is sketched in Figure 5.20. The mass flow rate is increasing linearly with the slope of 0.019 until inlet pressure reaches to 300kPa. At this point, by increasing the upstream pressure to 400kPa all the shock waves will move out of the nozzle and the mass flow rate will show different behaviour, which the rate of increasing for mass flow rate will reduce.

5.2 Complete domain

In order to have a good understanding of flow behaviour inside a nozzle, it is crucial to consider flow at down stream of a nozzle as well. On inside nozzle simulations, outlet boundary has a impose boundary condition which could mitigate some of the downstream effects like aeroacoustic waves and jet instabilities on flow behaviour, shock waves structure and their position inside nozzle. Therefore the simulations for complete domain have been done for both the nozzle with and without helical insert and the effect of different inlet pressure have been investigated.

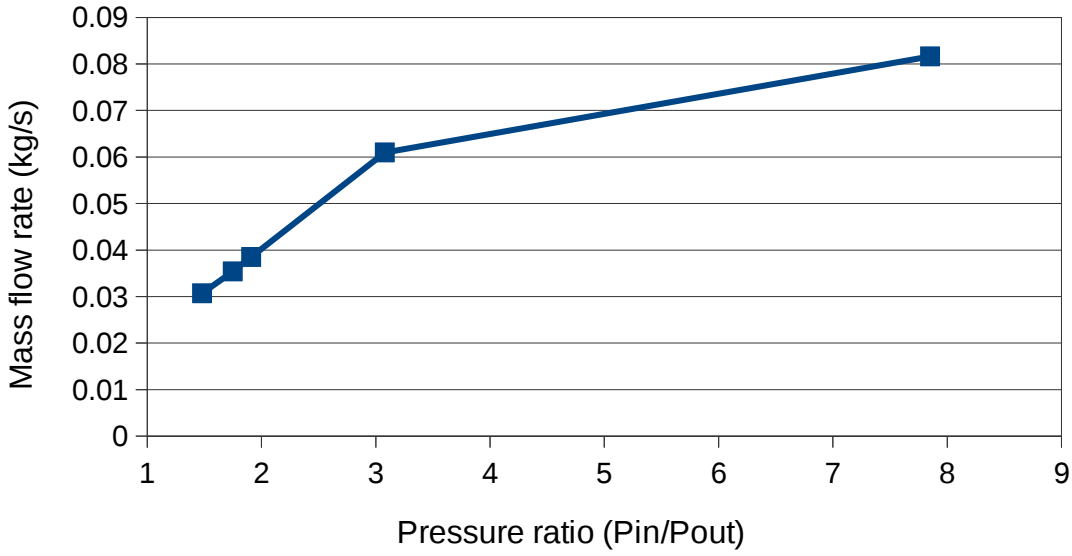

Figure 5.20: Mass flow rate diagram for nozzle with helical insert.

5.2.1 Without helical insert

This section contains the simulation results for complete domain of the nozzle without helical insert. Although simulations for the same nozzle was performed by Abbasalizadeh (2011), but for all of those simulations the numerical domain just contains the inside nozzle.

The geometry and mesh structure of the domain are shown in Figure 5.21. As the domain is symmetrical the simulations have been performed in 2D[3], with the total number of 166,400 cells. Both geometry and mesh were created using *blockMesh* tool of OF where creates fully structured mesh. The length of the domain in X direction after the outlet of nozzle is 0.4m where the total length of the domain is 0.6m and in Y direction the domain total length is 0.268m.

The boundary condition setup is shown in Table 5.3. The "Outlet-1" is the final outlet in X direction which is parallel to the outlet of the nozzle, and all other outlets are considered as "Outlet-2". The realizable $k-\varepsilon$ model has been adopted for turbulence modelling, with vanLeer discretisation for ε, and upwind method for k. The discretisation scheme for $\nabla.(\phi\mathbf{U})$ is vanLeerV and for the rest of divergence schemes are limited linear method. For gradient scheme the cell limited method has been selected. The pressure based transient *sonicFoam* solver is used to solve numerical equations.

The results for different inlet pressures are explained below:

[3]OpenFOAM always operates in 3D mode, in order to run it in 2D, the *empty* boundary condition is applied to third dimension.

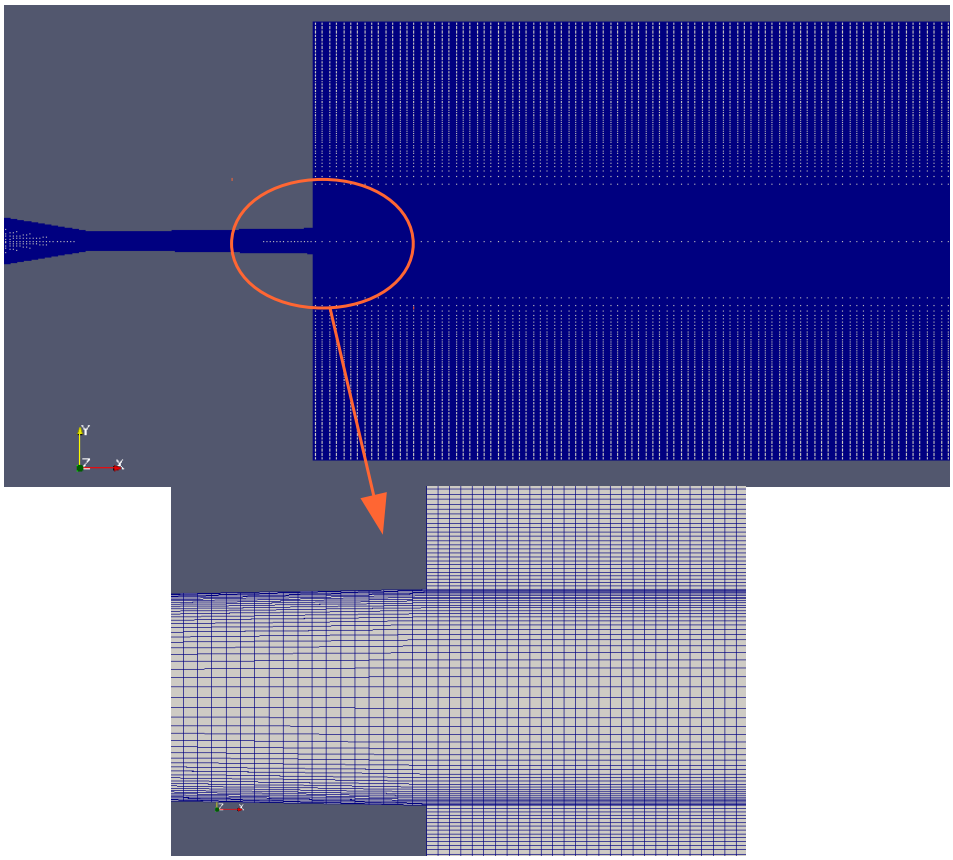

Figure 5.21: Geometry and mesh for complete domain of the nozzle without helical insert.

Table 5.3: Boundary condition for complete domain simulation of the nozzle without helical insert.

Zone	Type-velocity	Type-pressure	Type-Temperature
Inlet	pressureInletOutletVelocity	totalPressure	inletOutletTotalTemperature
Outlet-1	pressureInletOutletVelocity	waveTransmissive	inletOutletTotalTemperature
Outlet-2	pressureInletOutletVelocity	totalPressure	inletOutletTotalTemperature
Wall	fixedValue	fixedFluxPressure	fixedValue

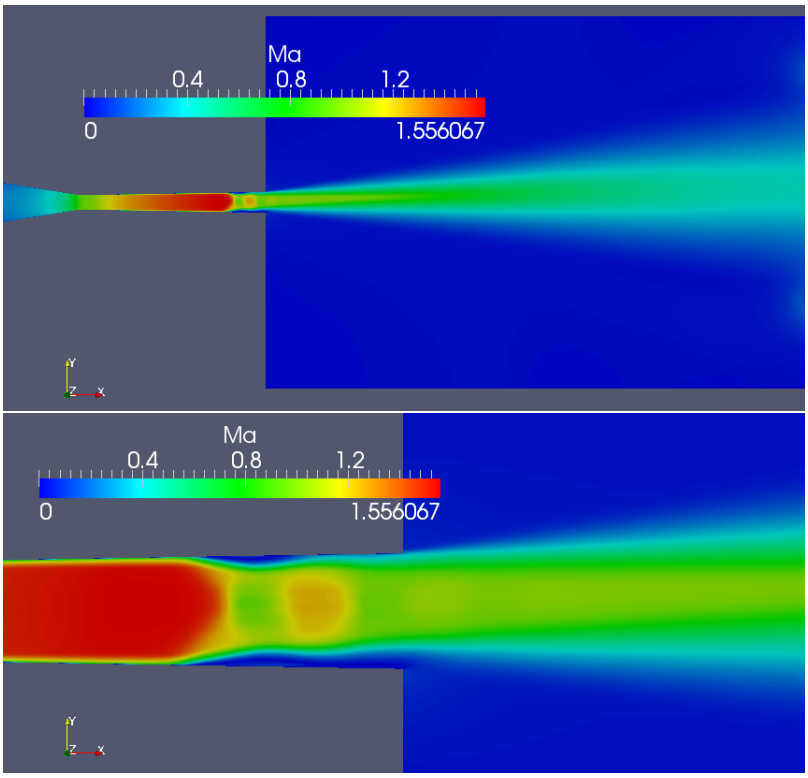

Figure 5.22: Mach number contours for complete domain simulations of the nozzle without helical insert at inlet pressure 190kPa. (The lower picture is zoomed at the outlet of nozzle)

5.2.1.1 Inlet pressure 190kPa

At inlet pressure 190kPa the Mach contour structure is shown in Figure 5.22; The nozzle is overexpanded, and the main Mach disk is inside the nozzle, however the shock waves and flow pattern are not symmetrical. This can be seen from the zoomed image of Figure 5.22, where the flow attaches to the upper side of the nozzle at the outlet due to Coanda effect. The flow structure will create FSS region on the lower side of the nozzle wall and RSS on the upper side of it.

The pressure diagram along the centre of the nozzle is sketched in Figure 5.26. The first shock cell which is the strongest, is inside the nozzle. However, after the outlet the pressure will reach quickly to atmospheric pressure and there are not any high pressure oscillation any more.

5.2.1.2 Inlet pressure 200kPa

By increasing inlet pressure to 200kPa, the shock waves structure remains similar and flow pattern is still asymmetric; however, the jet direction has changed and now there is a FSS

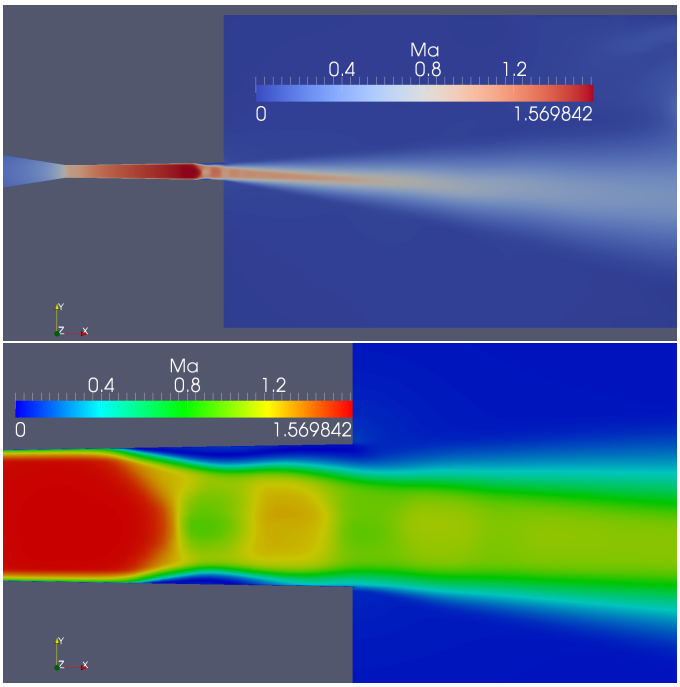

Figure 5.23: Mach number contours for complete domain simulations of the nozzle without helical insert at inlet pressure 200kPa.(The lower picture is zoomed at the outlet of nozzle)

region on the upper wall and an RSS region on the lower wall (Figure 5.23). The nozzle also remains overexpanded.

The pressure diagram along centre of the nozzle is illustrated in Figure 5.26. It is very similar to inlet pressure 190kPa, but due to pressure increase the main Mach disk has moved toward outlet. But for both pressures, shock cells will damp quickly, where at outside domain there are not any specific pressure changes.

The jet shows stable behaviour and although the simulations are transient, but solving for extra time steps did not provide any change to flow parameters. Temperature contours in Figure 5.24, shows the stability of jet.

5.2.1.3 Inlet pressure 250kPa

Increasing the inlet pressure to 250kPa will push all the shock waves almost out of the nozzle, Figure 5.25, and there are number of shock cells after the outlet. The first oblique shocks are inside of the nozzle and they create FSS region on both side of the nozzle wall. At the beginning of simulations, jet flow is symmetrical (Figure 5.25(a)), but after several time steps it start to become unstable and moves upward (Figure 5.25(b)). The jet remains at this condition with small instabilities at far field.

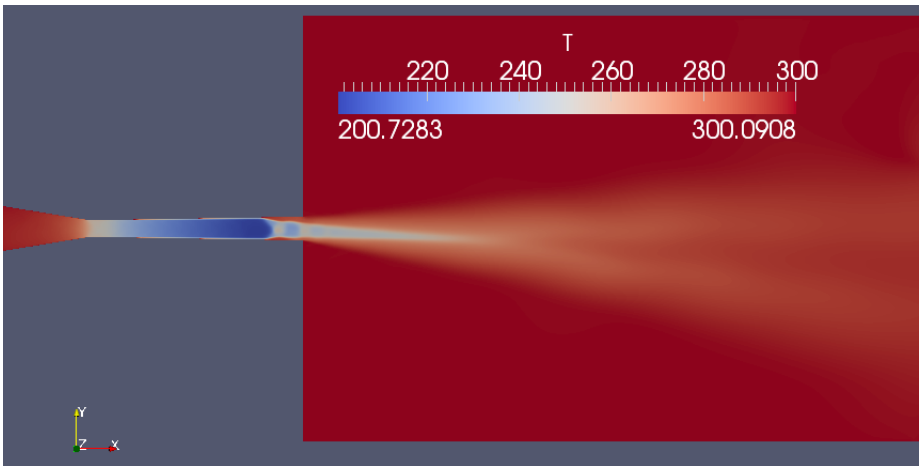

Figure 5.24: Temperature contours for complete domain simulations of the nozzle without helical insert at inlet pressure 200kPa.

The pressure along the centre of the nozzle is illustrated in Figure 5.26. Compare to lower pressures, the first shock is stronger and there are several shock cells after the exit. Although there are instabilities in the jet, but the pressure change along the centre is insignificant.

5.2.1.4 Inlet pressure 300kPa

When the inlet pressure reaches to 300kPa, the jet will show much more instabilities. The Figure 5.27 shows the jet at four different time steps. At the first time step t=0.006s the jet looks stable with almost straight free jet boundary. Instabilities on free jet starts at t=0.0084s (Figure 5.27b) mainly at the far field. At t=0.0171s (Figure 5.27c) the jet shows more instabilities which effects the shock cell structure as well. At t=0.0426s (Figure 5.27d) the jet instabilities is similar to previous time step but the direction of shock cells have shifted a little down ward. Further time step simulations did not show change on jet structure any more, and the free jet boundary will keep changing between Figure 5.27c and Figure 5.27d. Temperature contour at t=0.0426s is shown in Figure 5.28, in compared to inlet pressure 200kPa (Figure 5.24) the jet has more instabilities and shock cells are at the same temperature of air inside the nozzle.

The shock cells structure are quite similar for different time steps. Figure 5.29 is zoomed at shock cells for t=0.0426s. There are not any reverse flow inside nozzle any more and oblique shock waves start from exit of the nozzle. At 300kPa inlet pressure, diamond shocks have curvy jet boundary. The nozzle is still overexpanded as the pressure at the exit is lower than atmospheric pressure (Hagemann *et al.*, 1998).

The pressure along the centre of the nozzle at two time steps are sketched in Figure 5.30. Pressure diagram at the centre for different time steps are similar up to several shock cells

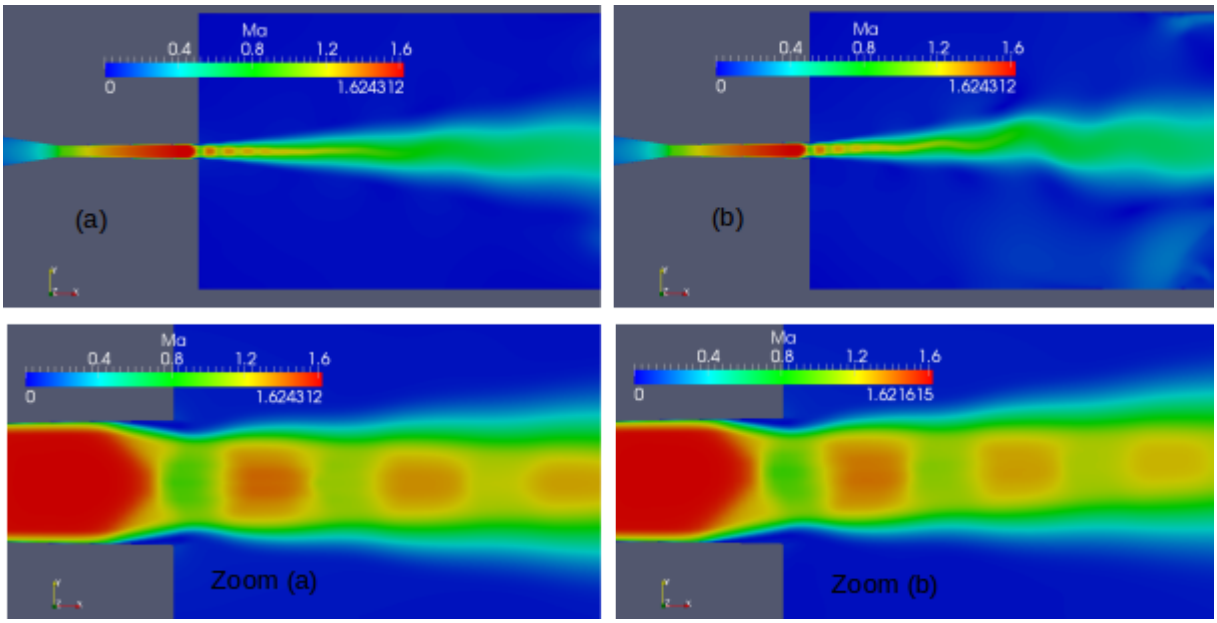

Figure 5.25: Mach number contours for complete domain simulations of the nozzle without helical insert at inlet pressure 250kPa (a) t=0.027s (b) t=0.0498s.

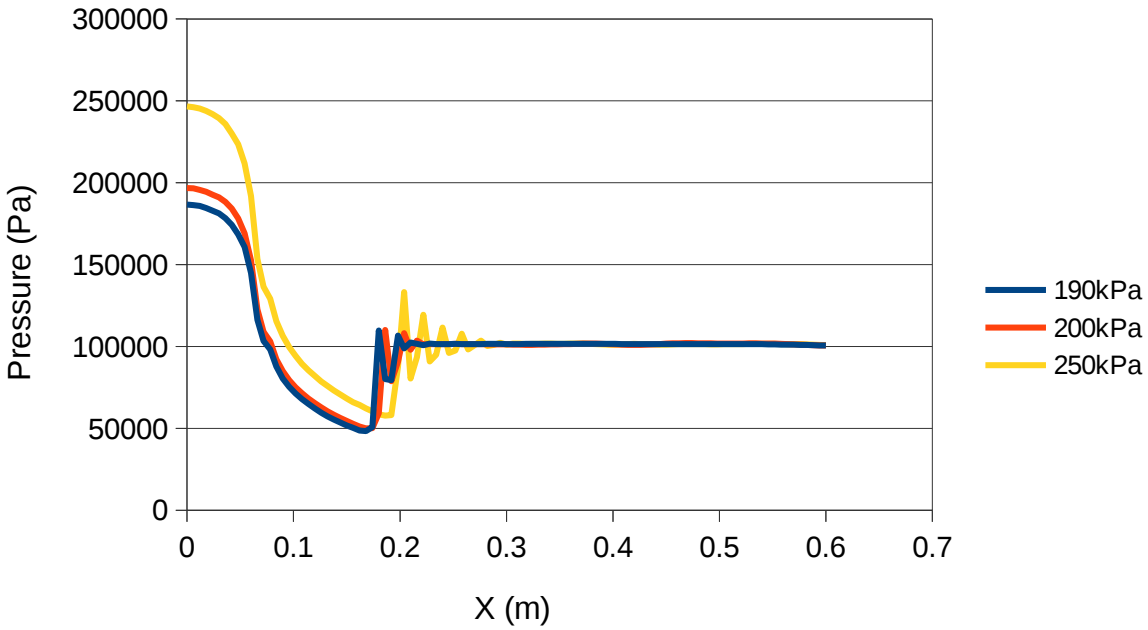

Figure 5.26: Pressure diagram along the centre of the nozzle without helical insert for inlet pressures 190kPa, 200kPa and 250kPa.

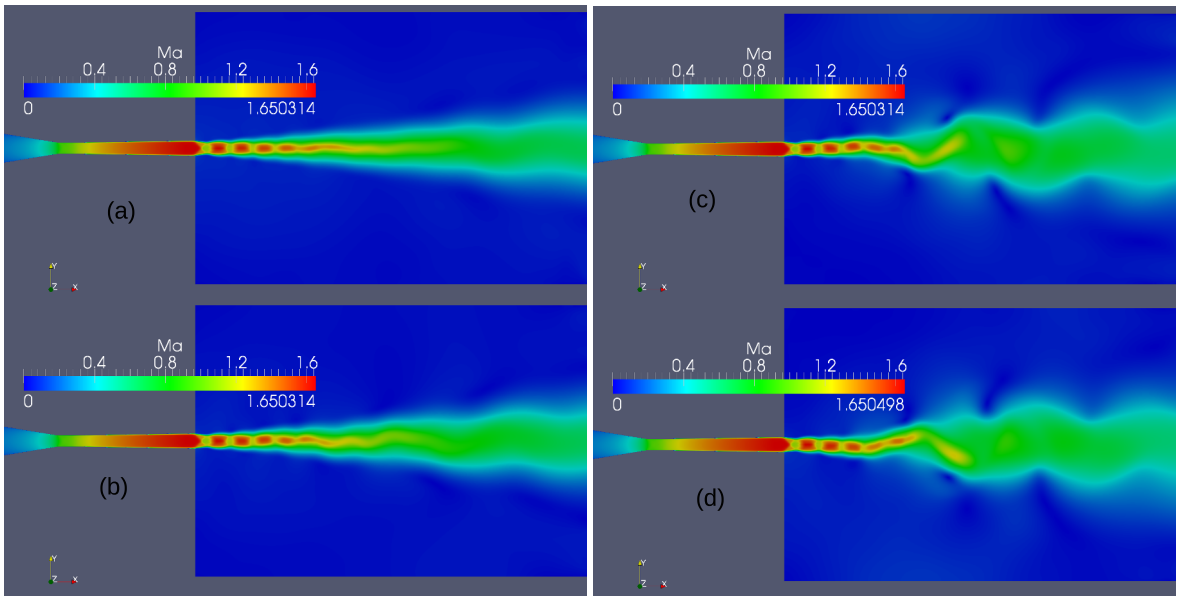

Figure 5.27: Mach number contours for complete domain simulations of the nozzle without helical insert at inlet pressure 300kPa (a)t=0.006s (b)t=0.0084s (c)t=0.0171s (b)t=0.0426s.

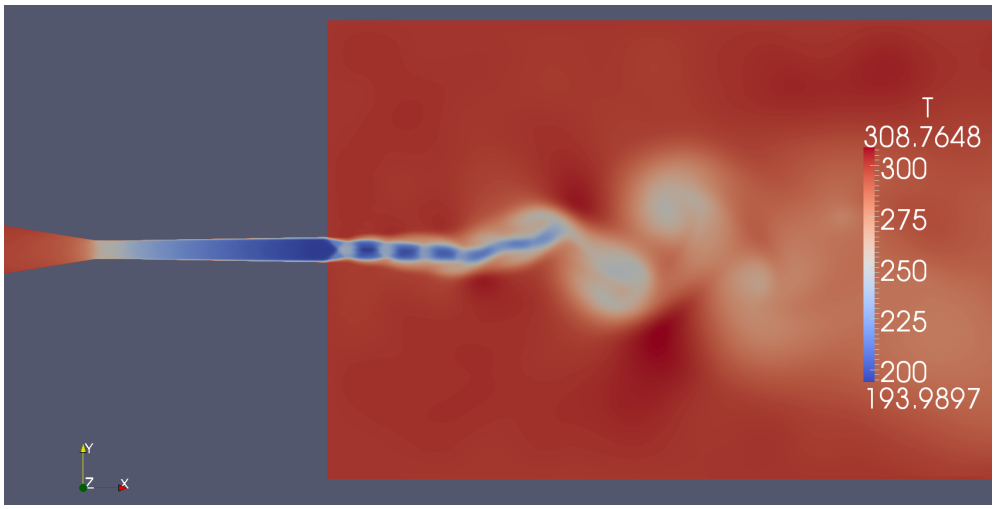

Figure 5.28: Temperature contours for complete domain simulations of the nozzle without helical insert for inlet pressure 300kPa at t=0.0426s.

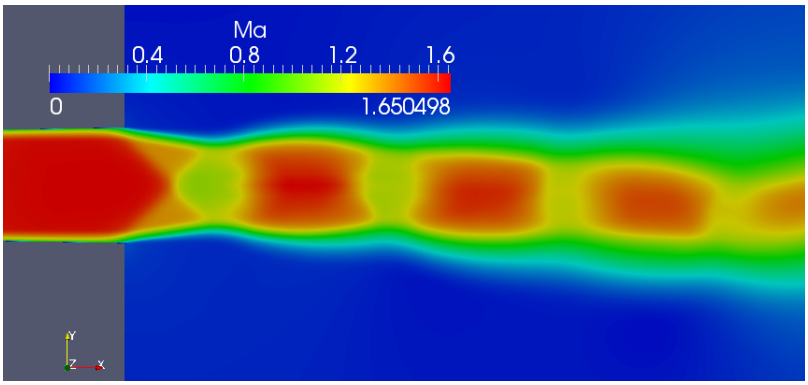

Figure 5.29: Mach number contours for complete domain simulations of the nozzle without helical insert at inlet pressure 300kPa for t=0.0426.

after the exit, however, because of jet instabilities there are some pressure oscillation after the shock cells.

The jet instabilities will create more pressure difference inside domain which will cause more noise and aeroacoustic waves. Figure 5.31 shows that on the free jet boundary there are several points of high pressure gradient. Considering the line $y = 0.0158$ and again the line in centre of the nozzle but just for domain outside of it, pressure along these two lines are illustrated in Figure 5.32. At the beginning the main pressure oscillations are along the shock cells, this is predictable because of high pressure gradient along the shocks. But after the shock cells, there are more pressure change in free jet boundary and there are not huge pressure gradient at centre of the domain.

5.2.1.5 Inlet pressure 400kPa

As the inlet pressure reaches to 400kPa the jet instabilities will increase. The Mach number contours at different time steps are shown in Figure 5.33. Compare to inlet pressure 300kPa the jet will reach to its maximum instability at a shorter time. As the nozzle operates at atmospheric condition, for all time steps, will remain overexpanded. At the beginning, Figure 5.33a & b, the jet seems stable, however, with further time step simulations the jet free boundary starts to change. Instabilities on the free jet boundary will increase up to around t= 0.0244s, Figure 5.33h, where further time step simulations did not show any major change in jet structure, although the jet boundary will alternate between Figure 5.33e to 5.33h.

Shock cells structures will not have an exact diamond shape as lower pressures, this can be seen from Figure 5.34. Although there are large instabilities on the jet, but it has no effect on the structure of shock cells and Mach waves and all the instabilities occur after the shock cells. The first oblique shock waves start at the exit of the nozzle without any effect on separation

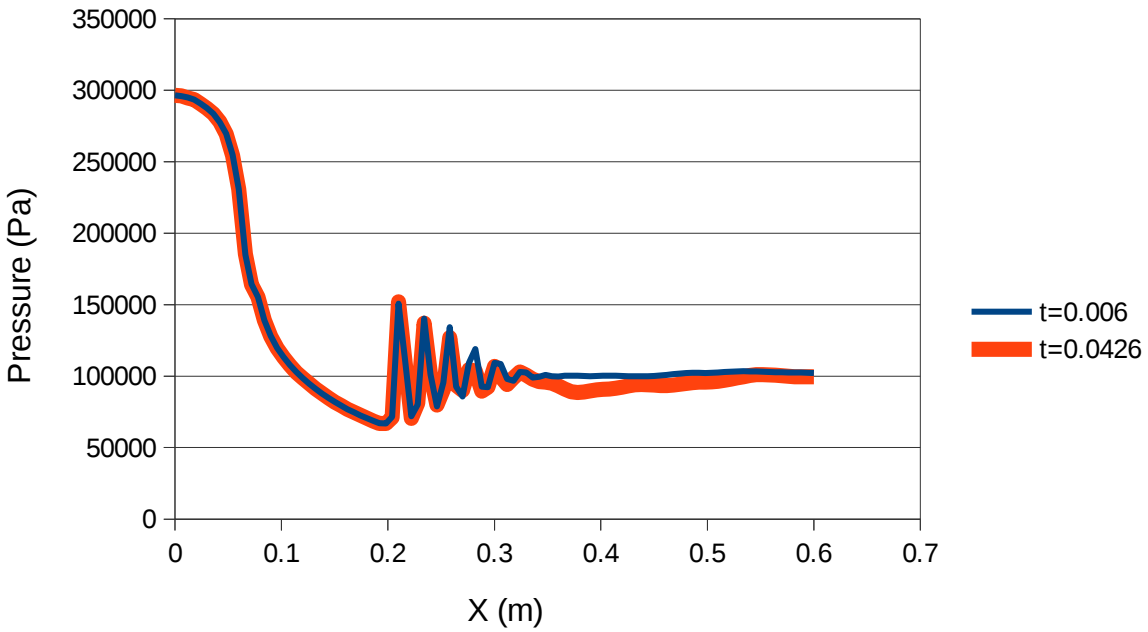

Figure 5.30: Pressure diagram along centre of the nozzle without helical insert for inlet pressure 300kPa.

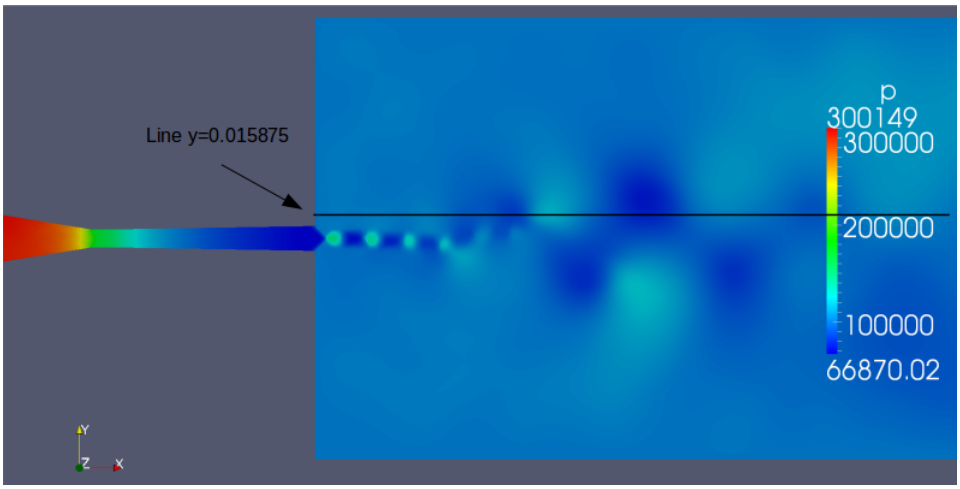

Figure 5.31: Pressure contours for complete domain simulations of the nozzle without helical insert for inlet pressure 300kPa at t=0.0426s.

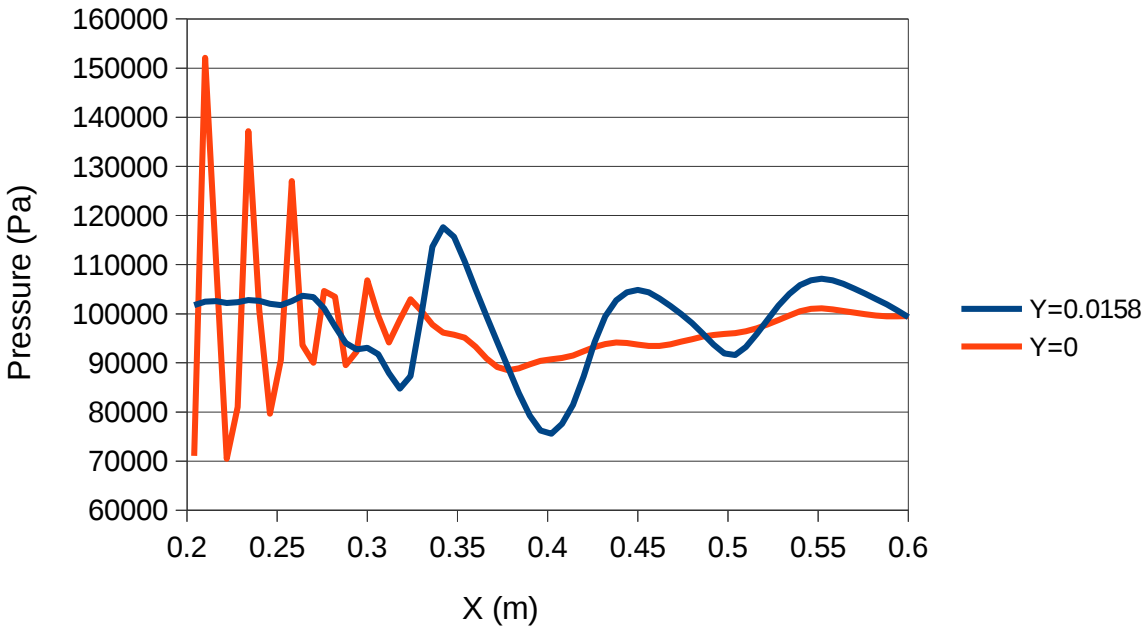

Figure 5.32: Pressure diagram along two lines at exit domain for the nozzle without helical insert for inlet pressure 300kPa.

of flow behind it. This is mainly due to much weaker oblique shocks in contrast to lower pressures. Therefore expansion fans which are because of shock waves reflection on shear layer are weaker as well.

The pressure contours for different time steps are illustrated in Figure 5.35. In stable conditions (Figure 5.35a) there are not any noticeable pressure difference inside domain apart from shock cells. Continuing simulations for extra time steps, which will create jet instabilities, have shown major pressure differences inside the domain (Figure 5.35b - e). As explained before the jet instabilities starts after the shock cells, Figure 5.36 shows the pressure diagram along centre of the nozzle for different time steps, and it can be seen that for different time steps, pressure variations happen after the shock cells. So the jet instabilities have not specific effect on shock cells structure. Shock cells for inlet pressure 400kPa are weaker compared to lower pressures. Figure 5.37 explains the strengths of shock cells and expansion fans at two different pressures.

Figure 5.35 demonstrated that after some time step simulations there will be pressure instabilities inside the domain. Static pressure on two lines, a line through centre of the nozzle as $Y = 0$, and a line along pressure differences inside domain as $Y = 0.0158m$ (explained in Figure 5.31), are illustrated in Figure 5.38. Both lines start from exit of domain at $x = 0.2$. At the beginning for $\Delta x = 0.15m$, the only pressure fluctuations are related to shock cells, and

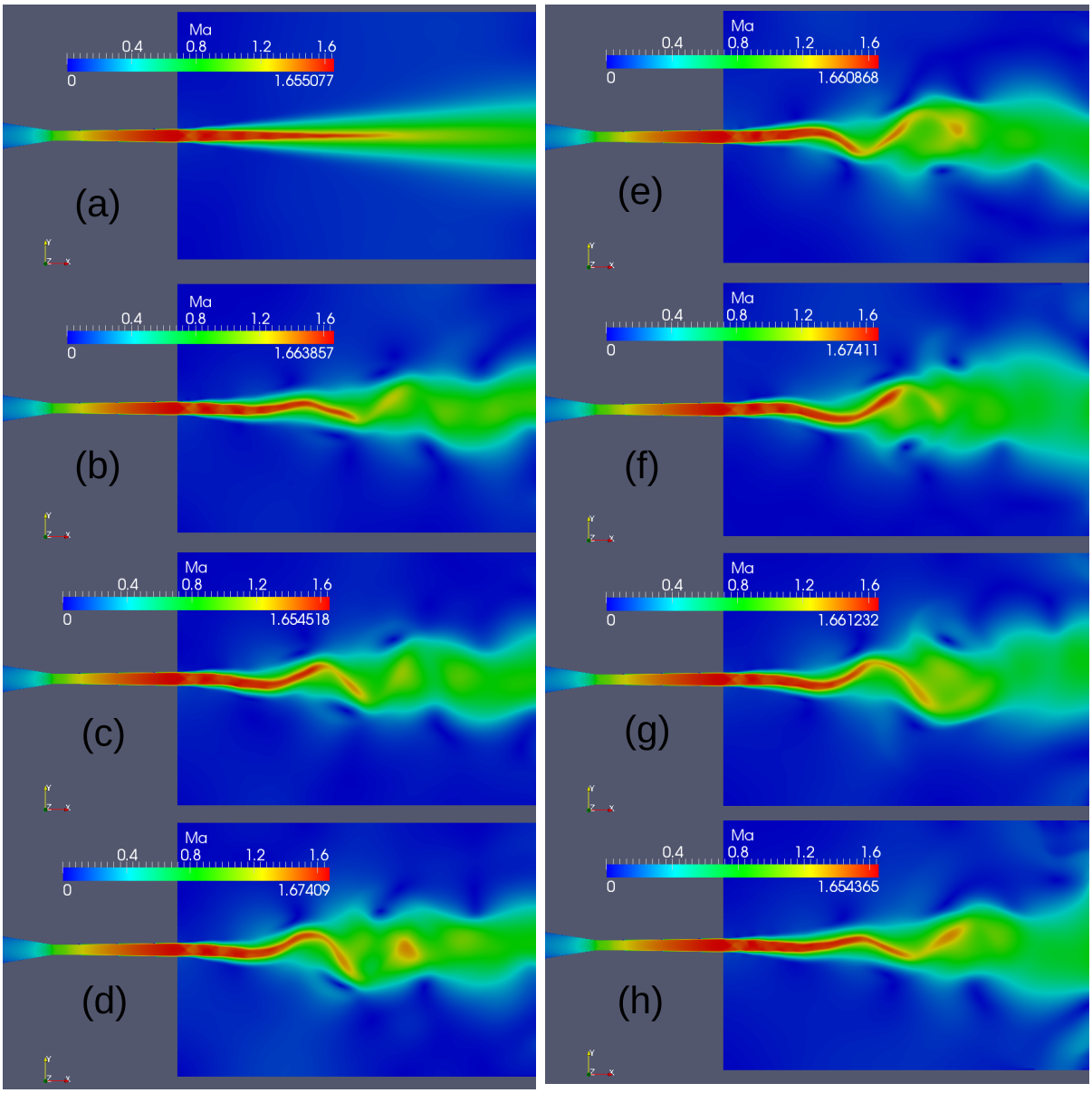

Figure 5.33: Mach number contours for complete domain simulations of the nozzle without helical insert at inlet pressure 400kPa (a)t=0.0048s (b)t=0.0147s (c)t=0.0154s (d)t=0.0166s (e)t=0.0196s (f)t=0.0214s (g)t=0.0226s (h)t=0.0244s.

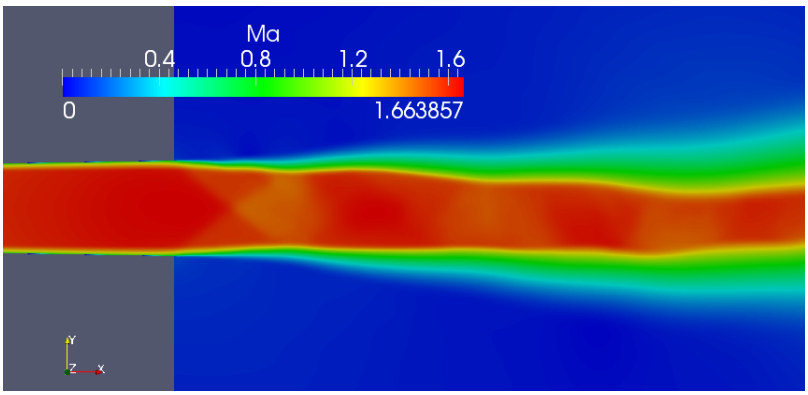

Figure 5.34: Mach number contours for complete domain simulations of the nozzle without helical insert at inlet pressure 400kPa for t=0.0147s.

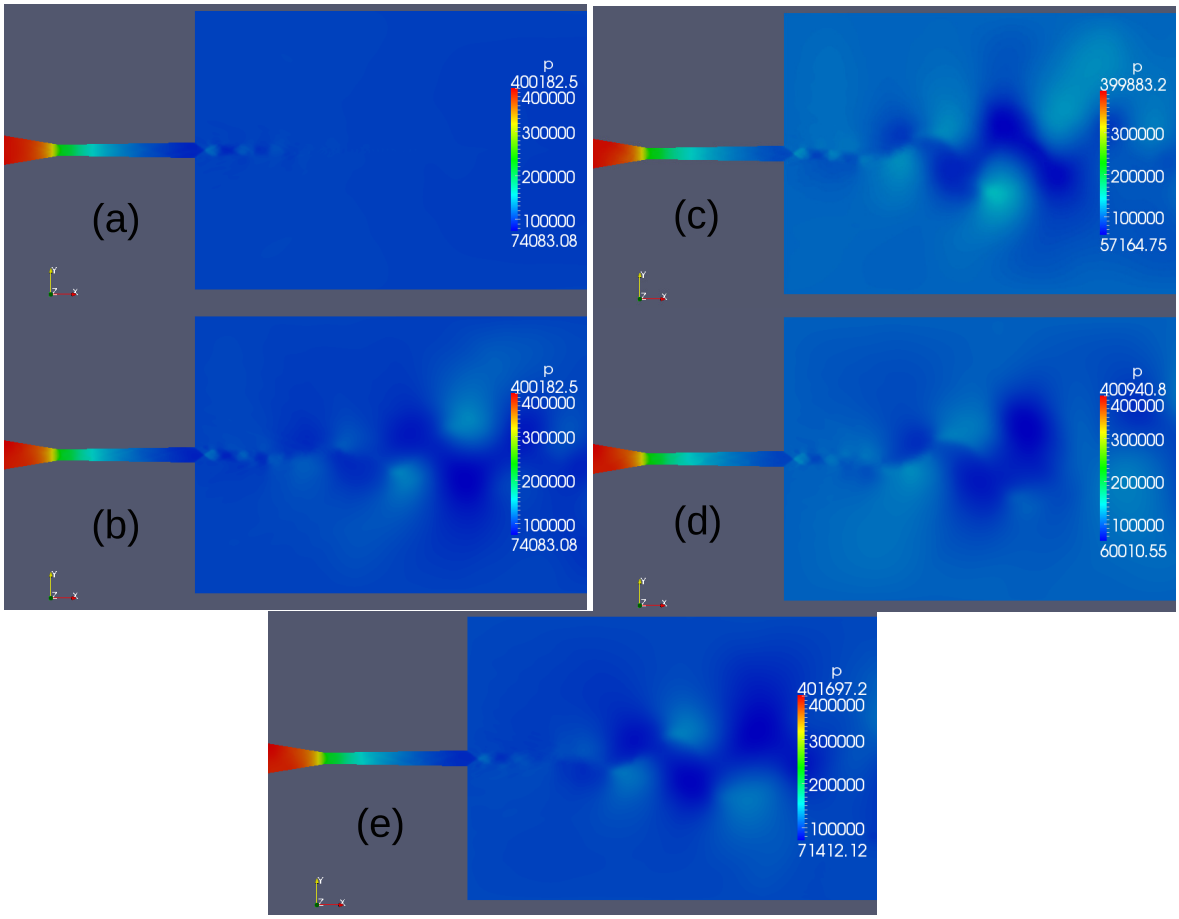

Figure 5.35: Pressure contours for complete domain simulations of the nozzle without helical insert for inlet pressure 400kPa (a)t=0.0048s (b)t=0.0147s (c)t=0.0166s (d)t=0.0226s (e)t=0.0259s

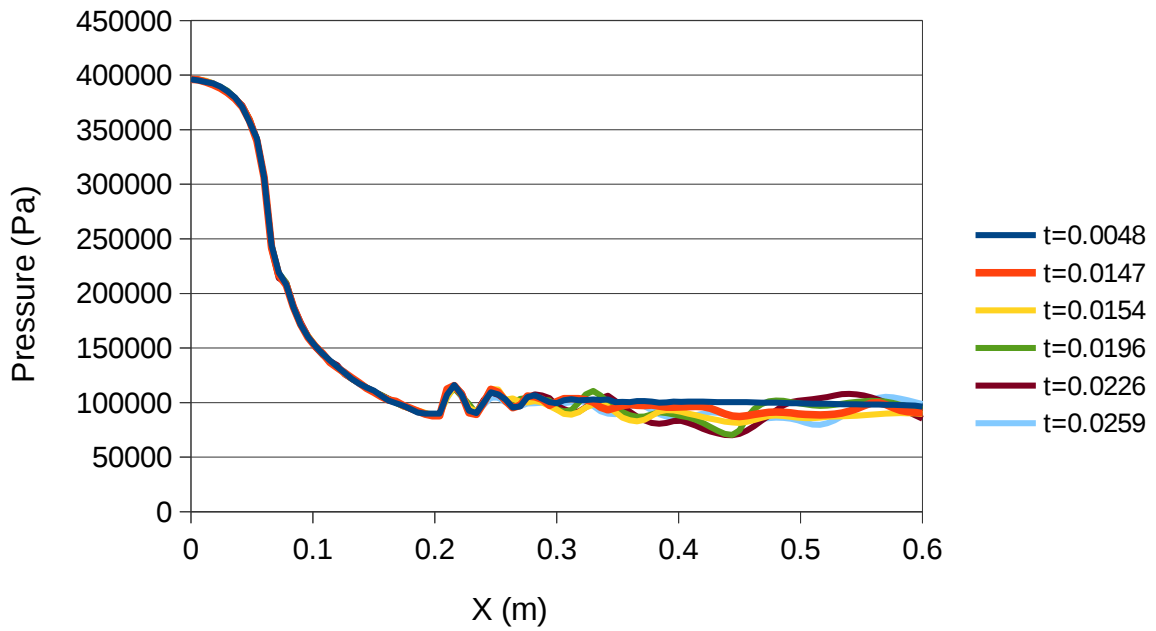

Figure 5.36: Pressure diagram along centre of the nozzle without helical insert for inlet pressure 400kPa.

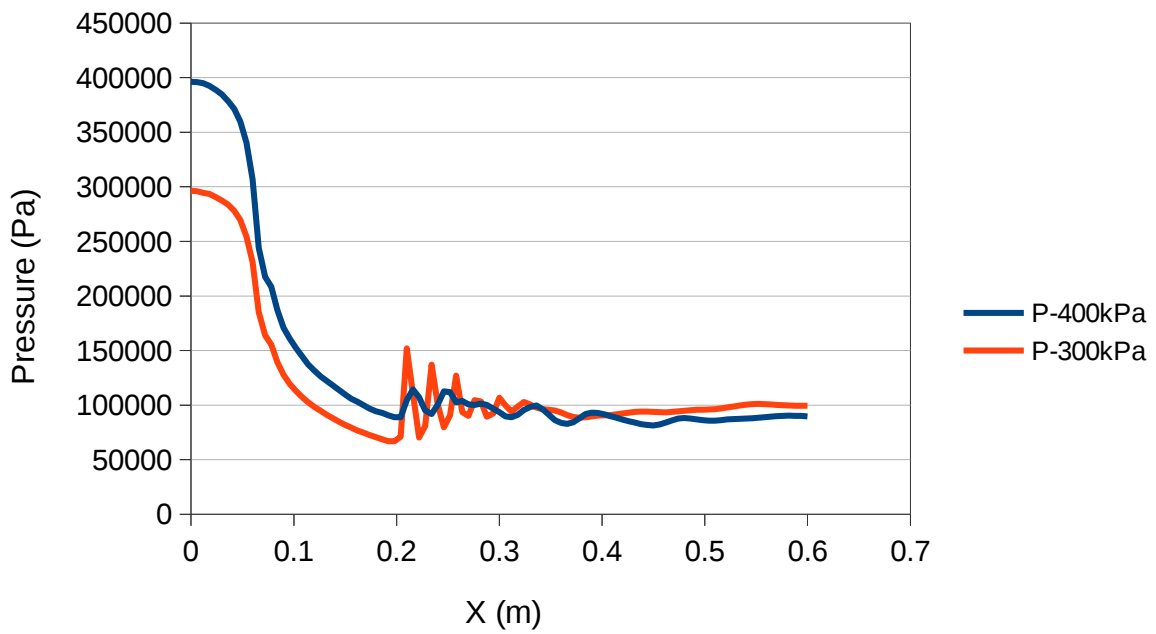

Figure 5.37: Pressure diagram along centre of the nozzle for inlet pressure 300kPa at t=0.0426s and inlet pressure 400kPa at t=0.0154

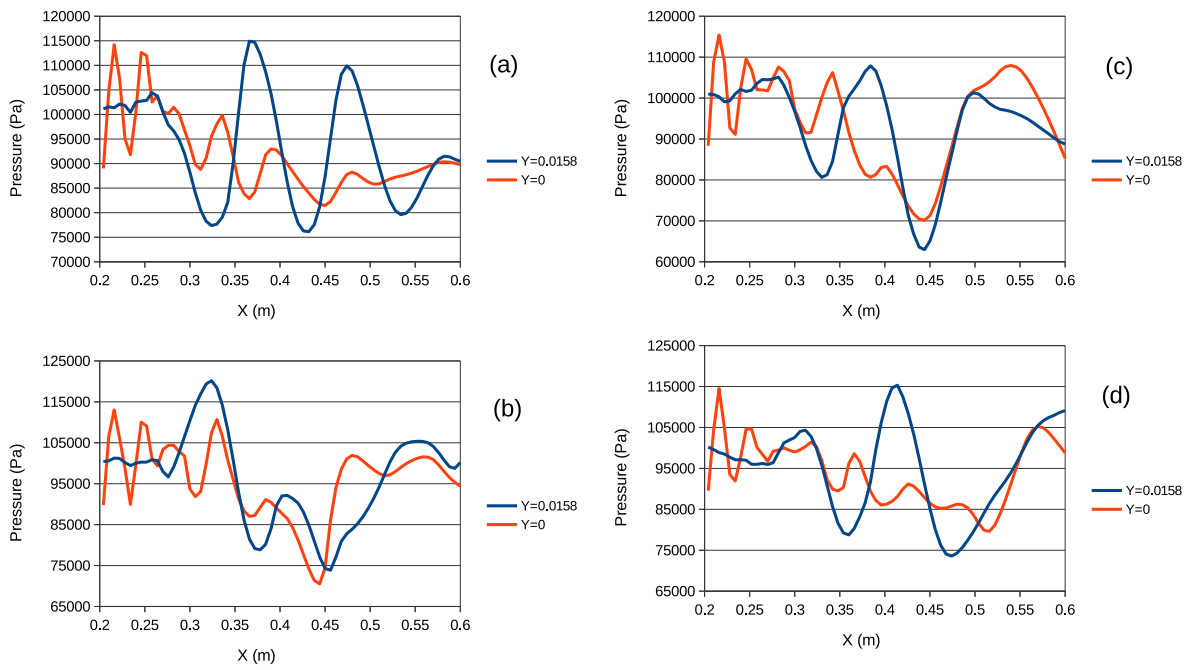

Figure 5.38: Pressure diagram along two lines at exit domain for the nozzle without helical insert for inlet pressure 400kPa at (a)t=0.0154s (b)t=0.0196 (c)t=0.0226s (d)t=0.0259s.

for all time steps are very similar. However, after the shock cells, there will be stronger pressure fluctuations along $Y = 0.0158m$. In general the amplitude and wave length of pressure fluctuations are higher inside domain compare to shock cells area.

Temperature contours for inlet pressure 400kPa are illustrated in Figure 5.39. The initial temperature has been considered as 300K. Although there is a massive temperature drop on the exit flow but the the domain will not effect that much. Temperature contours clearly represents the turbulence and instabilities on free jet boundary. As explained before for all time steps, instabilities on free jet boundary have not changed the shock cells structure.

5.2.1.6 Mass flow rate

In conditions where the exit pressure is reduced while the inlet pressure is fixed, a nozzle will be choked as soon as the flow at the throat reaches to Mach 1. In all discussed pressures above, the flow velocity on the throat is at sonic point and therefore for a given inlet pressure have reached to it's maximum mass flow rate (Choked). Although the nozzle is choked for a given inlet pressure and temperature, but the mass flow rate increases by increasing inlet pressure. Mass flow rate and pressure ratio (P_{in}/P_{out}) for different inlet pressures are illustrated in Table 5.4.

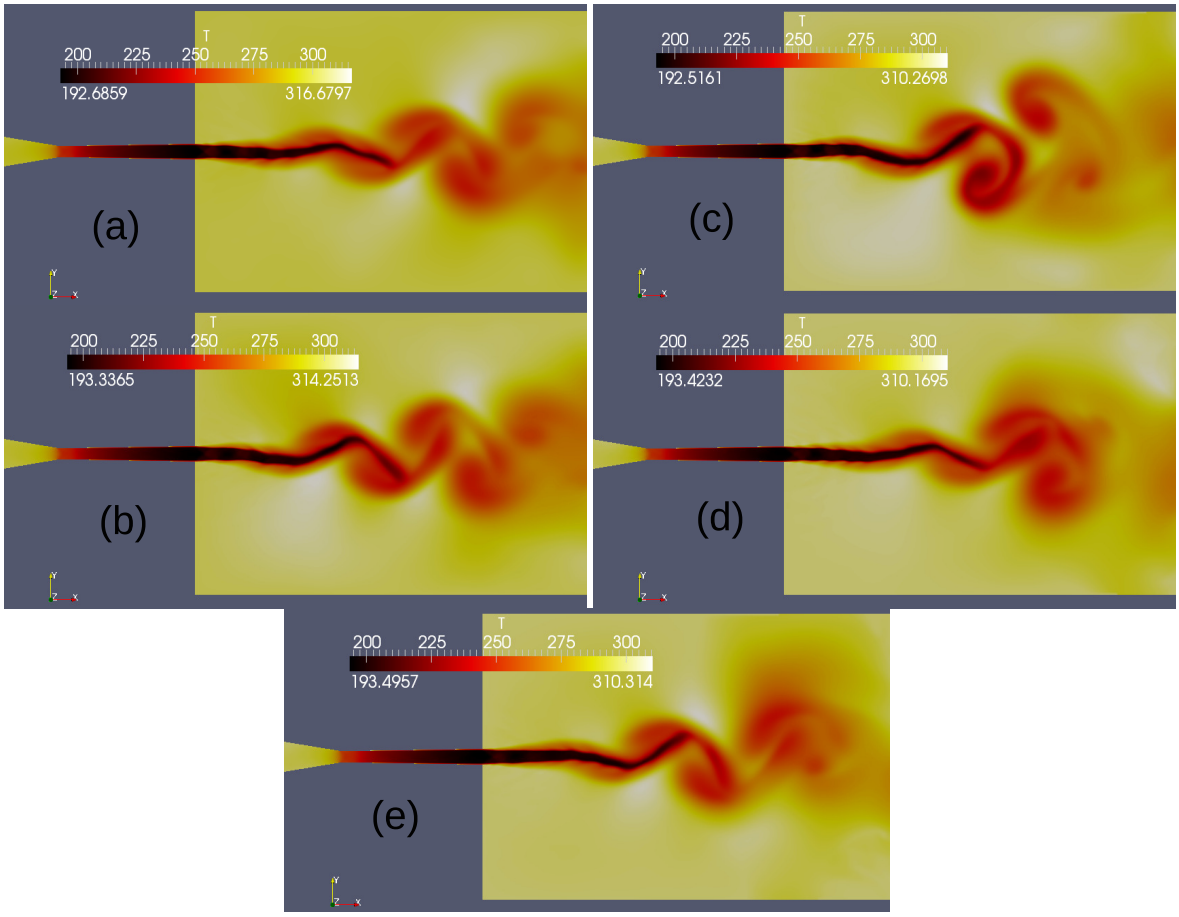

Figure 5.39: Temperature contours for complete domain simulations of the nozzle without helical insert for inlet pressure 400kPa (a)t=0.0147s (b)t=0.0154s (c)t=0.0214s (d)t=0.0244s (e)t=0.0259s

Table 5.4: Mass flow rate and PR for the nozzle without helical insert (2D simulations).

Inlet pressure	190kPa	200kPa	250kPa	300kPa	400kPa
Mass flow rate (kg/s)**	0.0097238	0.010231	0.0128309	0.0154477	0.0208115
Pressure ratio (P_{in}/P_{out})	1.9	2.0	2.42	4.39	4.49

** These numbers are for 2D simulations and they are not comparable to 3D simulations.

The mass flow rate in a choked nozzle will be fixed and independent of downstream conditions when upstream pressure, temperature and hence the density of a gas are fixed. This research proves that increasing the inlet pressure even in a choked nozzle will lead to increase in mass flow rate. Mass flow rate diagram for studying pressures is sketched in Figure 5.40. For first three inlet pressures (190kPa, 200kPa and 250kPa) where the shock cells start from inside of the nozzle, the mass flow rate is increasing with the constant rate. At pressure 270kPa and 300kPa where all shock cells are out of the nozzle the rate of increase of mass flow rate will be reduced. By increasing the inlet pressure to 400kPa, where the shock cells are weaker and start to lose the diamond shape the mass flow rate has increased with highest rate compare to lower pressures.

Based on this study there are three stages on mass flow rate behaviour with increase of the inlet pressure:

I. As far as a nozzle is operating at pressure ratios below its design point, where first shock cell starts from inside of the nozzle.

II. When the first shock cell is out of the nozzle.

III. Since shock cells become weaker and loose diamond shape.

5.2.2 With helical insert

This section covers the full domain simulation of the nozzle with helical insert. In order to better understand the structure of swirling supersonic flow, it is crucial to perform full domain simulations.

The domain and geometry is illustrated in Figure 5.41. For this problem snappyHexMesh (explained in 3.2.1.1) has been used to create the unstructured hexagonal mesh. Total length of the domain in X, Y and Z direction are 0.576m, 0.2m and 0.2m respectively. 4 million cells are generated with emphasis for refining mesh in areas close to the wall for proper y^+ values.

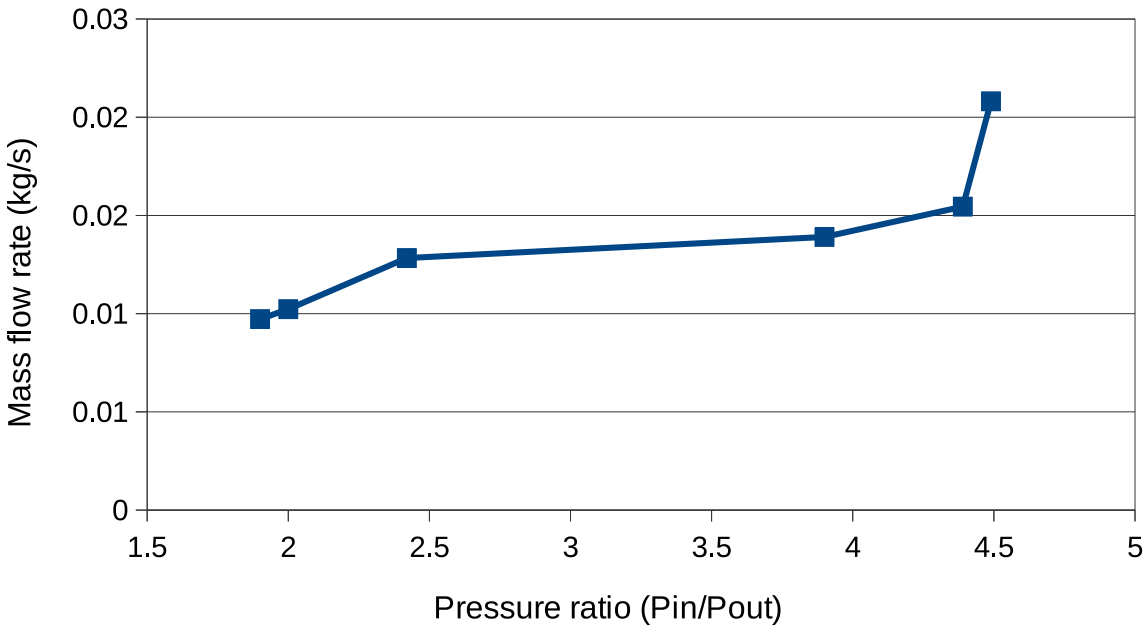

Figure 5.40: Mass flow rate diagram for the nozzle without helical insert (2D simulations).

Same as inside nozzle simulations, pressure based transient solver, *sonicFoam,* has been adopted with realizable $k-\varepsilon$ turbulence model to solve numerical equations. Boundary conditions are similar to full domain simulations without helical insert (Table 5.3). Discretisation method for momentum equation and ε is vanLeer, for k is upwind and limited linear for other divergence schemes.

Due to the large number of mesh and resource limitations, it was impossible to perform full domain swirling flow simulation at all pressure ranges same as the previous sections. Therefore, simulations are performed at two inlet pressures: 200kPa and 300kPa.

5.2.2.1 Inlet pressure 200kPa

Mach number contour at inlet pressure 200kPa is shown in Figure 5.42. The maximum velocity has increased from Mach 1.55 for non swirl condition (Figure 5.23) to Mach 1.76. This shows 13 percent increase on velocity which is consequence of increase in turbulence inside flow. Figure 5.43 demonstrates turbulence kinetic energy for the nozzle with and without helical insert and it is obvious that kinetic energy is higher in the nozzle with helical insert. Separation zone with swirling flow is different compared to non swirl condition. The FSS region on lower wall is much larger in the nozzle with helical insert although RSS region is smaller on upper wall. Greater separation zone will provide better mixing feature and thus will

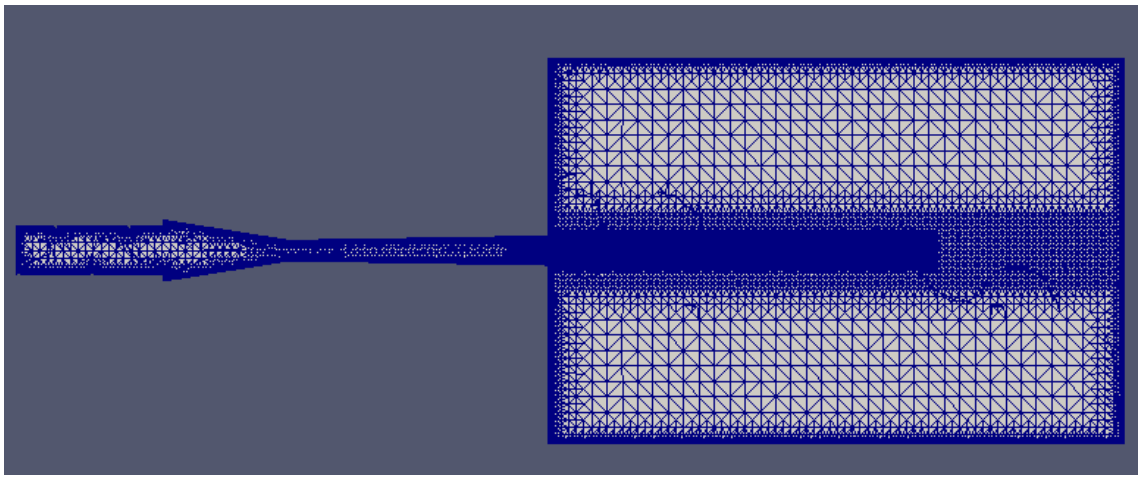

Figure 5.41: Geometry and mesh for complete domain of the nozzle with helical insert.

improve sand blasting performance. Other major difference is that unlike the nozzle without helical insert, the distinctive shape of shock cells are not visible in the nozzle with swirl flow, which is mainly due to weakness of shock cells.

The velocity outlet profile is plotted in Figure 5.44. Even though the tangential velocity has been increased as a result of helical insert, but there is not a major loss on the axial velocity at the outlet. It is clear that the size of separation zone for the swirl flow is much larger; Therefore mixing features of the flow will improve and provides better particle distribution.

Figure 5.45 plots the pressure along centre of the nozzle. As the flow inside the nozzle with helical insert has higher maximum velocity, thus there is more pressure drop in diverging section. After the shock flow goes through small expansion fan and then the pressure gradually increases till reaches atmospheric pressure at the outlet. However, for the nozzle without helical insert the flow after the main shock goes through series of small shock waves and expansion fans to reach ambient pressure.

Figure 5.46 plots central pressure after the outlet. At the beginning two diagrams, for swirl and non-swirl flow, are matching each other; But shortly after that pressure for the nozzle without helical insert are fluctuating with higher amplitude which shows there are some small shock cells at the outside of the nozzle. For the nozzle with helical insert, pressure fluctuations will damp much quicker, where in the length of six outlet diameters there won't be any pressure fluctuations inside the domain. Therefore swirl effect helps to reduce resistance at the exit of the nozzle and have particles with higher velocity that are impacting on the surface.

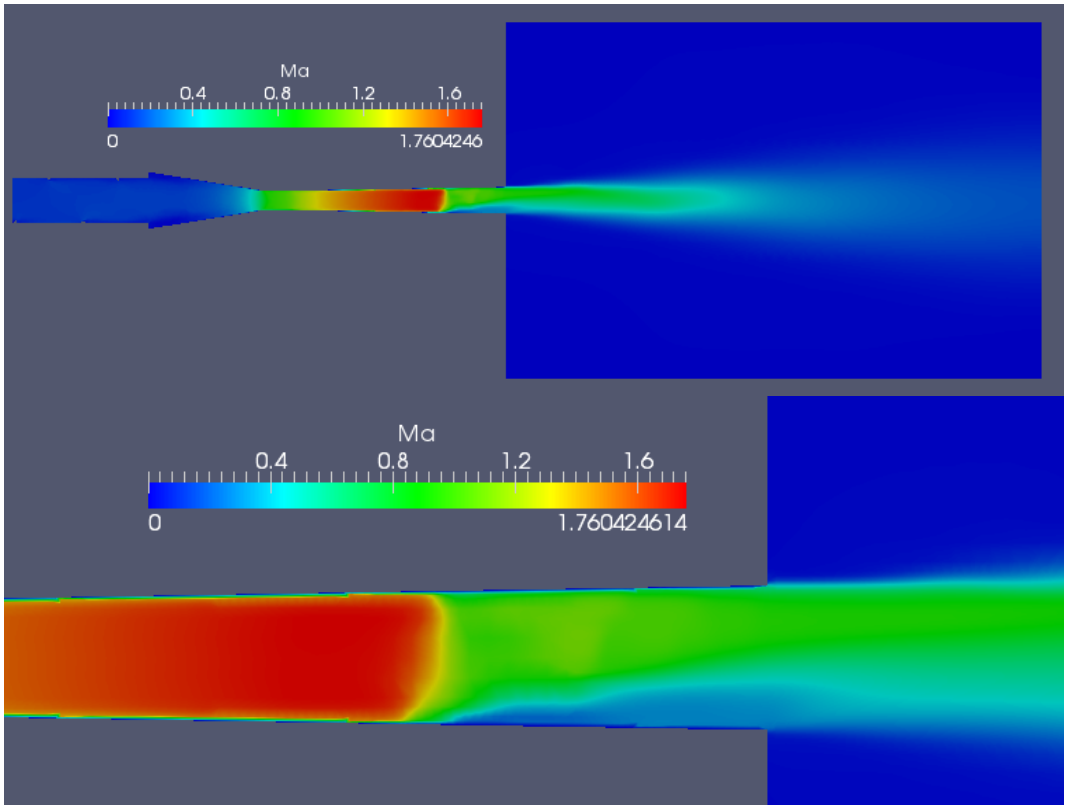

Figure 5.42: Mach number contours for complete domain simulations of the nozzle with helical insert at inlet pressure 200kPa.

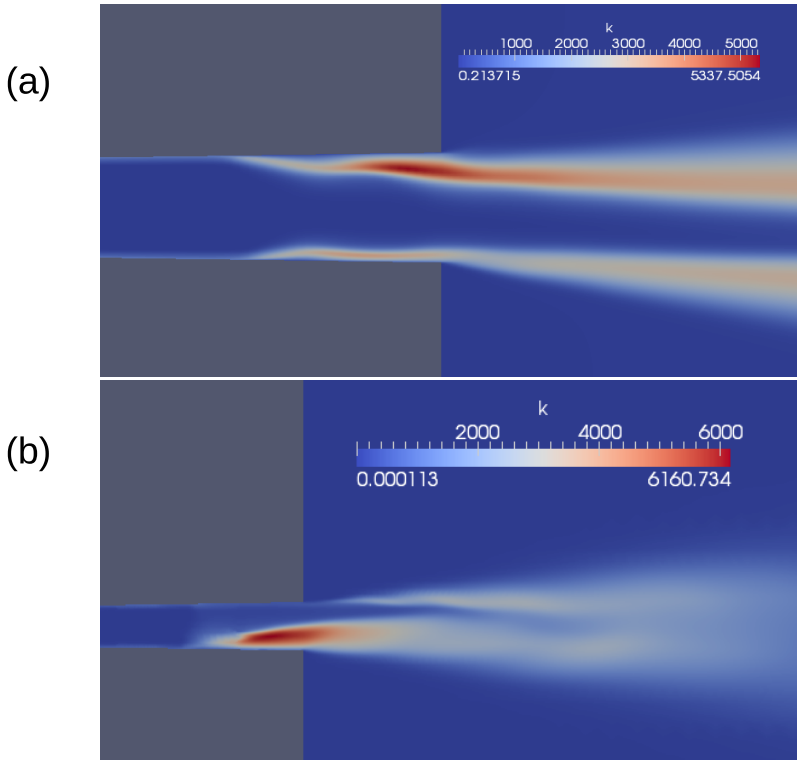

Figure 5.43: Turbulence kinetic energy (k) for the nozzle (a) without helical insert (b) with helical insert.

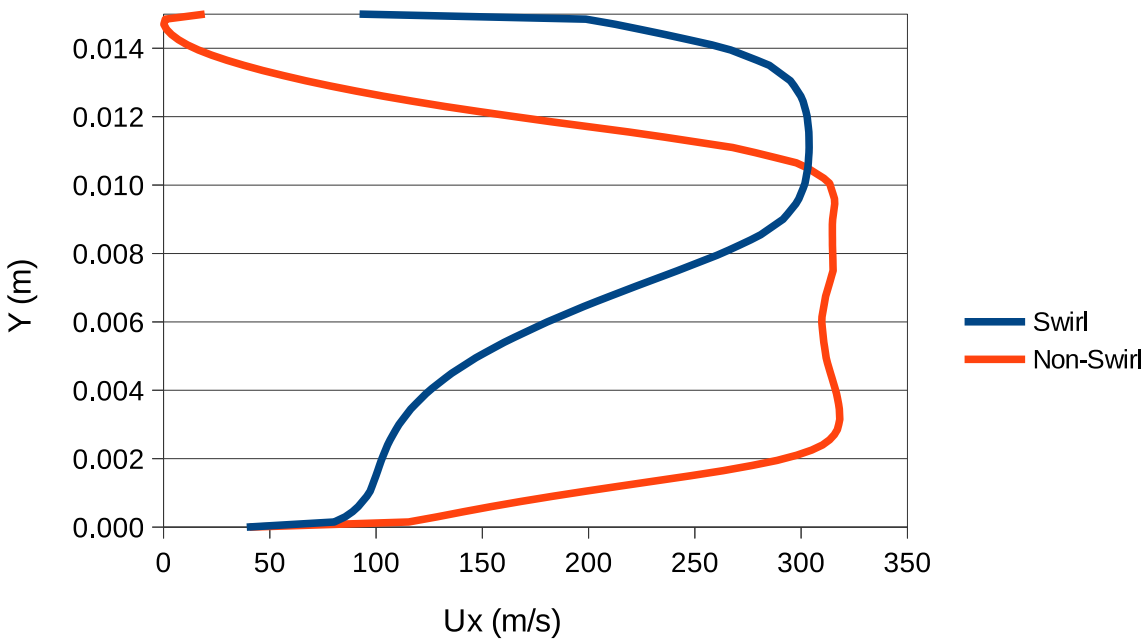

Figure 5.44: Velocity outlet profile at inlet pressure 200kPa.

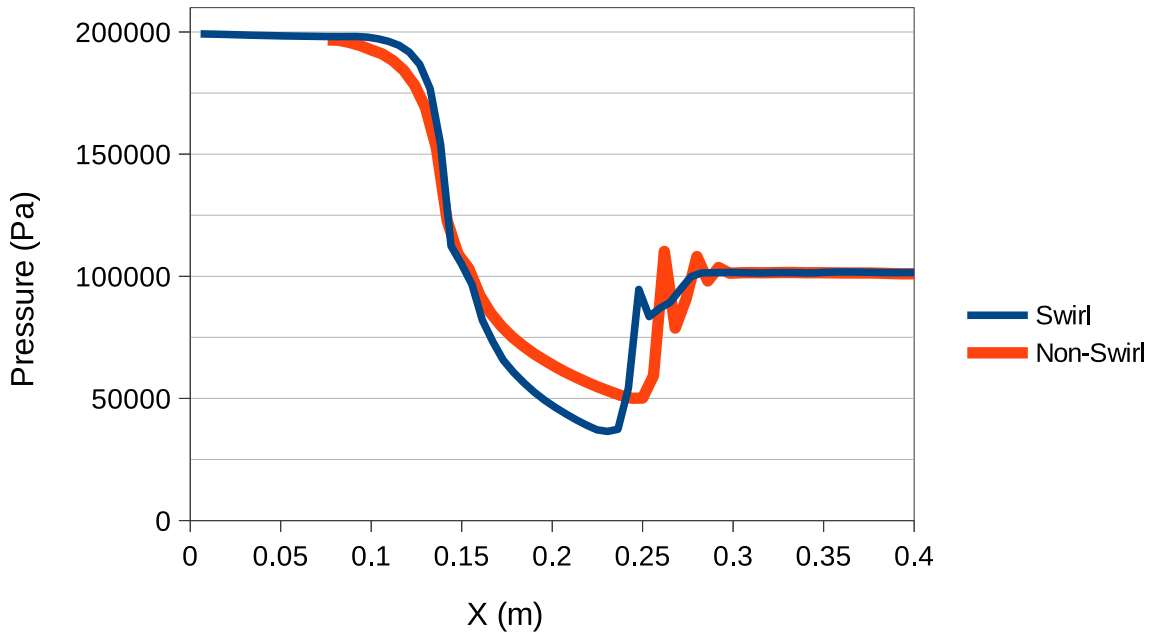

Figure 5.45: Pressure diagram along centre of the nozzle with helical insert at inlet pressure 200kPa.

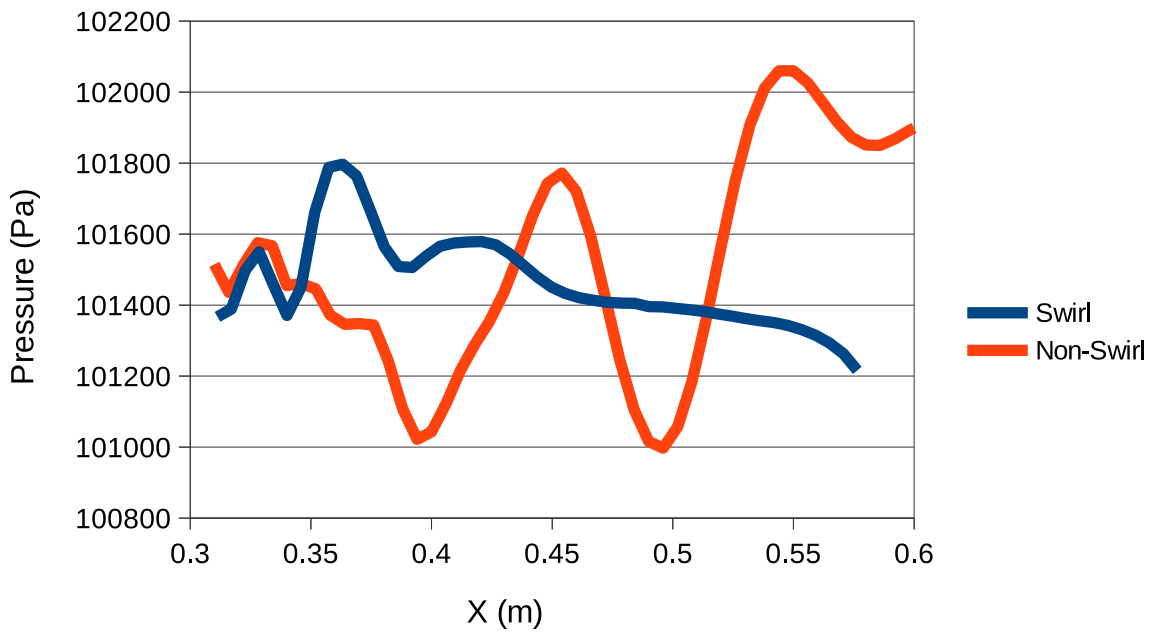

Figure 5.46: Pressure along centre of the domain from outlet of the nozzle with helical insert at inlet pressure 200kPa.

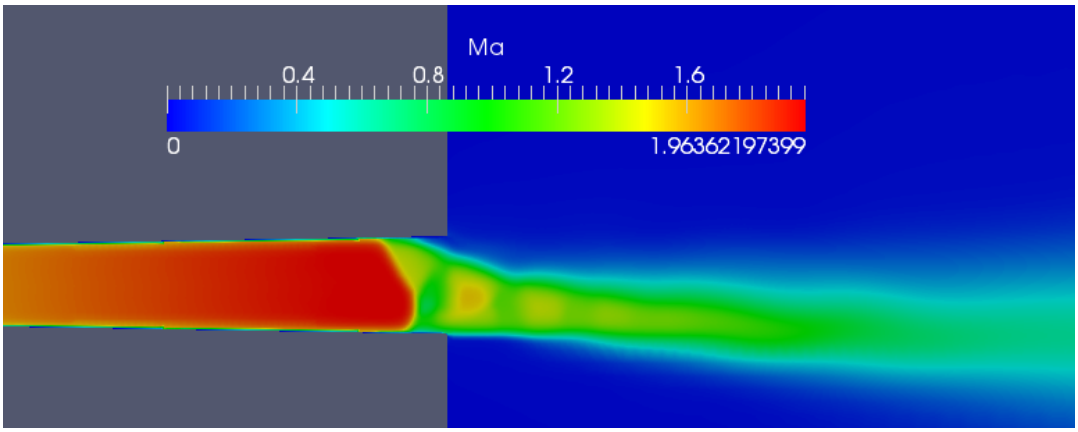

Figure 5.47: Mach number contours for complete domain simulations of the nozzle with helical insert at inlet pressure 300kPa, t=0.0065s.

5.2.2.2 Inlet pressure 300kPa

For inlet pressure 300kPa with helical insert the separation zone is larger. The size of separation zone and consequently angle of the jet increases as time steps are increasing. This is due to larger lambda feet in shock wave inside the nozzle that creates greater adverse pressure gradient. Figure 5.47 shows Mach number contours at t=0.0065s and Figure 5.48 illustrates Mach number contours at t=0.04s. Compared to non swirl situation (Figure 5.27), the maximum Mach number has increased from 1.65 to 1.96, which shows 18% increase as a result of more momentum inside the nozzle. In contrast to non swirl condition, where there were instabilities on jet boundary, with helical attachment although creates a larger separation zone but simulations did not show any instabilities even after many time steps.

Turbulence kinetic energy for the nozzle without helical attachment is shown in Figure 5.49. In non swirl condition the kinetic energy is more toward downstream due to instabilities on the jet. However, with swirl condition (Figure 5.50) maximum turbulence kinetic energy happens at the outlet of the nozzle and kinetic energy reduces by moving toward downstream. Therefore the swirl effect could be helpful on providing maximum mixing feature, before surface working area.

Velocity profile at the exit of the nozzle is plotted in Figure 5.51. The difference between the maximum velocity of swirl and non-swirl conditions has dropped significantly in compare to inlet pressure 200kPa; However the region that covers maximum velocity is greater in inlet pressure 300kPa. This shows that at higher inlet pressures, the swirl effect is toward the nozzle's wall and at the centre (core) is more non swirl flow, hence there is greater core zone with higher velocity.

Pressure diagram along the centre of the nozzle is illustrated in Figure 5.52. In converging

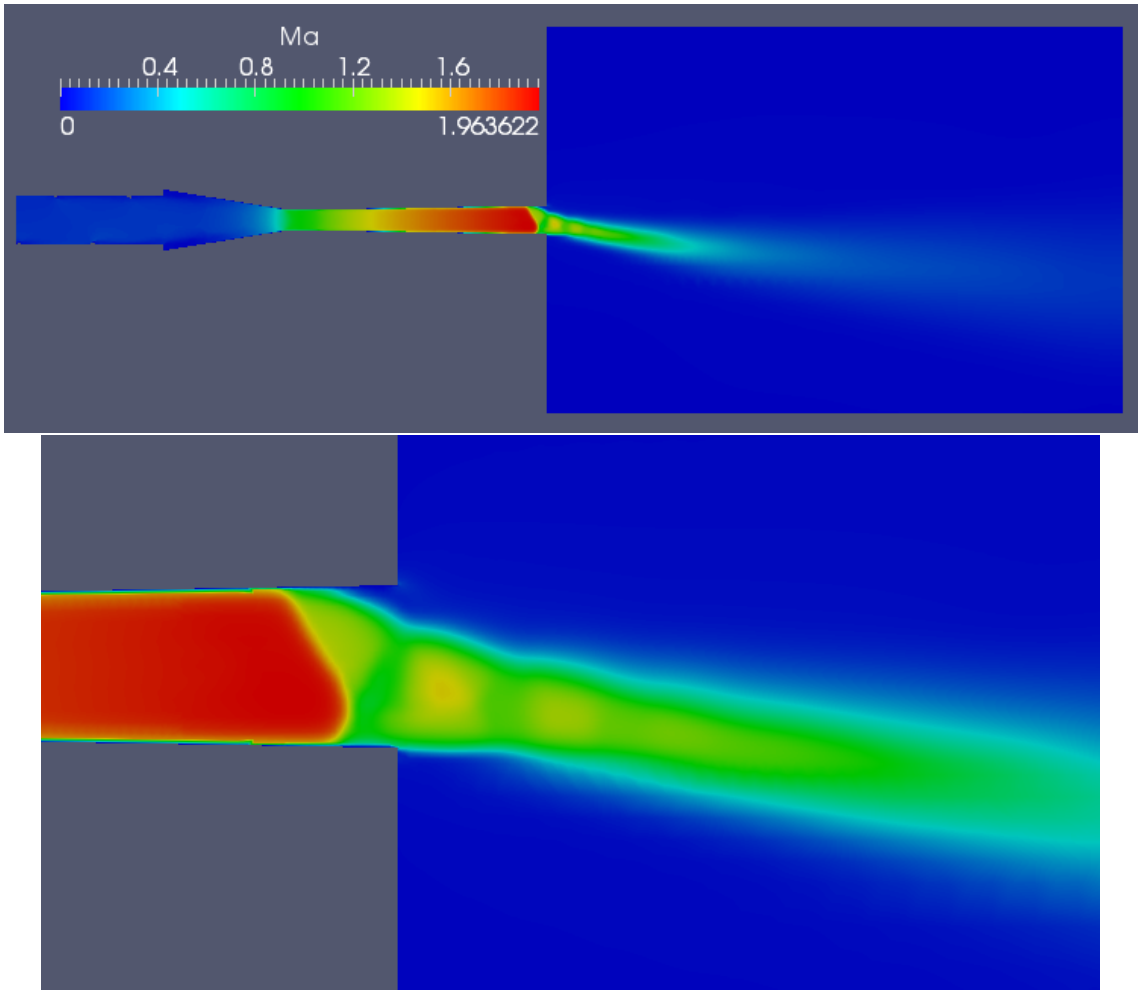

Figure 5.48: Mach number contours for complete domain simulations of the nozzle with helical insert at inlet pressure 300kPa, t=0.04s.

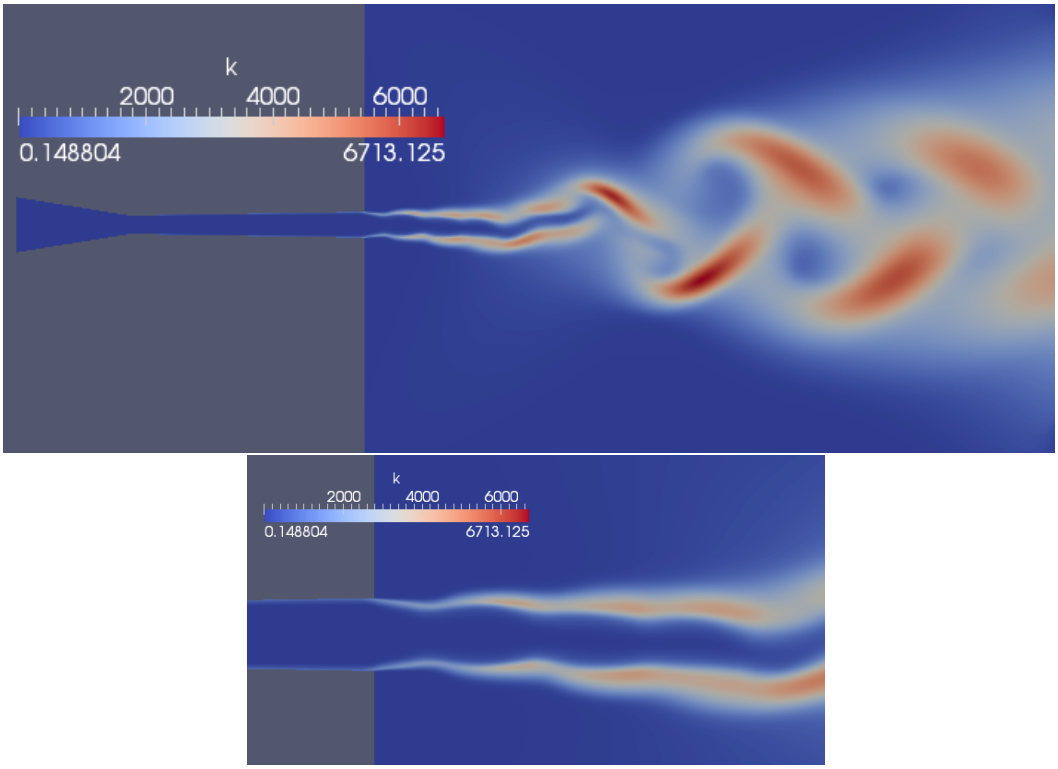

Figure 5.49: Turbulence kinetic energy (k) for the nozzle without helical insert at inlet pressure 300kPa. The lower image is zoomed at exit of the nozzle.

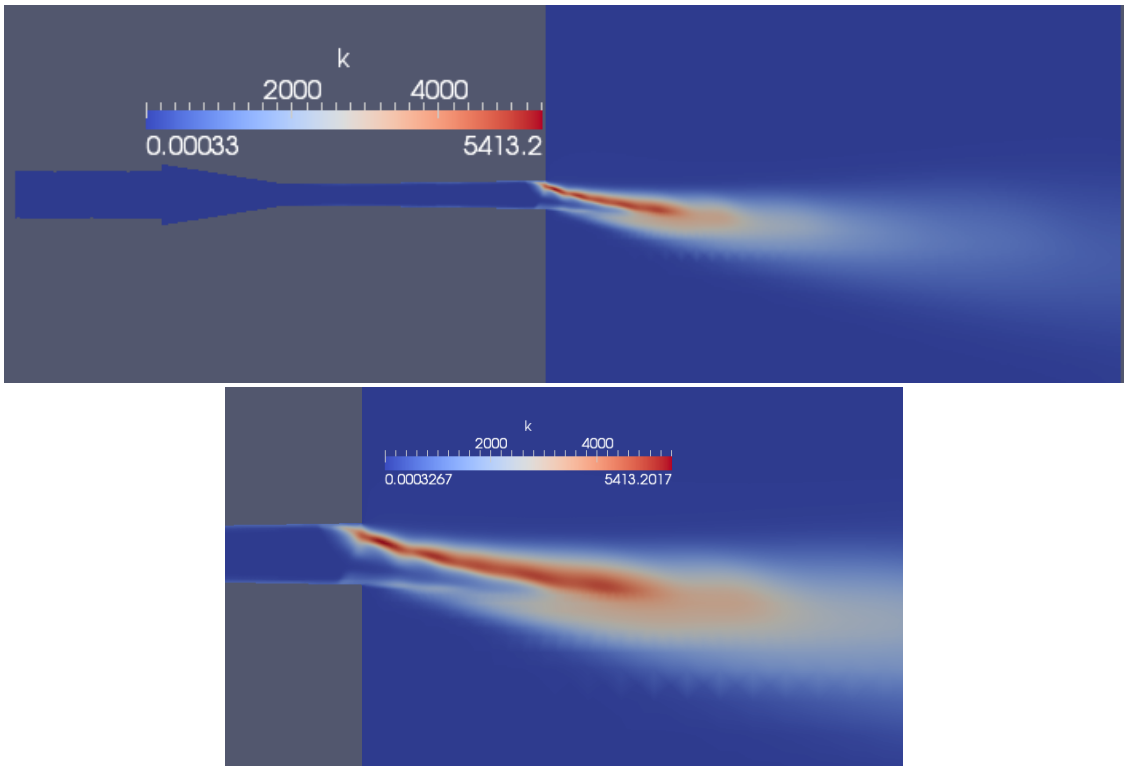

Figure 5.50: Turbulence kinetic energy (k) for the nozzle with helical insert at inlet pressure 300kPa. The lower image is zoomed at exit of the nozzle.

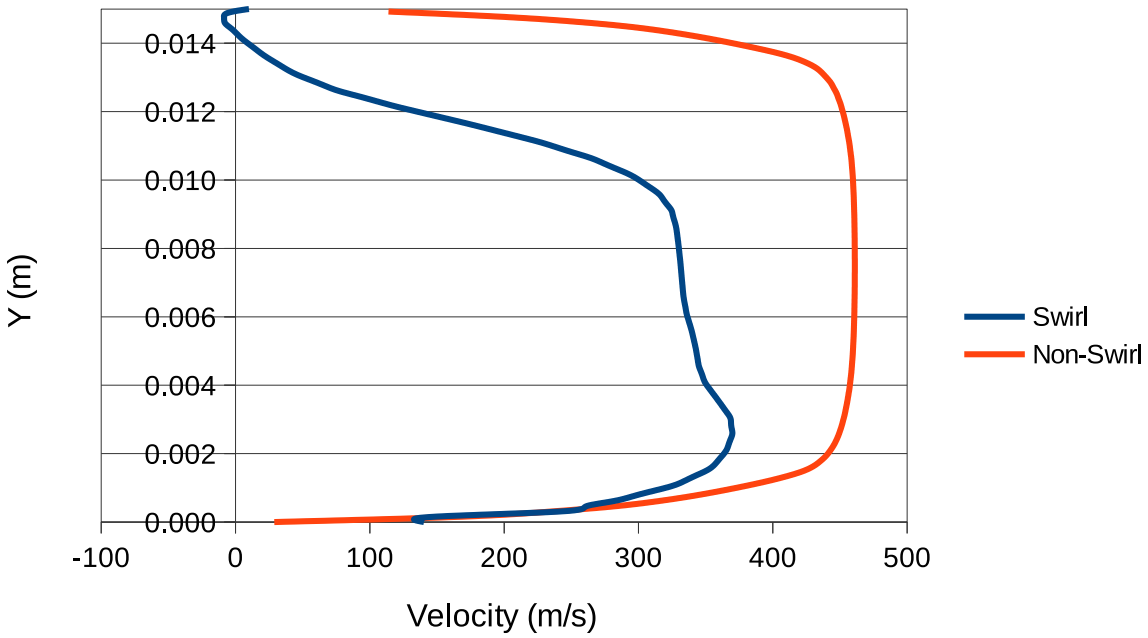

Figure 5.51: Velocity outlet profile for inlet pressure 300kPa.

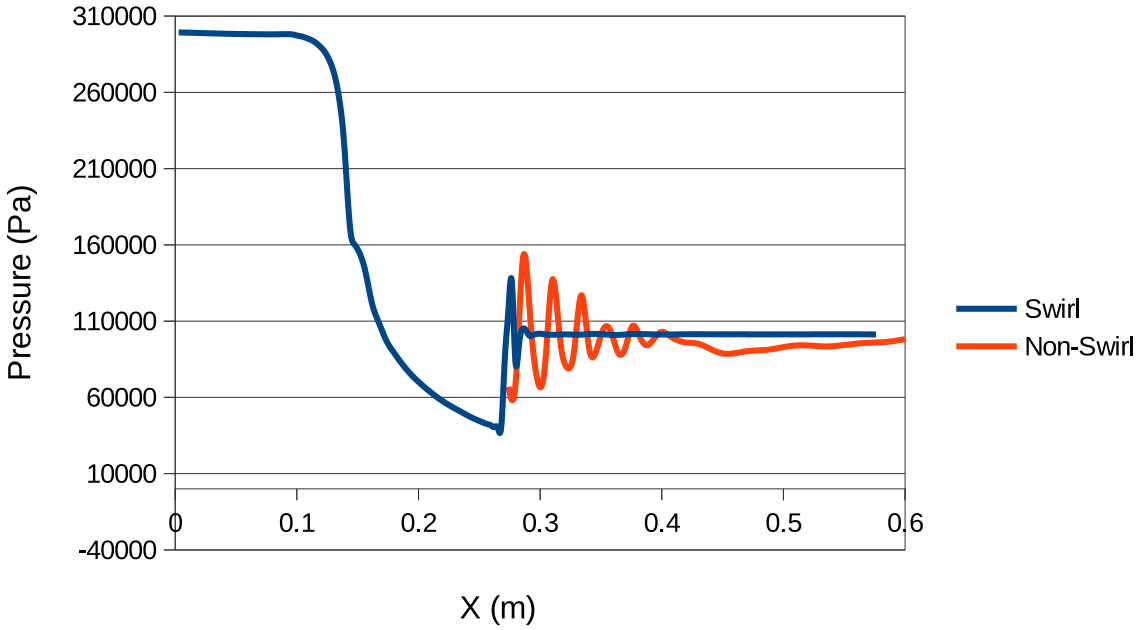

Figure 5.52: Pressure diagram along centre of the nozzle with helical insert at inlet pressure 300kPa.

section, for both swirl and non-swirl conditions, the pressure drops at the same rate up to the throat. After the throat, the pressure for swirl condition drops faster and goes well below atmospheric pressure. Figure 5.53 represents the centre line pressure from the outlet up to far end downstream. It can be seen that the pressure damps quickly and there is not any pressure fluctuation after shock cells. As the jet was angled due to separation, therefore pressure diagram from outlet was plotted along shock cells (line 1-2) as well (Figure 5.54). Although there are extra few weak shock cells but still shock waves damp quickly and has not shown any major fluctuations along the jet.

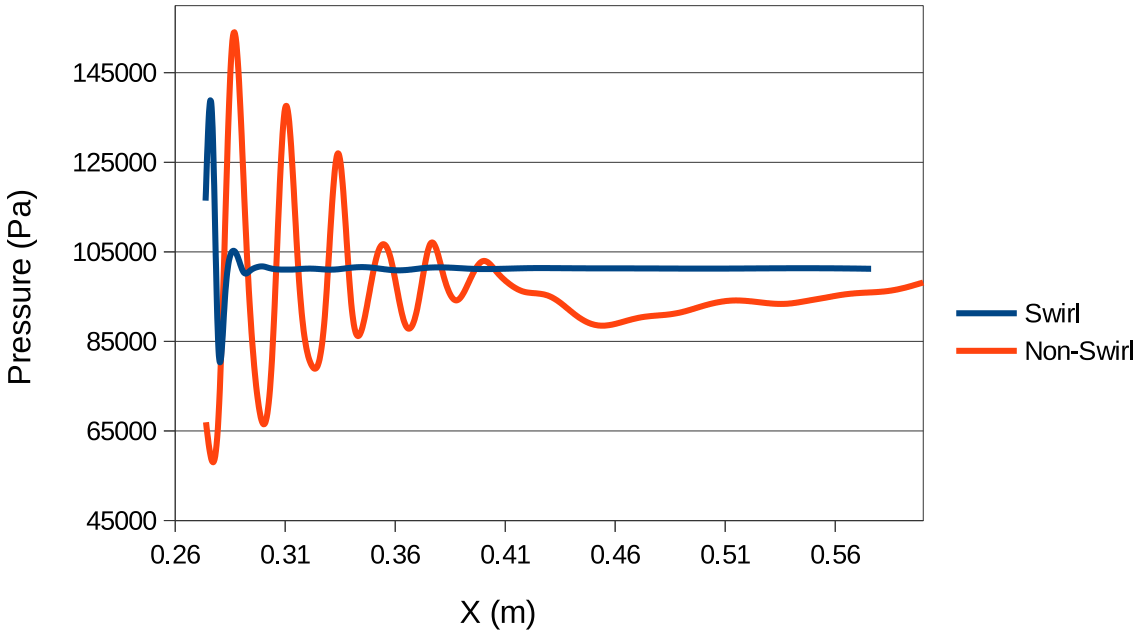

Figure 5.53: Pressure along centre of the domain from outlet of the nozzle with helical insert (line 1-1) at inlet pressure 300kPa.

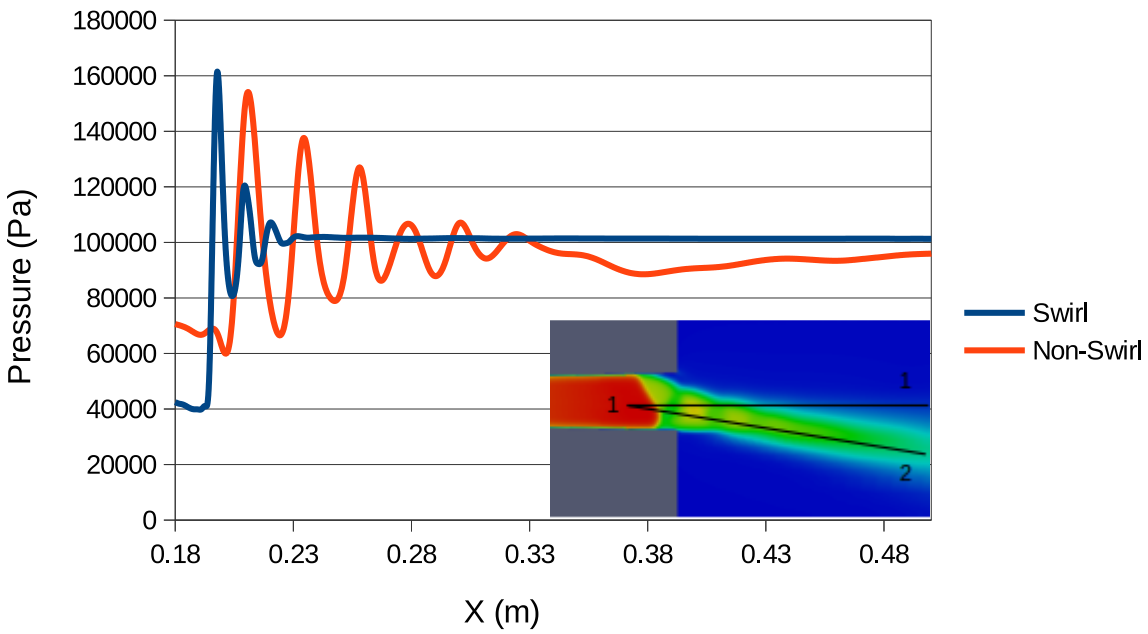

Figure 5.54: Pressure along shock cells from outlet of the nozzle with helical insert (line 1-2) at inlet pressure 300kPa.

Chapter 6

Verification and Validation (V&V)

The use of Computational Fluid Dynamic (CFD) for complex geometries and physics where conducting full scale experiments are either expensive or impossible, makes estimating error and uncertainty a crucial part of any numerical procedure. Recent research and studies have lead to detail methodology (Roache, 1998) and certain level of maturity in CFD verification and validation.

The purpose of Verification and Validation (V&V) are to evaluate accuracy and reliability of computational simulations. Verification and Validation (V&V) are the primary method to build confidence on numerical results. Verification is to assess the accuracy of the numerical solution by comparing it with known solution. In verification the relation of computational solution to the real world is not an issue. In validation the accuracy is assessed by comparing simulation with experimental data or real world solution.

One of the first famous diagrams about V&V was introduced by Schlesinger *et al.* (1979) (Figure 6.1). In this diagram conceptual model includes all data, mathematical equations and mathematical modelling data which describe physical system. In CFD, the conceptual model is composed of PDEs for conservation of mass, momentum and energy; Also includes all of the auxiliary equations related to turbulence, initial conditions and boundary conditions where each described in detail in Chapter 3. The computerized model is a computer programme or code that uses the conceptual model for modelling and simulation.

Different organizations have different definitions for V&V, but the AIAA definitions is the most accepted by CFD community and represents Figure 6.1, are described as follows (AIAA, 1998)

> Verification: The process of determining that a model implementation accurately represents the developer's conceptual description of the model and the solution to the model.

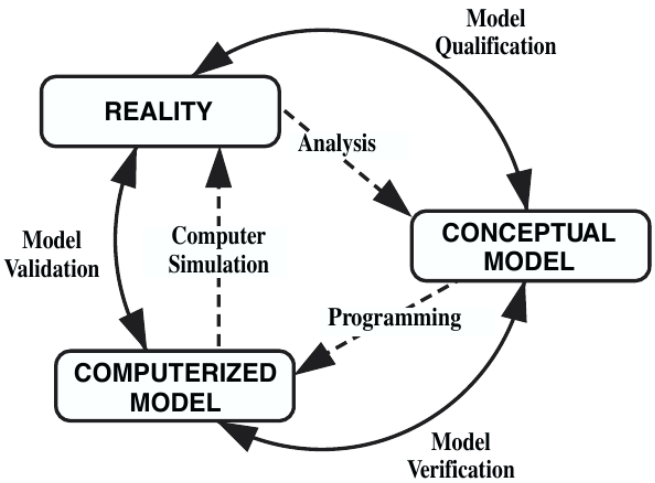

Figure 6.1: The Verification and Validation (V&V) role on computational simulation (Schlesinger *et al.*, 1979)

> Validation: The process of determining the degree to which a model is an accurate representation of the real world from the perspective of the intended uses of the model.

Verification proves that the conceptual model (governing equations and PDEs) is solved correctly by CFD software, but does not provide any relation between the solution and the real world. However, validation provides evidence on how accurately a CFD solution represents reality. Therefore, verification is the first step to validate CFD solutions, and at the final stage the solutions are compared to experiment (Oberkampf and Trucano, 2002).

6.1 Verification

Verification is not a physical issue, is mathematical and computer science issue (Roache, 1998). For most of CFD codes the main source of numerical errors and uncertainty are due to insufficient spatial and time step discretisation, computer round off, programming errors and insufficient convergence of iterative solution algorithm (Stern *et al.*, 2001).

6.1.1 Code verification

The first step is code verification. If a code has an error, then grid convergence and other error estimation methods will not satisfy verification process (Roache, 1997). For this study two

software has been used Ansys Fluent[1] and OpenFOAM[2]. Ansys Fluent is a major commercial software in the filed of CFD and has been used for many different applications. The density based solver in Fluent that has been used for simulations in Chapter 4 is verified by different researches such as (Ansys, 2010; Jassim *et al.*, 2008; Liu and Bellhouse, 2005).

OpenFOAM is open source software that has been subject of many researches. The 'sonicFoam' solver that is used for this study (Chapter 5) has several validation cases. The study by ShockTube (2011a) and ShockTube (2011b) has proved that sonicFoam with $k-\omega$ and $k-\varepsilon$ turbulence models provide best results to capture normal and oblique shock waves; study by Khodadadi *et al.* (2013) also validates the shock capturing capability of 'sonicFoam' solver of OpenFOAM, although proves that density based solver *'rhoCentralFoam'* is also capable to capture shock waves.

6.1.2 Grid independence study

One of the most important parameters that affects the accuracy of the CFD solutions is the quality of numerical grid. Grid dependency tests have been conducted in all cases, where extra grid refinement has not changed the results. As mentioned by Ferziger and Perić (2002), it is important for the refinement to be substantial and systematic, as the systematic grid refinement studies are the most reliable and common studies (Roache, 1994). Systematic refinement means that the grid is refined in all directions with the same ratio. The number of cells that are used for simulations are explained in respected chapters. Although The power of new computers and parallel processing makes possible to run large cases with higher number of mesh in a shorter amount of time, but it should be noted that extra non-necessary refinement, will create artificial and implicit dissipation that will change governing PDEs (Roache, 1997; Shirazi and Truman, 1989). This issue could become more series in supersonic simulations where high order non-linear schemes (such as TVD) are required to capture shock waves accurately (Carpenter and Casper, 1999).

6.1.3 Y-plus distribution

For turbulence modelling spatial considerations are required for grid resolution near the wall. As explained in section 3.5.4 the y^+ values need to be in log-law region. For all simulations there were attention to keep the average y^+ values around 30. For example the y^+ diagram for

[1] Ansys Fluent v12, 13, 14.5 and 15 has been used.
[2] OpenFOAM 2.2.x has been used.

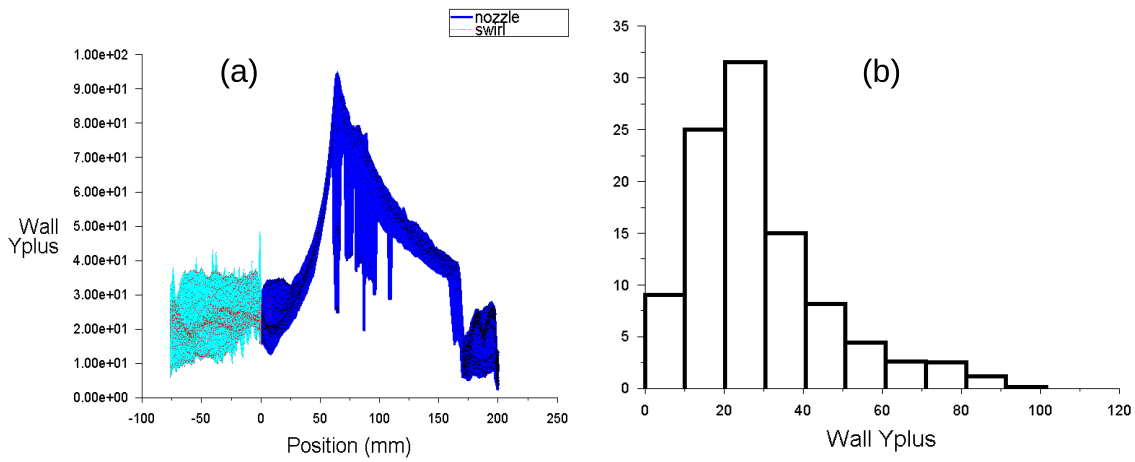

Figure 6.2: y^+ distribution for Fluent simulation inside of the nozzle with helical insert at inlet pressure 3atm.

Fluent simulations inside nozzle with helical insert at inlet pressure 3atm is shown in Figure 6.2.

6.1.4 Residual monitoring

Both explicit and implicit solvers use iterative process since the direct solution is very expensive. Therefore the convergence criteria is required to stop process. Studies by Axelsson (1996); Ferziger and Perić (2002) have suggested reliable criteria to determine iterative solution methods. For steady state simulations reaching to specific criteria is much simpler, actually a good convergence on steady computations indicate that no unsteady phenomena could be captured with transient solver (Xiao *et al.*, 2007). For this research, simulations have been continued up to five or six order of magnitude ($O(5)$) and on transient simulations (for both Fluent and OpenFOAM) there are at least 100 iterations per time step. For instance the residual monitoring for *sonicFoam* simulation of the nozzle with helical insert at inlet pressure 300kPa is illustrated in Figure 6.3, where due to transient effect and instabilities inside the domain the residuals will not converge more than five orders of magnitude.

Time step discretisation are equally important to get both stable and correct results. For compressible and supersonic flows, because the PDEs are usually in hyperbolic format (Lax, 1957) , hence it is necessary for explicit solver to keep Courant number (CFL) below 1 (Section 3.2.1). This has been achieved in all simulations since start point. For example, from residual monitoring shown in Figure 6.3, it can be seen that the CFL number have been kept well below 1.

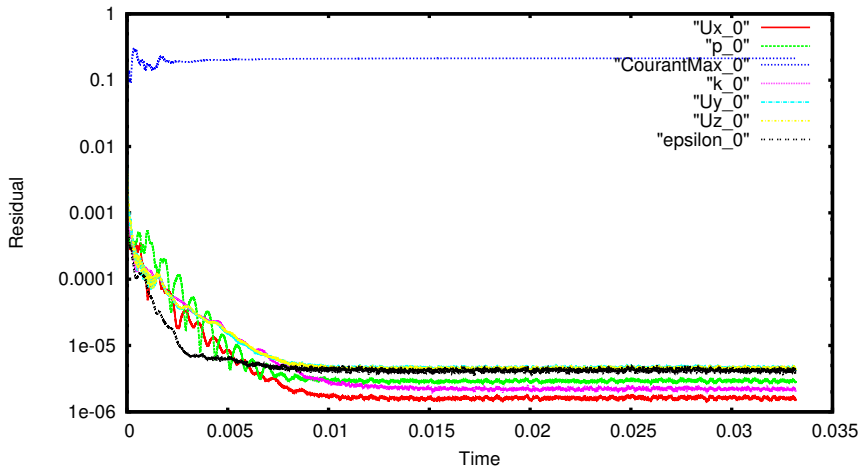

Figure 6.3: OpenFOAM (sonicFoam) residual monitoring for inside of the nozzle with helical insert at inlet pressure 200kPa.

6.2 Validation

Validation is a process to assess numerical modelling uncertainty by using benchmark experimental data, and when it is possible, estimating the sign and magnitude of numerical modelling error (Stern *et al.*, 2001). The fundamental strategy for validation is identification of the error and uncertainty in the conceptual model, quantification of the numerical error in the numerical solutions, prediction for experimental uncertainty, and finally comparison between simulation results and experimental data (Oberkampf and Trucano, 2002). However, due to the impracticality and the difficulty of performing exact validation experiments on complex systems, recommended method is to use small scale bench mark experiments (Marvin, 1995).

Because of the limitations on performing, in house, full scale experiment on the nozzle which is subject of this study, the benchmark experiment and simulation has been chosen to validate the numerical procedure. Experiments are based on research by Papamoschou and Zill (2004) and computational simulations are based on a study by Xiao *et al.* (2007). Both of these benchmark experiments and simulation, are performed on the same CD nozzle with exact similar geometry. Both cases are planar 2D converging-diverging nozzle with fixed area ratio (A_e/A_t) at 1.5 and the nozzle divergent angle is 3.89deg; Although the experiment by Papamoschou and Zill (2004) was conducted on the nozzle area ratio ranged from 1.0 to 1.5.

The computational domain is shown in Figure 6.4. The domain is 2D with the total number of 139650 cells. The full length of domain in the X direction is 0.55m and in Y direction is 0.215m. The numerical solution algorithm is same as what explained in Chapter 4 and 5. For OpenFOAM validation simulations realizable$k-\varepsilon$ model has been adopted and for Fluent

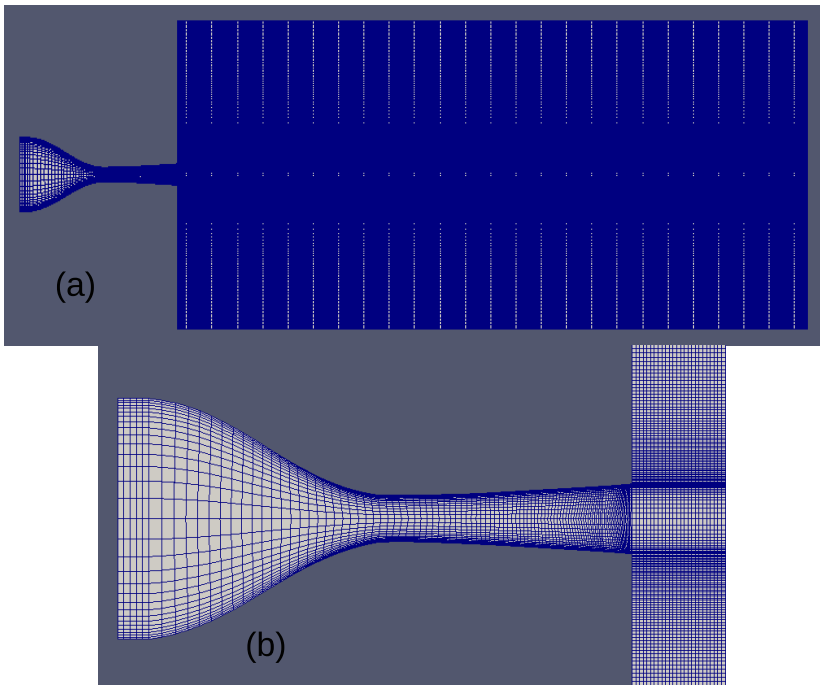

Figure 6.4: Computational domain and grid distribution by OpenFOAM for (a) Full domain (b) Zoom at the nozzle section.

simulations both $k-\omega$ and *RSM* model has been used where both models provided exact same results. Simulations by Xiao *et al.* (2007) also are based on two equation $k-\omega$ model.

6.2.1 Mach number contours and Schlieren photography

The research study by Papamoschou and Zill (2004) consisted of spark Schlieren photography of the internal and external flow, static pressure measurements along the centre of the nozzle, wall pressure measurements and recording of the acoustic sound in the vicinity of the nozzle exit. Figure 6.5 illustrates the comparison between Schlieren photography and OpenFOAM simulation for area ratio 1.5 and PR 1.5. Figures 6.5a & b are similar with slightly different illumination settings and field of view. Figure 6.5c shows the Mach number contours computed by OpenFOAM. The separation zones are almost identical with FSS region on one side and RSS at the other side causing the asymmetric flow pattern. Figure 6.5d is the contours of pressure gradient which shows more accurately the structure of asymmetric lambda shock and it is in good agreement with Schlieren photography. The side of separation and asymmetric shock (lambda feet) is not that important; Papamoschou and Zill (2004) has verified that the lambada feet chooses its orientation at the start-up of the run, but it will retain the same orientation throughout the run due to Coanda effect.

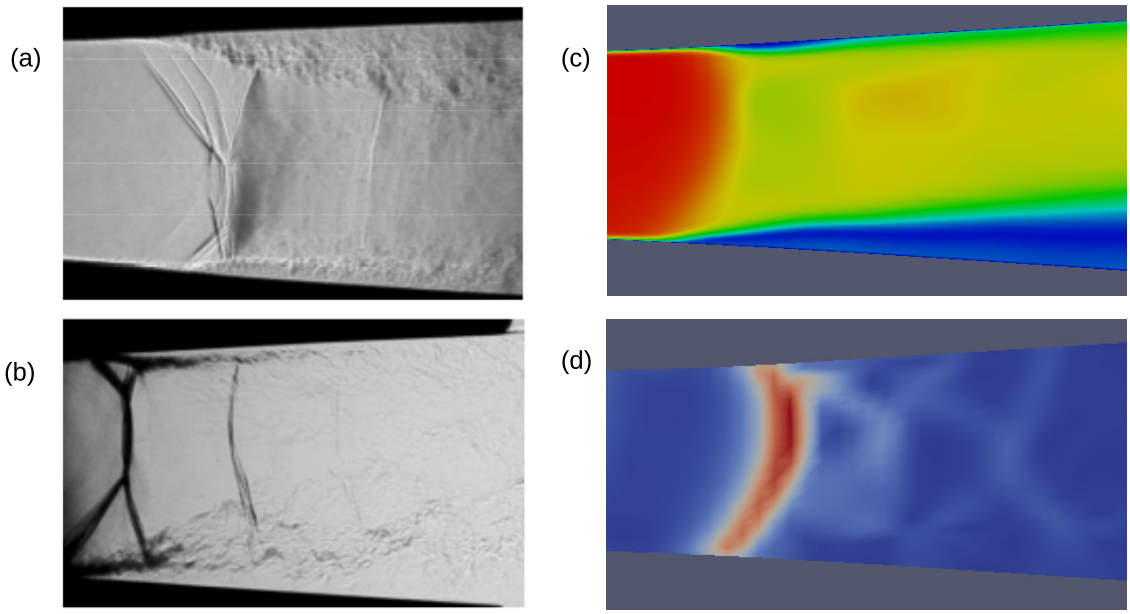

Figure 6.5: Shock and separated flow for $A_e/A_t = 1.5$ and PR=1.5 (a) & (b) are Schlieren photography with different illumination settings and field of view by Papamoschou and Zill (2004) (c) Mach number contours for OF simulations (d) ∇p contours for OF simulations.

Xiao *et al.* (2007) has studied the same planar 2D nozzle numerically. Similar to Xiao *et al.* (2007) the Fluent simulations are performed in steady state mode with density based solver. The Mach number contours for Fluent simulation at area ration (A_e/A_t) 1.5 and pressure ratio 2 is presented in Figure 6.6b. The Mach contours are compared with Xiao *et al.* (2007) computational results (Figure 6.6a). These two numerical models are identical in all aspects. As mentioned before both of $k-\omega$ and *RSM* turbulence models generated same results.

6.2.2 Shock wave location

The shock wave location versus pressure ratio is presented in Figure 6.7, in which OpenFOAM results are compared with experimental results of Papamoschou and Zill (2004), 1D inviscid theory and computations by Xiao *et al.* (2007). The term A_s refers to the area corresponding to the axial location of the Mach stem (normal shock) of the shock. Both of OpenFOAM and Fluent results (computation by Xiao *et al.* (2007)) are in good agreement with experimental data. At high pressure ratios shock locations predicted by OpenFOAM are closer to experimental trend line. The scatter of experimental data at high pressure ratios is due to unsteadiness in shock location, that computations by Xiao *et al.* (2007) (Also Fluent steady state simulations in this research) did not capture it due to steady state simulations. However OpenFOAM results, similar to experiments data, show unsteadiness in shock location.

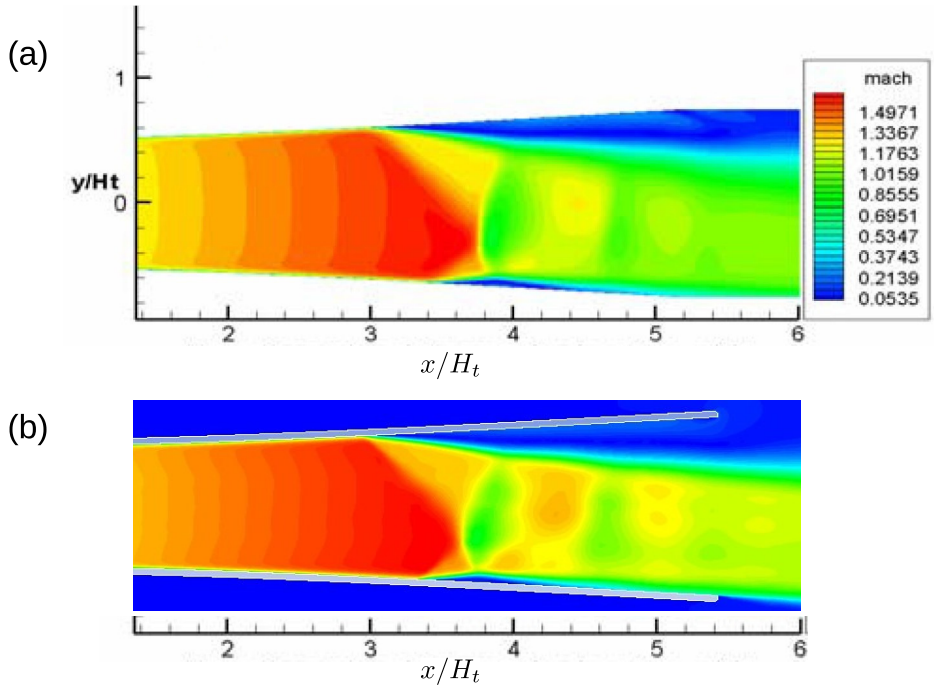

Figure 6.6: Mach number contours at $A_e/A_t = 1.5$ and PR=2.0 for (a) Simulation by Xiao *et al.* (2007) (b) Fluent simulation.

In Figure 6.7 there is a large difference between actual shock location and the position predicted by 1D inviscid theory; As the pressure ratio increases, the difference becomes even larger. The main reason for the difference is that the back pressure predicted by inviscid theory is lower, however in reality there are series of small shock waves and expansion fans (Figure 6.5) immediately after the main shock which are due to reflection of the lambda foot on shear layer.

6.2.3 Centre line pressure

Figure 6.8 plots the centre line pressure distribution for pressure ratio 1.5 and area ratio $A_e/A_t = 1.5$. The OF calculations are consistent with Papamoschou and Zill (2004) measurements. The slight difference between pressure measurements are due to instability and unsteadiness in shock location and side of free surface separation zone. Fluent results as mentioned before are identical to computations by Xiao *et al.* (2007). Downstream of normal shock, the air expands and then compresses rapidly to reach atmospheric pressure.

Figures 4.8 and 4.12 in chapter 4 illustrated the pressure distribution on centre line of the studied nozzle at pressure ratio 3 and 4 respectively for Fluent simulations. As explained before the results are compared with computational simulations by Abbasalizadeh (2011) and

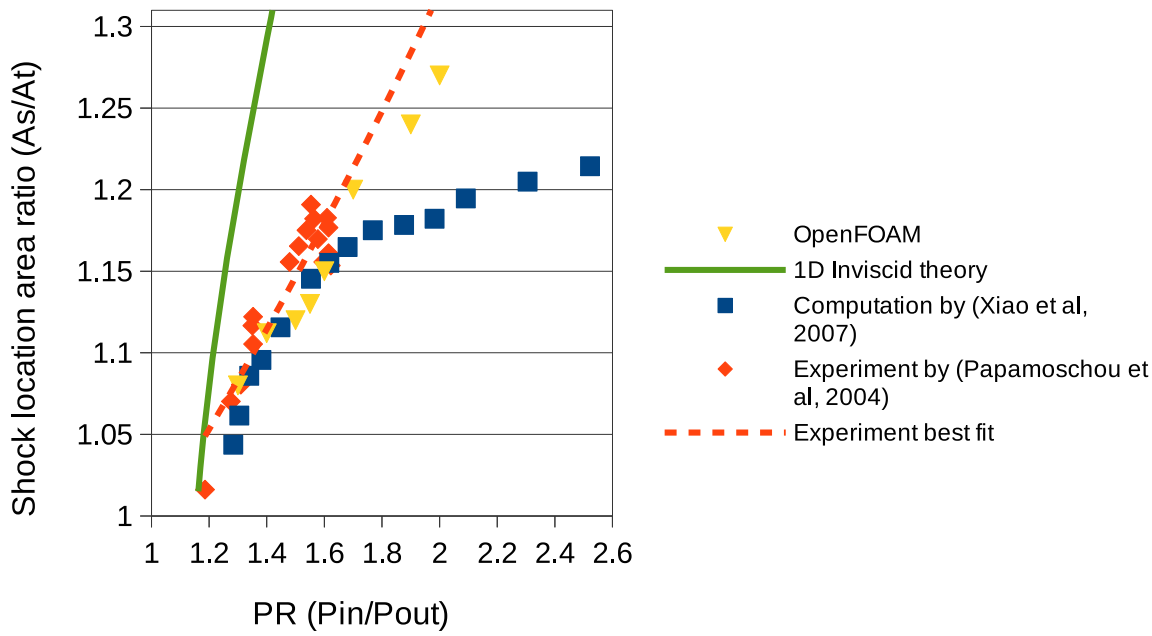

Figure 6.7: shock location versus nozzle pressure ratio.

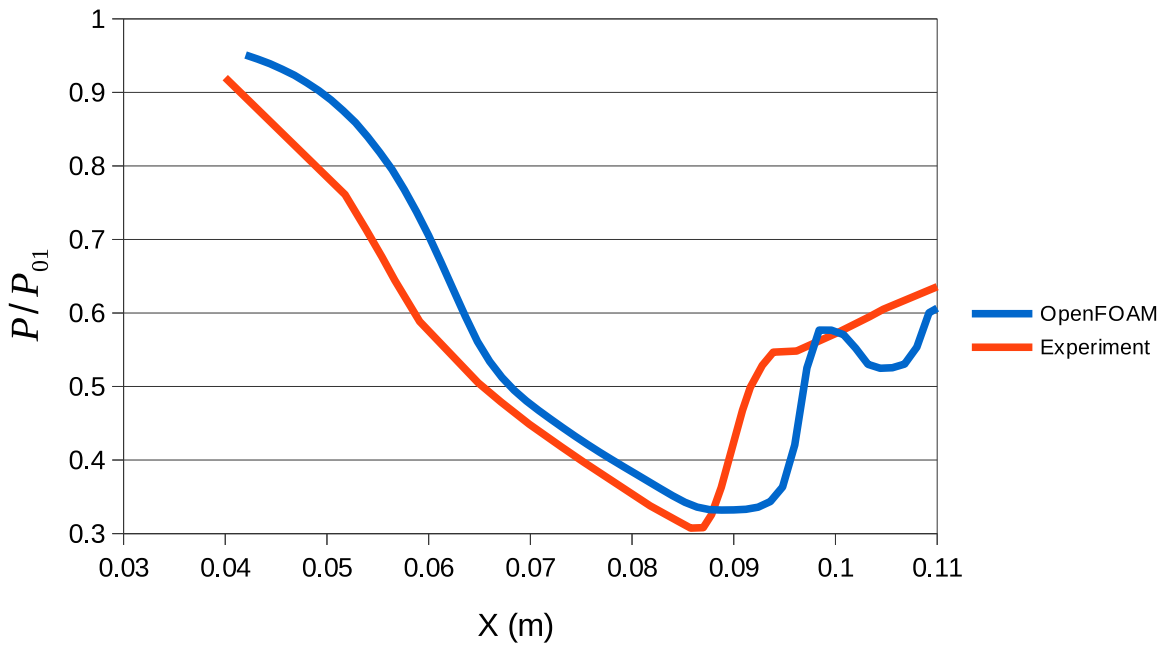

Figure 6.8: Pressure distribution along centre of the nozzle at pressure ratio PR=1.5 and area ratio $A_e/A_t = 1.5$ for OpenFOAM simulations and experimental test by Papamoschou and Zill (2004).

they are in good agreement. For non-swirl condition At PR 3 there is one strong shock wave with immediate expansion after it, but for PR 4 all shock waves are outside of the nozzle and therefore the pressure keep reducing up to outlet.

The lambda shock structure, even with the asymmetry effect at high pressure ratios, at centre of a nozzle has a normal shock (Mach disk); So, the pressure along the shock will be based on normal shock equation. The relation for the pressure along the normal shock is

$$\frac{p_2}{P_1} = 1 + \frac{2\gamma}{\gamma+1}\left(M_1^2 - 1\right) \tag{6.1}$$

where M_1 is the Mach number immediately upstream of the shock. The relation between M_1 and the local static pressure p_1 is

$$\frac{p_1}{p_{01}} = \left(1 + \frac{\gamma-1}{2}M_1^2\right)^{\frac{-\gamma}{\gamma-1}} \tag{6.2}$$

combining equations 6.1 and 6.2 will lead to relation between p_2 and p_1:

$$\frac{p_2}{p_{01}} = \frac{4\gamma}{\gamma^2-1}\left(\frac{p_1}{p_{01}}\right)^{\frac{1}{\gamma}} - \frac{(\gamma+1)^2 p_1}{(\gamma^2-1)\, p_{01}} \tag{6.3}$$

The equation 6.3 is plotted in Figure 6.9. However, the computational results and experimental measurements shown before for the centre line pressure do not satisfy equation 6.3. One of the reasons for this could be due to the unsteady shock structure since the equation 6.3 is for steady state shock.

6.2.4 Wall pressure

In this section the pressure distribution on top and bottom wall is compared with experimental data, shown in Figure 6.10. The pressure ratio of the investigated nozzle is 1.6. At this high pressure ratio there is a large separation zone as a result of asymmetric lambda shock. This creates a difference between the upper and lower nozzle surfaces in the pressure distribution and pressure recovery after the shock. Experimental plot is for upper surface, where separation zone exists as well. However, in OF simulation for PR 1.6 the separation zone is at the bottom wall. The difference is mainly due to unsteadiness in shock structure and Coanda effect. In experiments by Papamoschou and Zill (2004) has shown that during the given experiment the lambda feet did not flip. However, he suggested re-doing the experiment with exact similar

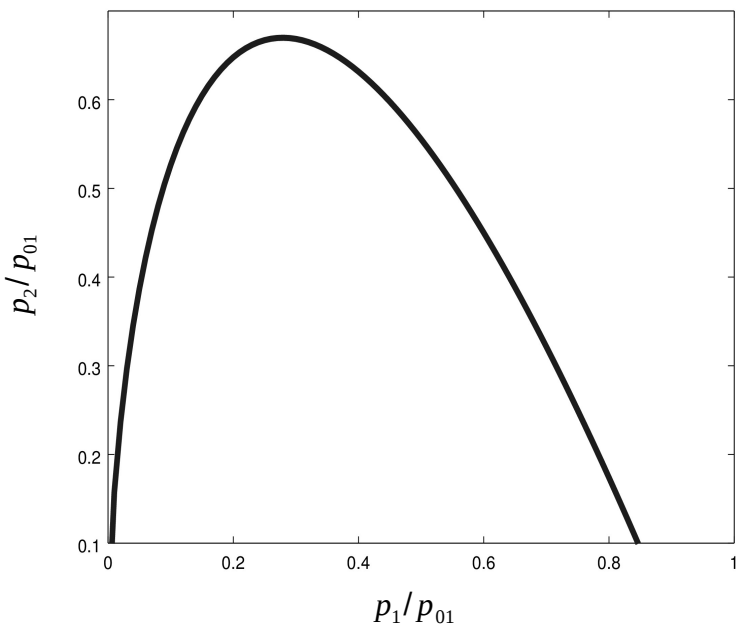

Figure 6.9: The static pressure relation before and after normal shock.

conditions the shock asymmetry could flip.

On the side of the free shock separation (FSS) zone , pressure recovers linearly with axial distance. This is similar to what has been measured by Bogar *et al.* (1983) and predicted numerically by Xiao *et al.* (2007). On the side of the restricted shock separation (RSS), the pressure shows initially faster increase and then gradually recovers to atmospheric pressure (ambient pressure). The asymmetric pressure recovery also creates a small sideways force, which evaluated by Papamoschou and Zill (2004) to be around 1-2 percent of nozzle thrust.

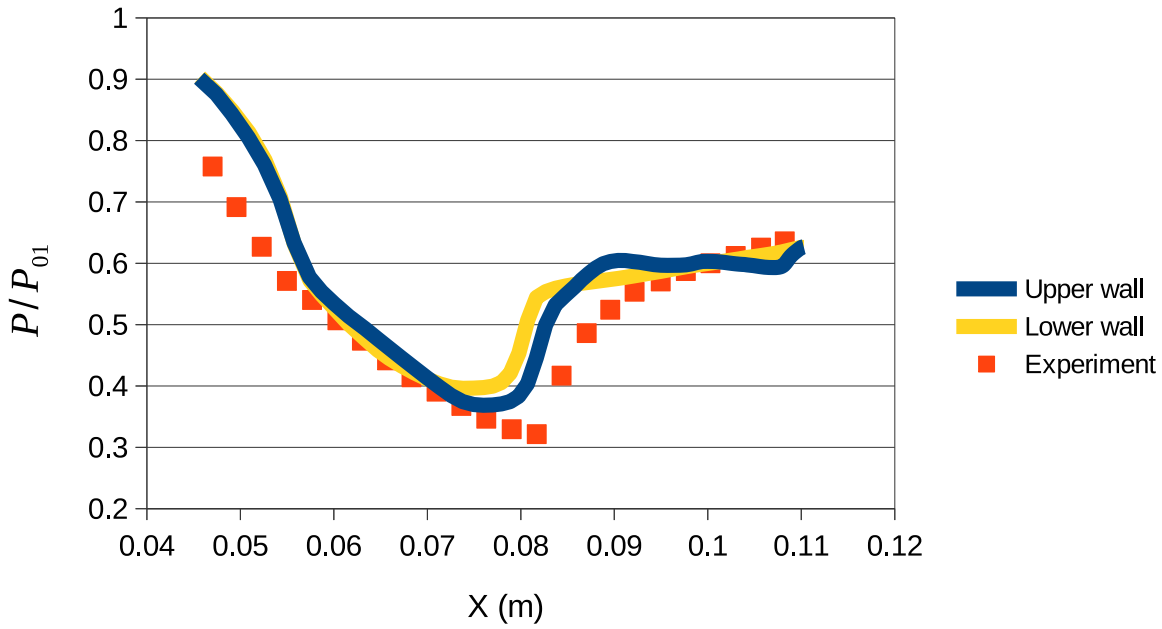

Figure 6.10: Wall pressure distribution at $A_e/A_t = 1.5$. Solid lines indicate OF simulation at PR=1.6 and symbols indicate experimental data by Papamoschou and Zill (2004) at upper wall for PR=1.609.

Chapter 7

Conclusion

7.1 Conclusion

The aim of this research was to study the effect of swirling flow inside a converging-diverging nozzle for sand blasting purposes. The swirl effect was created by a helical insert at the inlet of the nozzle. A numerical method was developed to investigate the shock waves structure, particles distribution and flow parameters inside the CD nozzle. The research was motivated by a need to reduce time and energy consumption in sand blasting operation.

Due to difficulties in conducting the full scale experiment, numerical method was adopted to analyse swirl flow inside the nozzle. Two CFD software were selected to perform simulations: Ansys FLUENT and OpenFOAM. FLUENT was used to analyse inside the nozzle and external domain simulations separately for both the nozzle with and without the helical insert. Because of resource limitation and license issues[1] it was not possible to do full domain (inside and outside the nozzle) simulations with FLUENT. . In contrast, OpenFOAM is open source software under GPL license, which gives the ability to use it without restriction on any number of processors. Therefore, for inside the nozzle and full domain simulations that high number of mesh were required OF was adopted to provide more accurate results.

As there is a lack of experimental data for supersonic swirl flow through a CD nozzle, the numerical method has been validated through experiments by Papamoschou and Zill (2004) and CFD simulation by Xiao *et al.* (2007) as a benchmark for calculations in this study. A comparison of results showed excellent agreement between validation simulations and Papamoschou and Zill (2004) experiments. Mach number contours for FLUENT and OF were matched accurately with experiment and CFD calculations. On the other hand, OF was

[1] FLUENT is a commercial CFD software which needs a separate license for parallel processing.

more accurate in predicting the shock location. This was mainly due to the capability of OF on capturing unsteadiness inside the flow. Simulations by Xiao *et al.* (2007) although being accurate, but they were not able to demonstrate unsteadiness in the flow as well as OF. Comparing the results for centre line pressure between FLUENT simulations and calculations by Abbasalizadeh (2011) on the same nozzle, showed good agreement in the calculations.

For this study, as highly swirling flowas high swirling flow was created inside the nozzle, there was a considerable degree of anisotropy in the stress and dissipation tensors which caused a highly anisotropic eddy viscosity of the swirl effect in the flow (Yajnik and Subbaiah, 1973). Thus, the isotropic turbulence models were not sufficient for precise results. The RANS models for anisotropic turbulence are limited to the modified $k-\varepsilon$ and Reynolds Stress Model (RSM). The realizable $k-\varepsilon$ model was adopted, which contains an alternative formulation for eddy viscosity and uses a modified transport equation for dissipation rate (Shih *et al.*, 1995a) for OF simulations. The RSM model that solves all six transport equations was used for FLUENT simulations. Both provided similar results and proved to be accurate for swirl flow simulations.

The simulation results from this study showed that, at different pressure ratios, separation zone will show different behaviour. FLUENT inside domain simulations for the nozzle without a helical insert showed mainly symmetrical shock and separation zone at various inlet pressures. For the nozzle with the helical insert, FLUENT showed asymmetric shock formation at pressure ratios 2 and 3 which caused a large FSS separation zone on the upper wall and small RSS zone on the lower wall of the nozzle. By increasing the inlet pressure to higher values and putting the nozzle at higher pressure ratios, meant that although the shock and separation zone remained asymmetric as shock cells were moving out of the domain, the separation zone became much smaller and shock waves became weaker. OF results for inside the nozzle with the helical insert demonstrated slightly different behaviour. The structure of the main shock wave was more symmetrical, although still the separation zone was clearly asymmetric up to inlet pressure 200kPa. At higher inlet pressures where the main Mach disk was close to the outlet, both shock wave and separation zones became symmetrical. Differences between FLUENT and OF results were minimal and mainly due to outlet boundary conditions. In FLUENT the outlet boundary condition was fixed pressure, but in OF it was wave transmissive to reconstruct non-reflective BC with a zero gradient for properties of reverse flow.

In contrast to FLUENT results for inside the nozzle without helical insert simulations, OF full domain simulations of the nozzle without a helical did present asymmetric shock and separation zone at lower pressure ratios ($PR < 2$). At inlet pressure 190kPa and 200kPa the

first lambda shock was inside the nozzle and exhibited a larger lambda foot on one side and a small one on the other side; Therefore FSS and RSS regions were created on each sides of the wall as a consequence of the Coanda effect. By increasing the inlet pressure to 250kPa all the shocks were outside of the nozzle. At early time steps the nozzle showed symmetrical shock and small FSS separation zone on both sides of the nozzle, but later time steps demonstrated unsteadiness on jet boundary and thus the flow at the outlet of the nozzle became asymmetric. At inlet pressure 300kPa and 400kPa all the shock cells were outside of the nozzle and there were jet instabilities which caused strong pressure fluctuations along the jet boundary. Jet instability did not affect the structure of shock cells. At inlet pressure 300kPa the shock cells had a clear diamond shape, however, at inlet pressure 400kPa shock cells became weaker and lost their diamond shape.

External domain simulations for both FLUENT and OpenFOAM proved that the swirl effect reduces amplitude of the pressure fluctuations along shock cells and increases the damping ratio for pressure. Consequently this will reduce the noise emission from the nozzle in order to minimise the sandblasting machine's impact on the surrounding environment.

Full domain simulations with OpenFOAM showed that due to the asymmetric lambda shock and large separation zone, the jet is angled at the outlet of the nozzle. As the inlet pressure increases the angle of divergence for the jet increases as well. At high pressure ratios ($PR > 3$) for the nozzle without swirl effect, there were large instabilities on the jet, while swirl simulations showed that there was not any significant instabilities on the jet boundary. By comparing turbulence kinetic energy, it is found that the nozzle with swirl effect has higher kinetic energy. At $PR = 2$ the maximum kinetic energy happens near the outlet at separation point for both a swirl and non-swirl nozzle; However at $PR = 3$ for the non-swirl nozzle, the maximum kinetic energy happens downstream while for the swirl nozzle the maximum kinetic energy remains at separation point at exit of the nozzle. Therefore the nozzle with the helical insert provides better mixing inside the nozzle.

In research both inside the nozzle and full domain simulations have been performed. Comparing the results shows that it is crucial to have full domain simulation for detailed analyses of shock waves structure and separation zone behaviour. Spatially at high pressure ratios ($PR > 2$) where the first shock is located outside or very close to the outlet of the nozzle, jet instabilities on downstream could alter shock and separation shape. However for some parameters such as centre line pressure the results were in strong agreement between full domain and inside nozzle simulations, apart from a slightly change in shock locations which were due to unsteadiness in the flow.

For all of the simulations, the nozzle was choked, which means the velocity at the throat

was at sonic point ($Ma = 1$). The understanding in fluid mechanics is that the mass flow rate will not increase in a choked nozzle; However, choked flow happens when the upstream pressure is fixed and downstream pressure is changing. A key conclusion of the study on the nozzle with various inlet pressures was that the mass flow rate would increase by increasing the inlet pressure even if the nozzle is chocked. It is shown that the mass flow rate will increase at the same rate as the inlet pressure is increasing. With regard to the mass flow rate versus pressure ratio, there were three stages, first up to the point where the first shock is inside the nozzle, second when the first shock is outside of the nozzle and the third when the first shock is outside of the nozzle and shock cells are losing their diamond shape.

One of the major goals of this research was to enhance mixing features of the nozzle. The swirl effect helped to create asymmetric flow separation which is a key ingredient in the mixing enhancement mechanism (Papamoschou, 2000). It has been shown by Gutmark *et al.* (1995) that jet instabilities will improve the mixing feature of the flow. In this research it was shown that at $PR < 2$ the jet instabilities are mainly inside the nozzle, however, at $PR > 2$ the jet instabilities are outside of the nozzle on the jet boundary. The helical attachment created a yarn effect inside the nozzle which enhances mixing inside the nozzle and prevents particles staying close to the nozzle wall by sweeping them away from it as a result of increasing tangential velocity. Another effect of swirl flow that improves the mixing feature was changing the structure of shock waves from one strong shock wave in non-swirl condition to a series of weaker shock waves and expansion fans in swirl conditions.

Two multiphase models were used for this research: Eulerian and DPM. It was shown that the Eulerian model is not sophisticated for granular supersonic flow unless there is a large volume fraction of the second phase. DPM results showed that maximum Mach number will reduce by particle injection in the non-swirl nozzle, however, with swirl effect, there was not a major loss on maximum Mach number. This effect was more influential at lower pressure ratios where the maximum Mach number reduction was 22 percent at inlet pressure 2atm and just 8 percent at inlet pressure 4atm. Unlike single phase simulations, in the Lagrangian approach, neither non-swirl nor swirl Mach number contours showed any unsteadiness inside the nozzle. This could be as a result of a reduction in the size of separation zones. In DPM simulations for the nozzle without a helical insert, as an effect of particles concentration at the centre of the nozzle, there were major changes to shock waves structure. Conversely, in the DPM simulations for the nozzle with a helical insert there were not any major changes to shock structure as there was better particle distribution inside the nozzle; In addition, swirl flow increases turbulent intensity inside the nozzle.

From the different parallel processing methods that were tried for this research, it was con-

cluded that it is important to decompose the computational domain in all directions. For two similar computational domains where one was decomposed in all directions and the other was just decomposed just in one direction,for the same number of processors, the results demonstrated 30-40% increase in computational speed of the decomposed domain in all directions.

Conclusions can be summarised as follows:

- Due to high swirl flow inside the nozzle, isotropic turbulence models are not able to capture all flow features; Therefore, it is crucial to use anisotropic turbulence models to solve flow equations.
- Swirl flow inside the nozzle created asymmetric shock with a large separation zone (FSS) as a result of the Coanda effect.
- Swirl effect reduces pressure fluctuations along shock cells, which will reduce the screech noise of the shock waves.
- At high pressure ratios, for the nozzle without swirl effect, there were significant instabilities on jet boundary; However, with swirl effect, instabilities were more toward the exit of the nozzle, and there were not major instabilities on jet boundary.
- Full domain simulation is crucial to understand shock waves structures and separation zones.
- In a choked nozzle, the mass flow rate will increase by increasing the inlet pressure. The mass flow rate in a choked nozzle will remain constant if the upstream conditions are constant and only downstream conditions are changing.
- The swirl effect improves the mixing feature significantly.
- The Eulerian multiphase model did not provide accurate results for granular supersonic flows, unless there was a large volume fraction of the second phase.
- The Lagrangian multiphase model (DPM), provided best results for granular particles with less than 10% percent volume fraction.
- Multiphase Lagrangian simulations showed that, after particles injection, maximum velocity reduces for the nozzle without a helical insert; However, for the nozzle with a helical insert there was not a significant reduction in maximum velocity.
- To reduce computational time in parallel processing, it is important to decompose the domain in all computational directions.

7.2 Future work

The research detailed in this thesis has opened up several areas for future study. The numerical modelling can be extended to perform more CFD simulations at various inlet pressures to find more accurate mass flow rate diagrams.

Due to resource limitations turbulence modelling was limited just to RANS simulations, however LES simulations could help to gain a better understanding of swirl flow inside and outside of supersonic CD nozzles.

A major part of this research was focused at pressure ratios higher than 2, as most sand-blasting machines operate at this pressure range, but simulations at lower pressures could also be crucial in understanding of swirl flow inside supersonic nozzles.

Helical insert have been used in order to create swirl flow inside the nozzle. However, there are many other ways to create swirl flow inside the nozzle. Extending the research to other methods used for the creation of swirl flow would significantly expand knowledge and understanding of flow behaviour in different conditions inside a converging-diverging nozzle.

This research was focused on the fluid dynamic of the flow inside and outside of the nozzle. As explained in previous chapters, swirl flow creates asymmetric shock and increases the size of the separation zone inside the nozzle. The study by Damgaard *et al.* (2004) explained that the lateral loads in an overexpanded nozzle could be very dangerous acting on a nozzle wall. Therefore, it is valuable for safety reasons and structural analysis to study side loads with the effect of swirl flow inside the converging-diverging nozzle.

In this study no particular attention was given to aeroacoustic analysis of supersonic swirl flow. Understanding the effect of swirl flow on aeroacoustic performance can help to reduce noise for many different applications. Research by Ahmad (2011) demonstrates that having a net swirl effect on jet, increases shear layer mixing and hence reduces noise propagated from a nozzle.

The nozzle that was the subject of this study is the standard nozzle with an area ratio (A_e/A_t) of 1.36. It has been shown by Papamoschou and Zill (2004) that a nozzle with an area ratio greater than 1.5 has asymmetric shock and therefore a bigger separation zone at a wider range of pressure ratios. Consequently, carrying out extra research on a nozzle with higher area ratios might help to design a new nozzle with better performance and mixing features.

The ability to use Computational Fluid Dynamic (CFD) for flow simulation has substantially increased in recent years. In addition, advances in computer speeds make it possible to use High Performance Computing (HPC) hardware and parallel processing to run larger and more complicated cases in a shorter period of time. However, there are some concerns

that HPC hardware is at the point of a paradigm shift toward heterogeneous parallel programming; Thus it is necessary to introduce new algorithms and software in order to utilize the full capability of future hardware (Slotnick *et al.*, 2014).

One of key reasons for instability and divergence of numerical solutions was the problem of reverse flow at outlet boundaries. There is still potential for study on the behaviour of reverse flow in order to have more accurate boundary conditions.

Due to resource limitations it was not possible to perform DPM simulations outside of the nozzle. Therefore the effect of particles on boundary jet and nozzle instabilities is still unknown.

References

Abbasalizadeh, M. 2011. *Investigation of Three Phase Nozzle flow In an Innovative Sand Blasting System*. Ph.D. thesis, Anglia Ruskin University, Faculty of Science and Technology.

Abdelhafez, A. 2009. *Effect of swirl on the choking criteria, shock structure, and mixing in underexpanded supersonic nozzle airflows*. Ph.D. thesis, University of Maryland.

Achtsnick, M., Geelhoed, P., Hoogstrate, A. and Karpuschewski, B. 2005. Modelling and evaluation of the micro abrasive blasting process. *Wear* 259(1), pp. 84–94.

Ahmad, A. 2011. *Experimental aeroacoustics study on jet noise reduction using tangential air injection*. Ph.D. thesis, School of Engineering and Materials Science Queen Mary, University of London.

AIAA. 1998. *AIAA Guide for the Verification and Validation of Computational Fluid Dynamics Simulations*. American Institute of Aeronautics & Astronautics.

Anderson, J. D. 1995. *Computational fluid dynamics*. McGraw-Hill.

Anderson, J. D. 2000. *Hypersonic and High Temperature Gas Dynamics*. American Institute of Aeronautics and Astronautics.

Anderson, J. D. 2003. *Modern compressible flow with historical perspective*. New York: McGrow-Hill.

Anderson Jr, J. D. 1985. *Fundamentals of aerodynamics*. Tata McGraw-Hill Education.

Andrews, M. and O'rourke, P. 1996. The multiphase particle-in-cell (mp-pic) method for dense particulate flows. *International Journal of Multiphase Flow* 22(2), pp. 379–402.

Ansys. 2010. *Ansys Fluent 13 User's Guide*. Ansys, Inc.

Axelsson, O. 1996. *Iterative solution methods*. Cambridge University Press.

Baldwin, B. S. and Lomax, H. 1978. *Thin layer approximation and algebraic model for separated turbulent flows*, vol. 257. American Institute of Aeronautics and Astronautics.

Barnhart, P. J. 1997. Npac-nozzle performance analysis code. Tech. rep., NASA.

Barton, I. 1998. Comparison of simple-and piso-type algorithms for transient flows. *International Journal for numerical methods in fluids* 26(4), pp. 459–483.

Beam, R. M. and Warming, R. 1978. An implicit factored scheme for the compressible navier-stokes equations. *AIAA journal* 16(4), pp. 393–402.

Bi, H. and Grace, J. 1995. Flow regime diagrams for gas-solid fluidization and upward transport. *International Journal of Multiphase Flow* 21(6), pp. 1229–1236.

Bogar, T., Sajben, M. and Kroutil, J. 1983. Characteristic frequencies of transonic diffuser flow oscillations. *AIAA journal* 21(9), pp. 1232–1240.

Bouzid, S. and Bouaouadja, N. 2000. Effect of impact angle on glass surfaces eroded by sand blasting. *Journal of the European Ceramic Society* 20(4), pp. 481 – 488.

Bowman, J. C. 1996. On inertial-range scaling laws. *Journal of Fluid Mechanics* 306, pp. 167–181.

Brennan, D. 2001. *The numerical simulation of two phase flows in settling tanks*. Ph.D. thesis, Imperial College London (University of London).

Brennen, C. E. 2005. *Fundamentals of multiphase flow*. Cambridge University Press.

Bühler, S., Luginsland, T., Obrist, D. and Kleiser, L. 2010. Parallel simulation of a compressible jet including nozzle modelling. *Proceedings in Applied Mathematics and Mechanics* 10(1), pp. 443–444.

Buntic-Ogor, I., Gyllenram, W., Ohlberg, E., Nilsson, H. and Ruprecht, A. 2006a. An adaptive turbulence model for swirling flow. *Conference on Turbulence and Interactions, TI2006, May 29 - June 2, 2006, Porquerolles, France* .

Buntic-Ogor, I., Gyllenram, W., Ohlberg, E., Nilsson, H. and Ruprecht, A. 2006b. An adaptive turbulence model for swirling flow. In: *Conference on Turbulence and Interactions, TI2006, May 29-June 2, 2006, Porquerolles, France*.

Campbell, C. S. 1990. Rapid granular flows. *Annual Review of Fluid Mechanics* 22(1), pp. 57–90.

Campbell, C. S. and Brennen, C. E. 1985. Computer simulation of granular shear flows. *Journal of Fluid Mechanics* 151, pp. 167–188.

Carpenter, M. H. and Casper, J. H. 1999. Accuracy of shock capturing in two spatial dimensions. *AIAA journal* 37(9), pp. 1072–1079.

Cebeci, T. 2012. *Analysis of turbulent boundary layers*. Elsevier.

Chacon, S. and Hamano, J. C. 2009. *Pro git*, vol. 288. Springer.

Chang, F. and Dhir, V. 1994. Turbulent flow field in tangentially injected swirl flows in tubes. *International Journal of Heat and Fluid Flow* 15(5), pp. 346–356.

Chasmawala, R. J., Hansen, S. M. and Jayaraman, S. 1990. Structure and properties of air-jet spun yarns. *Textile Research Journal* 60(2), pp. 61–69.

Chen, C., Chakravarthy, S. and Hung, C. 1994. Numerical investigation of separated nozzle flows. *AIAA journal* 32(9), pp. 1836–1843.

Chen, Z., Zheng, C., Feng, Y. and Hofmann, H. 1995. Distributions of flow regimes and phase holdups in three-phase fluidized beds. *Chemical engineering science* 50(13), pp. 2153–2159.

Chiesa, M., Mathiesen, V., Melheim, J. A. and Halvorsen, B. 2005. Numerical simulation of particulate flow by the eulerian–lagrangian and the eulerian–eulerian approach with application to a fluidized bed. *Computers & chemical engineering* 29(2), pp. 291–304.

Chima, R. V. 1996. A k-omega turbulence model for quasi-three-dimensional turbomachinery flows. *AIAA paper* (96-0248).

Chitjian, J. R. 1987. *Recirculating sandblasting machine*, [Online]. US Patent 4,646,482.

Choudhury, V. 2014. *A validation study of OpenFOAM for Hybrid RANS-LES simulation of incompressible flow over a backward facing step and delta wing*. Master's thesis, Mississippi State University.

Crank, J. and Nicolson, P. 1947. A practical method for numerical evaluation of solutions of partial differential equations of the heat-conduction type. In: *Mathematical Proceedings of the Cambridge Philosophical Society*. Cambridge Univ Press, vol. 43, pp. 50–67.

Crowe, C. T. 2014. *Multiphase flow handbook*. CRC press.

Cutler, A. and White, J. 2001. An experimental and cfd study of a supersonic coaxial jet. *AIAA* .

Daly, B. J. and Harlow, F. H. 2003. Transport equations in turbulence. *Physics of Fluids (1958-1988)* 13(11), pp. 2634–2649.

Damgaard, T., Östlund, J. and Frey, M. 2004. Side-load phenomena in highly overexpanded rocket nozzles. *Journal of Propulsion and Power* 20(4), pp. 695–704.

Davidson, L. 2011. *An Introduction to Turbulence Models*. Chalmers University of Technology.

Dehghan, M. and Tabrizi, H. B. 2012. On near-wall behavior of particles in a dilute turbulent gas–solid flow using kinetic theory of granular flows. *Powder Technology* 224, pp. 273–280.

Delery, J. M. 1985. Shock wave/turbulent boundary layer interaction and its control. *Progress in Aerospace Sciences* 22(4), pp. 209–280.

Deng, J., Zhang, X., Niu, P., Liu, L. and Wang, J. 2006. Wear of ceramic nozzles by dry sand blasting. *Tribology International* 39(3), pp. 274 – 280.

Drew, D., Cheng, L. and Lahey Jr, R. 1979. The analysis of virtual mass effects in two-phase flow. *International Journal of Multiphase Flow* 5(4), pp. 233–242.

Drew, D. and Lahey Jr, R. 1987. The virtual mass and lift force on a sphere in rotating and straining inviscid flow. *International Journal of Multiphase Flow* 13(1), pp. 113–121.

Drew, D. A. and Wallis, G. B. 1994. Fundamentals of two-phase flow modeling. *Multiphase Science and Technology* 8(1-4).

Dutton, J. 1987. Swirling supersonic nozzle flow. *Journal of Propulsion and Power* 3(4), pp. 342–349.

Dykhuizen, R. and Smith, M. 1998. Gas dynamic principles of cold spray. *Journal of Thermal Spray Technology* 7(2), pp. 205–212.

Džiugys, A. and Peters, B. 2001. An approach to simulate the motion of spherical and non-spherical fuel particles in combustion chambers. *Granular matter* 3(4), pp. 231–266.

Elghobashi, S. 1994. On predicting particle-laden turbulent flows. *Applied Scientific Research* 52(4), pp. 309–329.

Ergun, S. and Orning, A. A. 1949. Fluid flow through randomly packed columns and fluidized beds. *Industrial & Engineering Chemistry* 41(6), pp. 1179–1184.

Eslamian, E. 2010. *Observation and Understanding of Flow Behaviour In a Supersonic Jet*. Master's thesis, Queen Mary, University of London, School of Engineering and Material Science.

Eslamian, E., Shirvani, H. and Shirvani, A. 2012. Numerical investigation of swirl flow inside a supersonic nozzle. *Advances in Fluid Mechanics IX* 74, p. 131.

Eswaran, V. and Pope, S. 1988. Direct numerical simulations of the turbulent mixing of a passive scalar. *Physics of Fluids (1958-1988)* 31(3), pp. 506–520.

Fedkiw, R. P. 2002. Coupling an eulerian fluid calculation to a lagrangian solid calculation with the ghost fluid method. *Journal of Computational Physics* 175(1), pp. 200–224.

Fedkiw, R. P., Aslam, T., Merriman, B. and Osher, S. 1999. A non-oscillatory eulerian approach to interfaces in multimaterial flows (the ghost fluid method). *Journal of computational physics* 152(2), pp. 457–492.

FEPA. 2010. *Fepa Standard shapes and dimensions for precision superabrasives*. FEPA SAFETY CODE.

Ferziger, J. H. and Perić, M. 2002. *Computational methods for fluid dynamics*, vol. 3. Springer Berlin.

Frey, M. and Hagemann, G. 1998. Status of flow separation prediction in rocket nozzles. *AIAA paper* 3619, p. 1998.

Gentry, R. A., Martin, R. E. and Daly, B. J. 1966. An eulerian differencing method for unsteady compressible flow problems. *Journal of Computational Physics* 1(1), pp. 87–118.

Gerber, A. and Kermani, M. 2004. A pressure based eulerian–eulerian multi-phase model for non-equilibrium condensation in transonic steam flow. *International Journal of Heat and Mass Transfer* 47(10), pp. 2217–2231.

Ghosal, S. and Moin, P. 1995. The basic equations for the large eddy simulation of turbulent flows in complex geometry. *Journal of Computational Physics* 118(1), pp. 24–37.

Gibson, M. and Launder, B. 1978. Ground effects on pressure fluctuations in the atmospheric boundary layer. *Journal of Fluid Mechanics* 86(03), pp. 491–511.

Green Jr, L. and Nall, K. 1957. Control of flow separation in supersonic nozzles by means of boundary-layer injection. Tech. rep., Aerojet-General Corp., Azusa, Calif.

Guo, H.-F. and Chen, Z.-Y. 2009. Numerical simulation of tangentially injected turbulent swirling flow in a divergent tube. *International journal for numerical methods in fluids* 61(7), pp. 796–809.

Guo, H.-F., Chen, Z.-Y. and Yu, C.-W. 2009. 3d numerical simulation of compressible swirling flow induced by means of tangential inlets. *International journal for numerical methods in fluids* 59(11), pp. 1285–1298.

Gutmark, E., Schadow, K. and Yu, K. 1995. Mixing enhancement in supersonic free shear flows. *Annual Review of Fluid Mechanics* 27(1), pp. 375–417.

Hadjadj, A. and Onofri, M. 2009. Nozzle flow separation. *Shock Waves* 19(3), pp. 163–169.

Hagemann, G., Immich, H., Nguyen, T. V. and Dumnov, G. E. 1998. Advanced rocket nozzles. *Journal of Propulsion and Power* 14(5), pp. 620–634.

Hall, M. 1972. Vortex breakdown. *Annual Review of Fluid Mechanics* 4(1), pp. 195–218.

Hamed, A. and Vogiatzis, C. 1997. Overexpanded two-dimensional-convergent-divergent nozzle flow simulations, assessment of turbulence models. *Journal of propulsion and power* 13(3), pp. 444–445.

Haselbacher, A., Najjar, F. M., Massa, L. and Moser, R. 2010. Slow-time acceleration for modeling multiple-time-scale problems. *Journal of Computational Physics* 229(2), pp. 325–342.

Hayase, T., Humphrey, J. and Greif, R. 1992. A consistently formulated quick scheme for fast and stable convergence using finite-volume iterative calculation procedures. *Journal of Computational Physics* 98(1), pp. 108–118.

Hill, D. P. 1998. *The computer simulation of dispersed two-phase flow*. Ph.D. thesis, University of London.

Hirsch, C. 2007. *Numerical Computation of Internal and External Flows: The Fundamentals of Computational Fluid Dynamics: The Fundamentals of Computational Fluid Dynamics*, vol. 1. Butterworth-Heinemann.

Hopkins, M. A. and Shen, H. H. 1992. A monte carlo solution for rapidly shearing granular flows based on the kinetic theory of dense gases. *Journal of Fluid Mechanics* 244, pp. 477–491.

Hou, R. G., Huang, C. Z., Wang, J., Lu, X. and Feng, Y. X. 2007. Simulation of solid-liquid two-phase flow inside and outside the abrasive water jet nozzle. *Key Engineering Materials* 339, pp. 453–457.

Hu, H. H., Patankar, N. A. and Zhu, M. 2001. Direct numerical simulations of fluid–solid systems using the arbitrary lagrangian–eulerian technique. *Journal of Computational Physics* 169(2), pp. 427–462.

Hunter, C. A. 1998. Experimental, theoretical, and computational investigation of separated nozzle flows. *AIAA paper* 3107, p. 1998.

Ishii, M. 1975. Thermo-fluid dynamic theory of two-phase flow. *NASA STI/Recon Technical Report A* 75, p. 29657.

Issa, R. I. 1986. Solution of the implicitly discretised fluid flow equations by operator-splitting. *Journal of computational physics* 62(1), pp. 40–65.

Jang, W. and Aral, M. M. 2005. Three-dimensional multiphase flow and multispecies transport model techflow mp. Tech. rep., Georgia Institute of Technology.

Jasak, H. 1996. *Error analysis and estimation for the finite volume method with applications to fluid flows*. Ph.D. thesis, Imperial College London (University of London).

Jasak, H., Weller, H. and Gosman, A. 1999. High resolution nvd differencing scheme for arbitrarily unstructured meshes. *International journal for numerical methods in fluids* 31(2), pp. 431–449.

Jassim, E., Abdi, M. A. and Muzychka, Y. 2008. Computational fluid dynamics study for flow of natural gas through high-pressure supersonic nozzles: Part 2. nozzle geometry and vorticity. *Petroleum Science and Technology* 26(15), pp. 1773–1785.

Jiajun, C., Haynes, B. S. and Fletcher, D. F. 1999. A numerical and experimental study of tangentially injected swirling pipe flows in. In: *Second International Conference on CFD in the Minerals and Process Industries*. Available at: `http://www.cfd.com.au/cfd_conf99/papers/061CHEN.PDF`.

Jianxin, D., Yihua, F., Zeliang, D. and Peiwei, S. 2003. Wear behavior of ceramic nozzles in sand blasting treatments. *Journal of the European Ceramic Society* 23(2), pp. 323 – 329.

Kafui, K., Thornton, C. and Adams, M. 2002. Discrete particle-continuum fluid modelling of gas–solid fluidised beds. *Chemical Engineering Science* 57(13), pp. 2395–2410.

Karki, K. and Patankar, S. 1989. Pressure based calculation procedure for viscous flows at all speedsin arbitrary configurations. *AIAA journal* 27(9), pp. 1167–1174.

Karpuschewski, B., Hoogstrate, A. and Achtsnick, M. 2004. Simulation and improvement of the micro abrasive blasting process. *CIRP Annals-Manufacturing Technology* 53(1), pp. 251–254.

Keener, J., Coffer, A., Hitzrot, H., Hansen, L. and Hamilton, A. 1993. Feasibility study: Tank blasting using recoverable steel grit. Tech. rep., DTIC Document.

Kennedy, D., Vahey, J. and Hanney, D. 2005. Micro shot blasting of machine tools for improving surface finish and reducing cutting forces in manufacturing. *Materials & design* 26(3), pp. 203–208.

Khodadadi, A. R., Malekbala, M. R. and Khodadadi, A. F. 2013. Evaluate shock capturing capability with the numerical methods in openfoam. *Thermal Science* 17(4), pp. 1255–1260.

Kim, J.-H. and Samimy, M. 1999. Mixing enhancement via nozzle trailing edge modifications in a high speed rectangular jet. *Physics of Fluids (1994-present)* 11(9), pp. 2731–2742.

Kitagawa, A., Murai, Y. and Yamamoto, F. 2001. Two-way coupling of eulerian–lagrangian model for dispersed multiphase flows using filtering functions. *International journal of multiphase flow* 27(12), pp. 2129–2153.

Kitoh, O. 1991. Experimental study of turbulent swirling flow in a straight pipe. *Journal of Fluid Mechanics* 225, pp. 445–479.

Kline, E., Mort, G. and LeCompte, J. 1988. Research news. improved productivity from new blast nozzle geometry. *Journal of Protective Coatings & Linings* 5(2).

Kobayashi, T. and Yoda, M. 1987. Modified k-ε model for turbulent swirling flow in a straight pipe. *JSME international journal* 30(259), pp. 66–71.

Kraichnan, R. H. 1967. Inertial ranges in two-dimensional turbulence. Tech. rep., DTIC Document.

Kraichnan, R. H. 1971. Inertial-range transfer in two-and three-dimensional turbulence. *Journal of Fluid Mechanics* 47(03), pp. 525–535.

Kralj, C. 1996. *Numerical simulation of Diesel spray processes*. Ph.D. thesis, University of London.

Kuan, B., Yang, W. and Schwarz, M. 2007. Dilute gas–solid two-phase flows in a curved 90 degree duct bend: Cfd simulation with experimental validation. *Chemical Engineering Science* 62(7), pp. 2068–2088.

Kurganov, A. and Tadmor, E. 2000. New high-resolution central schemes for nonlinear conservation laws and convection–diffusion equations. *Journal of Computational Physics* 160(1), pp. 241–282.

Launder, B., Reece, G. J. and Rodi, W. 1975. Progress in the development of a reynolds-stress turbulence closure. *Journal of fluid mechanics* 68(03), pp. 537–566.

Launder, B. E. and Spalding, D. 1974. The numerical computation of turbulent flows. *Computer methods in applied mechanics and engineering* 3(2), pp. 269–289.

Lax, P. D. 1957. Hyperbolic systems of conservation laws ii. *Communications on Pure and Applied Mathematics* 10(4), pp. 537–566.

Lemmon, E. W., Jacobsen, R. T., Penoncello, S. G. and Friend, D. G. 2000. Thermodynamic properties of air and mixtures of nitrogen, argon, and oxygen from 60 to 2000 k at pressures to 2000 mpa. *Journal of Physical and Chemical Reference Data* 29(3), pp. 331–385.

Li, W.-Y. and Li, C.-J. 2005. Optimal design of a novel cold spray gun nozzle at a limited space. *Journal of thermal spray technology* 14(3), pp. 391–396.

Lijo, V., Kim, H. D., Setoguchi, T. and Matsuo, S. 2010. Numerical simulation of transient flows in a rocket propulsion nozzle. *International Journal of Heat and Fluid Flow* 31(3), pp. 409–417.

Lillard, R. P. 2011. *Turbulence modeling for shock wave/turbulent boundary layer interactions*. Ph.D. thesis, Purdue University.

Liou, M.-S. 1996. A sequel to ausm: Ausm+. *Journal of computational Physics* 129(2), pp. 364–382.

Liu, Y. and Bellhouse, B. J. 2005. Prediction of jet flows in the supersonic nozzle and diffuser. *International journal for numerical methods in fluids* 47(10-11), pp. 1147–1155.

Liu, Z., Ding, J., Jiang, W., Zhang, J. and Feng, Y. 2008. Numerical simulation of highly-swirling supersonic flow inside a laval nozzle. *Progress in Computational Fluid Dynamics, an International Journal* 8(7-8), pp. 536–540.

Lu, H., Ramsay, J. and Miller, D. 1977. Noise of swirling exhaust jets. *AIAA Journal* 15(5), pp. 642–646.

Luginsland, T., Bühler, S., Obrist, D. and Kleiser, L. 2010. A parallel code for les of compressible swirling jet flow undergoing vortex breakdown. *Proceedings in Applied Mathematics and Mechanics* 10(1), pp. 727–728.

Luginsland, T. and Kleiser, L. 2011. Large eddy simulations of swirling nozzle-jet flow undergoing vortex breakdown. *Proc. Appl. Math. Mech* 11, pp. 577–578.

MacCormack, R. W. 1982. A numerical method for solving the equations of compressible viscous flow. *AIAA journal* 20(9), pp. 1275–1281.

Majdalani, J. and Maicke, B. A. 2011. Explicit inversion of stodola's area-mach number equation. *Journal of Heat Transfer* 133(7), p. 071702.

Majdalani, J. and Maicke, B. A. 2013. Direct calculation of the average local mach number in converging–diverging nozzles. *Aerospace Science and Technology* 24(1), pp. 111–115.

Marvin, J. G. 1995. Perspective on computational fluid dynamics validation. *AIAA journal* 33(10), pp. 1778–1787.

McLaughlin, D. K., Morrison, G. L. and Troutt, T. R. 1975. Experiments on the instability waves in a supersonic jet and their acoustic radiation. *Journal of Fluid Mechanics* 69(01), pp. 73–95.

Menter, F., Kuntz, M. and Langtry, R. 2003. Ten years of industrial experience with the sst turbulence model. *Turbulence, heat and mass transfer* 4(1).

Menter, F. R. 1994. Two-equation eddy-viscosity turbulence models for engineering applications. *AIAA journal* 32(8), pp. 1598–1605.

Moin, P. and Mahesh, K. 1998. Direct numerical simulation: a tool in turbulence research. *Annual Review of Fluid Mechanics* 30(1), pp. 539–578.

Morrisette, E. L. and Goldberg, T. J. 1978. Turbulent-flow separation criteria for overexpanded supersonic nozzles. *NASA STI/Recon Technical Report N* 78, p. 30554.

Mouronval, A.-S., Hadjadj, A., Kudryavtsev, A. and Vandromme, D. 2003. Numerical investigation of transient nozzle flow. *Shock Waves* 12(5), pp. 403–411.

Murakami, M., Kito, O., Katayama, Y. and Iida, Y. 1976. An experimental study of swirling flow in pipes. *Bulletin of JSME* 19(128), pp. 118–126.

Muste, L. 1923. *Sand-blast machine*, [Online]. US Patent 1,467,488.

Najafi, A., Saidi, M., Sadeghipour, M. and Souhar, M. 2005. Numerical analysis of turbulent swirling decay pipe flow. *International communications in heat and mass transfer* 32(5), pp. 627–638.

Najjar, F., Ferry, J., Haselbacher, A. and Balachandar, S. 2006. Simulations of solid-propellant rockets: effects of aluminum droplet size distribution. *Journal of Spacecraft and Rockets* 43(6), pp. 1258–1270.

Neemeh, R., AlGattus, S. and Neemeh, L. 1999. Experimental investigation of noise reduction in supersonic jets due to jet rotation. *Journal of sound and vibration* 221(3), pp. 505–524.

Oberkampf, W. L. and Trucano, T. G. 2002. Verification and validation in computational fluid dynamics. *Progress in Aerospace Sciences* 38(3), pp. 209–272.

Oesterle, B. and Petitjean, A. 1993. Simulation of particle-to-particle interactions in gas solid flows. *International journal of multiphase flow* 19(1), pp. 199–211.

Olles, M. W., Lynn, N. F. and Majdalani, J. 2004. The isentropic mach number for arbitrary nozzle area ratio. *AIAA Paper* 3922.

OpenFOAM. 2013. *User Guide*. OpenFOAM Foundation.

Pandolfi, M. 1976. Transonic swirling flow in axisymmetric nozzles. *Meccanica* 11(3), pp. 157–161.

Papamoschou, D. 2000. Mixing enhancement using axial flow. *AIAA paper* 93, p. 2000.

Papamoschou, D. and Zill, A. 2004. Fundamental investigation of supersonic nozzle flow separation. *AIAA paper* 1111, p. 2004.

Park, D.-S., Cho, M.-W., Lee, H. and Cho, W.-S. 2004. Micro-grooving of glass using micro-abrasive jet machining. *Journal of materials processing technology* 146(2), pp. 234–240.

Patankar, S. 1980. *Numerical heat transfer and fluid flow*. CRC Press.

Pawlik, E. V., Perkins, G. S. and Phillips, W. M. 1981. *Sandblasting nozzle*, [Online]. US Patent 4,252,768.

Pei, P., Zhang, K. and Wen, D. 2012. Comparative analysis of cfd models for jetting fluidized beds: the effect of inter-phase drag force. *Powder Technology* 221, pp. 114–122.

Peric, M. 1985. *A finite volume method for the prediction of three-dimensional fluid flow in complex ducts*. Ph.D. thesis, Imperial College London (University of London).

Poinsot, T. J. and Lelef, S. 1992. Boundary conditions for direct simulations of compressible viscous flows. *Journal of computational physics* 101(1), pp. 104–129.

Porter, D. W., Hubbs, A. F., Robinson, V. A., Battelli, L. A., Greskevitch, M., Barger, M., Landsittel, D., Jones, W. and Castranova, V. 2002. Comparative pulmonary toxicity of blasting sand and five substitute abrasive blasting agents. *Journal Of Toxicology And Environmental Health Part A* 65(16), pp. 1121–1140.

Powell, A. 1953. On the mechanism of choked jet noise. *Proceedings of the Physical Society. Section B* 66(12), p. 1039.

Prandtl, L. 1927. Turbulent flow. Tech. rep., NASA.

Raykowski, A., Hader, M., Maragno, B. and Spelt, J. 2001. Blast cleaning of gas turbine components: deposit removal and substrate deformation. *Wear* 249(1-2), pp. 126 – 131.

Reynolds, O. 1895. On the dynamical theory of incompressible viscous fluids and the determination of the criterion. *Philosophical Transactions of the Royal Society of London. A* pp. 123–164.

Rhie, C. and Chow, W. 1983. Numerical study of the turbulent flow past an airfoil with trailing edge separation. *AIAA journal* 21(11), pp. 1525–1532.

Roache, P. J. 1994. Perspective: a method for uniform reporting of grid refinement studies. *Journal of Fluids Engineering* 116(3), pp. 405–413.

Roache, P. J. 1997. Quantification of uncertainty in computational fluid dynamics. *Annual Review of Fluid Mechanics* 29(1), pp. 123–160.

Roache, P. J. 1998. *Verification and validation in computational science and engineering*. Hermosa.

Roe, P. 1986. Characteristic-based schemes for the euler equations. *Annual review of fluid mechanics* 18(1), pp. 337–365.

Romine, G. 1998. Nozzle flow separation. *AIAA journal* 36(9), pp. 1618–1625.

Rouhani, S. and Sohal, M. 1983. Two-phase flow patterns: A review of research results. *Progress in Nuclear Energy* 11(3), pp. 219–259.

Ruith, M., Chen, P., Meiburg, E. and Maxworthy, T. 2003. Three-dimensional vortex breakdown in swirling jets and wakes: direct numerical simulation. *Journal of Fluid Mechanics* 486, pp. 331–378.

Rusche, H. 2003. *Computational fluid dynamics of dispersed two-phase flows at high phase fractions*. Ph.D. thesis, Imperial College London (University of London).

Salim, S. M. and Cheah, S. 2009. Wall y strategy for dealing with wall-bounded turbulent flows. In: *Proceedings of the International MultiConference of Engineers and Computer Scientists*. vol. 2.

Saqr, K. M., Aly, H. S., Wahid, M. A. and Sies, M. M. 2010. Numerical simulation of confined vortex flow using a modified k-epsilon turbulence model. *CFD letters* 1(2), pp. 87–94.

Sarkar, S. and Lakshmanan, B. 1991. Application of a reynolds stress turbulence model to the compressible shear layer. *AIAA journal* 29(5), pp. 743–749.

Schlesinger, S., Crosbie, R. E., Gagné, R. E., Innis, G. S., Lalwani, C., Loch, J., Sylvester, R. J., Wright, R. D., Kheir, N. and Bartos, D. 1979. Terminology for model credibility. *Simulation* 32(3), pp. 103–104.

Schöberl, J. 1997. Netgen an advancing front 2d/3d-mesh generator based on abstract rules. *Computing and visualization in science* 1(1), pp. 41–52.

Schwartz, I. R. 1975. Minimization of jet and core noise of a turbojet engine by swirling the exhaust flow. In: *Aero-Acoustics Conference, 2nd, Hampton*. AIAA, United States.

Seavey, M. 1985. Abrasive blasting above 100 psi. *Journal of Protective Coatings & Linings* 2(7).

Seiner, J. and Yu, J. C. 1984. Acoustic near-field properties associated with broadband shock noise. *AIAA journal* 22(9), pp. 1207–1215.

Settles, G. and Garg, S. 1996. A scientific view of the productivity of abrasive blasting nozzles. *Journal of Thermal Spray Technology* 5(1), pp. 35–41.

Shih, T.-H., Liou, W. W., Shabbir, A., Yang, Z. and Zhu, J. 1995a. A new k-ε eddy viscosity model for high reynolds number turbulent flows. *Computers & Fluids* 24(3), pp. 227–238.

Shih, T.-H., Zhu, J. and Lumley, J. L. 1995b. A new reynolds stress algebraic equation model. *Computer Methods in Applied Mechanics and Engineering* 125(1), pp. 287–302.

Shirazi, S. A. and Truman, C. R. 1989. Evaluation of algebraic turbulence models for pns predictions of supersonic flow past a sphere-cone. *AIAA journal* 27(5), pp. 560–568.

ShockTube. 2011a. Oblique shock on a 10 Â° cone at mach 2.5. Tech. rep., OpenSim.

ShockTube. 2011b. 1d flow; transient waves; contact surface. Tech. rep., OpenSim.

Shtern, V., Borissov, A. and Hussain, F. 1998. Temperature distribution in swirling jets. *International journal of heat and mass transfer* 41(16), pp. 2455–2467.

Silva, G. G., Jiménez, N. P. and Salazar, O. F. 2012. Fluid dynamics of gas-solid fluidized beds .

Singh, N. K. and Ramamurthi, K. 2009. Formation of coanda jet from sharp-edged swirl nozzle with base plate. *Experimental Thermal and Fluid Science* 33(4), pp. 675–682.

Sizikov, V. S. 2005. *Well-posed, ill-posed, and intermediate problems with applications*, vol. 49. Walter de Gruyter.

Slotnick, J., Khodadoust, A., Alonso, J., Darmofal, D., Gropp, W., Lurie, E. and Mavriplis, D. 2014. Cfd vision 2030 study: A path to revolutionary computational aerosciences. *NASA Langley Research Center* .

Spalart, P. R. and Allmaras, S. R. 1992. A one equation turbulence model for aerodinamic flows. *AIAA journal* 94.

Spitz, J. 1987. *Sand blasting nozzle*, [Online]. US Patent 4,633,623.

Spur, G., Uhlmann, E. and Elbing, F. 1999. Dry-ice blasting for cleaning: process, optimization and application. *Wear* 233, pp. 402–411.

Stern, F., Wilson, R. V., Coleman, H. W. and Paterson, E. G. 2001. Comprehensive approach to verification and validation of cfd simulations, part 1: methodology and procedures. *Journal of fluids engineering* 123(4), pp. 793–802.

Stodola, A. 1903. *Steam Turbines*. Springer-Verlag.

Summerfield, M., Foster, C. R. and Swan, W. C. 1954. Flow separation in overexpanded supersonic exhaust nozzles. *Jet propulsion* 24(5), pp. 319–321.

Sweby, P. K. 1984. High resolution schemes using flux limiters for hyperbolic conservation laws. *SIAM journal on numerical analysis* 21(5), pp. 995–1011.

Syred, N. and Beér, J. 1974. Combustion in swirling flows: A review. *Combustion and Flame* 23(2), pp. 143 – 201.

Tam, C. and Tanna, H. 1982. Shock associated noise of supersonic jets from convergent-divergent nozzles. *Journal of Sound and Vibration* 81(3), pp. 337–358.

Tam, C. K. 1995. Supersonic jet noise. *Annual Review of Fluid Mechanics* 27(1), pp. 17–43.

Tanna, H. 1977a. An experimental study of jet noise part i: Turbulent mixing noise. *Journal of sound and Vibration* 50(3), pp. 405–428.

Tanna, H. 1977b. An experimental study of jet noise part ii: shock associated noise. *Journal of Sound and Vibration* 50(3), pp. 429–444.

Tavoulareas, E. S. 1991. Fluidized-bed combustion technology. *Annual review of energy and the environment* 16(1), pp. 25–57.

Tennekes, H. and Lumley, J. L. 1972. *A first course in turbulence*. MIT press.

Thakre, P. and Yang, V. 2008. Chemical erosion of carbon-carbon/graphite nozzles in solid-propellant rocket motors. *Journal of Propulsion and Power* 24(4), pp. 822–833.

Thompson, H. D. and Hoffmann, J. D. 1990. Swirling flow in thrust nozzles. *Journal of Propulsion and Power* 6(2), pp. 151–157.

Van der Hoef, M., van Sint Annaland, M., Deen, N. and Kuipers, J. 2008. Numerical simulation of dense gas-solid fluidized beds: A multiscale modeling strategy. *Annu. Rev. Fluid Mech.* 40, pp. 47–70.

Van Doormaal, J., Raithby, G. and McDonald, B. 1987. The segregated approach to predicting viscous compressible fluid flows. *Journal of turbomachinery* 109(2), pp. 268–277.

Van Leer, B. 1979. Towards the ultimate conservative difference scheme. v. a second-order sequel to godunov's method. *Journal of computational Physics* 32(1), pp. 101–136.

Van Leer, B. 2006. Upwind and high-resolution methods for compressible flow: From donor cell to residual-distribution schemes. *Communications in Computational Physics* 1(192-206), p. 12.

Van Wachem, B., Schouten, J., Van den Bleek, C., Krishna, R. and Sinclair, J. 2001. Comparative analysis of cfd models of dense gas–solid systems. *AIChE Journal* 47(5), pp. 1035–1051.

Vatanakul, M., Zheng, Y., Jia, L. and Zhang, K. 2005. Regime transition in a gas–liquid–solid fluidized bed. *Chemical Engineering Journal* 108(1), pp. 35–45.

Versteeg, H. K. and Malalasekera, W. 2007. *An introduction to computational fluid dynamics: the finite volume method*. Pearson Education.

Vu-Quoc, L., Zhang, X. and Walton, O. 2000. A 3-d discrete-element method for dry granular flows of ellipsoidal particles. *Computer methods in applied mechanics and engineering* 187(3), pp. 483–528.

Weller, H. G., Tabor, G., Jasak, H. and Fureby, C. 1998. A tensorial approach to computational continuum mechanics using object-oriented techniques. *Computers in physics* 12(6), pp. 620–631.

White, F. 2003. *Fluid Mechanics*. McGraw-Hill.

Wilcox, D. C. 1988. Reassessment of the scale-determining equation for advanced turbulence models. *AIAA journal* 26(11), pp. 1299–1310.

Wilcox, D. C. 1998. *Turbulence modeling for CFD*, vol. 2. DCW industries La Canada, CA.

Wolfshtein, M. 1969. The velocity and temperature distribution in one-dimensional flow with turbulence augmentation and pressure gradient. *International Journal of Heat and Mass Transfer* 12(3), pp. 301–318.

Wörner, M. 2003. *A compact introduction to the numerical modeling of multiphase flows*. Forschungszentrum Karlsruhe.

Wüthrich, B. and Lee, Y. 2007. *Simulation and validation of compressible flow in nozzle geometries and validation of OpenFOAM for this application*. Master's thesis, ETH, Swiss Federal Institute of Technology Zurich, Institute of Fluid Dynamics.

Xiao, Q., Tsai, H.-M. and Papamoschou, D. 2007. Numerical investigation of supersonic nozzle flow separation. *AIAA journal* 45(3), pp. 532–541.

Xiao, Q., Tsai, H. M., Papamoschou, D. and Johnson, A. 2009. Experimental and numerical study of jet mixing from a shock-containing nozzle. *Journal of Propulsion and Power* 25(3), pp. 688–696.

Xu, B. and Yu, A. 1997. Numerical simulation of the gas-solid flow in a fluidized bed by combining discrete particle method with computational fluid dynamics. *Chemical Engineering Science* 52(16), pp. 2785–2809.

Yajnik, K. and Subbaiah, M. 1973. Experiments on swirling turbulent flows. part 1. similarity in swirling flows. *Journal of Fluid Mechanics* 60(04), pp. 665–687.

Yakhot, V. and Orszag, S. A. 1986. Renormalization-group analysis of turbulence. *Physical Review Letters* 57(14), p. 1722.

Yang, N., Wang, W., Ge, W. and Li, J. 2003. Cfd simulation of concurrent-up gas–solid flow in circulating fluidized beds with structure-dependent drag coefficient. *Chemical Engineering Journal* 96(1), pp. 71–80.

Yu, Y., Xu, J., Mo, J. and Wang, M. 2014. Principal parameters in flow separation patterns of over-expanded single expansion ramp nozzle. *Engineering Applications of Computational Fluid Mechanics* 8(2), pp. 274–288.

Yu, Y.-K. and Chen, R.-H. 1997. A study of screech tone noise of supersonic swirling jets. *Journal of sound and vibration* 205(5), pp. 698–705.

Zaman, K. B., Bridges, J. and Huff, D. 2011. Evolution from 'tabs' to 'chevron technology'-a review. *International Journal of Aeroacoustics* 10(5), pp. 685–710.

Zhang, J., Jackson, T. L., Najjar, F. and Buckmaster, J. 2009. High-fidelity multiphysics simulations of erosion in srm nozzles. *AIAA Paper* 5499, p. 2009.

Appendix A

Discretisation

Finite Difference method

Most common representation for finite difference method is based on Taylor series. If $u_{i,j}$ is the x component of velocity at point (i, j), then the velocity at point $(i+1, j)$, can be expressed by Taylor series as:

$$u_{i+1,j} = u_{i,j} + \left(\frac{\partial u}{\partial x}\right)_{i,j} \Delta x + \left(\frac{\partial^2 u}{\partial x^2}\right)_{i,j} \frac{(\Delta x)^2}{2} + \left(\frac{\partial^3 u}{\partial x^3}\right) \frac{(\Delta x)^3}{6} + \ldots \tag{A.1}$$

Solving equation A.1 for $(\partial u/\partial x)_{i,j}$, leads to:

$$\left(\frac{\partial u}{\partial x}\right)_{i,j} = \underbrace{\frac{u_{i+1,j} - u_{i,j}}{\Delta x}}_{Finite\,difference\,representation} \underbrace{- \left(\frac{\partial^2 u}{\partial x^2}\right)_{i,j} \frac{(\Delta x)^2}{2} - \left(\frac{\partial^3 u}{\partial x^3}\right) \frac{(\Delta x)^3}{6} - \ldots}_{Truncation\,error} \tag{A.2}$$

Or the above equation can be written as :

$$\left(\frac{\partial u}{\partial x}\right)_{i,j} = \frac{u_{i+1,j} - u_{i,j}}{\Delta x} + O(\Delta x) \tag{A.3}$$

where the term $O(\Delta x)$ represents the order of magnitude of the truncation error. Therefore the equation A.3 expressed the partial derivative as *first-order forward difference* method. Writing

Taylor series expansion for term $u_{i-1,j}$, about $u_{i,j}$, will lead to:

$$\left(\frac{\partial u}{\partial x}\right)_{i,j} = \frac{u_{i,j} - u_{i-1,j}}{\Delta x} + O(\Delta x) \tag{A.4}$$

where this time the partial derivative is expressed by *first-order rearward (backward) difference* method. Subtracting equation A.1 and A.4, results in

$$\left(\frac{\partial u}{\partial x}\right)_{i,j} = \frac{u_{i+1,j} - u_{i-1,j}}{2\Delta x} + O(\Delta x)^2 \tag{A.5}$$

which is *second-order central difference* expression for the partial derivative. Because in the truncation error the lowest terms involved was $O(\Delta x)^2$, therefore it is in second order accuracy.

Errors and Stability analysis

Round off error is the numerical error introduced after a repetitive number of calculations in which the computer is rounding the numbers. Considering below definitions :

A analytical solution of partial differential equation.

D exact solution of difference equation.

N numerical solution from a real computer with finite accuracy

Then we can write

$$\begin{aligned} Discretisation\,error &= A - D \\ Round\,off\,error &= \varepsilon = N - D \end{aligned} \tag{A.6}$$

Therefore the numerical solution can be expressed as:

$$N = \varepsilon + D \tag{A.7}$$

As the solution progresses from step n to $n+1$, it will be stable if :

$$\frac{\varepsilon_i^{n+1}}{\varepsilon_i^n} \leq 1 \tag{A.8}$$

If the ε_i's grow larger during marching the solution from n to $n+1$, then the solution is unstable. Considering unsteady, one dimensional problem, the random variation of ε with x and time, can be expressed analytically by a Fourier series as follows :

$$\begin{aligned} \varepsilon(x,t) &= \sum_{m=1}^{N/2} A_m(t)\, e^{ik_m x} \\ e^{ik_m x} &= \cos k_m x + i \sin k_m x \end{aligned} \tag{A.9}$$

where k_m is the wave number and N is the intervals between $N+1$ grid points. However, it is logical to assume an exponential variation with time; errors tend to grow or diminish with time. Hence we can write :

$$\varepsilon(x,t) = \sum_{m=1}^{N/2} e^{at} e^{ik_m x} \tag{A.10}$$

where a is a constant and could have different values for different m's.

Appendix B

Abrasive Blasting Media

There are a variety of abrasive blast materials that can be used in air or water blasting processes used to remove paint or any other contaminants from engine heads, valves, pistons, turbine blades in the aircraft, automotive industries, vessels and marine structures, and etc. Blast material particles, also referred to as "grit", are about 1/8" in diameter. These normally jagged or sharp-edged particles become rounded and somewhat reduced in size after being blasted against work-pieces (for example to remove paint).

Spent abrasive blast material may contain a variety of pollutants. Fresh, or unused abrasive blast media is even considered a "dangerous" or "special" waste in some states due to gill abrasion which can be fatal to some fish; therefore, abrasive blast media, used or unused, should not be discharged into State waters.

The general information of some common abrasive blasting media are summarized in following sections of the present appendix.

Corn cob

Corn cob blasting grit (Figure B.1) is a safe blasting media for delicate parts in addition to use as the preferred blasting grit for log homes and other wood surfaces. Corn cob grit abrasive will remove surface contamination, debris and coatings with little to no impact on the substrate. Corn cob is a biodegradable, organic blasting media that is obtained from the hard woody ring of the cob. It is resistant to break down and can be re-used multiple times in the blasting process. Corn cob is available in a variety of grit sizes and presents no health or environmental hazards. Virtually dust-free blasting with no sparking leaves a clean and dry surface.

Bulk density	0.41-0.51 g/cm^3
Particle Shape	Angular, multi- faceted
Hardness	4.5 Moh's

Figure B.1: Corn cob

Proper selection of corn cob grit size is important in blasting operations to balance aggressiveness with desired results.

Aluminium Oxide

Aluminum oxide (Figure B.2) is an atmospheric oxide with the chemical formula Al_2O_3. It is commonly referred to as alumina, Aluminum oxide is a sharp, abrasive blasting material used in sand blast finishing. It is harder than most common dry abrasive blast media and will cut even the hardest metals and surfaces.

Approximately 50% lighter than metallic media, aluminum oxide abrasive grain has twice as many particles per pound. The fast-cutting action minimizes damage to thin materials by eliminating surface stresses caused by heavier, slower cutting media.

Aluminum oxide grit powder has a wide variety of applications, from cleaning engine heads, valves, pistons and turbine blades in the aircraft industry to lettering in monument and marker inscriptions. It is also commonly used for matte finishing, as well as cleaning and preparing parts for metalizing, plating and welding. Aluminum oxide abrasive grain is the best choice for an abrasive sand blasting and polishing grain as well as for preparing a surface for painting .

Density	1.8-2 g/cm^3
Melting point	2072 $°C$
Boiling point	2977$°C$
Hardness	8-9 Moh's

Figure B.2: Aluminium Oxide

White Aluminium Oxide

White aluminum oxide (or white aluminum oxide) grit (Figure B.3) is a 99.5% ultra pure grade of blasting media. White aluminum oxide is increasingly being used in critical, high-performance microdermabrasion equipment. The purity of this media along with the variety of grit sizes available make it ideal for both traditional microdermabrasion processes as well as high-quality exfoliating creams .

White aluminum oxide is an extremely sharp, long- lasting blasting abrasive that can be recycled many times after the initial media blasting. It is the most widely used abrasive in blast finishing and surface preparation because of its cost, longevity and hardness. Harder than other commonly used blasting materials, white aluminum oxide grains penetrate and cut even the hardest metals and sintered carbide.

Approximately 50% lighter than metallic media, white aluminum oxide has twice as many particles per pound. The fast-cutting action minimizes damage to thin materials by eliminating surface stresses caused by heavier, slower-cutting media blasting grits. White aluminum oxide blasting media has a wide variety of applications, including cleaning engine heads, valves, pistons and turbine blades in the aircraft and automotive industries. White aluminum oxide is also an excellent choice for preparing a hard surface for painting.

Density	1.75-1.95 g/cm^3
Melting point	2000°C
Max usable Temperature	1900°C
Hardness	2000-2200 kg/mm^2

Figure B.3: White Aluminium Oxide

Bulk density	1.3 g/cm^3
Shape	Angular
Hardness	5-6 Moh's

Figure B.4: Crushed Glass Grit

Crushed Glass Grit

Crushed glass grit (Figure B.4) is manufactured from 100% post consumer, recycled bottle glass. This glass grit delivers superior performance relative to mineral/slag abrasives. Crushed glass grit contains no free silica, is non-toxic and inert and contains no heavy metals typically found in coal and copper slags.

The angular particles in crushed glass grit allow for aggressive surface profiling and removal of coatings such as epoxy, paint, alkyds, vinyl, polyurea, coal tar and elastomers. Glass grit is lighter weight than many slags, allowing for increased consumption efficiency and production time – up to 30-50% less glass grit used. Crushed glass grit delivers very low particle embedment, which produces a whiter, cleaner finish. Similar to many slags, crushed glass grit has a hardness of 5.0 – 6.0 on the Moh's Hardness Scale.

Since crushed glass grit is manufactured from recycled bottle glass, it contains no free silica which is commonly found in blasting sand. The use of post-consumer glass directly benefits the environment by diverting waste from landfills. Crushed glass grit is free of heavy metals such as arsenic, lead, asbestos, beryllium, titanium, etc., all typically found in coal and mineral slags.

Glass Beads

Glass bead (Figure B.5) or dry bead blasting uses spherical beads for cleaning metal parts without damaging the surface. This media offers a gentle cleaning process creating a softer, more cosmetic finish than angular abrasives. Glass bead abrasives provide a silica-free option for blast cleaning, peening, honing, descaling and light deburring. Glass beads can be recycled approximately 30 times. Chemically inert and environmentally friendly, glass beads are an acceptable method of metal cleaning or surface finishing when properly controlled.

Glass bead cleaning is suitable for soft metals such as aluminium and brass. Ideal for pistons, engine blocks and light rust removal. Glass bead is a good choice for the restoration of car parts, motorcycles and other components where a gentle cleaning action is required.

Plastic Abrasives

Plastic Abrasives (Figure B.6) such as Urea, Acrylic, and Melamine deliver a highly effective stripping rate, removing coatings and contaminants without damaging the base metal. They

Bulk density	1.5-1.6 g/cm^3
Specific density	2.5 g/cm^3
Shape	Round
Hardness	5-6 Moh's

Figure B.5: Glass Beads

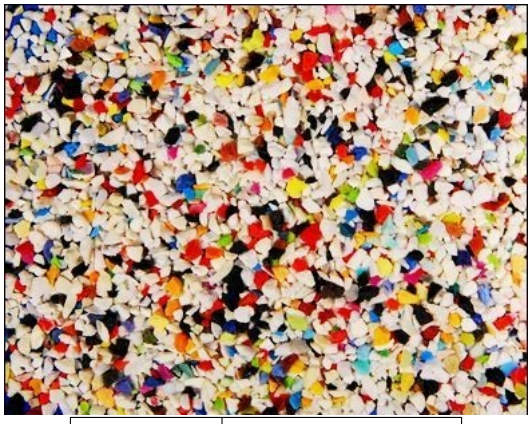

Density	1.16-1.5 g/cm^3
Shape	Angular-cubical
Hardness	2-4 Moh's

Figure B.6: Plastic Abrasives

are ideal for paint stripping, cleaning, deflashing and deburring operations on aluminium and other soft metals.

Plastic abrasives are widely used for restoring components in the aerospace and automotive industries.

Arcylic Acrylic media is the longest lasting media on the market. It is very gentle on the substrate and engineered for stripping the most sensitive surfaces while providing an effective stripping rate. Acrylic media offers an excellent range of stripping capabilities and is termed a multipurpose media by its users. Standard mesh sizes are 16-20, 20-30 and 30-40.

Melamine Melamine is engineered for stripping the most difficult surfaces while providing an effective stripping rate. Melamine is the most aggressive plastic abrasive, offering an excellent range of stripping capabilities. Melamine can be used as a replacement for glass beads and other harsh abrasives. Standard mesh sizes are 8-12, 12-16, 16-20, 20-30, 30-40 and 60-80.

Urea Urea is a plastic grain stripping abrasive used in sandblasting operations. It is the most widely used plastic media. Urea is environmentally friendly and recyclable - an alternative to chemical stripping. Urea is formulated to meet an increased level of stripping performance where stripping speed outweighs other considerations. Urea is able to strip tough coatings with an impressive strip rate. Urea is typically used for less sensitive applications. Standard mesh sizes are 8-12, 10-20, 12-16, 16-20, 20-30, 30-40 and 40-60.

Pumice

Pumice (Figure B.7) is a natural mineral - volcanic ash formed by the solidification of lava that is permeated with gas bubbles. Pumice powder is used chiefly as an abrasive and is among the softest of all media. Use pumice powder for less aggressive operations where the protection of the surface is of supreme importance. Pumice is the best media choice for tumbling plastics.

Silicon carbide

Silicon carbide (Figure B.8) is the hardest blasting media available. High-quality silicon carbide media is manufactured to a blocky grain shape that splinters. The resulting silicon carbide abrasives have sharp edges for blasting. Silicon carbide has a very fast cutting speed

Density	0.25 g/cm^3
Shape	Angular
Hardness	6 Moh's

Figure B.7: Pumice

Density	3.21 g/cm^3
Melting point	2730-3003 $°C$
Hardness	9-9.5 Moh's

Figure B.8: Silicon carbide

Bulk density	3.7-4.4 g/cm^3
Shape	Angular
Hardness	40-60 RC

Figure B.9: Steel grit

and can be recycled and reused many more times than sand. The hardness of silicon carbide allows for much shorter blast times relative to softer blast media.

Silicon carbide grit is the ideal media for use on glass and stone in both suction or siphon and direct pressure blast systems. The ability to be recycled multiple times results in a cost-effective silicon carbide grit blast media with optimal etching results.

Since silicon carbide grit is harder than aluminium oxide, it can be used efficiently for glass engraving and stone etching. Silicon carbide grit blast media has no free silica, does not generate static electricity and is manufactured to contain minimal magnetic content.

Steel grit

Steel grit blasting (Figure B.9) is used for aggressive cleaning projects such as stripping contaminants from steel and other industrial metals. The cleaning action of steel grit produces an etched surface providing excellent adhesive properties for a variety of paints and coatings.

Steel grit blasting is suitable for steel and foundry metals and is also used for aircraft and aerospace components.

Bulk density	4.5-4.7 g/cm^3
Specific density	7.4-7.6 g/cm^3
Shape	Round
Hardness	40-51 RC

Figure B.10: Steel shot

Steel shot

Steel ball (Figure B.10) shot-blasting is one of the most widely used methods for cleaning and stripping metal surfaces and components. The process involves firing small steel balls (1-6mm diameter) at high speed against the surface of the metal or component. The finish is determined by the size of the steel shot. Larger shot has a more aggressive Shape cleaning action and produces a rougher finish. Smaller steel shot creates a smoother, more polished surface.

Walnut shell

Walnut shell grit (Figure B.11)is the hard fibrous product made from ground or crushed walnut shells. When used as a blasting media, walnut shell grit is extremely durable, angular and multi-faceted, yet is considered a soft abrasive. Walnut shell blasting grit is an excellent replacement for sand (free silica) to avoid inhalation health concerns.

Cleaning by walnut shell blasting is particularly effective where the surface of the substrate under its coat of paint, dirt, grease, scale, carbon, etc. should remain unchanged or otherwise unimpaired. Walnut shell grit can be used as a soft aggregate in removing foreign matter or coatings from surfaces without etching, scratching or marring cleaned areas.

Density	0.5-1.18 g/cm^3
Shape	Angular
Hardness	3 Moh's

Figure B.11: Walnut shell

When used with the right walnut shell blasting equipment, common blast cleaning applications include stripping auto and truck panels, cleaning delicate molds, jewellery polishing, armatures and electric motors prior to rewinding, deflashing plastics and watch polishing. When used as a blast cleaning media, walnut shell grit removes paint, flash, burrs and other flaws in plastic and rubber molding, aluminium and zinc die-casting and electronics industries. Walnut shell can replace sand in paint removal, graffiti removal and general cleaning in restoration of buildings, bridges and outdoor statuaries. Walnut shell is also used to clean aircraft engines and steam turbines.

Olivine Sand

Olivine Sand (Figure B.12)as an abrasive media,is noted for its high Mohs Hardness, low uniform thermal expansion, sharp edges and its remarkable ability to resist fracture from thermal and impact shock. Olivine has been famous for years as an excellent abrasive media for Sand Blasting and Water jet Cutting. Especially Indian Olivine Sand is having Highest Hardness and Lowest Loss on Ignition makes it an ideal and economical abrasive media for Sand Blasting and Water jet Cutting.

The application for olivine are:

- Refractory Sand, to manufacture manganese steel castings, and to form alloys.

Specific density	3.32 g/cm^3
Bulk density	1.6-1.9 g/cm^3
Melting Point	1600 $°C$
Thermal Expansion	0.0083 $1/K$
Thermal Conductivity	0.0025 $cal/s-cm$
Hardness	6.5 Moh's

Figure B.12: Olivine Sand

- Refractory Industry uses Olivine Sand for forming bricks and shapes, as it has a high melting point, moderate thermal expansion, and stable crystalline structure.
- Temperature-loadable moulding sand and facing sand in foundry.
- Replacement of Garnet Sand for Shot Blasting.

Media abrasive for Shot-Blasting system

Abrasive Media	Properties	Applications	Advantages	Limitations
ALUMINIUM OXIDE	Very hard	Fast cutting; matte finishes; descaling and cleaning of coarse and sharp textures Cleaning hard metals (e.g. Titanium)	Recyclable	Must be Reclaimed and Reused for Economy
BAKING SODA(Sodium Bicarbonate)	Natural, water soluble, non-sparking, non flammable	General Paint Removal Stripping Aircraft Skins Cleaning Surfaces in Food Processing Plants Removing Paint from Glass	Less Material Used/Less Cleanup Low Nozzle Pressures (35-90 PSI)	May Damage Soft Brick
COAL SLAG	Hard, uniform density, low friability	General Paint, Rust & Scale Removal from Steel Paint Removal from Wood	Rapid Cutting	Tendency to Embed in Mild Steel May Contain Toxic Metals
COPPER SLAG	Hard, sharp edged	General Paint, Rust & Scale Removal from Steel Paint Removal from Wood	Rapid Cutting	Tendency to Imbed in Mild Steel May Contain Toxic Metals
CORN COB GRANULES	Medium hardness, non sparking	Paint & Rust Removal from Wood & Metal	Low Consumption Low Dust Levels Biodegradable	Does Not Create an Anchor Profile

DRY ICE(Carbon Dioxide)	Natural gas in solid state	Cleaning Aircraft Parts Cleaning Exotic Metals	No Residue Remains Minimal Cleanup	
GARNET	Very hard and heavy	General Paint, Rust & Scale Removal from Steel	Lower Nozzle Pressures (60-70 PSI) Low Dust Levels Fast Cleaning Rates Can be Recycled	
GLASS BEADS	Manufactured of soda lime glass	Decorative blending; light deburring; peening; general cleaning; texturing	Recyclable Provide High Luster Polished Surface	Does Not Create an Anchor Profile
NICKEL SLAG	Very hard, sharp edged	General Paint, Rust & Scale Removal from Steel	Rapid Cutting	Used in Wet Blasting May Contain Toxic Metals
NUT SHELLS	Soft, non-sparking	Very light deburring, fragile parts, Cleaning Soft Materials (e.g. Aluminium, Plastic, Wood), Deflashing of plastics, Cleaning Surfaces in the Petroleum Industry	High Removal Speed Non-Sparking Low Consumption	Non-Etching Potential Fire Hazard
OLIVINE	Natural mineral, hard, angular	Clean Light Mill Scale & Rust from Steel	Low Chloride Ion Level Low Conductivity	
PLASTIC MEDIA	Soft, non-abrasive, polyester	Cleaning Soft Metals & Composites Cleaning Metal Fabric Screens	Recyclable Does Not Damage Metal Surfaces Low Nozzle Pressures (20-40 PSI)	Anchor Profile Limited to Soft Substrates (e.g. Aluminium and Plastic)
STAUROLITE	Rounded grains, Hard, irregular shape	Cleaning Corroded, Pitted, Weathered Steel Creating Anchor Profile on New Steel	Good Feathering Low Dust Levels Recyclable 3-4 Times	May Contain Up to 5% Free Silica

STEEL GRIT & SHOT	Uniform size and hardness	Paint, Rust & Scale Removal from Steel	Can be Recycled 100-200 Times Low Dust Levels Superior Visibility Portable Blast Rooms Available Creates Anchor Profile	
Silica sand	quickly breaks up	the most commonly used abrasive	Rapid Cutting	high volume of dust created by the sand breaking when hitting the object.

Anglia Ruskin University

Numerical Investigation of Single and Multiphase Supersonic Swirl Flow in Convergent-Divergent Nozzle

Ehsan Eslamian Koupaei